Advanced design and experimental validation of MRI contrast agents for fluid pressure mapping using microbubbles

Robert H. Morris

A thesis submitted in partial fulfilment of the requirements of
Nottingham Trent University for the degree of Doctor of Philosophy

This research programme was carried out in collaboration with Aston University

August 2009

“You know, what these people do is really very clever. They put little spies into the molecules and send radio signals to them, and they have to radio back what they are seeing.”

Felix Bloch recalling Niels Bohr’s description of Nuclear Magnetic Resonance.

ACKNOWLEDGEMENTS

This work has been funded by the UK Engineering and Physical Sciences Research Council under grant number EP/C535219/1 for which we are very grateful. Additionally, funding for conference travel and subsistence has been provided by the CR Barber Trust through the UK Institute of Physics and the Magnetic Resonance in Porous Media student travel grant both of which allowed this work to be presented at conferences that were not included in the original grant application.

My Supervisor Martin Bencsik tirelessly pushed me to achieve the very best work possible for which I am eternally grateful. I owe the majority of my research style to him, including most importantly the benefits of keeping a good lab book, although sadly not the ability to own CDs without irreparably scratching them. His red fountain pen has graced many a publication (printed on A3) and invariably carries valuable assistance.

My parents Kathleen and Dennis Morris and partner Nicola Doy who provided unquestioning support throughout this work (and before) and along with Martin read this thesis and provided invaluable comments on it with no complaint. Thank you for everything.

The work which has been undertaken over the course of this project has relied on the assistance of a great number of people who often did not receive anything in return. These small acknowledgements do little to make up for the great effort which everyone has put into this work. In chronological order and hopefully without any omissions the following people have been instrumental in the success of this project:

Initially the simulation work was greatly aided by the thesis and Fortran80 code kindly supplied by Rohan Dharmakumar. Yvonne Perrie, Anil Vangala and later Randip Kaur of Aston University who have made the microbubbles used throughout this project and have attempted to improve the protocols and formulations used. David Parker of Nottingham Trent University who has made an incredible range of sample holders and other equipment for the project and tolerated strange, not to scale, back of the envelope drawings before we discovered Google Sketchup. Gareth Cave, Andrew Brooks and Neil Bowley also of Nottingham Trent University who helped on each occasion that we found ourselves out of depth with the chemistry of the project including an endless supply of super paramagnetic iron oxide particles and whatever chemicals we needed, however obscure. Graham Tilbury, previously of Nottingham Trent University who not only helped every time the SEM produced unexpected error messages but also helped to organise a weekly supply of cake through ‘Sweet

Thursday' which provided a well needed moral boost towards the end of the week for the chemistry and physics PhD students. David Fairhurst of Nottingham Trent University who taught both myself and Martin almost everything we ever needed to know about rheology and provided the initial 'Sweet Thursday' motivation. Sandy Milne of AM Glassware worked with us to develop the sintered glass cylinders to specifications which neither us nor him initially believed possible. Andrew Long and the University of Nottingham engineering technician Rodger Smith who helped us to embed the sintered cylinders in epoxy allowing our initial experiments to take place and giving us the know-how to reproduce it. Peter Morris who facilitated our access to the MRI scanner at the University of Nottingham. Malcolm Prior of the University of Nottingham helped understand some of the unexpected oddities of Paravision. Jane Braithwaite who kindly provided microscopes for microbubble investigations. Nikolaus Nestle of BASF whom we met at the MRPM conference in 2006 who became an integral part of the project providing constant advice on polysaccharide gels and their properties, and many an entertaining meal at curry houses across Europe. Eiichi Fukushima without whom we would not have had the initial stimulus for the solid gel study. Mike Newton of Nottingham Trent University who has provided assistance throughout the project in terms of knowledge, equipment and Bourbon biscuits, without whom I might not have automated our experiments so successfully driven by the 'highest form of efficiency'. Peter Gardiner of the Royal Holloway Institute for Environmental Research who kindly provided the vacuum equipment which we used to degas the gels, as well as every piece of glassware I have ever needed since. Bob Chettle of the University of Nottingham who provided MR electronics advice for low frequency duplexers, amplifiers and the work with John Owers-Bradley. Marius Mada, Elliot Woolley and John Owers-Bradley who worked with us to try and image the gas adsorption in our porous samples. Petrik Galvosas and Jörg Kärger of the University of Leipzig who very kindly worked with us to measure the diffusion of water in our gel samples, and along with Moisés Fernandez and Marcel Gratz made for some great company on evenings out both sides of the Atlantic. Glen McHale for helping with the mathematics of the analytical prediction of the optimum setting for the RARE effective echo time. Marie Pierre Krafft and Giles Waton who kindly explained the protocol for producing perfluoroalkylated microbubbles. Hannah Edwards formerly of the University of Nottingham who collected the incredible SEM images of our microbubbles and helped with our understanding of the gel interactions.

Last but not least, those with whom I have shared ideas, lab space and yet more cake over the course of this project, and without whom the last four years would have not have been so enjoyable - Christophe Trabi, Gary Wells, Hans Adriaensen, Carl Evans, Nicola Doy, Neil Shirtcliffe and David Willmer.

Thank you to everyone for helping make this work the success that it has been.

CONTENTS

ABSTRACT

This work is related to monitoring fluid pressure using Magnetic Resonance Imaging or MRI and includes numerical simulations and experimental MRI. The nature of this study is such that techniques other than MRI have been extensively used to assess the contrast agent for its physical behaviour. These techniques include rheometry, light scattering, optical and scanning electron microscopy.

Six MRI experiments in total were performed: The first two experiments use standard spin echo imaging techniques to test various lipid preparations which are then used as a contrast agent to pressure in a porous medium. The remaining experiments are performed using a fast imaging technique and investigate various improvements to the contrast agent which resulted in the development of an agent exhibiting an unprecedented level of sensitivity.

A variety of lipid preparations are utilised throughout the experiments. Initial testing reveals that the DSPC lipid offers the greatest stability, although a fluorinated lipid is used in a later study for an improved synergy between the shell and gas microbubble components. Having assessed the microbubble stability, preparations are prepared as in the work previously published in the area. This preparation is tested in two porous media to investigate the sensitivity of the contrast agent to changes in pressure. A sensitivity of 20% signal change per bar is found in porous media although a drift of $11\%\text{h}^{-1}$ is also observed.

An improved preparation was then developed by using an alternative polysaccharide gel, gellan gum. This medium allows a large increase in viscosity without compromising the diffusion coefficient of water throughout the gel network which is of key importance to the sensitivity of the technique. The suitability of the new preparation is assessed using viscosity, turbidity, diffusion and MRI measurements. The results show that a very stable contrast agent, demonstrating a sensitivity of 38% signal change per bar and negligible drift has been produced.

The contrast agent is then developed further to produce a soft solid for potential applications in granular dynamics. By cross linking another polysaccharide gel, carageenan gum, into which the microbubbles have been mixed, a contrast agent has been successfully tested. This agent is again assessed using diffusion and elastic stress measurements which demonstrate its suitability to monitor pressure.

Using a wide range of techniques including time lapse photography, rheology, diffusion NMR and MR imaging, contrast agents have been produced which meet specific applications. Contrast agents in both solid and liquid phases have been produced to allow measurements in porous media and in granular dynamic systems. These contrast agents have been optimised in terms of the lipids used for the microbubbles, the chemistry used for production of the suspending media, the protocols for production, assessment and application of each agent and MRI sequences used to collect images. In doing so a reliable method for tailoring contrast agents to pressure has been developed leading to novel experimental measurements which may be applicable to oil recovery and medicine alike.

PREFACE

This document is divided into nine chapters, each with several subsections. In the sections incorporating experimental work, I have elected to present the experiments from protocol design to results and discussion. This allows the clearest presentation of all experiments.

Chapter II offers the reader a review of the relevant literature and appropriate background to the work undertaken. Chapter III relates to the work on simulating the evolution of the NMR signal based on a single microbubble in a universe of diffusing protons and adaptations to this to test various parameters of the practical experiments.

The remaining chapters cover the practical experiments conducted using MRI and the associated measurements which were necessary for them to take place. This involved microscopy, rheology and novel optical measurements as well as diffusion NMR and traditional pressure measurements. The experimental protocols should be sufficiently descriptive that the experiments are fully repeatable given a small amount of equipment and access to an MRI scanner. The final section is concerned with a possible further extension in the hope that this interesting work can be taken in new directions in the future.

The appendices include a section of work carried out in collaboration with John Owers-Bradley and his group at the University of Nottingham with hyperpolarised Xenon gas and an attempt to apply this to our samples. The final appendix includes publications produced during the course of this work to which the reader is directed for reference.

From some of the work presented here, six peer reviewed publications have been accepted. It is the author's opinion that there are at least two further sections of this work which are of publishable standard, and this will hopefully take place in the near future.

I. INTRODUCTION

The last twenty years have seen major advances in non invasive imaging techniques. Although it has found applications predominantly in medical diagnostic imaging, magnetic resonance techniques have many other diverse uses from chemical engineering [1] to bore hole logging to determine optimum sites for oil recovery [2] and from testing the quality of rubber in car tyres [3] to on line process monitoring of fruit damage [4].

MRI is intrinsically sensitive to density of water which is somewhat useful for medical applications. However, it is also possible to measure time constants for the exchange of energy between the nuclear spins under investigation and both their surrounding environment and each other, by collecting several images and post processing them. These images are considerably more useful for medical interpretation than the water density measurements as different tissue types have radically different time constants bringing about exceptional contrast. It is also possible to measure physically relevant processes such as fluid flow or molecular diffusion coefficients. In certain circumstances it is desirable to measure a process to which MRI is not intrinsically sensitive. To achieve this, contrast agents can be used. Contrast agents are materials which locally alter the NMR signal. This could be as simple as a paramagnetic particle suspension to enhance contrast relative to the surroundings or a hyperpolarised gas [5].

The pressure of a fluid saturating a porous medium can be measured non-invasively by conventional means only at the surface of the sample. This surface pressure does not allow the user to determine the internal pressure of a heterogeneous sample. A method has been previously developed to measure the local fluid pressure of a gas flowing in porous media with MRI [6]. This was however found to be unsuitable for media with high permeability such as sandstones.

It has been shown [7] using MRI, that a gas encapsulated within suspended micrometer sized phospholipid monolayer spheres (microbubbles) causes changes in the NMR signal intensity as a result of pressure changes in the surrounding medium. In this work, such a contrast agent and some that are more advanced, are applied to the understanding of the fundamental properties of fluid flow through porous media exhibiting permeability and pore size distributions similar to that of common sandstones.

I.1 Practical Motivation

The demand for oil is expected to have risen to 118 million barrels per day by 2030 [8]. The price per barrel is likely to continue to increase rapidly due in part to the increased demand and reduced availability. At the time of writing, the cost per barrel is around $75 although it was as high as $145 on the 3rd June 2008. If the current trend continues, it is predicted (as a worst case scenario) that the current reserves of crude oil will be depleted as soon as 2042 [9]. One of the many reasons for this is due to the fact that in many cases it is currently possible to extract less that 40% of the available oil [10]. Increasing this yield would greatly prolong the available supply.

Despite great efforts to understand the processes which are undertaken to recover oil, both from the practical and fundamental points of view, there are still few measurement methods allowing three dimensional pressure determination within a sample. In the majority of cases, oil is trapped within the structure of porous rock often several kilometres under the surface. The oil extraction process in these cases requires a method for inducing flow of this oil from within the structure. For this reason it is desirable to understand as many features of the process as possible. It is very common to use a second fluid to push the oil out of the rock. Inhomogeneities in the structure of the reservoir rock cause variations in distribution of pressure as the secondary fluid is driven into the sample. Better understanding of these processes could allow for development of new techniques for extracting a greater quantity of oil from a given reservoir.

This project was intended to determine some of the fundamental principles underlying the process of a fluid flowing through a porous sample and the effect that this flow has on the distribution of pressure throughout a rock core. This could then be scaled up to both large samples representing an oil saturated region in the rock bed and to include the two phase flow as is the case for oil displaced by water or some other liquid.

In addition to the petrochemical industries, these contrast agents may have medical applications. Although it is clear that the agents developed in this work are not suitable for *in vivo* medical imaging in their current form, due to the high concentrations that would be necessary, we have successfully produced agents which are sufficiently robust to withstand the pressure ranges found in the body. By increasing the magnetic susceptibility of the microbubbles, it should be possible to open up a range of imaging techniques to allow the monitoring of blood pressure in the body.

As is often the case with research of this nature, the project has taken many different directions, leading to a range of varied applications. The project has developed partly in response to interactions with other scientists at the various conferences at which work has been presented. The major application which has been found outside of the original scope of this project is the investigation of pressure in soft solids, using MRI. The motivation for this is found primarily in chemical engineering and in spite of finding a somewhat narrow range

of applications, they may be fundamental in understanding applications in a wider area of granular dynamics.

References

[1] M. D. Mantle and A. J. Sederman, "Dynamic MRI in chemical process and reaction engineering," *Progress in Nuclear Magnetic Resonance Spectroscopy*, vol. 43, no. 1–2, pp. 3–60, 2003.

[2] R. L. Kleinberg, A. Sezginer, D. D. Griffin, and M. Fukuhara, "Novel NMR apparatus for investigating an external sample," *Journal of Magnetic Resonance*, vol. 97, no. 3, pp. 466–485, 1992.

[3] R. A. Komoroski, S. N. Sarkar, and E. W. Wooten, "NMR Imaging of Elastomeric Materials.," *Macromolecules*, vol. 22, no. 2, pp. 600–607, 1998.

[4] R. R. Milczarek, M. E. Saltveit, T. C. Garvey, and M. J. McCarthy, "Assessment of tomato pericarp mechanical damage using multivariate analysis of magnetic resonance images," *Postharvest Biology and Technology*, vol. 52, no. 2, pp. 189–195, 2009.

[5] T. Watanabe, "Recent topics in NMR imaging and MRI," *Magnetic Resonance in Medical Sciences*, vol. 1, no. 1, pp. 38–49, 2002.

[6] M. Bencsik and C. Ramanathan, "Direct measurement of porous media local hydrodynamical permeability using gas MRI," *Magnetic Resonance Imaging*, vol. 19, no. 3–4, pp. 379–383, 2001.

[7] A. Alexander, T. McCreery, T. Barrette, A. Gmitro, and E. Unger, "Microbubbles as novel pressure-sensitive MR contrast agents," *Magnetic Resonance In Medicine*, vol. 35, no. 6, pp. 801–806, 1996.

[8] Energy Information Administration, "Annual report," tech. rep., 2007.

[9] S. Shafiee and E. Topal, "When will fossil fuel reserves be diminished?," *Energy Policy*, vol. 37, no. 1, pp. 181–189, 2009.

[10] Western Research Institute, "Wetting behavior of selected crude oil/brine/rock systems," tech. rep., 1995.

II. BACKGROUND AND THEORETICAL

In order to prepare the reader for the experimental work, an overview of the relevant literature and theory is presented here. This work sits on the border of chemistry and physics and has an early motivation from medicine. In consequence, some of the background material is heavily weighted toward these other disciplines. For this reason, where appropriate, the papers are summarised from the point of view of their physical implications and the reader is referred to the original articles for more application specific information.

II.1 MRI Principles

This section is intended for the reader with little or no MRI experience in the hope that a sufficient understanding of the experimental work is accessible. This is presented from the point of view of MR imaging using hydrogen nuclei only, although this general description also applies with little modification to various other nuclei suitable for NMR. To further aid the accessibility, a qualitative approach is adopted where possible.

For NMR to be possible, nuclei with intrinsic non-zero angular momentum are required. This allows interaction with an applied magnetic field and, with the application of a suitable radio frequency field, a small but detectable voltage can be induced in an appropriately placed coil. Before the application of any magnetic fields, a system of hydrogen nuclei (protons) will be at overall thermal equilibrium with no net magnetisation. If a static magnetic field B_0 is applied to this system, a small fraction of nuclei will reach a higher energy state. The difference in energy between this higher state and lower state is given by the Zeeman energy ($\Delta E = \frac{\hbar\gamma B_0}{\mu}$, where $\hbar$ is Planck's constant over two pi, γ is the gyromagnetic ratio and μ is the permeability) and is therefore proportional to the magnitude of the applied field. The population of nuclei in the higher energy state is also inversely proportional to the temperature of the system. The overall magnetisation is related to the quantity of nuclei which are in this higher energy state by equation II.1, i.e. not only to the factors already mentioned but also to the density of the nuclei.

$$M_0 \propto \frac{N_{High} - N_{Low}}{N_{High} + N_{Low}}, \tag{II.1}$$

where N_{High} and N_{Low} are the number of nuclei in the high and low energy states respectively.

These quantities are related by following the relationship between the equilibrium magnetisation M_0 and the

applied field:

$$M_0 = \frac{N\gamma^2\hbar^2 I(I+1)B_0}{3\mu kT}, \tag{II.2}$$

where N is the number of nuclei in the system, I is the spin quantum number ($-\frac{1}{2}$ for protons), B_0 is the magnetic field strength, k_B is Boltzmann's constant ($1.38\times10^{-3}JK^{-1}$) and T is the temperature in Kelvin. This shows that by increasing the magnetic field strength, or by reducing the temperature, the magnetisation can be increased.

In a thermally polarised system in a magnetic field as described here, this magnetisation is too weak to be measured using a magnetometer or similar device (as for example, at B_0 = 2.35 Tesla (T) the fraction of nuclear spins which contribute to the NMR signal is only 8×10^{-6} [1]). Instead, a series of other magnetic fields can be applied by means of radio frequency pulses, manipulating this magnetisation into a measurable form.

The Radio Frequency (RF) pulses applied to the system must be at the frequency given by the Larmor relationship (equation II.3) in order to have an effect.

$$\omega_0 = \gamma B_0, \tag{II.3}$$

where ω_0 is the angular frequency of the pulses and B_0 is the static magnetic field strength. By applying RF pulses at this frequency, it is possible to rotate the direction of the magnetisation relative to the static magnetic field.

By varying the time and amplitude of this applied pulse (at the frequency given by the Larmor relationship), specific angles (known as the flip angle, α) relative to the static magnetic field can be obtained according to equation II.4.

$$\alpha \int_0^{TP} \gamma|\mathbf{B_1}(t)|dt, \tag{II.4}$$

where TP is the time for which the pulse is applied and $|\mathbf{B_1}(t)|$ is the strength of the radio frequency field. When no external RF field is present, the net magnetisation will always attempt to return to the equilibrium state by precessing (at the Larmor frequency) about the direction of the static magnetic field. In doing so, a time varying magnetic field is created which can be monitored using a 'pick-up coil' placed perpendicularly to the direction of the static magnetic field. The induced voltage is proportional to the angle of the net magnetisation relative

to the static magnetic field and is zero when it is at equilibrium. By monitoring this voltage over time, some properties of the material under NMR investigation can be assessed. This process is known as longitudinal relaxation.

II.1.1 Spin-Lattice Relaxation

This is also known as T_1 or longitudinal relaxation and is a measure of the time taken for the magnetisation to return to the direction of the static magnetic field from an excited state. If we consider a hypothetical single isolated nucleus, the return to the ground state from the excited, takes around 10^5 years in a process known as spontaneous emission (because the magnetic dipole transition is much weaker than optical electric dipole transitions) [2]. If other nuclei are however present in the sample, stimulated emission occurs in which the nuclei interact with their environment allowing the bulk magnetization (M) to return to equilibrium (aligned with the static magnetic field along the z axis) in a much more rapid exponential process with time constant T_1 (typically less than ten seconds). The evolution of the component of the magnetisation along the z axis (M_z) is given by equation II.5.

$$M_z(t) = M_z(0)e^{-t/T_1} + M_0(1 - e^{-t/T_1}), \tag{II.5}$$

This relaxation occurs as the nuclei interact with the 'lattice' as a consequence of their rapid motion due to thermal energy. This leads to local magnetic field variations near the Zeeman energy either as a result of interaction with other moving nuclear magnetic moments, which is known as dipole dipole interaction, or because of fields generated by other molecules with unpaired electrons which is a mechanism that only occurs in samples comprised of more than one nuclear species.

II.1.2 Spin-Spin Relaxation

Although commonly referred to as a relaxation mechanism, the system does not actually lose energy as a result of Spin-Spin relaxation and hence this expression is misleading. A more accurate description is spin-spin dephasing, in which the relative directions of the nuclear magnetic moments in the system become scrambled. If an ideal system (no field or sample inhomogeneities) is supplied with energy at the Larmor frequency for an appropriate time duration, the bulk magnetisation can be made to lie perpendicular to the z axis in what is often termed the transverse plane (and hence spin-spin relaxation is also known as transverse relaxation). The nuclear magnetic moments will then precess around the direction of the static magnetic field as the system relaxes with T_1. The bulk magnetisation will again induce a time varying voltage in an appropriately placed pick up coil as in the case of spin-lattice relaxation. This voltage will be sinusoidal modulated by an exponential decay with time constant T_2. The sinusoidal component does not carry any useful information about the system so we can determine the evolution of the bulk magnetisation in the rotating reference frame. This is achieved by considering the signal from a point of reference which moves around the z axis at the Larmor frequency. In

this way, the change in signal is seen only as an exponential with time constant T_2 as given by equation II.6

$$M_{xy}(T_E) = M_{xy}(0)e^{-T_E/T_2}. \tag{II.6}$$

This rotating reference frame allows easy visualisation of nuclear magnetic moments which are precessing at a slightly different frequency to the reference frame such as those at higher or lower magnetic field strengths. It also allows relative changes in the speed of precession (caused by magnetic field variations) to be considered as phase changes, i.e. a slower precession will appear to lag behind a faster precession when viewed in the rotating reference frame.

The signal measured in the transverse plane is the superposition of all of the nuclear magnetic moments in the measurement volume and will be maximal when they are all aligned. If it were possible to measure the signal from a single magnetic moment with no neighbours there would be no signal decay via this mechanism. However, each magnetic moment creates its own magnetic field which influences its neighbours very slightly. Because of these slight variations, over time the measured signal will decay to zero as the phases of the magnetic moments (in the rotating reference frame) become scrambled or 'dephased'. If there are any inhomogeneities in the static magnetic or radio frequency fields, or inhomogeneities in the sample, the induced signal will decay more rapidly than before. The new exponential time constant is known as T_2^* and is that which is most often measured in realistic samples.

II.1.3 Spin Manipulation

In order to make useful measurements, it is desirable to be able to manipulate the spin system in some way to interrogate each of these relaxation constants or to investigate specific properties of the nuclei's environment. There are several possible ways to measure these exponential time constants and some of the manipulation techniques which can be used to achieve these are discussed in this section. By measuring these relaxation rates, it is possible to determine many properties of the sample.

II.1.3.1 Free Induction Decay - FID

The most basic method for determining some of the spin system properties is the application of a single RF pulse to tilt the bulk magnetisation into the transverse plane and measuring the resulting signal known as a Free Induction Decay or FID. In a relatively homogeneous sample, this results in a signal exhibiting a single exponential decay (with time constant T_2^*), although with real samples containing more than one nuclear environment, it can be biexponential. This signal will decay to zero as the phases of the magnetic moments (in the rotating reference frame) become scrambled. This method is used mostly on systems with static magnetic field strengths greater than 1T. It is often used for the initial set-up of various scanner settings such as transmit and receive amplifier gains, although there are many applications of the technique, particularly for samples which are undergoing motion and hence rapid assessment of the relaxation times are required, for example couette

flow [3] or bubbly pipe flow [4]. The signal measured in the pick up coil is a sinusoidal voltage modulated by a monoexponential envelope (in a homogeneous system, see Fig. II.1). Although very simple to implement, it is not possible, for example, to acquire an FID easily in an inhomogeneous field or to gather T_1 relaxation information so other techniques are used to acquire further information in such circumstances.

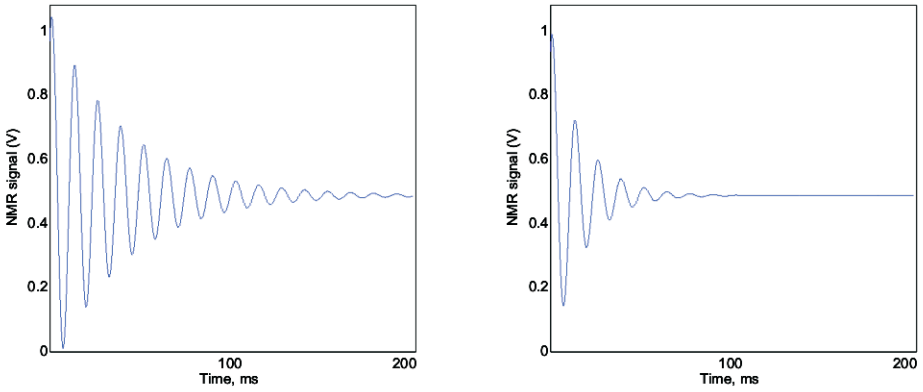

Fig. II.1: Two simulated FID signals with two different values of T_2^*. The left hand side has a T_2^* twice as long as the right hand side whilst both have the same Larmor frequency and amplitude.

II.1.3.2 Spin Echo - SE

As previously mentioned, Spin-Spin relaxation is phase scrambling of the magnetic moments. In non ideal systems, T_2^* can be very rapid and it is often advantageous to be able to somehow recover the signal after its initial decay. Hahn [5] found that in many situations this is indeed possible by applying a second RF pulse after a time τ which flips the direction of the magnetic moments in the system like a mirror image (flip angle $\alpha = 180°$, see Fig. II.2). After a further time τ the signal will be recovered. This is best described by considering a system of three protons with a fixed location in three different fields in the rotating reference frame (at the Larmor frequency for the proton in the intermediate field). The protons start in phase from the x axis for example. The first proton at a relatively low field will precess more slowly than the others resulting in a phase lag, whilst the higher field proton will develop a phase in advance of the others. After some time the relative phases of the magnetic moments will have become scrambled. If however the direction of the magnetic moments is mirrored about the x axis, the higher field proton will still precess as rapidly as before although back toward the x axis from which they started. After the same length of time as between the two RF pulses, the magnetisation will return to its initial value before again decaying. The time between the excitation pulse and the time at which the signal is maximal is known as the echo time T_E.

This 'refocusing' of the magnetisation results in the generation of an 'echo' which will have an amplitude as given by equation II.7 for $t = T_E$ and can be repeated several times to allow determination of the spin-spin relaxation exponential time constant. Because of molecular self diffusion, the spins will not remain in the same magnetic field during this process, and in consequence the magnetisation will not return to its original value, instead returning to some percentage of it. The drop in peak magnetisation of each echo is another measure of

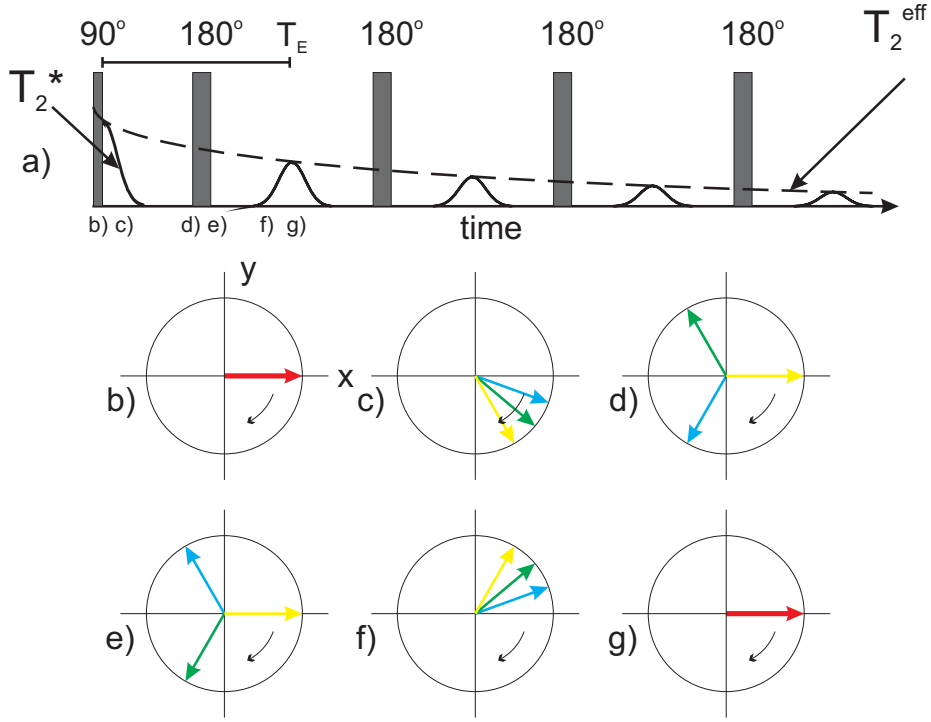

Fig. II.2: Rephasing to generate a spin echo. a) Measured Signal superimposed over pulse sequence, b) Magnetisation after tipping into transverse plane, c) Dephasing magnetisation, d) Dephased magnetisation, e) System after application of refocusing pulse along x, f) Magnetisation near beginning of echo envelope, g) Magnetisation at the echo time after the initial pulse. Diagrams b-g are in the rotating reference frame. Red arrow is all magnetic moments in phase; yellow ,green and blue arrows are fast medium and slowly dephasing magnetic moments.

the properties of the system and takes place exponentially with time constant T_2^{eff}.

This sequence is commonly used as it is less affected by static inhomogeneities in the magnetic field [6]. It is however still sensitive to motion of the nuclei. By choosing a suitable value for the echo time, the effect of the diffusive motion can be minimised or enhanced to determine the diffusion coefficient of the NMR molecule. This can for example be achieved by creating a separate interval between the initial excitation pulse and the first refocusing pulse known as the mixing time. By varying this time in a system with a field gradient G, the signal acquired with a train of equally spaced refocusing pulses can be used to determine the diffusion in the sample by fitting the echo amplitudes to equation II.7.

$$A(T_E) = M_{xy}(0)e^{-T_E/T_2}e^{-\frac{\gamma^2 DG^2 T_E^3}{12}}, \tag{II.7}$$

where $A(T_E)$ is the echo amplitude and D is the diffusion coefficient [7].

II.1.3.3 Gradient Echo - GE

In some situations, it may not be desirable to also refocus dephasing due to local gradients. Gradient echo sequences use applied gradients far larger than the local field variations to dephase or refocus the magnetic moments. Because the gradients are considerably larger, the effects of the local gradients become negligible.

Typically the tip angle used for gradient echo sequences is considerably lower than those used for spin echo sequences. In consequence, the bulk magnetisation returns to zero far faster than for a 90° pulse which in turn means that the sequence can be repeated far more rapidly. By varying this tip angle it is possible to change the contrast of images from T_2^* weighted with low angles to T_1 weighted with larger angles which is of great benefit for medical imaging, where a variety of contrasts can assist detection and diagnosis.

The most basic gradient echo sequence uses two applied gradients to refocus the magnetic moments. A gradient is applied with a given magnitude-time product and polarity, the magnetic moments are flipped with a 180° pulse as in the spin echo sequence and the same magnitude-time product and polarity of gradient is applied to refocus the magnetisation. This is very effective when the local field variations are small and the static magnetic field is homogeneous. Because this sequence only refocuses the effects of the gradients applied for imaging, it is particularly sensitive to internal field variations. Owing to the fact that the work undertaken in the course of this research is intended for the study of fluid pressure in porous media, the gradient echo sequences are generally disregarded in favour of spin echo based sequences which are not as sensitive to the internal field variations caused by the susceptibility difference between the solid porous medium and the liquid under investigation. The exception to this is the diffusion coefficient study conducted at the University of Leipzig in which a stimulated gradient echo sequence was used, as only a homogeneous liquid sample was tested and hence the magnetic susceptibility effects were negligible.

II.1.4 Spatial Encoding

The techniques for spin manipulation discussed thus far will only allow determination of the average information over the entire sample volume. In order to obtain localised information it is necessary to introduce some procedure by which a single finite region can be interrogated. The various techniques used to achieve this are known generically as spatial encoding and are covered briefly in this section.

II.1.4.1 In Plane

In order to generate a two dimensional magnetic resonance image, variations in the static magnetic field must be introduced. This is most commonly achieved by applying a ‘gradient field’ using an additional coil which generates a magnetic field with a spatially varying strength. This field generally has a linear spatial dependence such as that produced by a ‘Golay coil’ (see Fig. II.3). With this coil the field is of maximum magnitude at the top and bottom with zero effect in the centre, the field above the centre is in the opposite direction to that below the centre. When this is combined with the static magnetic field of the MRI scanner, protons in the central point will have the same Larmor frequency as in the static field only, whilst those above and below will have a Larmor frequency which increases or decreases respectively with distance from the centre.

The Larmor frequency in the system now has spatial dependence which can be written as in equation II.8 (shown for x but also true for other dimensions).

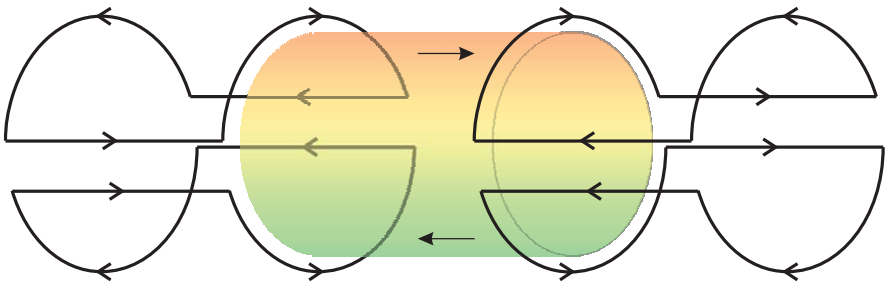

Fig. II.3: Image of a Golay coil. Four current carrying part-cylinders generate a field which acts parallel to z (left to right in the image) and which varies perpendicular to it. The coloured central volume in the image is the area in which the coil is effective. Red in this region is high intensity positive fields (along z) whilst green in the same intensity but negative.

$$\omega(x) = \gamma(B_0 + x.G_x). \tag{II.8}$$

There are several steps to generate a two dimensional image with this gradient, which involve phase and frequency encoding which are considered here:

II.1.4.1.1 Phase Encoding

If the system starts with all magnetic moments aligned, we can cause a spatially dependent dephasing by applying this gradient field. Assuming that the local variations in the magnetic field are small compared to the applied gradient strength (typically 1^{-5}T) once the gradient is removed, the final relative phases (in the rotating reference frame) will be remembered unless another gradient is applied or the phases become scrambled due to T_2^*. This is known as phase encoding and by varying the strength of the applied gradient, it is possible to generate a one dimensional profile. Phase encoding can also be performed in two dimensions to generate an image in a process known a single point imaging. This is however a very lengthy strategy as after each point is collected, the sample needs to recover to equilibrium (the repetition time) before the next gradient can be applied. An alternative strategy is to use frequency encoding.

II.1.4.1.2 Frequency Encoding

Frequency encoding uses the same gradients as in phase encoding but this time the magnetic resonance signal is collected during the application of the gradient. Using frequency encoding removes the need to wait for the repetition time between steps in the second dimension. In spin warp imaging, after the excitation RF pulse, a phase encoding step is performed at a given intensity before measuring the magnetic resonance signal during the application of a frequency encoding gradient. This is then repeated with different phase encoding gradient intensities.

The collected signal from both of these techniques is known as k-space. k-space has as many dimensions as

the final image, with each dimension corresponding to a gradient. For example, a two dimensional image collected with spin warp, will have a k-space with phase encode gradient strength and frequency encode gradient strength axes. k-space will be collected a line at a time, with a single excitation pulse before each line. In the case of single point imaging, each point in k-space is collected with an excitation pulse. Because the image has been encoded in terms of spatial frequencies, a two dimensional Fourier transform will recover the position dependent magnetic resonance information i.e. position and spatial frequency are a Fourier pair.

At each point, a train of echoes can be acquired using the Spin Echo technique previously described maximising the possible information collected. By sampling the points using a different ordering strategy or collecting more than one point per excitation pulse, it is possible to improve the speed with which the sequence can be executed. Assuming that the gradients are the only factor which cause dephasing in the system, k-space will be symmetrical about its centre. Because of this, one strategy for improving the speed is to acquire only a selected region of k-space. This is known as partial k-space acquisition [8] and by collecting only one quarter of k-space the speed can be radically increased in comparison to a full single point acquisition. This can however lead to some artefacts and loss of signal to noise ratio.

An alternative strategy is to use a train of echoes to collect lines of k-space. This is achieved by using refocusing pulses instead of excitation pulses in the spin warp strategy. This offers an enormous increase in the speed with which the imaging can take place as there is no need to wait for the repetition time between k-space lines. This can give images as quickly as every 30 milliseconds in comparison to around 1.5 minutes for the single point technique. This is however at the expense of the weighting and Signal to Noise Ratio (SNR) of the images. The difficulty with this technique is to acquire sufficient points of data in a short enough time frame that the relaxation due to diffusion or field inhomogeneities does not have a detrimental effect on the SNR of the image.

II.1.4.2 Slice Selection

The method allowing selection of the slices in which imaging is performed was developed by Garroway, Grannel and Mansfield [9] at the University of Nottingham. As the length of the excitation RF pulse is varied, the bandwidth of the NMR frequencies which it is exciting also varies. The longer the pulse the narrower the bandwidth. It is this effect which is exploited in slice selection. A second field gradient is present along the z axis (parallel to the static magnetic field) which has a linear variation in field strength with distance from its centre. As with the transverse coil, the field is of equal magnitude but opposite polarity at either end. In combination with the static magnetic field this results in distribution of Larmor frequencies from one end of the imaging volume to the other. With this gradient present, varying the width of the excitation pulse (e.g. the initial 90° pulse) the physical width of the band excited by each pulse will also be varied according to equation II.9. The centre of the slice is determined by the frequency of the applied pulse. In this way, a slice can be selected using the RF pulses whilst the X-Y imaging strategy previously explained is used to further break down

this slice into individual voxels (3D equivalent of a pixel). Although described here along the z direction, it is possible to use any of these gradients along any dimension to produce images from different planes in the sample. In medical imaging these are known as coronal, sagittal and axial (or transverse) and refer to images perpendicular to the x, y and z directions respectively.

$$\Delta z = \frac{\Delta\omega}{\gamma G_z}, \quad z_{centre} = \frac{\omega_1 - \omega_0}{\gamma G_z}, \tag{II.9}$$

where Δz is the slice thickness, $\Delta\omega$ is the pulse bandwidth, G_z is the gradient strength, ω_0 is the Larmor frequency with no applied gradients and ω_1 is the frequency required for a slice centred at z_{centre}.

II.1.5 MRI Pulse Sequences

In order to manipulate the spin system as detailed in the previous sections, requires the application of a series of gradient and RF pulses. The order in which these are applied, their timings and the various properties of each pulses is known as a 'pulse sequence'.

There is a vast range of possible pulse sequences which yield useful images and spectroscopic data. Those used for imaging purposes are usually classified as either Gradient Echo (GE) or Spin Echo (SE) sequences based on the primary method used for refocusing the magnetisation. These sequences are then often subdivided based on the method used to traverse k-space, from simple point-wise acquisition at each k-space point to complex spiral trajectories.

Two imaging pulse sequences have been used in this study: Multi Slice Multi Echo or MSME which is the implementation of the basic 2D spin echo imaging sequence with slice selection on Bruker (Billerica, MA, USA) scanners; and Rapid Acquisition with Relaxation Enhancement or RARE [10] which is a sequence for fast imaging. Some important properties of these sequences are discussed in this section. Sequences used in related publications are also discussed.

Both MSME and RARE imaging sequences have been used in this work as they are spin echo sequences. Although the MR sensitivity to fluid pressure variations could be improved by using gradient echo based sequences (which are more sensitive to internal gradients), the additional artefacts caused when imaging inside a consolidated porous medium would rapidly deteriorate the MR signal.

II.1.5.1 MSME

In the MSME sequence, after slice selection, a train of echoes (with a given echo time) is collected for a single line in k-space for a given phase encoding step. Refocusing pulses are applied and the line is recollected,

until the desired number of echoes have been reached. After the repetition time, the phase encode gradient is changed and another echo train is collected. This is repeated until k-space has been fully traversed (see Fig. II.4). The sequence is costly in terms of time as each k-space line requires an excitation pulse and hence a repetition delay, although large amounts of information are collected in this time due to the multiple echoes. This resulting data can be used to produce a number of images collected at a specific times after the excitation pulse which can be used to assess pixel T_2^{eff} values. In this study, we found that the T_2^{eff} measurements do not yield additional information and as such the speed of the sequence provides little benefit in comparison to the much faster RARE imaging sequence for example.

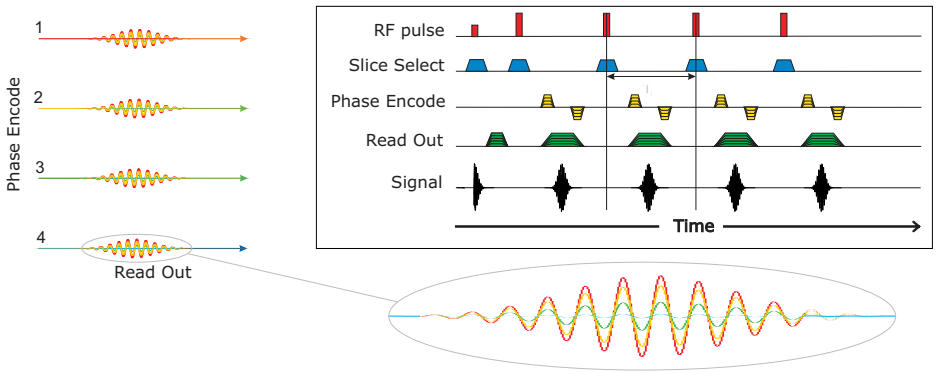

Fig. II.4: Order of k-space acquisition (echoes are from red to blue) and Pulse sequence for an 4x512 MSME acquisition with 4 echoes

II.1.5.2 RARE

RARE [10] imaging is a very rapid imaging sequence which gives T_2^{eff} weighted images. The pulse sequence and k-space acquisition order are shown in Fig. II.5. In this sequence, a single image is collected, with the echo train used to form the image. This requires definition of a new parameter, the effective echo time, or T_E^{eff} which is the time at which the central point in k-space is acquired and has values typically in the order of 250ms. A further parameter, the 'RARE factor' determines the number of lines acquired per excitation, e.g. for an image matrix which is 32 x 32 pixels, a RARE factor of 16 will require two excitation pulses, whilst 32 will require one. In this study we set the RARE factor to the number of k-space lines, offering an Echo Planar Imaging (EPI) like scenario in which whole two dimensional images are collected from a single excitation pulse, typically in less than 500ms. With a sufficiently long repetition time to allow the system to return to equilibrium, images can be acquired every 7 seconds as most of our samples exhibited a bulk T_1 around six seconds. This permits observation of rapidly changing processes within static fluids, although it is unsuitable for flowing fluids as the spins are excited once only and hence molecular displacement must be negligible compared with the voxel size for the time duration of the image acquisition.

II.1.5.3 Inversion Recovery

Both of the sequences detailed in this section thus far yield T_2^{eff} weighted images. Sometimes, it is desirable to measure the local T_1 information. Measuring T_1 is often a lengthy process as it is necessary to observe

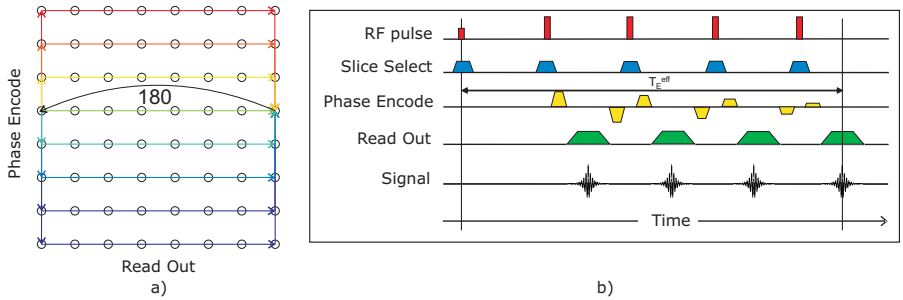

Fig. II.5: a) Order of k-space acquisition (blue to red). Each circle represents a point in k-space. b) Pulse sequence for an 8x8 RARE acquisition

the evolution of the longitudinal relaxation which is often greater than three seconds. One basic sequence for measuring T_1 is known as inversion recovery and involves applying an initial inversion pulse before a standard imaging sequence (see Fig. II.6). The time between this inversion pulse and the start of the imaging sequence is known as the inversion time. By collecting the signal after a variety of inversion times, it is possible to fit the signal to equation II.10 and thereby determine T_1. By selecting the values of the inversion time carefully it is possible to measure the value of T_1 with as few as 4 inversion times [11] . This process is however very lengthy, often taking in excess of 10 minutes to acquire a two dimensional T_1 map.

$$M_z = M_0\left(1 - 2e^{\frac{-TI}{T_1}}\right), \tag{II.10}$$

where M_z is the longitudinal magnetisation, M_0 is the bulk magnetisation and TI is the inversion time. It is also possible to achieve fat suppression (or more specifically, suppression of materials with low T_1 values) by imaging with an inversion time matched to the recovery time of fat which is around 400ms (for a polarising field strength of 2.35T). This is because the tissue will have no transverse component prior to the start of the imaging part of the sequence. This is particularly useful for medical imaging when there may be areas of fat which may mask otherwise clear lesions on images.

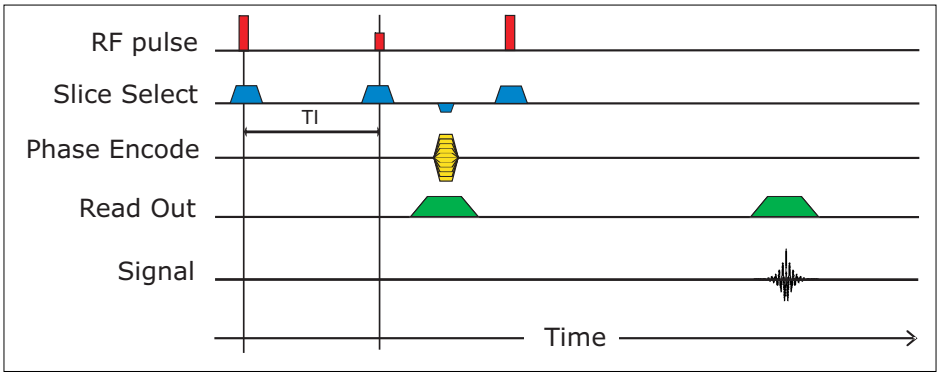

Fig. II.6: Inversion Recovery pulse sequence, k-space acquisition is per line.

II.1.5.3.1 Fast Inversion Recovery

Because the Inversion Recovery IR sequence is so lengthy, it is often necessary to find alternative strategies to speed up the measurement. One common method for achieving this is to replace the spin echo sequence in standard IR with a rapid imaging sequence such as RARE [12]. This allows rapid acquisition of a T_1 map although like with the standard RARE sequence, each pixel in the image is collected at a different time relative to the excitation pulse, which must be accounted for when fitting is performed to estimate the local values of T_1.

II.1.5.4 Diffusion Measurements

Pulsed Field Gradient (PFG) NMR is a subset of NMR which is used primarily for studies of molecular motion, such as diffusion. The original PFG technique was developed by Stejskal and Tanner [13] and uses additional field gradients to those used for a standard NMR experiment, superimposed over the static magnetic field B_0 to encode the positions of the spins in the system. The general concept of the sequence is to allow generation of gradient echoes with similar shapes yet varying amplitudes based on the extent to which diffusion is occurring in the system.

The PFG sequence allows the molecular self diffusion coefficient to be readily obtained. The Stejskal Tanner sequence is the most commonly used PFG sequence for diffusion measurements. A single refocusing pulse is applied midway between the excitation pulse and the echo as in the standard spin echo imaging sequence. A stimulated spin echo modification to this sequence may also be used in which the single refocusing pulse is replaced by two 90° pulses separated by a time known as the 'storage interval'. The first of these pulses is applied at a time τ (known as the preparation interval) after the initial excitation pulse. The echo is then formed a further time τ after this (known as the read interval). The first of these pulses acts to tip the magnetisation into the longitudinal direction thus allowing it to decay with the longitudinal relaxation time T_1. The second pulse then tips it back into the transverse plane for generation of the echo. The gradients are applied as in the basic spin echo imaging sequence (see Fig. II.4) and the phase labelling which they impart on the system is preserved during the storage interval which can now be varied over a much greater range than with the standard sequence. To ensure that a stimulated echo is properly produced, the integrals of the two applied gradients must be equal. Although it is also possible to generate a stimulated echo if these integrals are equal and opposite, Cotts *et al.* [14] showed that the interaction between the applied gradient and any background gradients in the system (i.e. unwanted cross terms) can not be compensated for which may lead to false measurements of the molecular self diffusion coefficient.

II.1.5.4.1 13-Interval Sequence

The 13-Interval sequence as developed by Cotts *et al.* [14] uses a sequence of gradients which suppresses undesired coherence pathways by applying 4 gradient pulses instead of two resulting in thirteen time intervals (see Fig. II.7).

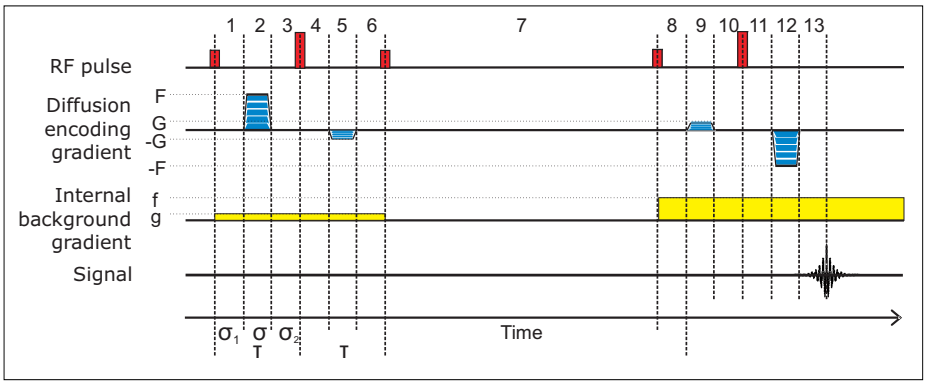

Fig. II.7: 13 Interval PFG NMR sequence with pairs of unequal gradients, reproduced from reference [15]

As in the Stejskal and Tanner sequence, the background gradient is accounted for, but now it may change from a value g to a value f during the storage interval which may correspond to change in the local environment, for example movement between different sized pores in a porous sample. Because of the capability of this sequence, it is possible to suppress many unwanted artefacts due to inhomogeneities in the sample. There will however now be a signal attenuation caused by the cross term A_c in addition to the signal attenuations resulting from the applied and background gradients A_p and A_b respectively (equations II.14) [16].

$$A_p = \sigma^2 \left\{ [\Delta + \tau - (\sigma_2 - \sigma_1)](G+F)^2 + 2(\tau + \sigma_2 - \sigma_1)F^2 - \frac{1}{3}\sigma(G^2+F^2) \right\}, \tag{II.11}$$

$$A_b = \frac{2}{3}\tau^3(f^2+g^2), \tag{II.12}$$

$$A_c = \sigma[a(G-F) + 2\tau^2 F](g-f), \tag{II.13}$$

$$where\ a = \sigma_1 + \sigma_1\sigma + \frac{1}{3}\sigma^2, \tag{II.14}$$

σ, σ_1, σ_2 *and* τ are as indicated in Fig. II.7. Δ is the time from the centre of the excitation pulse to the start of the third applied gradient. F and G are the intensities of the applied gradient pulses whilst f and g are the intensities of the background gradients during the preparation and reading phase of the sequence respectively. As can be seen, the attenuation due to the cross term contains influences of both the applied and background gradients.

In order to suppress the cross term in this work (which may arise from dissolved gases in the sample), we have used Magic Pulsed Field Gradient (MPFG) ratios developed by Galvosas *et al.* [16]. There are two parameters which are varied to suppress the cross term: the timing of the gradient pulses relative to the τ intervals (see

Fig. II.7) and the sign and intensity ratio between the two sets of gradients G and F. It is shown by Galvosas *et al.* [16] that when the gradients are centred with respect to the τ interval, the ratio between the F and G gradients (η) simplifies to a single value given by equation II.15

$$\eta = \frac{G^p}{F^p} = \frac{G^r}{F^r} = 1 - \frac{2\tau^2}{a}, \tag{II.15}$$

where G and F are the gradient intensities for superscript p and r relating to the preparation interval and to the read interval. τ is the echo time as before. The value of a is given by equation II.16

$$a = \sigma_1^2 + \sigma_1\sigma + \frac{1}{3}\sigma^2. \tag{II.16}$$

The echo condition is given by equation II.17

$$F^p + G^p = F^r + G^r, \tag{II.17}$$

and so the amplitudes of the two sets of gradients must be similar. By setting $G = G^r = G^p$ and $F = F^r = F^p$ and combining the previous equations, a simplified relationship is given by II.18

$$\eta = \frac{G}{F} = 1 - \left\{8/\left(1 + \frac{1}{3}\left(\frac{\sigma}{\tau}\right)^2\right)\right\}. \tag{II.18}$$

The consequence of this is that G/F will always be between -7 and -5 as the value of δ is always greater than zero and less than τ. Although this will usually result in fairly high gradient values, it is relatively easy to set such gradients on modern spectrometers.

In order to achieve a large gradient time integral as required by this sequence (in contrast to basic imaging sequences), it is necessary to deliver gradients with high intensity rather than long duration to minimise the effect of T_2 on the signal intensity decay. To accommodate this, there are three modifications that have been made to allow optimum delivery of energy to the gradient system. These will be discussed briefly here but the reader is referred to the extensive review on this subject by Stallmach and Galvosas [17] for a deeper understanding of this area.

II.1.5.4.2 Automated Mismatch Correction

In order for the echo to appear at the precise moment in time at which it is expected, it is essential that the gradients are applied at a precise time and intensity. Various factors along the gradient drive chain may

influence the effectiveness of the deployment. The shift in echo location (Δt) is defined by equation II.19

$$\Delta t = -\frac{d(\mathbf{G}\sigma)\mathbf{g}}{\mathbf{g}^2}, \tag{II.19}$$

where $d(\mathbf{G}\sigma)$ represents the mismatch between the expected and actual gradient time integral. As long as this shift is small compared to the width of the spin echo envelope, it is still possible to determine the correct spin echo attenuation without compensating for the mismatch. For analogue systems it is easy however to compensate for such mismatches by adjusting the duration or amplitude of the second gradient pulse (interval five in Fig. II.7) until the spin echo occurs at the correct time. In the case of a digital system, it is often the case that the temporal resolution is insufficient to allow for a suitable correction [18]. In this work, the spectrometer control software developed by Galvosas automatically corrects for misplaced echoes due to gradient mismatches during application of the pulse sequence. This is achieved by using an autocorrelation function thus rendering the technique immune to noise influences, unlike attempting to determine the maximum of the echo in the time domain. Signals are acquired for a small read gradient both with and without pulsed field gradients and an autocorrelation performed between the two echoes. This method allows determination of the mismatch ($d(\mathbf{G}\sigma)$)for low signal to noise ratios. For suitable sequences, this also presents an alternative method to account for mismatches whereby, instead of adjusting either the amplitude or duration of the gradient pulses, a small read gradient is applied during echo acquisition for a time duration corresponding to the extent by which the echo has shifted allowing the position to be corrected even in a system with insufficient temporal resolution for the former method.

II.1.5.4.3 Gradient Shape Optimisation

In order to drive a gradient coil, a high current is applied to it usually through a high power operational amplifier. Although the desired current profile applied to the coil may be a step, to generate the instantaneous increase in current (an infinitely fast change in current) requires application of an infinite voltage. This is clearly not possible with a real power supply which will be limited by some finite DC voltage. The gradient coil is effectively an inductor-resistor combination. When a voltage is applied to the circuit the current will rise with a exponential time constant of $-\frac{R}{L}$ up to the DC value. During this evolution the amplifier will be overloaded. In this overloaded state, many factors influence the current delivered generating current errors in the form of ripple, hum and noise of the DC power supply causing random mismatches. To avoid this, a current profile equivalent to that which would be measured in the case of the step profile i.e. an exponential given by the coil parameters according to equation II.20 is applied to the coil.

$$I(t) = \frac{V_{max}}{vR_{coil}}\left[1 - e^{-(t/\tau)}\right], \tag{II.20}$$

V_{max} is the maximum voltage output of the amplifier, R_{coil} is the coil resistance, v is a parameter which specifies the response of the current source, and τ is a time constant given by

$$\tau = \left(t_{ramp}\right) / \left(ln\left[\frac{V_{max}}{v - IR_{coil}}\right]\right), \tag{II.21}$$

where t_{ramp} is the ramp time of the pulse and I is the desired pulse current. A similar profile is applied for the other edge of the pulse. It is important then to remember that the integral of the pulse will be different to a square pulse and, as such the maximum amplitude and or the pulse duration will need to be varied for the same effect as a square pulse. When changing the pulse amplitudes, it is not necessary to vary any of the properties of these ramps other than the ramp duration. In this way, the ramp properties need to be determined only once for a given amplifier thus allowing relatively easy amplitude variation (see Fig. II.8).

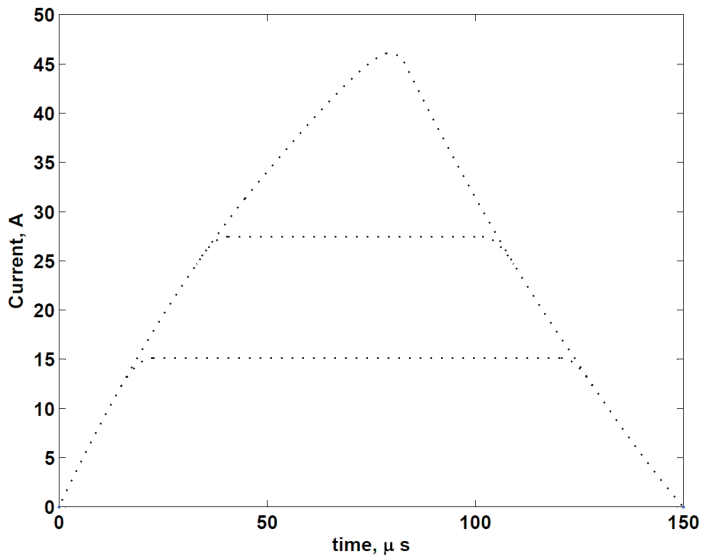

Fig. II.8: Optimised gradient pulse shapes. Changing the maximum amplitude does not require varying the exponential parameters. Reproduced from reference [15]

II.1.5.4.4 Mains Triggering of the Pulse Sequence

The final modification to the system is to trigger the pulse sequence at a constant mains voltage phase. Because the observation times in PFG NMR experiments are typically in the order of several hundred milliseconds, the 50Hz mains hum may introduce large gradient mismatches if the sequence is run randomly with respect to the mains. In combination with the other modifications, the synchronous triggering with the 50Hz wave will allow for a further improvement to gradient mismatches. It is particularly important for very sensitive experiments, such those in porous media, as at the low observation times required for enhanced diffusion, which may be less than a 50Hz period, the effect can be very significant.

II.1.6 Magnetic Susceptibility Effects

The extent to which the molecules of a material align in the presence of a magnetic field is known as the magnetic susceptibility and varies widely from material to material. It is defined by equation II.22.

$$M = \chi \frac{B_0}{\mu}, \tag{II.22}$$

where M is the material magnetisation, χ is the magnetic susceptibility B_0 is the applied magnetic field and μ is the permeability. Whilst magnetic moments in ferromagnetic materials are regularly aligned in the absence of a magnetic field, diamagnetic and paramagnetic materials on average have randomly aligned magnetic moments. In diamagnetic materials, χ will be negative and close to zero resulting in a small internal field which acts to oppose the external field. The ability of the moments to align parallel to the external field is due to the orbital motion of electrons which behave much like current carrying loops generating magnetic fields. These fields cancel in diamagnetic materials. In paramagnetic materials however this cancellation will not be complete resulting in a value of χ close to but greater than zero (for example, brain tissue typically has a magnetic susceptibility of -10^{-6} [19]). Although when outside a magnetic field paramagnetic materials have no overall magnetisation, unpaired electrons do induce a non zero magnetic moment. When an external magnetic field is applied, these magnetic moments align with the applied field. The magnetic moments in ferromagnetic materials cannot be manipulated with NMR as in paramagnetic materials, as their internal ordering prevents useful interaction with radio frequency fields. They also cause polarisation in surrounding diamagnetic and paramagnetic materials resulting in localised variations in the Larmor frequency.

In order to uphold Amperes current law, the magnetic flux everywhere must be zero, i.e. two neighbouring magnetic fields of different strength or direction must have a gradual change of field strength (or spatial gradient) between them [20]. Because the product of the internal field and the externally applied fields is a constant, a difference in magnetic susceptibilities will result in a difference of magnetic fields and hence the establishment of local internal magnetic field gradients. This is a common cause of imaging artefacts in the brain for example, in which the sinus spaces which are filled with air contact neighbouring areas of bone and soft tissue generating strong internal gradients [21]. A similar artefact is seen in porous media in which gradients are established between the solid and liquid phases [22]. This same effect is also used to our advantage with functional MRI used for brain activity measurements. In the Blood Oxygenation Level Dependent (BOLD) technique, the changes in the Larmor frequency caused by the susceptibility differences between oxygenated and deoxygenated blood are used to locate areas of the brain which are using oxygen and hence are activated [23].

II.1.6.1 Diffusion in a Field Gradient

The effect responsible for decay of the MR signal in the presence of a magnetic field gradient is diffusion. As the molecules experience Brownian motion within such a gradient, they move between various strengths of magnetic field depending on their physical location. This can be used to great advantage for the study of many physical processes. One of the most common applications of this technique is in the study of porous media. At a physical boundary in such a medium, the molecules will bounce back (known as 'reflection') which can cause brighter areas at the boundaries. This is known as edge enhancement [24]. The effects in these two situations are described in the following sections.

II.1.6.1.1 Free Diffusion

The protons in water at room temperature (21°C) diffuse at approximately $2.27 \times 10^{-9} m^2 \cdot s^{-1}$ [25] which is commonly referred to as the molecular diffusion coefficient. This effect is easily measured and can be used for many applications. It is a very important property in assessing the viscosity of Newtonian fluids (see equation II.23) and is essential to estimate the efficacy of a fluid used to suspend solid particles or create emulsions.

$$D = \left(\frac{1}{6\pi\eta r}\right) kT, \tag{II.23}$$

where D is the diffusion coefficient, η is the viscosity, r is the particle radius, k is Boltzmann's constant and T is the temperature of the fluid.

In terms of general MRI measurements, excited nuclei in a sample with a high molecular diffusion coefficient will be more likely to move out of the excited volume as opposed to a sample which diffuses slower. This same sample in a field gradient will comprise of molecules experiencing many different field strengths in comparison to one which diffuses more slowly. This effect is exploited in this study to determine the pressure of a fluid containing micron sized gas bubbles which cause micron scale magnetic fields at their boundary in relation to their size. Molecules diffusing in the fields of a bubble larger or smaller than the diffusion length will dephase much more slowly than those in the the field of a bubble close to the diffusion length and in consequence the signal attenuation will be related to the bubble size and hence the external pressure.

II.1.6.1.2 Restricted Diffusion

NMR sensitivity to restricted diffusion has found many applications, not only in the study of mineral based porous systems but also in biological systems. It has become an useful diagnostic tool in the study of Multiple Sclerosis [26] in which a diffusion image is used to estimate a property known as the Apparent Diffusion Coefficient (ADC). The ADC is measured over various brain regions and the values then further processed to determine the degree of ordering within the white matter, which can be seen as a porous network of long fibres. A high value of the ADC suggests that individual fibres are packed in bundles which run parallel and have few gaps, as there is extensive reflection of water molecules trapped between fibres. A low ADC on the other hand

suggests that the fibres in these bundles are not parallel and have increased spaces between them, thus allowing water to diffuse more readily as would be expected as the fibres external structure deteriorates. The ADC can also be used to locate and assess tumours in the body [27]. Areas with particularly high ADC values in the brain, for example, can also be representative of a tumour as it has a reduced space for the water molecules to diffuse compared to the surrounding ordinary brain tissue.

NMR sensitivity to restricted diffusion is also useful in assessing non-biological systems. Performing diffusion measurements in a porous medium can give a measure of the pore size distribution and the pore connectivity as well as information such as the body to throat ratio and the actual geometry of the pores [28].

II.1.6.2 Diffusion Around Compressible Spherical Field Perturbers

Throughout the course of this work, micron sized gas bubbles (microbubbles) have been suspended in a liquid or gel based medium to measure changes in fluid pressure with MRI. The diffusion of water molecules around these microbubbles gives rise to the sensitivity of the experimental work presented herein. The basis behind the effect is discussed in this section.

The difference in magnetic susceptibilities ($\Delta\chi$) between the fluid in which a microbubble is suspended and the gas encapsulated in it causes local variations or perturbations, $\Delta B(r,\theta)$, in the static magnetic field according to equation II.24 [29]:

$$\frac{\Delta B(r,\theta)}{B_0} = \frac{4}{3} B_0 \Delta\chi \left(\frac{R}{r}\right)^3 (3\cos^2\theta - 1), \tag{II.24}$$

where R is the microbubble radius and r is the radial distance from the centre of the microbubble at angle θ from the direction of the applied static magnetic field of magnitude B_0.

At present it is not known how the gas filled microbubble radius varies with pressure, but the ideal gas law can be assumed to hold as a first approximation. Because the spatial extent of the polarising field perturbations is dependent on the bubble radius, a change in the size of microbubble due to a change in pressure results in field perturbation variations. As the proton-carrying molecules in the suspending fluid diffuse around a microbubble, they sample different magnetic field strengths as a result of the perturbations. Therefore, a hypothetical proton experiencing an identical diffusion path relative to the microbubble will sample different field strengths if the microbubble has experienced a change in external pressure. This effect is demonstrated in Fig. II.9. The greater the field perturbations sampled by the proton, the greater the extent to which the signal will decay due to dephasing, which yields image contrast to fluid pressure.

Extensive work has been published regarding this system, both theoretical and using numerical simulation. For spin echo sequences it has been shown [30] that each microbubble diameter has a corresponding theoretical

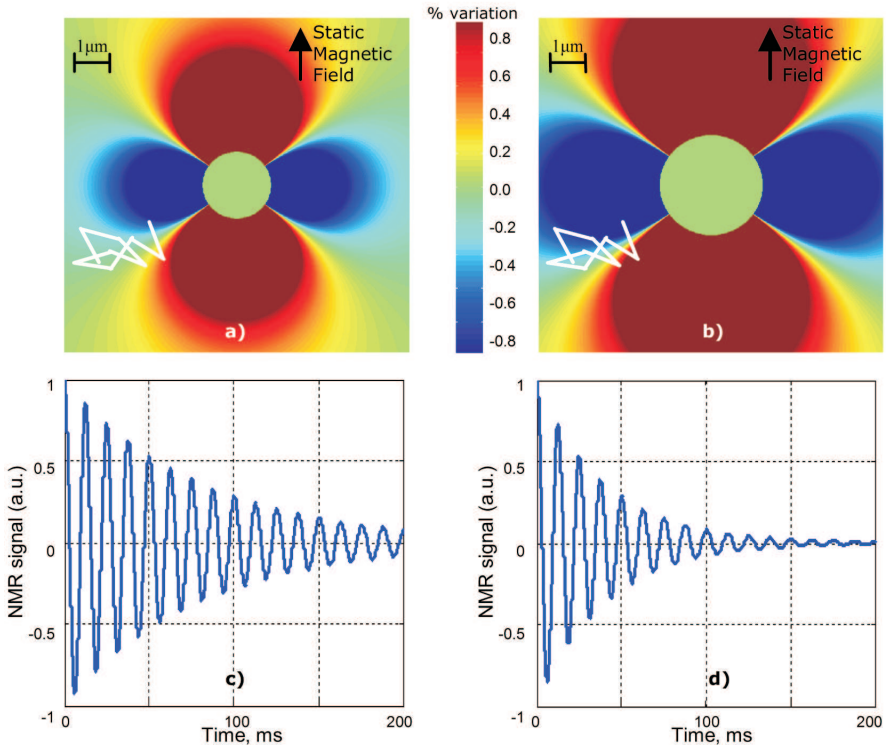

Fig. II.9: Schematic colour-coded plot of the relative magnetic field perturbations caused by gas filled microbubbles (central discs) in a static field at 3 Tesla produced from equation II.24 for a magnetic susceptibility difference of 12.56×10^{-6} and microbubble sizes of a) $2\mu m$ and b) $3\mu m$ both with plots showing the path of a proton undergoing the same random walk (white path). c) and d) are sketches of the FID measured in the presence of the gas-filled microbubbles above.

echo time for which maximum effective spin-spin relaxation rate R_2^{eff} (reciprocal of T_2^{eff}) is obtained. Numerical simulations have also been published which determine the sensitivity of NMR signal intensity to changes in pressure [31], although the experimental studies which are available to date offer insufficient data to conclude upon the validity of these two theoretical works. This lack of data arises because to date there has been no published experimental investigation into the NMR signal response from a monodisperse bubble distribution which is assumed in the simulation studies.

II.2 MR Applications in Porous Media

The application of Magnetic Resonance to the study of porous media is a relatively recent development. Since 1990 it has been recognised as an independent branch of scientific study with the establishment of the Magnetic Resonance in Porous Media conferences at the University of Bologna, Italy by Giulio Cesare Borgia, Paola Fantazzini and Robert Brown. Although originally the main focus of investigations into porous media was for the petrochemical industry, each year brings about more diverse applications, providing exciting insights into new science. In the following sections, some of the main applications will be discussed and although this is by no means exhaustive, it will hopefully cover the basic concepts behind the majority of the new ideas which are of interest to this community.

II.2.1 Fluid Flow

The science concerned with the properties of a flowing fluid is vast. Fluids are often assumed to be Newtonian and flowing through a single channel. This can then be extended for a non-Newtonian fluid. The next level of complexity is for a porous sample which can be considered as a series of short, interconnected channels. Their length can be made to vary in order to better represent real world samples. For each of these additional stages, the mathematics required to describe these features becomes more complex and the sample is often considered to be relatively homogeneous. The inherent inhomogeneity of real world samples means that, for the most part, these cases only go some of the way to understanding the pressure distribution in the samples [32].

Physical measurements of the pressure offer greater insight into determining the underlying variations in an inhomogeneous sample although invasive techniques result in changes of structure rendering them somewhat less valid than for a non invasive approach. For a more complete understanding of the actual physical processes, a combination of these measurements and simulations is desirable.

Fluid flow can be assessed with MRI for all major flow types under investigation, be it laminar (constant velocity at a given position across the width of the channel with a parabolic profile), turbulent (variations in velocity across the channel which change randomly) or stagnant and vortex flow (laminar flow becomes disturbed by narrowings in the channel resulting in areas which have zero velocity (stagnant) or rotational motion (vortex)) [33]. The MRI technique known as Time-Of-Flight or TOF relies on the requirement of an excitation and refocusing pulse to generate an echo. If the sample receives only one of these pulses, an echo will not be generated. In the extreme case, the volume excited by the first pulse will have flowed out of the region excited by the refocusing pulse and hence there will be no signal. With imaging sequences, parts of the image which represent fluid which has flowed into the volume will have no signal thus allowing the flow to be visualised. The distance which the front has travelled into the image will be proportional to its velocity whilst its shape gives information on the pipe geometry, roughness and the fluid viscosity and is dependent on the thickness of the slice, the echo time and the flow velocity [33].

II.2.2 Diffusion

The use of diffusion measurements in porous media is of increasing relevance for investigating various exchange processes. At the fundamental level, diffusion measurements give an insight into the mobility of a fluid's molecules which may or may not be restricted by some boundary. In the majority of porous media, the length scale of the diffusion process is several orders of magnitude smaller than that of the pore size for an MR experiment taking place in thirty seconds. In this case, the majority of the signal will be from free fluid with some artefacts due to reflections of molecules at the boundaries (see section II.1.6.1.2). In porous media with nanometre pores however, the length scales will be very similar which can lead to both an increase in the diffusion coefficient as the molecules travel a smaller distance in the same time (although this is rarely seen in

practice as the internal gradients caused by susceptibility differences between the liquid and solid media will attenuate the signal) as well as faster molecular exchange between pores.

An alternative method to collect a greater quantity of diffusion information is to acquire a diffusion spectrum. In a sample with a distribution of diffusion coefficients such as a porous medium with a variety of pore sizes, the echo attenuation in a PGSE sequence (see section II.1.5.4) will contain information from each diffusion coefficient. By performing an inverse Laplace transform, the contributions of each of these diffusion coefficients can be isolated and a spectrum generated. By repeating the PGSE for a variety of mixing times and using a two dimensional inverse Laplace transform it is possible to collect a two dimensional spectrum which has allowed investigation of exchange between pores. This is the case in the Diffusion Diffusion COrrelation SpectroscopY or DDCOSY experiment [34]. In this way, if there is no exchange between environments with different diffusion coefficients, all of the measured values will lay on the diagonal (corresponding to the one dimensional profile, see Fig. II.10 a) and b)). If however there has been molecular exchange between two regions with different diffusion coefficients, there will be off diagonal regions (see Fig. II.10 c)) where the two diffusion coefficients have appeared with different values. The relative intensities of these peaks reveal the relative sizes of the pore volumes responsible for the diffusion coefficients and this can provide extensive information about the microscopic inhomogeneities of a sample which appears macroscopically homogeneous [35] such as the connectivity between pores of differing sizes.

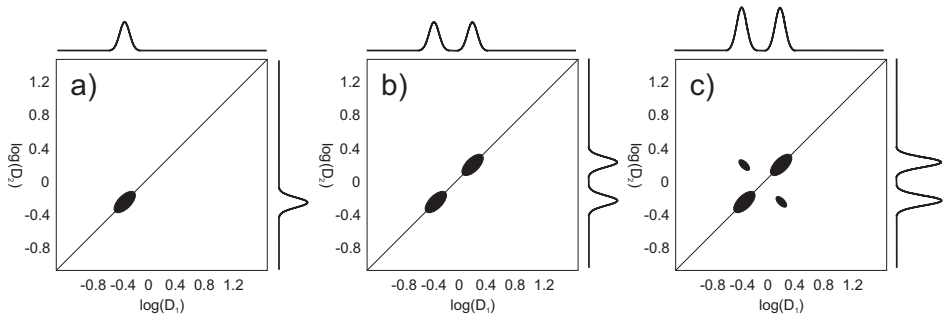

Fig. II.10: Two sample spectra from a DDCOSY experiment. a) represents a simple sample in which there is a single diffusion coefficient, note how the single peak lies on the diagonal. b) represents a sample with pores of different sizes in which there are two diffusion coefficients and as such two peaks are evident. Because there is no exchange between them, both of these still remain on the diagonal. In c) there is exchange between the two different diffusion coefficient regions and as such, off diagonal peaks have appeared. These exchange peaks would not be visible on a one dimensional diffusion spectrum as they occur in line with the two on diagonal peaks (see spectra).

II.2.3 Multiphase Flow in Packed Bead Columns

One of the most commonly used models for a porous system is a column which has been packed with glass (or similar material) spheres. Although not connected, the contact points of these spheres generate a pore structure which mimics those found in consolidated porous media without the concern of paramagnetic impurities or wide variation in the pore sizes over the sample. Of particular interest to many processes is multi phase flow in which more than one phase is flowing through the system. The fluids can travel in any direction relative to

each other and often at different velocities.

One of the most commonly encountered multiphase flow regimes in industry is trickle flow. In this regime, gas is driven along a column of solid catalysts while a liquid product is 'trickled' through the same column, both at controlled flow rates. Although used in many industrial processes, very little is known about the local interactions in the system. MRI is a very powerful tool for assessing such reactors, and much has been learnt in recent years about this kind of system. The velocities of the two phases, the extent to which liquid is pooled in pores or immobilised (liquid hold up) and the surface wetting of the beads can all be determined with MRI. The imaging performed is often time of flight, in which encoding is performed in one region and then, some time later, the new location of the encoded spins will be related to their velocity. By collecting images at several different times, the flow along a column can be determined, or the stability of the flow can be assessed by collecting images at different locations along the column at the same time. Sample images taken from an extensive review by Mantle *et al.* [36] are included in Fig. II.11.

Fig. II.11: Sample results from the work of Sederman and Gladden investigating two phase trickle flow of liquid and gas through a packed column (40mm diameter) of 5mm glass beads [37]. The original image of two-phase gas-liquid trickle flow in a) has been thresholded to identify liquid rivulets. Voxels containing liquid-solid contact (the edges of the rivulets in b)), i.e. surface wetting are shown in c).

This method has drawbacks for samples experiencing turbulent flow. Because an excitation pulse is required prior to the acquisition of each image, in a system in which the flow along the column varies randomly, collected images from the same region will be different. Recently this has been overcome by Sederman *et al.* [38] who modified the RARE sequence to collect several images in succession from a single excitation pulse, thus allowing measurement without misrepresenting turbulent flow. Because these images are collected so quickly, it is possible to determine the flow for two phases in a porous system experiencing both laminar and turbulent flow regimes.

II.2.4 Filtration

Many industrial chemical processes involve one or more filtration steps. Ranging in complexity, many filters are replaced far ahead of the point at which their function is impaired, as there are very few methods for non destructively testing filters which may be large and opaque. One method for non-invasively testing the blockage of filter media is MRI. It is a common task to separate out solid particles from fluids. This can be

easily monitored with MRI providing high contrast between liquids and solids allowing determination of the particulate content and mobility of the fluid. A particularly good example of MRI of filtration media is that of Dirckx [39] in which a pleated filter paper is used to separate an aqueous suspension of Iron (III) Oxide. Because of the extent to which Iron (III) Oxide perturbs the MR signal, this measurement is exceptionally sensitive. As the particulate material collects in the folds of the filter, the signal intensity is attenuated as its concentration increases (see Fig. II.12).

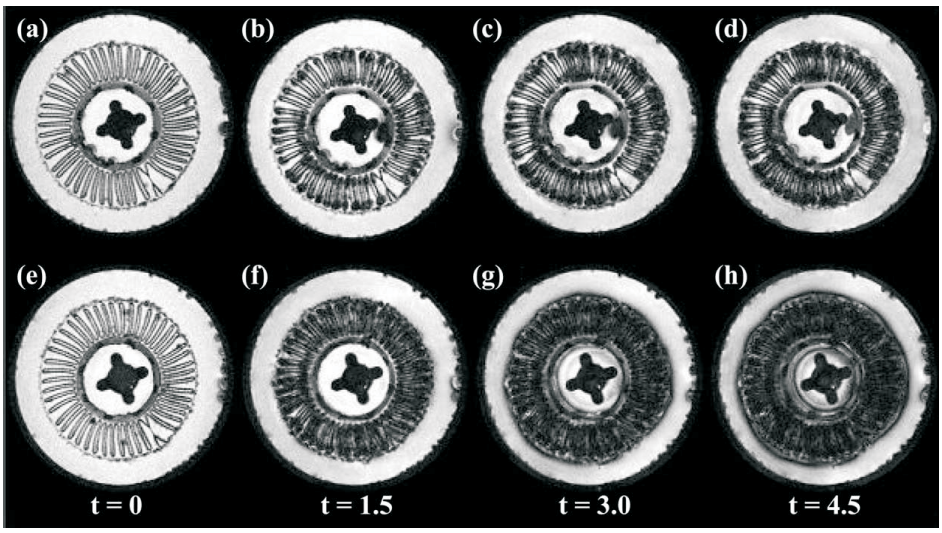

Fig. II.12: Transverse section of pleated filter undergoing flow of aqueous Iron (III) Oxide suspension, images show two concentrations of Iron (III) Oxide (low top, high bottom) over time (left to right). ©2000, AIChE. All rights reserved. Reproduced from reference [39]

Whilst this system could also be qualitatively assessed optically, a quantitative estimate of the filter saturation is available using this method. Additionally, by using a low cost unilateral NMR system, it may be possible to perform regular on-line monitoring of such a process in a large scale industrial environment. Recently, investigations into the possibility of observing contamination in a electrically conductive catalyst/filter medium of activated carbon monoliths has been presented [40]. This is an excellent representation of the typical challenges involved with applying MR technology to real industrial processes in which the majority of media are not immediately accessible for direct measurements. Using a single sided MR instrument, the MR MOUSE © (ACT Aachen, Germany), measurements of hydrocarbon uptake into the monolith has been measured despite its inherent conductivity, thus indicating the degree of contamination both non-destructively and non-invasively.

II.3 MRI of Pressure

An area of science which remains to be better exploited in terms of MR investigation is the study of pressure. In contrast to the tens of thousands of MR papers published each year, the study of pressure barely accounts for double figures. There are several measurement strategies, which can be classed as direct and indirect methods. The direct methods rely on intrinsic measurement capabilities of MRI (for example spin density) to determine the pressure of the sample under investigation. The indirect measurement methods in comparison require the use of a contrast agent to allow determination of the sample pressure or rely on the measurement of a parameter

which varies indirectly with pressure (such as T_1 or T_2). The three basic methods for measurement of pressure using MRI are detailed in the following sections.

II.3.1 Partial Pressure Measurements

The pressure of a fluid containing dissolved gas can be determined by measuring its partial pressure. This partial pressure is a measure of the quantity of gas which is dissolved in the liquid. The greater the pressure exerted on the fluid, the higher the concentration of gas which will be dissolved in it [41].

By using the Fluid Attenuated Inversion Recovery (FLAIR) sequence, it is possible to estimate this partial pressure. The FLAIR sequence is most often used in medical applications to suppress the signal from the Cerebro-Spinal Fluid (CSF) whilst still allowing the signal from the brain to be acquired. This is achieved by setting the inversion time to the point at which the magnetisation of the CSF is zero, whilst the surrounding brain tissue signal still recovers, typically around 2000-2500ms [42]. It had been previously observed that on occasion, the CSF would not be adequately suppressed because the relaxation had been enhanced by the partial pressure of oxygen in the fluid [41]. This phenomenon has been investigated and the relationship between R_1 (reciprocal of T_1) and the partial pressure of oxygen was found to be linear. It was clear from this that by measuring the relaxation rate of the CSF or some other fluid, the partial pressure of oxygen (and subsequently the pressure of the fluid) can be determined.

In the work of Zaharchuk *et al.* [43], the partial pressure of oxygen dissolved within *in vivo* CSF, as well as in a water based CSF like phantom, is investigated by measuring the spin lattice relaxation rate using a 2 to 10 point 3D Modified Fast Inversion Recovery (MFIR) sequence. In the 2 point sequence images are acquired for no inversion pulse and an inversion time of 3.2s, whilst for the ten point sequence a linear distribution between these is used. In this way, it is possible to estimate the spin lattice relaxation rate and thus the oxygen content from which the partial pressure is determined. Measurements are made in both phantoms and in human and foetal CSF, bladder urine, and vitreous humour. These images are used to obtain estimates for the partial pressure of oxygen which are compared to values previously published using invasive methods.

This technique clearly currently holds the most promise for medical applications, particularly for conditions such as pulmonary artery occlusion (causing local increases in arterial pressure) [44] and, as it requires no contrast agent, presents no additional risk in comparison to a standard MRI scan. The use of alternative nuclei both hyperpolarised and not hyperpolarised has also been reported in the literature such as ^{19}F for studies of partial pressure in porcine lungs during partial liquid ventilation [45] and hyperpolarised helium for estimation of regional intrapulmonary oxygen partial pressure [46]. Because of the invasive nature of the contrast agents required, these remain less promising than the method of Zaharchuck.

II.3.2 Gas

Of key importance in the measurement of pressure in the gas phase is the work of Bencsik and Ramanathan [47, 48]. By using the density of Heptafluoropropane gas in a variety of samples experiencing gas flow, the local pressure and subsequently the local hydrodynamic permeability is determined. Because the gas is compressible, when the pressure is increased the density of gas molecules will rise and in consequence the signal intensity will become greater. Two samples are tested: the first is a custom produced model porous media comprising of a single cylinder interspersed with thin plastic sheets containing a single aperture permitting gas flow; the second sample is an oil reservoir rock allowing the method to be tested in a sample of interest to the oil industry.

The results for the first sample demonstrated well the effectiveness of the technique, with a large difference between MR profiles of static and flowing gas. The division of the two profiles yields the effect of pressure. It shows a definite increase in signal intensity at the porous walls, with the first and second having the greatest effect (see Fig. II.13).

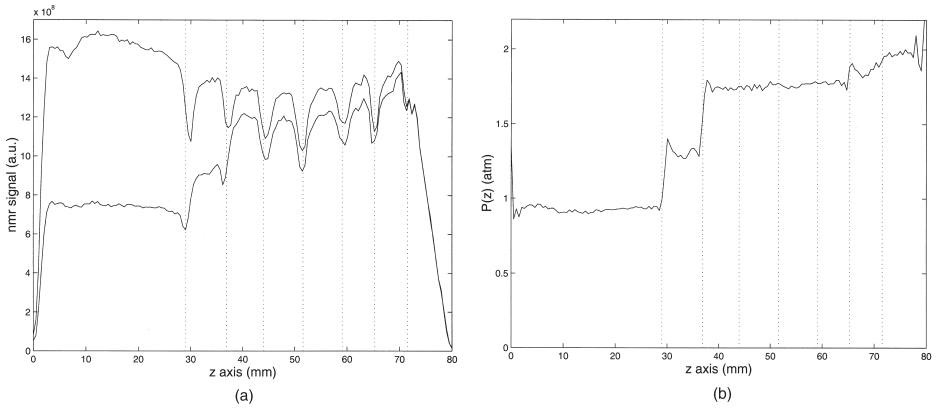

Fig. II.13: Results from the model porous medium. a) 1D profiles of the static gas at 2atm (upper curve) and flowing gas (lower curve) acquired at 2.35 T. Plastic sheets are indicated by dotted lines. In the flowing gas experiment, outlet flow rate is 9.6mL/min. b) Division of the flowing gas profile by the static gas profile in a) before normalising to the applied gas pressure. Reproduced from [47]

The oil reservoir rock is held in a compressible jacket to prevent bypass flow whilst the gas is driven into one end. The sample is imaged when saturated with static gas. The gas is then left to flow through the sample and imaged again. Once more, the two are divided to give the effect due to pressure. This is then used to calculate the local hydrodynamic permeability along the length of the sample. The results are very revealing in terms of the local structure for 25,000 repetitions. The gas is driven through the sample in opposite directions demonstrating the severe inhomogeneity of the sample as the two profiles are not mirror images. (see Fig. II.14)

There are several limitations of this technique which are briefly discussed here. The first is the loss of signal due to rapidly moving gas molecules leaving the imaging volume. This is the most limiting factor for this

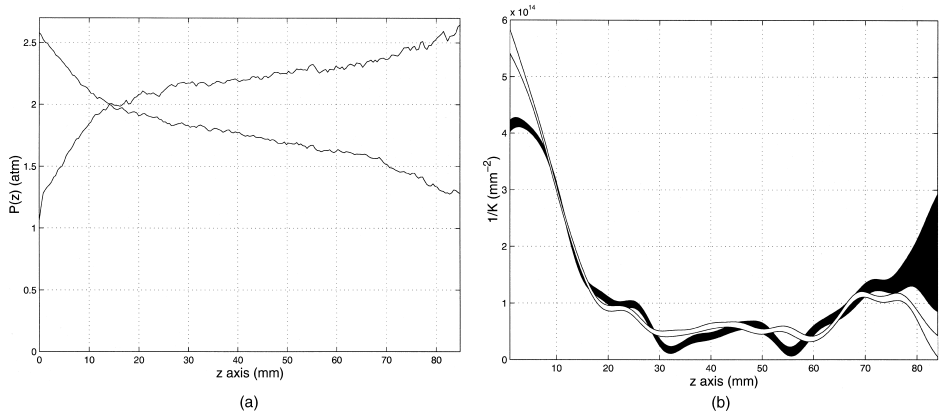

Fig. II.14: Bencsik's oil reservoir rock results. Gradient echo profiles for a North Sea sandstone are used to estimate the pressure drops in a). These curves are not mirror images about the centre of the system as would be the case in a homogeneous system. The upper and lower curves (at x=80mm) are for gas flowing from left to right and right to left respectively. Profiles were reconstructed from 25 000 acquisitions with TR = 127ms. Spatial resolution = 417μm. The spatial distribution of the reciprocal of the permeability, derived from both curves of a) are shown in b). The white curve corresponds to the gas flowing to the right, the black curve corresponds to the gas flowing to the left. Spatial resolution = 3 mm. Reproduced from [47]

experimental protocol and sets the maximum possible permeability of sample that can be imaged using this technique. The experiments must be sufficiently lengthy for good signal and accuracy, typically around 2 hours. The technique only works in dry samples, in one direction at a time and is severely affected by adsorption of gas on the surface of the pores. It is only suitable for single phase flow and will only work in samples that do not contain too many magnetic impurities and have a structure which is homogeneous over the size of each voxel. With this in mind, the technique is a very powerful way to determine the local structure of samples with low permeability.

II.3.3 MRI of Pressure Using Microbubbles

MRI is inherently sensitive to proton density and to the relaxation rate constants or characteristic times, spin-lattice T_1 and spin-spin T_2. These properties offer many insights into a vast array of systems but do not permit comprehensive measurements in all cases. In many situations, it is possible to achieve alternative contrast by using a 'contrast agent'. By using these contrast agents, it is possible to enhance or produce sensitivity to tumours and even organ function. Their use in non medical applications is less widespread, although there are still numerous examples from hyperpolarised carbon for increased signal intensity to aqueous solutions of manganese chloride to trace paths in opaque porous media [49]. In this study, various contrast agents to pressure are developed and tested based on previous work in this field using gas filled microbubbles, suspended in a proton rich fluid.

II.3.4 Previous Work

In the next sections, the previous work in this area will be briefly reviewed to highlight to the reader the novelty of the work presented in this thesis.

II.3.4.1 Experimental Work

The initial concept for using gas filled microbubbles to yield MRI contrast to pressure was published by Alexander [50] in 1996. It was demonstrated that using MRI one could measure the pressure applied to a closed and static fluid system. Lipid coated microbubbles were suspended in a viscous medium and subjected to varying pressure in a syringe barrel whilst running two separate simple imaging sequences. It was intended to be used as a medical contrast agent to allow non-invasive pressure imaging of the cardiovascular system. The microbubbles were between four and nine microns diameter and suspended in a medium which was designed with several functions in mind. The first and primary function was to prevent excessive migration of the microbubbles by using a highly viscous liquid, for which 2% aqueous methyl cellulose was selected. The preparation was then made 'biocompatible' with the addition of various buffers and other components. Microbubbles containing a wide range of gasses were tested for their mean and standard deviation diameters and relaxivities. The microbubbles containing neon were found to have the highest relaxivity, although it was the air filled bubbles which had the greatest variations in T_2^* for changes in pressure.

The signal intensity was found to continuously drift over the duration of the experiment and the authors attribute this to the continual rising of the microbubbles. The authors also suggested that the microbubbles are damaged during pressurisation resulting in release of their gases and subsequently causing the hysteresis (above the level expected by migration alone) observed when the samples are pressurised and released. For concentrations of gas between 1.25% and 5%, the change in signal intensity per increment in pressure was very similar suggesting that smaller concentrations are as effective as greater concentrations, and may in fact be superior as the 10% gas concentration had a reduced change in signal intensity per change in pressure. It was shown that the stability of the preparations may be related to the solubility of the gas in water, with CO_2 being most unstable and a fluorocarbon gas being most stable. Despite its intended application as a medical contrast agent, its lethal dose (the dose required to kill 50% of the test population, often referred to as LD50) in mice is 10cc/kg which is at least 5 times less than the required concentration for sufficient sensitivity.

II.3.4.2 Theoretical Work

II.3.4.2.1 Modelling of Relaxation

In continuation of the work of Alexander, Dharmakumar [31] investigated the optimisation of the contrast agent discussed in the previous paragraph and the imaging sequence to permit *in vivo* measurements. This was achieved using Monte Carlo methods. The fundamental basis for this work was to investigate the effect on the NMR signal of both the relaxation due to the microbubbles and contributing factors from the blood such as oxygenation levels and their susceptibility changes. One of the key objectives was to ensure that the variations in relaxation due to changes in the radius of the microbubbles dominates the other relaxation elements such as deoxygenated red blood cells. Sensitivity is defined as the change in signal intensity per change in pressure and it is the optimisation of this that is the goal of his work.

For the analytical method, the equations for the rate constants R_2^* for an FID and R_2^{eff} for a CPMG sequence are modified to include changes in pressure. These are then further modified to be expressed in terms of sensitivity. It is found that both the rate constants and sensitivities are linearly related to the microbubble density but quadratically related to the strength of the permanent magnetic field, and the magnetic susceptibility difference between the gas in the microbubbles and the suspending medium. By keeping these parameters fixed and varying the echo time in these equations, the dependency on T_E can be investigated. It is seen to increase up to a point at which it plateaus. For T_2^* measurements, the sensitivity and relaxation rate increases monotonically for increasing bubble size before plateauing. In the CPMG sequence (i.e. T_2^{eff} measurements), as the bubble radius increases, the sensitivity and relaxation rate increases quadratically up to a critical radius after which it returns to zero considerably more slowly (see Fig. II.15).

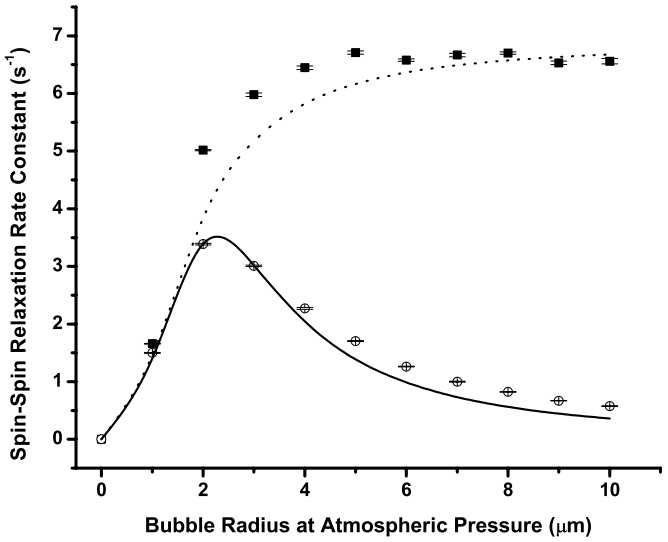

Fig. II.15: Plot showing the dependence of bubble size on R_2^* and R_2^{eff}. Black squares denote R_2^* simulation; dotted line denotes R_2^* theory; open circles denote R_2^{eff} simulation; and solid line denotes R_2^{eff} theory. Reproduced from [51]

Random walk Monte Carlo simulations were used to corroborate the results determined analytically. The general concept of the simulation is model a single microbubble surrounded by 10^4 protons. The volume surrounding the microbubble (the edges of which are where the field perturbations due to the microbubble reaches 2% of its maximum value) is discretised into cells of length $\sqrt{2D\Delta t}$ where D is the proton diffusion length and Δt is the residence time in each cell, which for this simulation was always kept constant at $10\mu s$. The field surrounding the microbubble is calculated using the equation for a spherical perturber given by Weisskoff [29]. The protons are forbidden from entering the central microbubble and are allowed to move between neighbouring cells for each iteration of the simulation. Each proton starts with a phase of zero which is then evolved based on the field surrounding the microbubble. After the echo time has elapsed, the phase of the protons are flipped to simulate the effect of the refocusing pulse for the case where the value of T_2^{eff} is to be estimated. The parameters are then systematically varied and the corresponding sensitivity calculated.

The first simulation is for the rate constant versus the bubble radius. The simulation agrees very well with the analytically determined result for both the CPMG and FID. The simulation must however be scaled by an arbitrary factor to actually overlay the analytical result. The same is true of the sensitivity versus bubble size. The relaxation rate constant is then determined for varied microbubble concentrations in the liquid. The two results are again very similar, both showing the linear relationship predicted although the scaling factor is again required. The next result is the relaxation rate constant for the field strength multiplied by the susceptibility difference. For this simulation, the analytical prediction is quadratic although the simulation is linear. The relaxation rate for varying echo spacing is then determined and agrees well with the theory. The final step in this work is to correlate the simulations with the limited experimental results of Alexander [50]. The agreement is very good although again some scaling is necessary to overlay the two data sets, and the few experimental results are not sufficiently extensive to provide a comprehensive validation.

The major difference between the simulation, experimental and theoretical results might be the consequence of the size distribution of microbubbles. The simulation accounts for a single microbubble in contrast to the distribution of sizes found in the experiments. Those of Alexander [50] are performed using microbubbles between four and nine microns.

II.3.4.2.2 Potential Sensitivity Enhancements

In continuation of his previous work, Dharmakumar produces an estimation of the magnetic susceptibility and subsequent relaxation rate constants for microbubbles which contain Super Paramagnetic Iron Oxide (SPIO) particles within their membranes in a 2006 publication [52]. This is achieved by including the contribution of the membrane shell into the field equation. In order to achieve a significant susceptibility contribution from the shell, several thousand particles would need to be included in the membrane. It is too complex to include in the analytical equations and so numerical methods are used to assess the microbubble's effect on the NMR signal. This is achieved using finite element analysis of the field perturbation caused by $\frac{1}{8}$ of a microbubble with magnetically active agents (SPIOs) on its surface. The resulting magnetic field is then fitted to the equation for the perturbations in B_0 with an additional term for an effective magnetic susceptibility difference as given in equation II.25.

$$\Delta B_z = \frac{1}{3}\Delta\chi_{\text{eff}} B_0 \left(\frac{R}{r}\right)^3 \left(3\cos^2\theta - 1\right), \tag{II.25}$$

From this simulation, it is found that up to a critical point, it is possible to increase the susceptibility of the microbubble by increasing the concentration of the particles in the shell. Beyond this point however, it is better

to increase their diameter (see Fig. II.16).

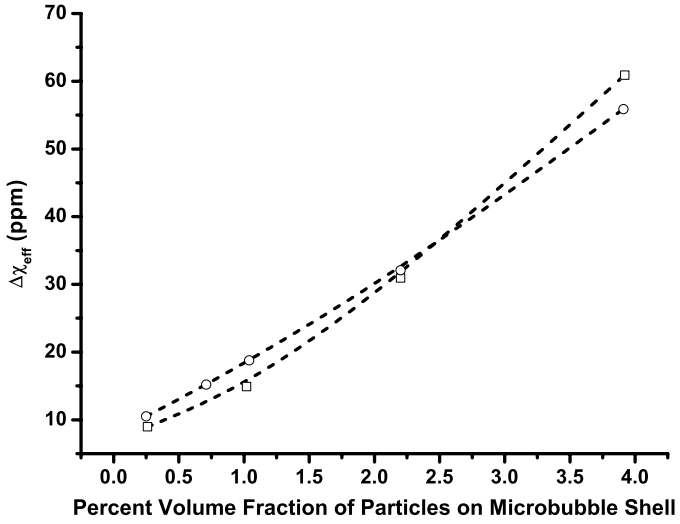

Fig. II.16: Plot of the relationship between the volume fraction of magnetic particles and the effective magnetic susceptibility. Squares denote changing volume fraction by changing particle size and circles denote changing volume fraction by changing particle density. In both cases, particle susceptibility was fixed at 10000ppm and microbubble radius was fixed at $2\mu m$. Reproduced from [51]

This is then extended to determine the effect of the SPIO containing shell on the relaxation rate for changes in pressure. The increased susceptibility of the shell greatly increases the sensitivity of the technique in terms of the changes of relaxation rate for changes in pressure. From this, it is clear that by including the SPIOs in the membranes of the microbubbles, it would be possible to use them in an *in vivo* application. It seems however that the inclusion of these particles in the membranes of the microbubbles will be very challenging. The first challenge is selection of the appropriate material for inclusion in the membranes. It is important that the material has a high magnetic susceptibility but it must also be sufficiently small that it can be included in the membrane (The DSPC molecule often used in the microbubble membranes is approximately $3.4nm$ [53] long in comparison to the smallest SPIO particle which is $62nm$ [54]) Although this may offer a method to increase the chances of making *in vivo* measurements, this study provides no practical implementation of the techniques, offering only estimation through simulation of the improvement in the sensitivity.

II.3.4.3 Microbubble Contrast Agent Design

As the key element for measuring pressure using the microbubble technique, it is important to optimise as many parameters of the contrast agent as possible. The three main components of our contrast agent are the shell material of the bubbles, the gas which these shells encapsulate and the medium in which they are suspended. In the following sections, each of these components properties will be discussed.

II.3.4.3.1 Shell Materials

The shell material is needed to ensure that the gas bubbles remain as stable as possible. The thickness of the shell, its rigidity, its ability to retard the diffusion of the gas molecules into the liquid and resilience of the shell to compression are all used to assess the suitability of the shell material. The main shell materials are discussed in this section.

II.3.4.3.1.1 Albumin

Albumin was one of the first shell materials used in commercial microbubbles approved by the Federal Drug Administration (FDA) for use as an ultrasound contrast agent such as Albunex® and Optisan® (both GE Healthcare, WI, USA). Albumin shells are generally one of the most rigid materials used as a shell component [55] and as such tend to rupture when compressed. Their major advantage for *in vivo* studies is biocompatibility. Because our study is entirely *in vitro* and the shell's stability to compression is of key importance, albumin is a poor choice of shell material for our work.

II.3.4.3.1.2 Polymers

More recently polymer materials have been used as a shell material [56]. These offer the greatest tuneability in terms of their properties although the expertise and equipment necessary to effectively engineer these shell components make them somewhat inaccessible in this study. The greatest problem encountered with polymer shells for ultrasound contrast agent is introducing biocompatibility whilst maintaining the desired properties. Often more than one polymer is used to build a full shell thus allowing the permeation of gas to be reduced whilst an outer later may either introduce some level of biocompatibility or a target site to allow them to be directed *in vivo*.

II.3.4.3.1.3 Lipids

The relevant literature in this area is divided into two groups. The first pertains to production techniques, whilst the second is related to the analysis of damage and ageing of the microbubbles. There is a comprehensive review of microbubble physicochemistry for ultrasound and drug delivery applications by Ferrara *et al.* [57] which covers much of the information in both of these sections from the application point of view and the reader is directed to this for information not covered in the coming sections.

The microbubbles used in the work of Alexander [50] are produced so as to have a lipid shell surrounding an air bubble. The necessary background to the production of these microbubbles is covered in this section. The microbubbles which we have used in our study are produced similarly. Lipids are hydrophobic hydrocarbon or fluorocarbon chains covalently bonded to hydrophilic head-groups (often by a glycerol molecule) [57]. When at a liquid gas interface, the lipid molecules are in the lowest energy state with their hydrophobic chains in the gas and the hydrophilic head groups in the liquid. In the case of a microbubble, this results in a lipid coating

(see Fig. II.17)

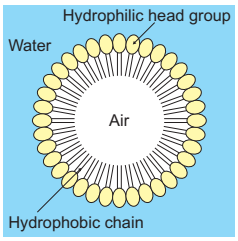

Fig. II.17: Schematic representation of lipid coating on a microbubble.

Lipid molecules in a solvent have three main states, or phases which they adopt depending on their environment. Variations in both lipid concentration and temperature can induce a state change. The fundamental states are as follows:

- Fluid - The lipid/solvent suspension has low concentration or high temperature and the lipids have little interaction with each other.

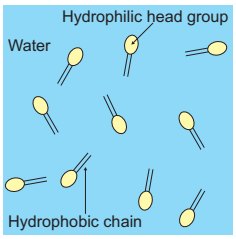

Fig. II.18: Schematic representation of lipid molecules in a fluid state.

- Gel - The suspension is of moderate concentration and temperature. The lipids interact with each other forming one of several possible arrangements associated with 'subphases':
  - Lamellar - sheets of lipids with hydrophobic chains facing inwards forming a bilayer
  - Micelle - lipids arrange to form small spheres with hydrophobic chains facing inwards
  - Vessicle - the lipid bilayer arranges into a sphere containing a central volume of liquid

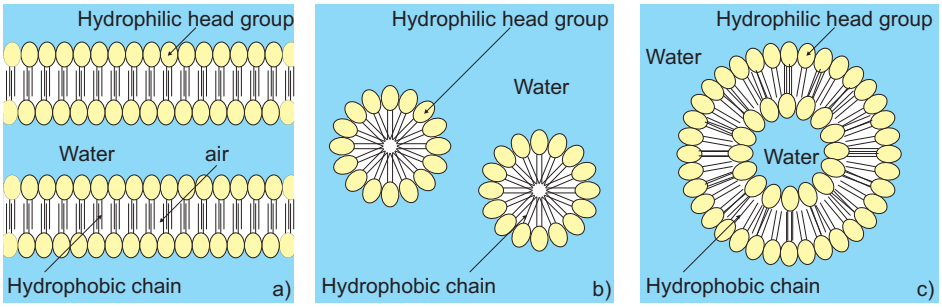

Fig. II.19: Schematic representation of lipid molecules in the three gel states: a) Lamellar, b) Micelle and c) Vessicle.

- Crystal - The final state is for very high concentrations (i.e. little or no solvent) or low temperatures. The density and enthalpy of the system is such that almost no movement of lipids is possible, leading in most cases to a solid ordered matrix. This is often the state in which the lipids are purchased.

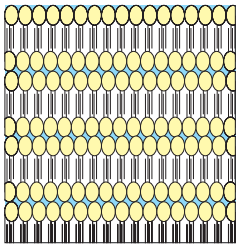

Fig. II.20: Schematic representation of lipid molecules in the crystal state.

The temperatures which will induce a change in phase are known as phase transition temperatures. In order to produce microbubbles, we need a concentration such that lamellar sheets are formed which will self assemble around gas bubbles introduced during the chosen assembly technique. The temperature must be within the range for lipids in the gel phase, i.e. lower than the gel-liquid phase transition temperature, T_{GL}. This temperature is approximately proportional to the number of carbons in the alkyl chain of the lipids [58].

It is important that this transition temperature is known, as if the microbubble experiences temperatures above this it will rupture as the lipids disperse. Similarly if the lower gel-crystal transition temperature (T_{GC}) is reached, the membrane will become very brittle resulting again in fracture. This is one of the reasons that longer chain lipids produce more stable microbubbles. There is also considerable evidence that the density of the lipids in the membrane causes reduction in the surface tension [59] and increases the surface viscosity [60] as well as better preventing escape of the gas from inside [61–63].

II.3.4.3.2 Gases

The properties of the gas which is encapsulated in bubbles can have a strong effect on the contrast agent. Although it is important to inhibit the transport of gas molecules through the shell of the bubble, the solubility of the gas in the surrounding liquid is a more influential factor in predicting the stability of the bubble. Another important property of the gas is its magnetic susceptibility. Although its influence on the overall effectiveness of the contrast agent is less than most other factors, the difference in susceptibility between the gas and liquid phases has a direct bearing on the sensitivity of the NMR experiment. Finally, there is a quantity of work which suggests that by matching the gas to the membrane, some synergy may greatly improve the stability of the microbubbles; for example perfluorohexane saturated nitrogen gas and perfluoroalkylated-glycerophosphatidylcholine membrane [64]. Whilst the results demonstrate this to be the case in contrast to microbubbles containing air and a standard lipid, there is no comparison between these new synergistic components and microbubbles comprising this lipid component and nitrogen gas or a standard lipid and perfluorohexane saturated nitrogen. In this work, we demonstrate that the difference between these preparations

is in fact minimal and that it is the great reduction in solubility of the perfluorohexane saturated nitrogen that makes a large impact on the stability for the range of pressure variations that we have explored.

II.3.4.3.3 Stability

The mechanisms by which the microbubbles are damaged either in time or as a result of application of pressure is of primary concern for both their intended medical applications in which they need to remain stable until they reach their destination and for our applications in which they must remain stable for reasonably long term measurements. There is extensive work in this area using various techniques to assess the damage.

II.3.4.3.3.1 Experimental Assessment of Stability

There are several techniques used to assess the damage processes occurring with the microbubbles. The differences between these methods are dealt with in this section.

- Fluorescence microscopy - The microbubbles are between one and ten microns and are within the diffraction limit of optical microscopy (approximately 500nm resolution). In order to enhance the visibility of the membrane over the gas and surrounding medium, fluorescence microscopy can be used. One of several fluorescent dyes are added to the microbubble preparations [62] and washed off before collecting the initial microscope images. To allow the samples to be imaged with the microscope, it is necessary to contain the microbubbles on the sample stage. This can be achieved using specific hardware manufactured from an optically transparent, rigid material for example acrylic, such as a perfusion chamber [61], or by making a well of inert vacuum grease on a glass slide into which the sample can be included and capped with another glass slide [62].

- Langmuir Blodgett Trough - The Langmuir Blodgett trough method is used to measure the surface tension of lipid layers. The lipids are suspended in a 'dispersing medium' such as chloroform which is volatile but will not affect the molecules. A known quantity of lipid molecules is then added to a PTFE bath containing water. The bath contains a moving PTFE bar which is used to reduce the area available to the molecules (see Fig. II.21). By moving from a high surface area to low surface area and measuring the pressure applied to the bar, it is possible to determine the surface tension and some membrane properties (such as rigidity) of various lipids. The resulting graph shows the points at which a change of state occurs. This information can be fed back into the commonly used Epstein-Plesset (EP) model [65] to determine the impact of the microbubble shell on their stability.

- Dissolved oxygen measurements - In order to monitor the dissolution of the gas into the surrounding medium, dissolved oxygen measurements are often used [66]. The protocol is very simple and requires measurement of the dissolved gas before and after inclusion of the microbubbles and then for a duration of time after. This then allows the quantity of gas escaping from the microbubbles to be determined which can again be used to test the validity of and improve the EP model.

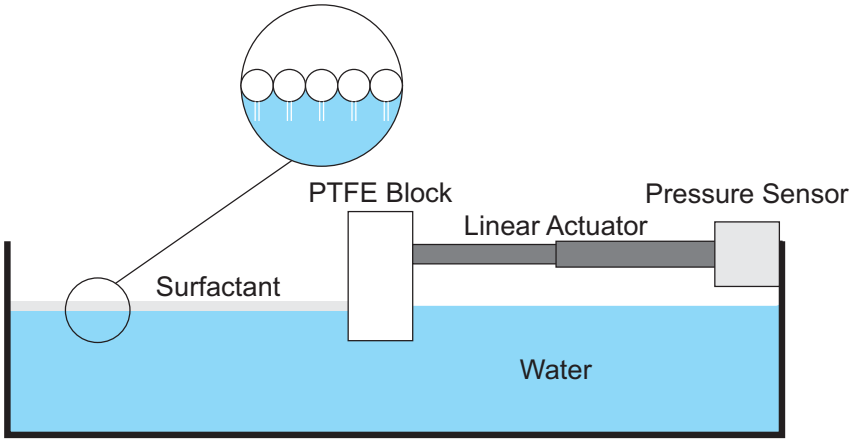

Fig. II.21: Schematic of a Langmuir Blodgett trough.

The majority of studies are based on a combination of several of the above techniques which when combined give a better overall view of the processes. Several methods are used to manipulate the microbubbles during investigation such as application of pressure, ultrasound or micropipetting depending on the properties of interest and the environment in which they will be deployed.

By using these methods, it has been found that the structure of the lipid membrane is not a simple surface as was once thought. In fact, the microbubble shell appears to have a cell like structure, not dissimilar to that of honeycomb [62]. Currently it is believed that there are four possible mechanisms by which the shell of the microbubbles become damaged. Through optical fluorescence microbubble observations, their shells are seen to initially take on a new structure before undergoing a transition into one of these damage mechanisms (see bullet points and Fig. II.22 [62]).

- Zippering - During zippering, part of the microbubble shell is pushed outwards from its circumference. The hydrophobic chains on opposing sides then are in an energetically favourable state when touching. As the chain immediately above contacts its opposite chain, a greater force is felt between the two causing contact between them and so on until the whole bubble has undergone the process. This causes a rapid change in bubble shape from a tear-drop like shape to a gas free elongated micelle if the force is sufficient to eject the gas bubble without breaking the shell. (Fig. II.22a)).

- Shedding - Shedding starts in much the same way as zippering, but where the chains combine in zippering, in shedding the micelle is ejected leaving a single smaller microbubble still intact. This relies on the surface tension of the microbubble being high enough to maintain integrity during the shedding process but sufficiently low that is does not rupture. It also frequently occurs in microbubbles with several differently sized components in the shell such as PEG molecules as a rapid change in energies is experienced when the touching molecules are different. (Fig. II.22b)).

- Buckling - Buckling is a very common cause of damage to the microbubble shells and often happens

when they are subjected to pressure forces. The honeycomb structure begins to fold with the plate areas maintaining their structure whilst the boundaries between them shift. This causes the surface to take on a crinkled appearance which can be maintained for some amount of time without damage. It is however possible that the microbubbles break instantly, rupturing the shell and expelling the gas. Buckling is frequently caused during application of pressure, which is possibly due to an induced change of state of some lipids in the shell, producing these strange patterns. (Fig. II.22c)).

- Coalescence - One of the major problems when using a sample with a significant concentration of microbubbles is that of coalescence. When two microbubbles come into contact with each other, they may occasionally coalesce. However, when pressure is applied whilst they are touching, buckling may weaken the surface structure of the microbubbles causing the two membranes to join. This is a highly unstable state and will usually result in either rupture of the membrane or ejection of a small part of it to yield a single larger microbubble with a single membrane. In terms of the measurements made in this work, many problems are caused as changes in the signal intensity and sensitivity are directly related to the microbubble size distribution. (Fig. II.22d)).

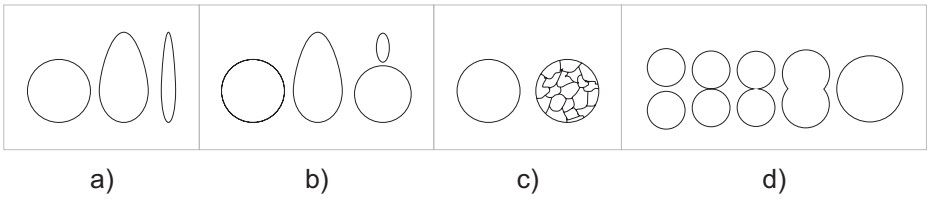

Fig. II.22: Schematic Representations of microbubble damage mechanisms. a) Zippering, b) Shedding, c) Buckling and d) Coalescence.

II.3.4.3.3.2 Effect of Lipid Carbon Chain Length

The choice of lipid for the membrane of the microbubble is one which can greatly influence the stability of the bubble. Anecdotal evidence from our early experiments suggested that, up to a point, increasing the number of carbons in the acyl chain of the lipid improves the stability of the microbubble preparations. The work of Borden and Longo [61] confirms this with an experiment in which a dissolution chamber is used with an inverted optical microscope to observe the dissolution rate of various microbubble preparations. It is found (see Fig. II.23) that increasing the chain length exponentially increases the resistance of the microbubble membrane. It is also demonstrated in this work that increasing the chain length increases the resistance of the shell to air permeation and this is the most likely reason for the observed stability increase.

II.3.4.3.3.3 Modelling - Epstein Plesset

The theoretical approach to the problem of microbubble damage is based around the Epstein-Plesset model [65]. This model is related to the properties of a gas bubble which is dissolving in a surrounding liquid (or growing if it is in a oversaturated liquid) and hence changing in size. This change in size is partially related to

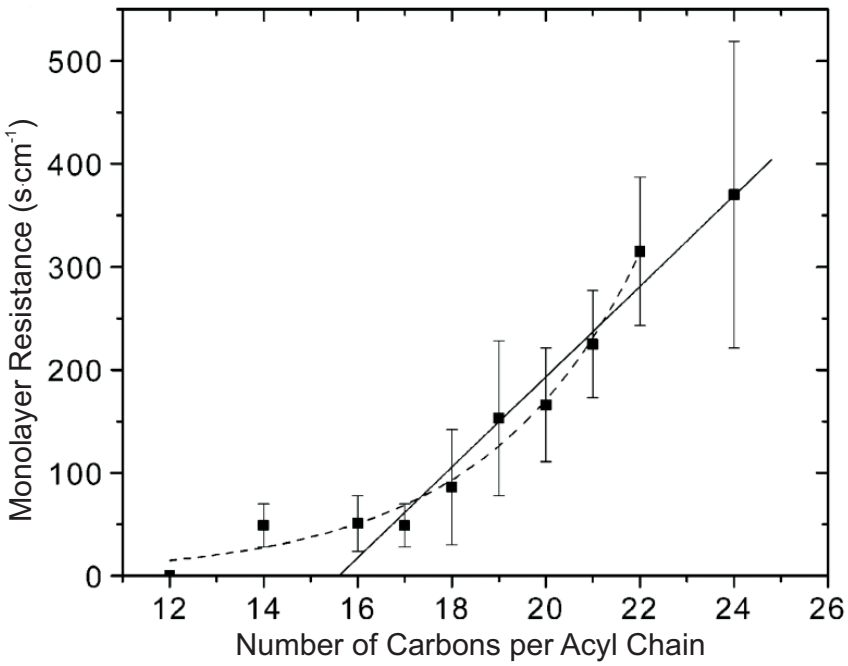

Fig. II.23: Microbubble shell resistance versus acyl chain length. Error bars are standard deviation, exponential (dashed) and linear (solid) trend lines attempt to fit two possible theoretical estimates. Reproduced from [61], all rights reserved Langmuir 2002.

the diffusivity of the gas and therefore a diffusion related transport term should be included in the model. However, the complexity of this is such that it is neglected in the Epstein-Plesset model. There is a volume of work on testing the validity of the EP model with both coated and uncoated gas bubbles. It is generally accepted that this transport term can be neglected based on the fact that the concentration of gas inside the bubble is far greater than the gas dissolved in the surrounding medium. Where this is not the case however, the transport term would be necessary for a reasonable approximation. Because the area around the microbubble which is relevant to the diffusion process is considerably larger than the microbubble, its size is only of relevance to determine the 'interfacial area' over which mass transfer between phases occurs.

For bubbles which are travelling through the surrounding medium, the estimation of the diffusion may be somewhat low as it is enhanced by its movement which must then be accounted for. However, for our application the microbubbles can be considered stationary thus making the approximation suitable. In addition to the shrinkage or growth of the bubbles, the surface tension of the gas liquid interface must be considered in the model. At this point it worth noting that although the EP model does not contain a term for a membrane thickness (as it is concerned only with gas bubbles) it is possible to relate it to coated microbubbles by using the diffusion across a lipid membrane as a measure of the exchange between gas and liquid interface.

A major work to validate the EP model was performed by Duncan *et al.* [59]. This work uses a set-up with two micropipette manipulators and two water cells, one with air-undersaturated water and another with fully air saturated water. The microbubbles are produced using one 8 μm pipette and transferred with a 50 μm pipette

from the saturated water to the undersaturated water. They are monitored in both water samples using an inverted microscope with x40 magnification objective and x5 magnification eyepiece to determine the rate of dissolution. The surface tension of the shells in the saturated solution can be be varied by adding surfactants. In the undersaturated solution, the microbubbles are lipid coated (corresponding approximately to zero surface tension) by cooling through the liquid-gel transition temperature. The radii of microbubbles captured by the small pipette are measured during dissolution until the point where they are sucked into the pipette. The pipette does have a small effect on the dissolution rate although it is fully corrected for.

The measured dissolution rates for both the saturated and undersaturated solutions agree very well with the theory based on the variations of the diffusion constant in the literature for water and air. The lipid used is DSPC, as in our experiments, and is cooled as described previously. During observations of the coated microbubbles in the undersaturated solution, the shell is seen to buckle and shed as seen in the work of Borden *et al.* [62] returning to a smaller spherical shape. In this manner, it is possible for it to loose some of the gas to the surrounding medium without rupturing. A final experiment is performed in which the lipid coated bubble is suspended in the fully saturated water and monitored. This represents an approximation at the infinitely saturated liquid case as the microbubble has zero surface tension and no other mechanism to loose gas. They have been tested for 6 hours with no change in microbubble radius.

II.3.4.3.3.4 Conclusions

The understanding of microbubble damage is key to improving the preparation of microbubbles. It is through the work of Duncan and Borden that many major developments have been made in the selection and formulation of microbubble shell preparations for many applications. Although the majority of our work is carried out using a single lipid shell, we have selected a lipid with a chain length that produces relatively stable preparations.

II.3.4.4 Functionalised Microbubbles

The production of coated microbubbles lends itself well to engineering and adapting the microbubble properties in such a way as to better control a specific experiment. This may involve for example, the addition of different lipid components to control the breaking threshold of the microbubble shell, to control the electric charge on the surfaces of the microbubbles or the addition of specific components to their surface to adjust their biocompatibility or to allow them to be targeted to specific sites in the body [67].

Changing the surface chemistry of the microbubbles is a relatively simple procedure, best achieved by adding molecules to the microbubble membrane before or after their formation. Post-formation can be performed using two main methods. One method is more straight forward but is generally rejected on the grounds that it reduces the biocompatibility (which is of little concern for our applications). The molecules can be attached

either with a bridge molecule or by covalent bonding. The bridge method is often achieved using molecules with amino groups allowing binding with carboxyl groups on the microbubble shell by means of a variety of bridge molecules [68]. The second method uses a thiol group on the microbubble as the binding site which is more challenging to attach, though it offers a more stable bond. A more successful bonding and more effective microbubble chemistry is achieved by combining the microbubbles with the other molecules before they are formed. It is important however that the molecules are similarly sized to the lipids to prevent damage either to the microbubble shell or to the molecule itself. If the desired molecules are significantly larger than the lipids, the post formation method may be necessary.

The predominant function of the secondary molecules is to allow specific targeting of the microbubbles to various sites around the the body and is often achieved using antibodies. For our applications however, there is some interest in using this method to attach paramagnetic molecules to the microbubbles in order to enhance sensitivity. This may be achieved by combining a molecule which is strongly paramagnetic with the microbubble lipids before formation. Of particular interest is dysprosium oxide which forms a white powder that may be included directly in the formation providing enhanced magnetic susceptibility.

Another common surface modification is the application of a 'PEG brush'. Using a similar process to that of the secondary molecules in the previous paragraph, PolyEthyleneGlycol (PEG) molecules can be included in the microbubble layers. This mimics the situation found in naturally occurring coated microbubbles. These microbubbles occur in natural water systems [69, 70] and are formed predominantly of lipids from decaying biological material and are particularly stable. The PEG molecules are often used to prevent coalescence of microbubbles although it is essential that they are in the 'brush regime' for this to work. The brush regime starts when there is a sufficiently high concentration of PEG molecules over the microbubble shell that repulsion between the chains of the molecule cause them to lie perpendicular to the surface of the shell. Two approaching microbubbles will experience the same repulsion as between the PEG chains which will act to prevent the microbubbles contacting hence reducing the likelihood of coalescence.

II.3.4.5 Production Methods

In order to reproduce some of the prior work discussed in the previous sections, it was necessary to either purchase or produce these lipid coated microbubbles. Although there are several commercially available and FDA approved microbubble contrast agents for ultrasound use [71], they are relatively expensive and polydisperse. The additional control which is afforded if they are produced locally is an attractive benefit. For these reasons, all the microbubbles in this work are produced through collaboration with Yvonne Perrie's group at Aston University.

There are four main methods for producing gas filled microbubbles:

- Sonication in which audible frequencies are used to generate the gas bubbles in the suspension of fluid and lipid through cavitation;
- Shear mixing in which gas bubbles are introduced using a device which rapidly shears through the suspension;
- Flow focusing which is more complex: In this method, gas is injected in a controlled manner into the suspension resulting in a relatively narrow distribution of microbubble sizes;
- The final method encompasses several techniques and here is referred to as manual assembly. These methods differ from the others (which could be referred to as self assembly) in that they require the membrane to be grown or 'assembled' around the gas bubbles.

Each of these methods are described in the following sections.

II.3.4.5.1 Sonication

The first stage in the sonication methods is to achieve the laminar dispersion of lipids in water as described in section II.3.4.3.1.3. As their primary application is for the drug delivery sector, the methods are predominantly protected by patents (for example [72–75]). The sonicator uses near ultrasound energy to induce cavitation in the suspending fluid [76]. When the cavity is created, the hydrophobic chains are in an energetically favourable state when inside the cavity whilst the head groups remain in the surrounding liquid. This results in a lipid monolayer membrane around each. The problems associated with the sonication methods is primarily the requirement of specialist equipment which is quite costly to purchase. Additionally, if it is desired to include a different gas within the lipid membrane, it is necessary to perform a multi-step sonication process. Initially, the liquid is sonicated to produce a dense foam which will be partially filled with gas due to cavitation and, as time progresses with that of the head-space (the volume of gas above the suspension). This will result in a sample with a variety of trapped gases. To ensure that the majority of microbubbles are filled with the gas of the head-space, which can be varied for different microbubbles, the fluid is sonicated until there is little bulk fluid visible (i.e. when the cavitation is complete) before the head-space is filled with the desired gas and sonication continued. This breaks up and reforms the cavitation-produced bubbles with the head-space gas and creates more head-space gas filled microbubbles from the remaining surfactant molecules. The distribution of microbubble size is slightly more narrow than the shear mixing method detailed in the next section although it is still polydisperse.

II.3.4.5.2 Shear Mixing

The shear mixing methods are very similar to the sonication methods with the main difference being that they use a shearing motion in the liquid to introduce bubbles to the fluid. Depending on the specific protocol used, the gas is either again introduced by cavitation due to rapid shearing of the fluid or introduced by a vortex like

effect, drawing in gas from the head-space making this method suitable for rapidly producing microbubbles which can be filled with a variety of gases. This is traded off against the fact that the distribution of microbubble sizes is very broad, often in the order of ten microns. This is the method preferred for the manufacture of the microbubbles produced for our work as the equipment is comparatively inexpensive and produces a very high yield of microbubbles relatively quickly.

The size of the microbubbles is controllable up to a point by varying the speed of the shearing motion, with faster shearing giving smaller bubbles. At too slow a speed, neither cavitation nor vortexing occurs whilst at too high a speed, the membrane is just disrupted with no formation of bubbles.

II.3.4.5.3 Flow Focusing and Microfluidics

In the case where it is desirable to have a very narrow distribution of microbubbles, flow focusing and microfluidics are currently the most effective methods. They are however time consuming and costly to implement, as well as to run. The concept uses the properties of gas liquid interfaces to produce monodisperse gas microbubbles. There are several variants of the technique, the most simple of which has a device with a single sharp edged narrowing in the centre (see left hand side Fig. II.24). In this microfluidic device the lipid suspension is driven from left to right whilst the gas is driven bottom to top. As the gas is driven upwards, an elongated bubble is formed and because the fluid is flowing left to right, the bubbles are cleaved on the edges of the channel forming microbubbles of a well defined constant size. The diameter of the bubbles is somewhat controllable by varying the ratio of the fluid and gas phase flows although laminar flow is necessary, so the possible adjustments somewhat rely on the width of the channel.

The next level of complexity is shown on the right hand side in Fig. II.24. In this set-up the flows of liquid and gas are concentric which allows significantly more control over the diameter of the microbubbles than the perpendicular method described previously. The additional complexity of concentric flow, requires specialised fittings in contrast to the first method.

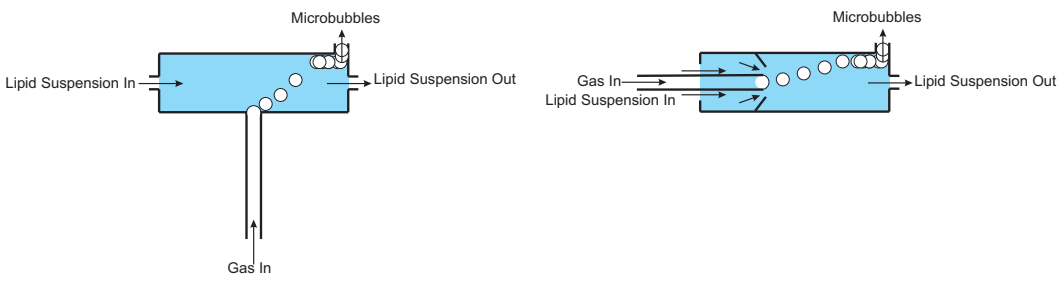

Fig. II.24: Schematic representations of simple implementations of microfluidic devices, reproduced from the work of Xu [77] and Talu [78]

Until 2007 the flow focusing method produced microbubbles which whilst highly monodisperse, are centred

around 100*nm* or less. In consequence, they were probably not useful for our studies, as they are too small to allow sensitive measurements. In 2007 however, the technique was developed to allow the production of microbubbles centred around the range of commercial microbubble contrast agents. The technique is now suitable for producing monodisperse microbubbles with an peak in the distribution at 3.5μm [79] as a result of further optimisation.

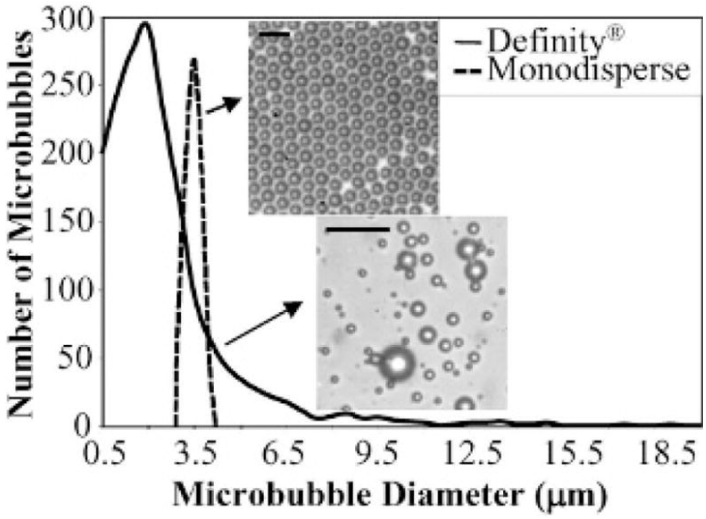

Fig. II.25: Comparison between size distribution of microbubbles in commercial ultrasound contrast agent Definity® and microbubbles produced using the flow focusing technique developed by Talu *et al.*. Reproduced from [79], All rights reserved 2007 Molecular Imaging.

II.3.4.5.4 Manual Assembly

The other methods are all encompassed by manual assembly. This includes microbubbles with polymer or other rigid shells. This offers far greater control over the surface and assembly process at the expense of the ease with which they can be produced. They require some sort of template to be effectively produced [80] and in consequence often result in a relatively poor yield. Because the methods for each shell type differ greatly and they have little relevance to this study, they are not covered here.

II.3.4.6 Suspending Medium

This section is concerned with the theory surrounding the suspending medium for the contrast agent, including rheological analysis and the chemical properties of polysaccharide gels which are used both in our work and that of Alexander [50].

II.3.4.6.1 Rheology

Rheology is the study of the viscoelastic and flow properties of a medium. There are a variety of ways in which these properties can be studied although they all have common features. The three main methods used for measuring the rheological properties of samples are flow, creep and oscillation.

There are several manufacturers of commercial rheometers who produce instruments which are capable of making highly accurate measurements with little operator input. The majority of these instruments are rotational rheometers in which shear forces are applied to the medium using a rotating motion whilst the torque required to generate these forces is measured to determine the rheological properties of the sample. To transfer these forces to the medium requires the use of a tool or 'geometry'. These geometries are available in various different types which will be dealt with briefly here.

II.3.4.6.1.1 Geometries

Each of the following geometries are available in a variety of materials. The most common are stainless steel, aluminium, acrylic and quartz which are selected depending on the medium under test. The ideal geometry is as light as possible whilst maintaining chemical compatibility with the sample under test. Acrylic is the lightest and as such the least affected by inertial effects, but has poor resistance to chemicals and temperature variations. Stainless steel is more robust and stable to variations in temperature and to chemicals which would attack the acrylic but its greater weight requires some inertial compensation. Finally for media which are very chemically reactive, quartz geometries can be used although they are very costly.

- **Parallel Plate**: A circular plate is held just in contact with the top of the volume of interest, which is applied to a lower flat plate which may have some form of temperature control. The bottom plate is fixed whilst the top plate can be rotated. The separation between the plates can be varied at the users discretion. This is ideal for samples which contain particles. By setting the distance between the two plates to 10 times the particle size, problems which they may cause can be eradicated [81]. Unfortunately however, the distribution of stress across the radius of the geometry is not uniform. Modern rheometers correct for this however, so it is not necessarily of primary concern and in consequence this is most often the geometry of choice.

- **Cone and Plate**: The cone and plate geometry is similar to parallel plates except the movable plate is a truncated cone. This compensates for stress variations along the radius of the plate but is only suited to homogeneous samples as particulates can migrate to the centre and jam the geometry.

- **Concentric Cylinder**: The concentric cylinder geometry is a static cup (into which a specific volume of sample is placed) with a movable cylinder which is pushed into it. There are three main designs of these geometries which are useful for low viscosity solutions which would not remain trapped between the open geometries discussed so far. They also allow measurement of samples with minimal variations over the length of the radius if a cone and plate geometry is unavailable (as is the case with the rheometer used in the experimental section).

  - *Recessed End* - The basic design for the concentric cylinder geometry. Ideal for very low viscosity samples. Some variations over length of radius which accounted for by the rheometer as in the parallel plate geometry.

– *Conical End* - The equivalent of the cone and plate geometry with the same equation set for shear rate and stresses but suitable for low viscosity samples.

– *Mooney Ewart* - In order to eliminate the variations in the shear forces across the base of the rotating plate, the Mooney Ewart [82] geometry is designed so that the ratio of the clearance between the two cylinders to the radial distance is constant. This eliminates the variations in shear forces across the surface of the geometry. This geometry lends itself very well to the study of non-Newtonian fluids in which a variation in shear forces across the sample could cause major changes in its rheological behaviour. The equations determining the shear force and rate for this geometry are an adaptation the cone and cylinder geometries.

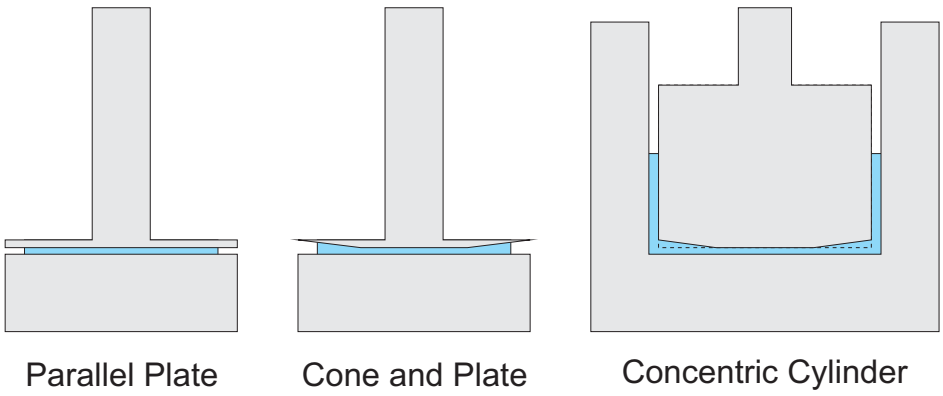

Fig. II.26: Schematics of the three main geometry types. The concentric cylinder is a Mooney Ewart geometry with the recessed end geometry shown with a dashed line.

II.3.4.6.1.2 Experiments

There are three main experiments which can be undertaken with a commercial rheometer. These are Flow, Creep and Oscillation. There are also several alternative methods to perform rheology of samples without a rotational rheometer. Three such experiments will be discussed briefly here followed by some general discussion of alternative methods to obtain rheological information.

- **Flow**: In order to study the properties of a flowing fluid, a method for generating flow is necessary. The rheological measurements can be initially divided into two categories based on the nature of this flow: the first is rotational, in which the medium is held between two surfaces and rotated to induce flow; the second is linear flow in which the medium is driven along a channel or pipe along a single axis to measure its properties.

  The measurement of the properties of a fluid during flow are related by the following three equations:

$$\text{Shear Rate}(s^{-1}), \dot{\gamma} = v/d. \tag{II.26}$$

$$\text{Shear Stress}(Pa), \sigma = F/A. \tag{II.27}$$

$$\text{Viscosity}(Pas), \eta = \frac{\sigma}{\dot{\gamma}} \tag{II.28}$$

There are several different models used to describe a flowing fluid which are covered briefly here:

- *Newtonian* - For a Newtonian fluid, the shear rate is directly proportional to the shear stress with the constant of proportionality representing the viscosity. There are no fluids that are completely Newtonian, although many have Newtonian behaviour within large ranges of shear rates.
- *Shear Thinning (Pseudoplastic)* - For pseudoplastic materials, as the shear rate is increased, the viscosity of the material decreases. This is a relatively common behaviour, in everyday life with examples such as paints, salad cream and various household products. Their shear stress is described mathematically by the 'power law' model

$$\sigma = K_2 \dot{\gamma}^{n-1} \tag{II.29}$$

  where K_2 is the viscosity coefficient and n is the shear rate index which is less than 2 for shear thinning fluids.
- *Shear Thickening (Dilatent)* - Dilatent materials have the opposite behaviour to pseudoplastic materials in that as the shear rate is increased, their viscosity also increases. This is a less common behaviour although there are still some common examples such as cornflour or colloidal solutions such as clay slurry. Again, this is described by the power law model although this time the value of n is greater than 2.
- *Plastic* - Plastic materials are the final group and are represented by materials which do not begin flow from zero shear but from a given threshold value. There is a second property for these materials known as yield stress which is the shear stress needed to induce flow which could then be either pseudoplastic or dilatent.

- **Creep**: The creep experiment is used for the investigation of flow mechanisms most commonly seen in everyday life such as pouring and dripping. It is a very slow flow experiment that can be used to speed up processes such as sedimentation and observe their corresponding effects on the viscosity. It sees application particularly in the consumer product areas as it can be used to determine if a fluid will drip

or pour from a bottle for example. The theory and methods are the same as for the flow experiments with the exception of the magnitude of the torques applied and the forces measured. For our highly viscous homogeneous samples it is of little benefit.

- **Oscillation**: The oscillation technique is considerably more complex than that of flow and is included as a brief overview rather than a comprehensive review as the extensive mathematics which is required to process the results is not necessary for understanding the measurement. Some fluids do not only exhibit a flow response when stressed. In viscoelastic liquids, after the applied stress is released, the fluid may attempt to return to its prior state. This effect is known as viscoelasticity. Oscillation measurements are capable of simultaneously measuring the viscous and elastic behaviour of the medium under investigation. The general principle is to apply an oscillatory motion to the sample to shake it back and forth and to measure the resulting forces. It is useful not just for characterising the viscoelastic properties but also to determine structural changes in semi solids and similar materials. It is a particularly challenging measurement as high torques may be necessary to apply a sufficient displacement to the sample but also small torques are required to detect the smaller changes without damaging the sample.

The actual processing of the data is very complex and dealt with by the rheometer control software and is not critical to the understanding, design or interpretation of the experiments. By simple modification of the formula for shear stress, the basis of the oscillation experiment is seen. The shear force applied is an oscillatory motion defined by $F = F_0 \cos\omega t$ and this is substituted into the shear equation as follows:

$$\sigma = \frac{F}{A} = \frac{F_0 \cos(\omega t)}{A}, \tag{II.30}$$

where A is the surface area over which the sample is sheared. From this the amplitude of the rotating plate at steady state (a) and subsequent shear strain for a sample between plates separated by distance h can be determined as in equation II.32.

$$a = a_0 \cos(\omega t - \phi), \tag{II.31}$$

$$\gamma = \frac{a_0 \cos(\omega t - \phi)}{h}. \tag{II.32}$$

The shear rate, which is in quadrature phase with respect to the strain is given as:

$$\dot{\gamma} = \frac{d\gamma}{dt} = \frac{1}{h}\frac{da}{dt} = \omega(a_0)\cos\left(\omega t - \phi + \frac{\pi}{2}\right). \tag{II.33}$$

These equations are best described using complex notation as they are harmonic.

$$\sigma^* = \sigma_0 exp(j\omega t), \tag{II.34}$$

$$\gamma^* = \gamma_0 exp[j(\omega t - \phi)]. \tag{II.35}$$

$$\tag{II.36}$$

The original definitions correspond to the real parts of each of these equations.

By using this measurement method it is possible to determine a variety of parameters:

- G*, the Complex Shear Modulus - This is the ratio between complex stress and strain and is determined experimentally from a sweep through a range of frequencies. It gives rise to the storage, G', and loss, G'', moduli which are the real and imaginary components respectively:

$$G^* = \frac{\sigma^*}{\gamma^*} = G' + iG''. \tag{II.37}$$

- G', the Storage Modulus (Pa) - This is a measure of the degree of structure within the material and is representative of the elastic storage of energy. It will be high in more ordered samples such as highly concentrated gels and increase or decrease if structure is enhanced or destroyed.
- G'', the Loss Modulus (Pa) - This is related to the viscosity of the sample and will be high if the sample is more viscous than elastic such as low concentration high viscosity gels.
- η', the Dynamic Viscosity (Pas) - This is the loss modulus over the angular frequency. It is representative of the in phase part of the viscosity and in consequence will be related to the shear viscosity (η) only in purely viscous samples.
- σ, Delta (°) - This is the phase difference between the stress and strain waves. With increasingly viscous and elastic behaviour, this will increase and decrease respectively. So long as the inertia has been properly accounted for, this will always be between 0° and 90°.

In order to measure these properties, the following five parameters must be known:

Torque (for amplitude of the stress wave), dimensions of the system (to calculate the amplitude of the stress wave and for inertial calibration which is very important with low torques), displacement amplitude (amplitude of the strain wave), phase difference between the stress and strain waves which must be corrected for inertia and finally the frequency which is varied to allow characterisation of the sample.

Thus, for a well defined environment (as provided by a commercial rheometer) it is simple to make a

complex and highly informative measurement of a soft elastic solid which could not be measured using a flow method.

- **Alternative Methods** There is a near infinite quantity of methods for measuring the rheological properties of a sample without a rotational rheometer. Generally, the principles are similar, in that a method for varying the conditions of the sample is used whilst it is probed to obtain some parameters from which the viscosities can be calculated. Of the methods available, the most common are the Rheo-NMR produced by Magritek (Wellington New Zealand) and custom solutions engineered specifically for a product.

  The Rheo-NMR can be produced in one of two orientations, either with a laminar flow in a pipe which is imaged by either spin labelling velocity imaging and used to assess the flow front to get the degree of Newtonicity and viscosity; or like a traditional column type rotational rheometer which is also velocity imaged in cross section to get the shear forces across the sample. The results are marginally less accurate than achievable with a traditional rheometer although the cost of the instrument is considerably less.

  The custom solutions are common in industrial environments in which it is desirable to have a single measurement repeated, resulting in an accurate analysis of the sample. There are endless examples such as the dental paste rheometer [83] in which a sample is probed laterally rather than rotationally using a reciprocal motion, the force of which is measured during application.

References

[1] S. Zweben, T. Kornack, D. Majeski, G. Schilling, C. Skinner, R. Wilson, and N. Kuzma, "Evaluation of possible nuclear magnetic resonance diagnostic techniques for tokamak experiments," 2002.

[2] M. D. Fayer, *Elements of Quantum Mechanics*. Oxford University Press, USA, 2001.

[3] D. Kruk and B. Blicharska, "Analysis of the shape of FID signal and NMR spinning sidebands for the Couette flow," *Physica B: Condensed Matter*, vol. 301, no. 3–4, pp. 349 – 358, 2001.

[4] M. Sankey, Z. Yang, L. Gladden, M. Johns, D. Lister, and B. Newling, "SPRITE MRI of bubbly flow in a horizontal pipe," *Journal of Magnetic Resonance*, vol. In Press, Corrected Proof, 2009.

[5] E. Hahn, "Spin echoes," *Physical Review*, vol. 80, pp. 580–594, 1950.

[6] H. Y. Carr and E. M. Purcell, "Effects of diffusion on free precession in nuclear magnetic resonance experiments," *Phys. Rev.*, vol. 94, pp. 630–638, May 1954.

[7] B. Blumich, *NMR Imaging of Materials (Monographs on the Physics and Chemistry of Materials, 57)*. Oxford University Press, USA, 2003.

[8] D. M. Grant and R. K. Harris, *Encyclopedia of Nuclear Magnetic Resonance*. John Wiley and Sons Ltd, 1996.

[9] A. N. Garroway, P. K. Grannell, and P. Mansfield, "Image-Formation in NMR by a Selective Irradiative Process," *Journal of Physics C-Solid State Physics*, vol. 7, no. 24, pp. L457–L462, 1974.

[10] J. Hennig, A. Nauerth, and H. Friedburg, "RARE imaging - a fast imaging method for clinical MR," *Magnetic Resonance In Medicine*, vol. 3, no. 6, pp. 823–833, 1986.

[11] R. Ogg and P. Kingsley, "Optimized precision of inversion-recovery measurements for constrained scan time," *Magnetic Resonance in Medicine*, vol. 51, no. 3, 2004.

[12] G. Bydder, J. Hajnal, and I. Young, "MRI: Use of the inversion recovery pulse sequence," *Clinical Radiology*, vol. 53, no. 3, pp. 159 – 176, 1998.

[13] E. O. Stejskal and J. E. Tanner, "Spin diffusion measurements: Spin echoes in the presence of a time-dependent field gradient," *The Journal of Chemical Physics*, vol. 42, no. 1, pp. 288–292, 1965.

[14] R. M. Cotts, M. J. R. Hoch, T. Sun, and J. T. Markert, "Pulsed Field Gradient Stimulated Echo Methods For Improved NMR Diffusion Measurements In Heterogeneous Systems," *Journal of Magnetic Resonance*, vol. 83, no. 2, pp. 252–266, 1989.

[15] P. Galvosas, *PFG NMR-Diffusionsuntersuchungen mit ultra-hohen gepulsten magnetischen Feldgradienten an mikroporosen Materialien*. PhD thesis, der Universitat Leipzig, 2002.

[16] P. Galvosas, F. Stallmach, J. Karger, and Tu, "Background gradient suppression in stimulated echo NMR diffusion studies using magic pulsed field gradient ratios," *Journal of Magnetic Resonance*, vol. 166, no. 2, pp. 164–173, 2004.

[17] F. Stallmach and P. Galvosas, *Spin echo NMR diffusion studies*, vol. 61 of *Annual Reports on NMR Spectroscopy*. 2007.

[18] P. Galvosas, F. Stallmach, G. Seiffert, J. Karger, U. Kaess, and G. Majer, "Generation and application of ultra-high-intensity magnetic field gradient pulses for NMR spectroscopy," *Journal of Magnetic Resonance*, vol. 151, no. 2, pp. 260–268, 2001.

[19] D. Zald, *The Orbitofrontal Cortex*. Oxford University Press, USA, 2006.

[20] J. R. Reitz, F. J. Milford, and R. W. Christy, *Foundations of Electromagnetic Theory (4th Edition)*. Addison Wesley, 1992.

[21] K. Farahani, U. Sinha, L. Chiu, and R. Lufkin, "Effect of field strength on susceptibility artifacts in magnetic resonance imaging," *Computerized medical imaging and graphics : the official journal of the Computerized Medical Imaging Society*, vol. 14, no. 6, pp. 409–413, 1990.

[22] M. D. Hurlimann, "Effective gradients in porous media due to susceptibility differences," *Journal of Magnetic Resonance*, vol. 131, no. 2, pp. 232 – 240, 1998.

[23] S. Ogawa, T. Lee, A. Kay, and D. Tank, "Brain magnetic resonance imaging with contrast dependent on blood oxygenation," *Proceedings of the National Academy of Sciences of the United States of America*, vol. 87, no. 24, pp. 9868–9872, 1990.

[24] B. Putz, D. Barsky, and K. Schulten, "Edge enhancement by diffusion in microscopic magnetic resonance imaging," *Journal of Magnetic Resonance (1969)*, vol. 97, no. 1, pp. 27 – 53, 1992.

[25] D. Eisenberg and W. Kauzmann, *The Structure and Properties of Water (Oxford Classic Texts in the Physical Sciences)*. Oxford University Press, USA, 2005.

[26] M. A. Horsfield, "Using diffusion-weighted MRI in multicenter clinical trials for multiple sclerosis," *Journal of the Neurological Sciences*, vol. 186, no. Supplement 1, pp. S51 – S54, 2001.

[27] S.-C. Chang, P.-H. Lai, W.-L. Chen, H.-H. Weng, J.-T. Ho, J.-S. Wang, C.-Y. Chang, H.-B. Pan, and C.-F. Yang, "Diffusion-weighted MRI features of brain abscess and cystic or necrotic brain tumors: Comparison with conventional MRI," *Clinical Imaging*, vol. 26, no. 4, pp. 227 – 236, 2002.

[28] Y.-Q. Song, "Novel NMR techniques for porous media research," *Cement and Concrete Research*, vol. 37, no. 3, pp. 325 – 328, 2007.

[29] R. Weisskoff, C. Zuo, J. Boxerman, and B. Rosen, "Microscopic susceptibility variation and transverse relaxation - theory and experiment," *Magnetic Resonance in Medicine*, vol. 31, no. 6, pp. 601–610, 1994.

[30] R. J. S. Brown and P. Fantazzini, "Conditions For Initial Quasi-Linear T(2)(-1) Versus Tau For Carr-Purcell-Meiboom-Gill NMR With Diffusion And Susceptibility Differences In Porous-Media And Tissues," *Physical Review B*, vol. 47, no. 22, pp. 14823–14834, 1993.

[31] R. Dharmakumar, D. Plewes, and G. Wright, "On the parameters affecting the sensitivity of MR measures of pressure with microbubbles," *Magnetic Resonance in Medicine*, vol. 47, no. 2, pp. 264–273, 2002.

[32] Z. Chen, *Computational Methods for Multiphase Flows in Porous Media (Computational Science and Engineering)*. Society for Industrial and Applied Mathematic, 2006.

[33] C. Westbrook and C. Kaut, *MRI in Practice*. Blackwell Science, 1998.

[34] P. Callaghan, *Principles of Nuclear Magnetic Resonance Microscopy*. Oxford University Press, USA, 1994.

[35] P. T. Callaghan, S. Godefroy, and B. N. Ryland, *Use of the second dimension in PGSE NMR studies of porous media*. Ulm, Germany: Elsevier Science Inc, 2002.

[36] M. D. Mantle and A. J. Sederman, "Dynamic MRI in chemical process and reaction engineering," *Progress in Nuclear Magnetic Resonance Spectroscopy*, vol. 43, no. 1–2, pp. 3–60, 2003.

[37] A. J. Sederman and L. F. Gladden, "Magnetic resonance imaging as a quantitative probe of gas-liquid distribution and wetting efficiency in trickle-bed reactors," *Chemical Engineering Science*, vol. 56, no. 8, pp. 2615–2628, 2001.

[38] A. Sederman, M. Mantle, and L. Gladden, "Single excitation multiple image RARE (SEMI-RARE): ultra-fast imaging of static and flowing systems," *Journal of Magnetic Resonance*, vol. 161, no. 1, pp. 15 – 24, 2003.

[39] C. J. Dirckx, S. A. Clark, L. D. Hall, B. Antalek, J. Tooma, J. M. Hewitt, and K. Kawaoka, "Magnetic resonance imaging of the filtration process," *AIChE Journal*, vol. 46, no. 1, pp. 6–14, 2000.

[40] H. Adriaensen, M. Bencsik, and S. Brewer, "Monitoring of hydrocarbon uptake in highly conductive porous media using a unilateral NMR instrument," *Diffusion Fundamentals*, vol. 10, p. 21, 2005.

[41] F. T. Braga, A. J. da Rocha, G. H. Filho, R. K. Arikawa, I. M. Ribeiro, and R. B. Fonseca, "Relationship between the concentration of supplemental oxygen and signal intensity of csf depicted by fluid-attenuated inversion recovery imaging," *AJNR Am J Neuroradiol*, vol. 24, no. 9, pp. 1863–1868, 2003.

[42] W. G. Bradley and G. M. Bydder, *Advanced MR Imaging Techniques*. Informa HealthCare, 1997.

[43] G. Zaharchuk, A. J. Martin, G. Rosenthal, G. T. Manley, and W. P. Dillon, "Measurement of cerebrospinal fluid oxygen partial pressure in humans using MRI," *Magnetic Resonance in Medicine*, vol. 54, no. 1, pp. 113–121, 2005.

[44] J. Yu, S. Rajaei, M. Ishii, M. L. Law, K. Emami, J. M. Woodburn, S. Kadlecek, V. Vahdat, and R. R. Rizi, "Measurement of Pulmonary Partial Pressure of Oxygen and Oxygen Depletion Rate with Hyperpolarized Helium-3 MRI: A Preliminary Reproducibility Study on Pig Model," *Academic Radiology*, vol. 15, no. 6, pp. 702–712, 2008.

[45] S. Laukemper-Ostendorf, A. Scholz, K. Burger, C. P. Heussel, M. Schmittner, N. Weiler, K. Markstaller, B. Eberle, H. U. Kauczor, M. Quintel, M. Thelen, and W. G. Schreiber, *F-19-MRI of perflubron for measurement of oxygen partial pressure in porcine lungs during partial liquid ventilation*. 2002.

[46] A. J. Deninger, B. Eberle, M. Ebert, T. Grossmann, W. Heil, H. U. Kauczor, L. Lauer, K. Markstaller, E. Otten, J. Schmiedeskamp, W. Schreiber, R. Surkau, M. Thelen, and N. Weiler, "Quantification of regional intrapulmonary oxygen partial pressure evolution during apnea by He-3 MRI," *Journal of Magnetic Resonance*, vol. 141, no. 2, pp. 207–216, 1999.

[47] M. Bencsik and C. Ramanathan, "Direct measurement of porous media local hydrodynamical permeability using gas MRI," *Magnetic Resonance Imaging*, vol. 19, no. 3–4, pp. 379–383, 2001.

[48] M. Bencsik and C. Ramanathan, "Method for measuring local hydraulic permeability using magnetic resonance imaging," *Physical Review E*, vol. 6306, no. 6, 2001.

[49] T. Osuga and S. Han, "Proton magnetic resonance imaging of diffusion of high- and low-molecular-weight contrast agents in opaque porous media saturated with water," *Magnetic Resonance Imaging*, vol. 22, no. 7, 2004.

[50] A. Alexander, T. McCreery, T. Barrette, A. Gmitro, and E. Unger, "Microbubbles as novel pressure-sensitive MR contrast agents," *Magnetic Resonance In Medicine*, vol. 35, no. 6, pp. 801–806, 1996.

[51] R. Dharmakumar, *Magnetic-Susceptibility-Based Functional MRI for Heart Disease*. PhD thesis, Graduate Department of Medical Biophysics, University of Toronto, 2004.

[52] R. Dharmakumar, D. Plewes, and G. Wright, "A novel microbubble construct for intracardiac or intravascular MR manometry: a theoretical study," *Physics in Medicine and Biology*, vol. 50, no. 20, pp. 4745–4762, 2005.

[53] M. Shibakami, R. Goto, and M. Nakamura, "Phase separation of binary membranes composed of articial cyclic lipid and distearoyl phosphatidylcholine," *Japanese Journal of Applied Physics*, vol. 46, no. 8B, pp. 5617–5620, 2007.

[54] S. M. Lee, S. H. Lee, H. Y. Kang, S. Y. Baek, S. M. Kim, and M. J. Shin, "Assessment of Musculoskeletal Infection in Rats to Determine Usefulness of SPIO-Enhanced MRI," *American Journal of Roentgenolology*, vol. 189, no. 3, pp. 542–548, 2007.

[55] P. A. Dayton, K. E. Morgan, A. L. Klibanov, G. H. Brandenburger, and K. W. Ferrara, "Optical and acoustical observations of the effects of ultrasound on contrast agents," *Ieee Transactions on Ultrasonics Ferroelectrics and Frequency Control*, vol. 46, no. 1, pp. 220–232, 1999.

[56] E. Schutt, D. Klein, R. Mattrey, and J. Riess, "Injectable microbubbles as contrast agents for diagnostic ultrasound imaging: The key role of perfluorochemicals," *Angewandte Chemie-International Edition*, vol. 42, no. 28, pp. 3218–3235, 2003.

[57] K. Ferrara, R. Pollard, and M. Borden, "Ultrasound microbubble contrast agents: Fundamentals and application to gene and drug delivery," *Annual Review of Biomedical Engineering*, vol. 9, pp. 415–447, 2007.

[58] M. Morrow, J. Whitehead, and D. Lu, "Chain-length dependence of lipid bilayer properties near the liquid crystal to gel phase transition," *Biophysical Journal*, vol. 63, pp. 18–27, 1992.

[59] P. B. Duncan and D. Needham, "Test of the epstein-plesset model for gas microparticle dissolution in aqueous media: Effect of surface tension and gas undersaturation in solution," *Langmuir*, vol. 20, no. 7, pp. 2567–2578, 2004.

[60] D. H. Kim, M. J. Costello, P. B. Duncan, and D. Needham, "Mechanical properties and microstructure of polycrystalline phospholipid monolayer shells: Novel solid microparticles," *Langmuir*, vol. 19, no. 20, pp. 8455–8466, 2003.

[61] M. A. Borden and M. L. Longo, "Dissolution behavior of lipid monolayer-coated, air-filled microbubbles: effect of lipid hydrophobic chain length," *Langmuir*, vol. 18, no. 24, pp. 9225–9233, 2002.

[62] M. A. Borden, G. Pu, G. J. Runner, and M. L. Longo, "Surface phase behavior and microstructure of lipid/peg-emulsifier monolayer-coated microbubbles," *Colloids and Surfaces B-Biointerfaces*, vol. 35, no. 3–4, pp. 209–223, 2004.

[63] G. Pu, M. L. Longo, and M. A. Borden, "Effect of microstructure on molecular oxygen permeation through condensed phospholipid monolayers," *Journal of the American Chemical Society*, vol. 127, no. 18, pp. 6524–6525, 2005.

[64] F. Gerber, M. Krafft, G. Waton, and T. Vandamme, "Microbubbles with exceptionally long life - synergy between shell and internal phase components," *New Journal of Chemistry*, vol. 30, no. 4, pp. 524–527, 2006.

[65] P. S. Epstein and M. S. Plesset, "On the stability of gas bubbles in liquid-gas solutions," *The Journal of Chemical Physics*, vol. 18, no. 11, pp. 1505–1509, 1950.

[66] S. Kentisha, J. Leea, M. Davidson, and M. Ashokkumar, "The dissolution of a stationary spherical bubble beneath a flat plate," *Chemical Engineering Science*, vol. 61, no. 23, pp. 7697–7705, 2006.

[67] D. J. Kirby, V. W. Bramwell, and Y. Perrie, "Microspheres for the delivery of t8 sub-unit vaccines: entrapped or adsorbed antigen?," *Journal of Pharmacy and Pharmacology*, vol. 59, pp. A2–A2, 2007.

[68] A. L. Klibanov, "Microbubble contrast agents - targeted ultrasound imaging and ultrasound-assisted drug-delivery applications," *Investigative Radiology*, vol. 41, no. 3, pp. 354–362, 2006.

[69] D. E. Yount, "Skins of varying permeability: A stabilization mechanism for gas cavitation nuclei," *The Journal of the Acoustical Society of America*, vol. 65, no. 6, pp. 1429–1439, 1979.

[70] B. D. Johnson and R. C. Cooke, "Bubble populations and spectra in coastal waters - photographic approach," *Journal of Geophysical Research-Oceans and Atmospheres*, vol. 84, no. NC7, pp. 3761–3766, 1979.

[71] Food and Drug Administration, "Information for healthcare professionals - micro-bubble contrast agents (marketed as definity (perflutren lipid microsphere) injectable suspension and optison (perflutren protein-type a microspheres for injection)," July 2008.

[72] D. Needham, "US Patent 6210611 - Methods for producing gas microbubbles having lipid-containing shells formed thereon," April 3, 2001.

[73] M. Schneider, D. Bichon, P. Bussat, and J. Puginier, "US Patent 5380519 - Stable microbubbles suspensions injectable into living organisms," January 10, 1995.

[74] H. Dugstad, J. Klaveness, P. Rongved, and R. Skurtveit, "US Patent 6217850 - Method of making lyophilized microbubble compositions useful as contrast agents," April 17, 2001.

[75] H. Dugstad, J. Klaveness, P. Rongved, and R. Skurtveit, "US Patent 6221337 - Microbubbles surrounded by a monolayer of negatively charged phospholipids as contrast agents," April 24, 2001.

[76] R. Feng, Y. Y. Zhao, C. P. Zhu, and T. J. Mason, "Enhancement of ultrasonic cavitation yield by multi-frequency sonication," *Ultrasonics Sonochemistry*, vol. 9, no. 5, pp. 231–236, 2002.

[77] J. H. Xu, S. Li, G. G. Chen, and G. S. Luo, "Formation of monodisperse microbubbles in a microfluidic device," *AIChE Journal*, vol. 52, pp. 2254–2259, 2006.

[78] E. Talu, M. M. Lozano, R. L. Powell, P. A. Dayton, and M. L. Longo, "Long-term stability by lipid coating monodisperse microbubbles formed by a flow-focusing device," *Langmuir*, vol. 22, pp. 9487–9490, 2006.

[79] E. Talu, K. Hettiarachchi, S. Zhao, R. L. Powell, A. P. Lee, M. L. Longo, and P. A. Dayton, "Tailoring the size distribution of ultrasound contrast agents: Possible method for improving sensitivity in molecular imaging," *Molecular Imaging*, vol. 6, no. 6, pp. 384–392, 2007.

[80] J. Bertling, J. Blomer, and R. Kummel, "Hollow microsperes," *Chemical Engineering and Technology*, vol. 27, no. 8, pp. 829–837, 2004.

[81] TA Instruments, *CSL2 Rheometer Manual*. TA Instruments, 1990.

[82] M. Mooney and R. H. Ewart, "The conicylindrical viscometer," *Physics*, vol. 5, no. 11, pp. 350–354, 1934.

[83] P. H. DeHoff and K. J. Anusavice, "Creep functions of dental ceramics measured in a beam-bending viscometer," *Dental Materials*, vol. 20, no. 3, pp. 297–304, 2004.

III. NUMERICAL SIMULATION

For the work presented in this thesis, two numerical simulations have been produced. The first was based upon the work of Dharmakumar [1] and is concerned with determining the NMR signal from a system of protons diffusing around a single gas filled microbubble. The second numerical simulation was to determine the optimum setting of the echo time in terms of T_2^{eff}. Both of these simulations are covered in the following sections.

III.1 Modelling R_2^{eff} for the CPMG Sequence

In order to determine the effect of various microbubble and system parameters on the NMR signal, a numerical simulation was produced. This software needed to be capable of calculating the signal for changes in microbubble radius and magnetic susceptibility differences, changes in sequence parameters such as the echo time or RF pulse durations and variations in the properties of the contrast agent such as diffusion. The initial simulation work focused primarily on the production of a MATLAB® routine which would predict the NMR signal from a Carr-Purcell-Meiboom-Gill (CPMG) sequence [2] for a system of protons diffusing around a single gas filled microbubble.

The CPMG sequence is particularly relevant to situations where there is a source of systematic interference from field inhomogeneities. If the phase of the system of nuclear spins is manipulated by applying RF pulses of appropriate frequency, duration and phase which affect the signal but not the interference, only the NMR signal (and random interference) will be refocused. This process is known as phase cycling. The most common order of phase cycling is to use a constant phase of refocusing pulse but to alternate the direction of the excitation pulse and the receiver together. e.g. 90°_{+x}, 180°_{+y}, receive $_{+x}$, 90°_{-x}, 180°_{+y}, receive $_{-x}$.

All of the spin echo based experimental work discussed in this thesis is based on the CPMG sequence. As such it was used as the basis of the simulation to determine the effect of microbubbles on the NMR signal.

The first version of the software was based on the work of Dharmakumar [1] who kindly supplied a copy of his own code written in FORTRAN80. Initially all protons are aligned along the positive y direction, as though a 90°_{+x} excitation pulse had been applied to a system of protons aligned to the static magnetic field B_0. They are allowed to diffuse in three dimensions outside a single central microbubble in time steps of Δt and thus undergo phase changes directly reflecting the strength of magnetic field perturbations which they experience.

After a set period of time which corresponds to half the echo time T_E, the phase of each proton is flipped by 180° as would be achieved by the refocusing pulse applied in the CPMG sequence. For a specified number of echoes, the phase is flipped every T_E.

III.1.1 Homogeneous Linear Field Gradients

To verify that the simulation was capable of successfully predicting the NMR signal for a given system, the field gradients caused by the microbubble in the previous routine was replaced with a linear field gradient for the case of which a theoretical R_2^{eff} is available [3](see Fig. III.1). The R_2^{eff} determined by the simulation was found to lie within 5% of the theoretical estimate. We decided to validate the software using this linear field gradient as there is neither theoretical or experimental results for the case of a single microbubble.

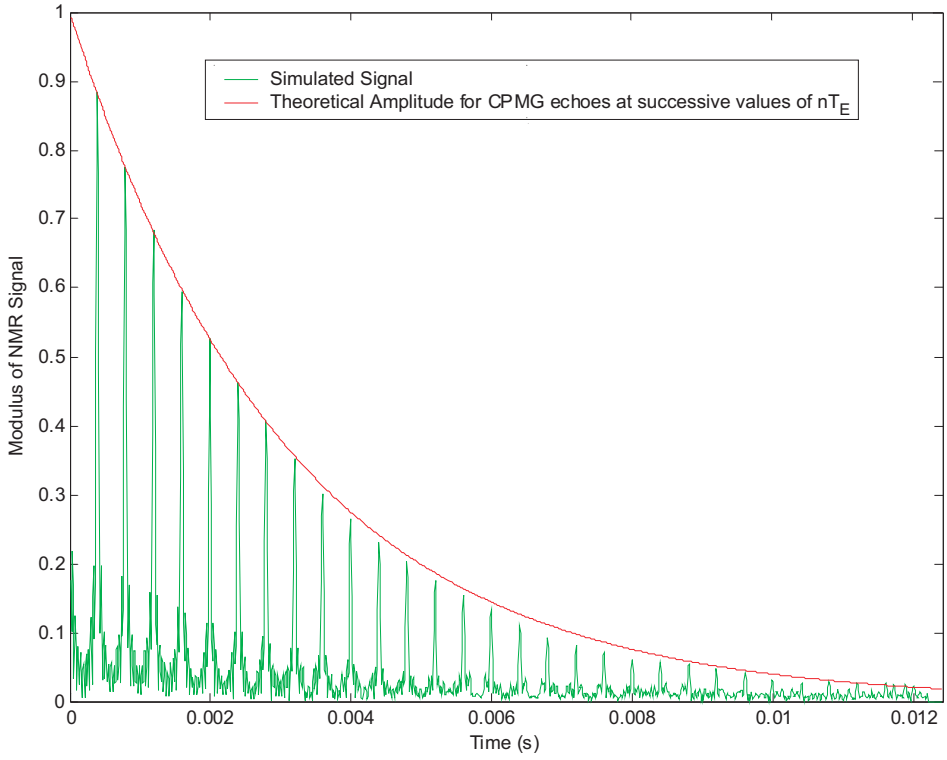

Fig. III.1: Plot of modulus of simulated signal intensity over time produced by 10,000 protons diffusing in a linear field gradient with the following parameters: $T_E = 400\mu s$; $\Delta t = 1 \times 10^{-6}$; $B_0 = 2.35T$; $G = 11.1Tm^{-1}$; $T_2 = \infty$. The simulation takes less than two minutes to run on an AMD Athlon® 3200+ (2GHz) with 4GB RAM running Microsoft Windows® XP Professional.

III.1.2 Spherical Perturber

III.1.2.1 Importance of Simulation Temporal Step Size

The software initially written to simulate the signal from diffusing protons around a spherical perturber used a temporal step size, Δt, of $10\mu s$ as previously recommended [1]. This step size corresponds the the distance which each proton moves in one of the six directions. An important question was to determine the largest time between simulation steps which would allow the application to produce an accurate result in the shortest

possible time. Because the spatial extent of the magnetic field perturbations decrease as the microbubble radius becomes smaller, allowing the protons to diffuse for too great a time between observations can result in the very localised effect of these fields surrounding the microbubble to be erroneously sampled by the numerical simulation.

This problem was solved by producing another MATLAB® routine which reduces the value of this time step (Δt) until two consecutive values of R_2^{eff} are found which agree within 2% for a specific bubble size, which is then changed before the Δt optimisation procedure is repeated. The results showed that a value for Δt of 1μs is sufficient for all microbubble radii greater than 2.5μm and 0.25μs is sufficient for microbubble radii ranging from 1 to $2.5\mu m$ (see Fig. III.2). To allow for decreases in size due to applied pressure, the latter value is used for all simulations.

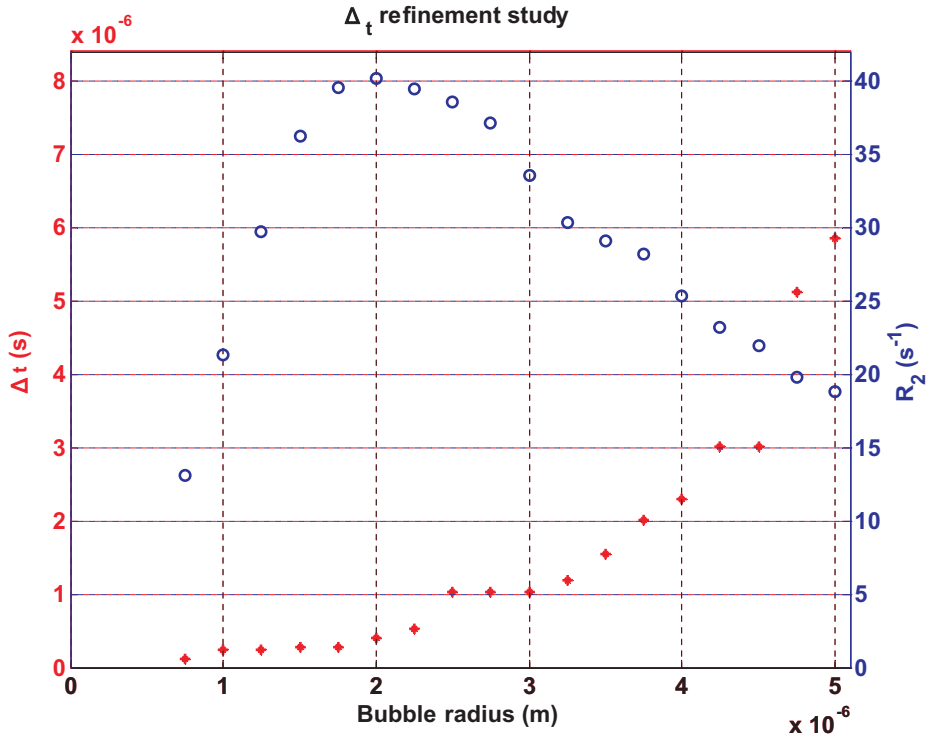

Fig. III.2: Plot to demonstrate the effect of changing the step size in the simulation of protons surrounding a microbubble. For a range of microbubble sizes (x axis) the R_2^{eff} is calculated (right hand axis). The value of the step size (Δt) is reduced until two values of R_2^{eff} are found within 2%. The final values of Δt and R_2^{eff} are then plotted. The following parameters are used for the simulation:$T_E = 400\mu s$; $\Delta t = 1 \times 10^{-6}$; $B_0 = 2.35T$; $\Delta\chi = 12.56 \times 10^{-6}$; $T_2 = \infty$. The simulation takes three days to run on an AMD Athlon® 3200+ (2GHz) with 4GB RAM running Microsoft Windows® XP Professional.

III.1.2.2 Effect of Step Size on $\Delta\chi B_0$

An interesting consequence of having optimised the size of the simulation step time (Δt) is the improved agreement of the simulation and theoretical results. In the work of Dharmakumar [1] the simulated variations of the effective spin spin relaxation rate (R_2^{eff}) against the product of the magnetic field intensity and susceptibility

difference ($B_0\Delta\chi$) do not agree with the theoretical estimates: The simulation predicts a linear relationship whilst the theory is quadratic.

This is not the case in our optimised simulation. It is found that with the Δt value set as previously described for each value of $B_0\Delta\chi$, the relationship between R_2 and $B_0\Delta\chi$ is quadratic, as expected from theory [1].

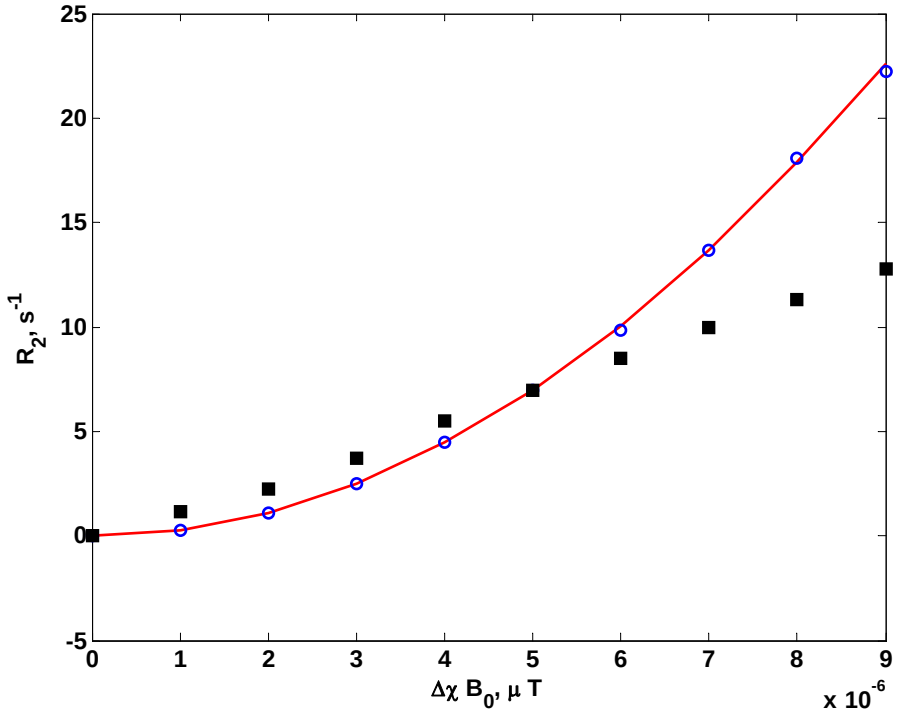

Fig. III.3: Comparison between results of the simulation with reduced value of Δt (blue circles, $\Delta t = .25\mu s$) and that of Dharmakumar (black squares, $\Delta t = 10\mu s$) [1]. The red line is the theory. The results of the two simulations are scaled to fit the theoretical prediction by simple multiplication of the data. The following parameters are used for the simulation:$T_E = 6ms$; $B_0 = 2.35T$; $\Delta\chi = 12.56\times10^{-6}$; bubble size = $2\mu m$; $T_2 = \infty$. The simulation takes 1 hour and 20 minutes to run on an AMD Athlon® 3200+ (2GHz) with 4GB RAM running Microsoft Windows® XP Professional.

III.1.2.3 Number of Protons

The effect of changing the number of protons simulated was also explored to ensure the greatest level of accuracy possible. A MATLAB® routine which increases the number of protons until two values of R_2^{eff} fall within 5% of each other was produced and run for 10 different bubble sizes. It was found that 10,000 protons (or more) produced consistent results for all bubble sizes so this value was maintained for all simulations.

III.1.3 Extensions of Software

The random walk simulation provides useful insight into the origin of the signal sensitivity for the MRI experiments. This code could be used to investigate the following three applications as a possible extension. In this way, it would be possible to obtain a fuller understanding of the proton system.

III.1.3.1 Concomitant Fields

Maxwell's equations stipulate that it is not possible to create a magnetic field gradient which acts solely in one direction. A gradient dB_z/dz will always generate transverse components dB_z/dx and dB_z/dy which are known as concomitant fields. If we determine the field vectors at low and high field we see that whilst these concomitant fields have minimal effect at high polarising field strengths they can be significant when the polarising field strength is similar to the gradient:

$$B = \sqrt{(B_0 + G_z)^2 + G_x^2 + G_y^2} \tag{III.1}$$

At present the simulation is based upon the field perturbations described in equation II.24. At low fields, such as those experienced with single sided sensors, well logging tools and MRI scanners dedicated to hyperpolarised gas imaging, this may not be the case. A possible extension of the simulation is to include the x and y components of the field to make the simulation applicable to lower polarising field strengths.

III.1.3.2 Bandwidth Screening

As the protons diffuse around the microbubbles, they experience a wide range of polarising field intensities. This corresponds to a wide range of NMR Larmor frequencies. It is possible that this could have a severe impact if the bandwidth of the excitation and refocusing pulses is too narrow. By implementing a bandwidth screening process in the simulation, in which protons in fields outside the bandwidth are disregarded, it is possible to somewhat assess the implications of this on the experiments. This could be of great significance, particularly as the most influential polarising fields in the simulation and theoretical predictions are those that are the closest to the microbubble and indeed are the strongest and most likely to be screened by an insufficiently wide pulse bandwidth. In a typical MRI sequence, for example the MSME sequence used in the experimental work presented in this thesis, the pulse bandwidth is around 2.7kHz. For a microbubble of two micron diameter, fields up to nearly a radius from the edge of the bubble will be screened with this bandwidth(see Fig. III.4).
The effect of this screening has been incorporated into the CPMG simulation and effect of changing the pulse bandwidth explored. A range of pulse bandwidths is shown in Fig. III.5. The pulse bandwidth used in the MSME studies is shown on the plot and represents an intermediate case for which the spin echoes are defined although a larger bandwidth may improve the signal.

III.1.3.3 Porous Media

The final adaptation involves modelling the effect of a pore-like structure into the system. The generally accepted method [4] for simulating such an addition is to introduce a boundary into the simulation environment which causes either an instant return of phase to the equilibrium state or a rapidly increased phase in the event of a collision. This represents the loss of one magnetic moment previously contributing to the transverse magnetisation caused by a collision with a solid wall. This is of course only one factor involved in the reduction of T_2^{eff}. Because of the susceptibility difference between the wall which is solid and the medium which is a

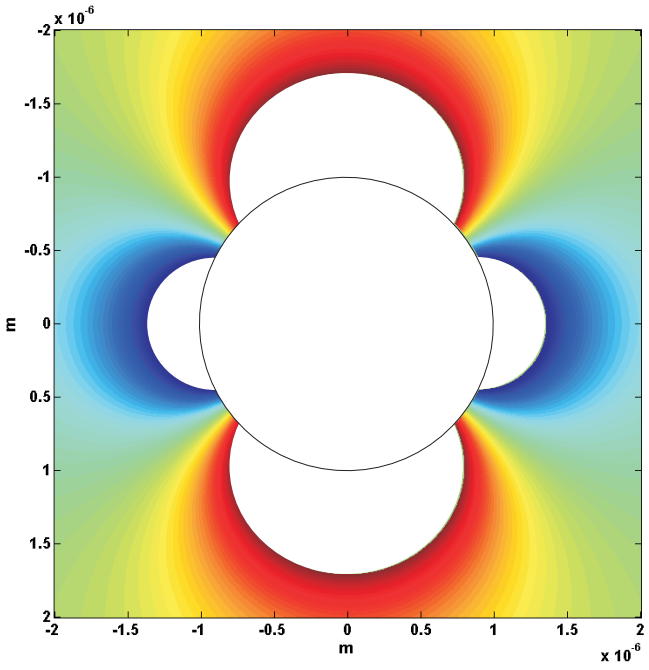

Fig. III.4: Plot of fields surrounding a microbubble of two micron diameter in a 2.35T polarising magnetic field. The microbubble is pictured white in the centre with a black outline representing the membrane, whilst the white areas around this are those containing protons which are not influenced by the excitation pulse owing to the bandwidth screening of a 2ms pulse corresponding to a bandwidth of 2.7kHz.

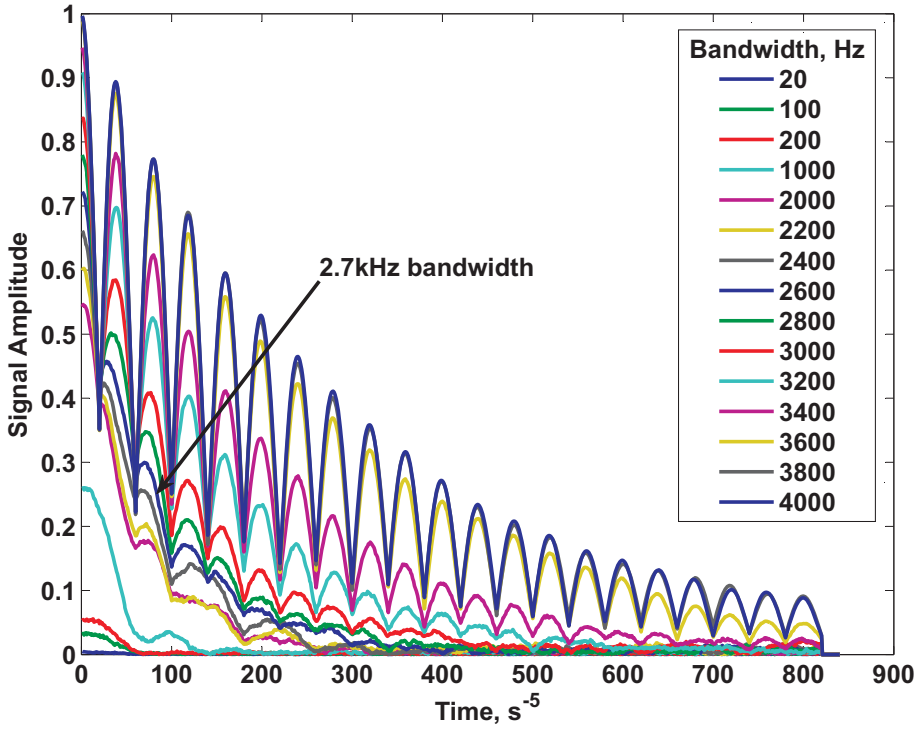

Fig. III.5: Trains of simulated spin echoes produced by simulation accounting for effect of bandwidth screening. The arrow marks the pulse bandwidth used in the MSME experiment.

liquid, there will be another field gradient established from the wall into the fluid resulting in a more rapid loss of phase coherence than would be achieved with the initial simulation method. For simple boundaries this field could be easily implemented for a more accurate simulation, although for a polarising field of 2.35T, magnetic susceptibility differences between water and glass can be well compensated for by using echo time on the order of 1ms, although this is not the case for higher field strengths for which this application of the software may be very useful.

III.1.4 Discussion and Conclusions

The simulation section of this work was largely based on the work of Dharmakumar [1]. Several major modifications to the software were however made to make it far faster at producing a result, and more robust in terms of the possible simulations which can be produced using the basic structure. These are listed below:

- Validation of the software using a linear field gradient
- Optimisation of the temporal step size to produce a better fit to theoretical predictions
- Confirmation of the number of simulated protons

To achieve the possible extensions described in this section will most likely require minimal adaptation of the software although this unfortunately was not possible during the project. The optimised code is included for reference in appendix A.

III.2 Optimisation of the Effective Echo Time for the RARE Sequence

In an MRI experiment, it is important to optimize as many parameters as possible to enhance the signal sensitivity, allowing the best possible measurements to be made. Most often the signal is acquired within a short fraction of the NMR exponential decay, and in this case, the most sensitive measurement of small changes in T_2 is found when as follows:
For a given sample the signal amplitude A in the rotating reference frame is given by equation III.2.

$$A = A_0 e^{\frac{-t}{T_2}}, \tag{III.2}$$

where A_0 is the amplitude after the initial excitation pulse, t is the time and T_2 is the spin-spin relaxation rate. The effect on the signal intensity as a result of small changes in T_2 is found by differentiating with respect to T_2.

$$\frac{dA}{dT_2} = A_0 e^{\frac{-t}{T_2}} \frac{t}{T_2^2}. \tag{III.3}$$

To find the time at which this function is maximal, we differentiate again with respect to time and find the when it is equal to zero.

$$\frac{t}{T_2} = 1, t = T_2. \tag{III.4}$$

For the case of the static fluids explored in this study, the RARE sequence with single shot planar imaging was found to yield an excellent compromise between spatial and temporal resolutions, whilst the sensitivity to pressure changes can be maximised by varying the effective echo time T_E^{eff} with respect to the effective spin-spin relaxation time T_2^{eff}. In the following sections the optimum setting required to yield maximum sensitivity to small changes in T_2^{eff} is determined both semi-analytically and using Monte Carlo simulation in MATLAB ® (Mathworks,MA, USA).

III.2.1 Semi-analytical

In this section, the method used to semi-analytically determine the optimum effective echo time in terms of T_2^{eff} is described.

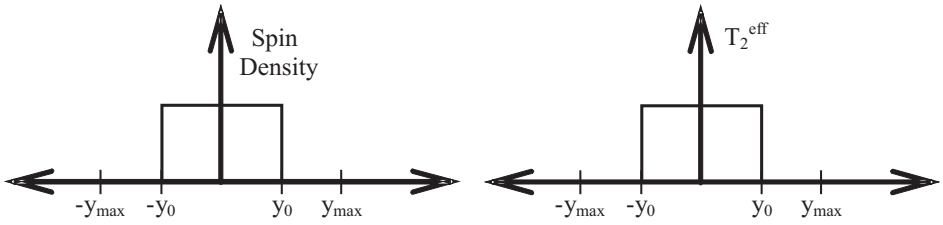

Fig. III.6: Simple homogeneous sample profiles used to estimate optimum echo time

For a homogeneous sample defined as in Fig. III.6, we can determine the expected NMR signal (assuming no relaxation occurs):

$$A = \int_{-y_0}^{y_0} e^{i\gamma G_y y t} dy = \frac{1}{\gamma G_y y t}\left[e^{i\gamma G_y y t}\right]_{-y_0}^{y_0} = \frac{e^{-i\gamma G_y y_0 t} - e^{i\gamma G_y y_0 t}}{i\gamma G_y y t} = \frac{-2\sin(\gamma G_y y_0 t)}{\gamma G_y t}, \tag{III.5}$$

where γ is the proton gyromagnetic ratio, G_y is the strength of the phase encoding imaging field gradient, t is the time and $2y_0$ is the extent of the sample along the y-axis. We can then extend this to account for relaxation by integrating the NMR signal along the y-axis and assuming that the exponential decay during the read gradients can be neglected due to a sufficiently short encoding time. The signal intensity for a modulus MRI image is well approximated by:

$$A(T_2^{\text{eff}}, T_E^{\text{eff}}) = \int_0^{2T_E^{\text{eff}}} \left| 2\frac{\sin(\gamma G_y y_0 (t - T_E^{\text{eff}}))}{\gamma G_y (t - T_E^{\text{eff}})} \right| e^{-t/T_2^{\text{eff}}} dt. \tag{III.6}$$

By defining $\alpha = \gamma G_y y_0$ and substituting $x = \alpha(t - T_E^{\text{eff}})$, we can simplify equation III.6 to

$$A(T_2^{\text{eff}}, T_E^{\text{eff}}) = \frac{2\gamma_0}{\alpha} F(\alpha T_2^{\text{eff}}, \alpha T_E^{\text{eff}}), \tag{III.7}$$

where the function $F(\alpha T_2^{\text{eff}}, \alpha T_E^{\text{eff}})$ has been defined as:

$$F(\alpha T_2^{\text{eff}}, \alpha T_E^{\text{eff}}) = e^{\frac{-T_E^{\text{eff}}}{T_2^{\text{eff}}}} G(\alpha T_2^{\text{eff}}, \alpha T_E^{\text{eff}}), \tag{III.8}$$

while the function $G(\alpha T_2^{\text{eff}}, \alpha T_E^{\text{eff}})$ is given by the integral

$$G(\alpha T_2^{\text{eff}}, \alpha T_E^{\text{eff}}) = \int_{-\alpha T_E^{\text{eff}}}^{\alpha T_E^{\text{eff}}} |\text{sinc}(x)| \, e^{\frac{-x}{\alpha T_E^{\text{eff}}}} \, dx. \tag{III.9}$$

For the volume defined in Fig. III.6, the maximum measured frequency in the experiment is given by

$$F_{max} = \frac{\gamma G_y y_{max}}{2\pi}. \tag{III.10}$$

To prevent Nyquist ghosting, the lowest sampling rate must be at least twice that of the highest frequency originating from the NMR. By using $\frac{Nb}{T_E^{\text{eff}}}$ as the sampling rate and setting the field of view to twice the extent of the sample results in

$$\frac{Nb}{T_E^{\text{eff}}} = \frac{\gamma G_y y_0}{\pi}, \tag{III.11}$$

where Nb is the number of digital points sampled (typically in excess of 70). Assuming that T_2^{eff} and T_E^{eff} are in the order of 2 and 0.5s respectively, the value of α can be assumed to be typically greater than 140 for which the exponential term in equation III.9 tends to 1 giving

$$G(\alpha T_2^{\text{eff}}, \alpha T_E^{\text{eff}}) \approx \int_{-\alpha T_E^{\text{eff}}}^{\alpha T_E^{\text{eff}}} |\text{sinc}(x)| \, dx. \tag{III.12}$$

For sufficiently large values of αT_E^{eff} the integral of the modulus of the sinc(x) term is independent of T_2^{eff} giving

$$F(\alpha T_2^{\text{eff}}, \alpha T_E^{\text{eff}}) \approx e^{\frac{-T_E^{\text{eff}}}{T_2^{\text{eff}}}}. \tag{III.13}$$

The maximum of the first derivative of F with respect to T_2^{eff} gives the optimum setting for T_E. This can be found by setting the second derivative to zero,

$$\frac{d^2F}{dT_2^{\text{eff}}} = \left(\frac{-2T_E^{\text{eff}}}{T_2^{eff3}}\right)\left(1 - \frac{T_E^{\text{eff}}}{2T_2^{\text{eff}}}\right)F = 0, \tag{III.14}$$

which gives

$$T_E^{\text{eff}} = 2T_2^{\text{eff}}. \tag{III.15}$$

III.2.2 Monte Carlo

Although the result found in the previous section is quantitatively correct, for practical MRI purposes the qualitative deterioration of an image that would be acquired with this set up needs to be assessed. The effect

of thermal noise can also be accounted for by using a Monte Carlo simulation, in which an idealised circular homogeneous image has its corresponding train of spin echoes multiplied by an exponential decay for a range of different T_2^{eff} values before noise is added. The mean amplitude of the resulting MR image is then calculated in terms of T_2^{eff}. Visual inspection of the reconstructed images (Fig. III.7) allows qualitative estimation of the image artefacts, and highlights particularly those due to the increasing attenuation of the centre of k-space. Quantitation of the SNR (mean signal divided by the standard deviation of noise) in the set of generated images also permits verification of the result in equation III.15.

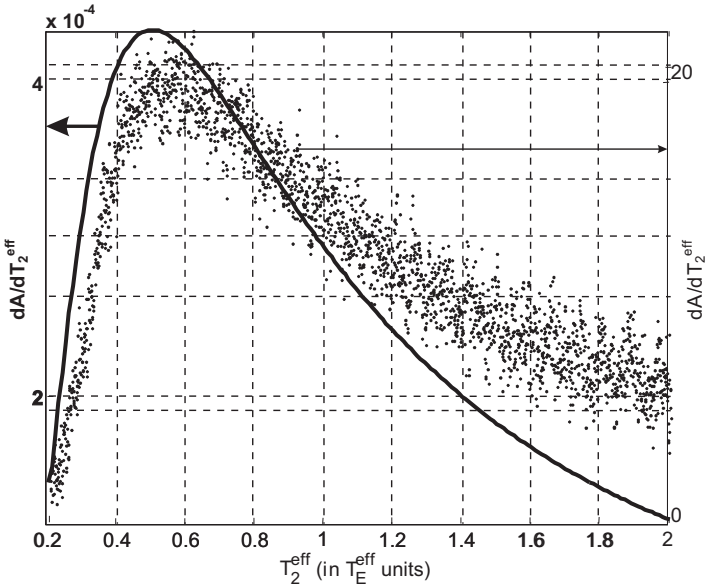

Fig. III.7: Plot of gradients of semi-analytical (solid line) and Monte Carlo (single points) simulation signals, showing the optimum value for T_E^{eff} to measure small changes in the value of T_2^{eff}. A Gaussian convolution (width = $0.5T_2^{\text{eff}}$) is applied to the MR signal found from the Monte Carlo data prior to obtaining the gradient. Both tests suggest that setting T_E^{eff} to twice the value of T_2^{eff} yields optimum sensitivity to a change in T_2^{eff}

III.2.3 Overview

The methods explored in the two previous sections correlate well, although small differences can be seen due to the thermal noise that is not accounted for in the semi-analytical solution. When the condition $T_E^{\text{eff}} = 2T_2^{\text{eff}}$ is fulfilled, the centre of k-space suffers from strong attenuation, yielding image artefacts, mostly in the form of DC signal loss (see Fig. III.8), resulting in spuriously enhanced edges together with reduced intensity within the central volume. By setting T_E^{eff} at a value slightly lower around $1.6T_2^{\text{eff}}$, an excellent sensitivity to pressure changes is maintained whilst image artefacts are substantially reduced.

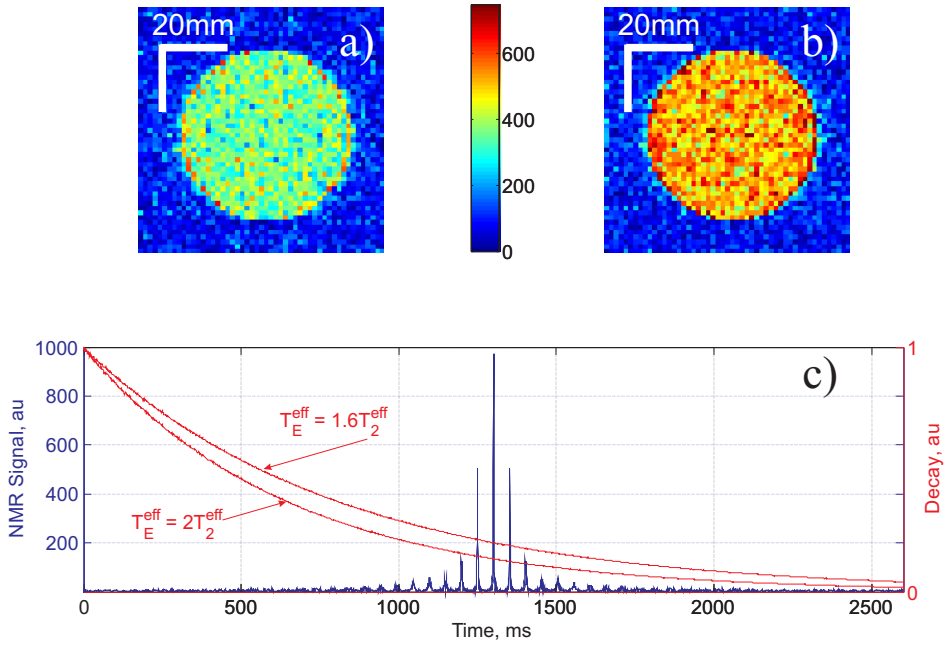

Fig. III.8: Demonstration of k-space clipping due to length of relaxation. (a) Image with $T_E^{\text{eff}} = 2T_2^{\text{eff}}$; (b) image with $T_E^{\text{eff}} = 1.6T_2^{\text{eff}}$; The pixel intensities are in arbitrary units. (c) The RARE echo train with no relaxation, superimposed with the relaxation curve for the case $T_E^{\text{eff}} = 2T_2^{\text{eff}}$, and for the case $T_E^{\text{eff}} = 1.6T_2^{\text{eff}}$ (red curves).

References

[1] R. Dharmakumar, *Magnetic-Susceptibility-Based Functional MRI for Heart Disease*. PhD thesis, Graduate Department of Medical Biophysics, University of Toronto, 2004.

[2] S. Meiboom and D. Gill, "Modified spin-echo method for measuring nuclear relaxation times," *Review of Scientific Instruments*, vol. 29, no. 8, pp. 688–691, 1958.

[3] M. Goldman, *Quantum Description of High-Resolution NMR in Liquids (International Series of Monographs on Chemistry)*. Oxford University Press, USA, 1991.

[4] E. Toumelin, C. Torres-Verdin, B. Sun, and K.-J. Dunn, "Random-walk technique for simulating NMR measurements and 2D NMR maps of porous media with relaxing and permeable boundaries," *Journal of Magnetic Resonance*, vol. 188, no. 1, pp. 83 – 96, 2007.

IV. EXPERIMENTAL COMPONENTS AND DESIGN

The MRI experiments presented in this thesis share many common elements in terms of external hardware. The design and equipment required to produce these experiments are detailed in this chapter. This includes the individual components which are used to produce the contrast agent itself and methods for producing and monitoring the fluid pressure applied to the samples.

IV.1 Contrast Agent Components

Throughout the course of this work several pressure contrast agents have been developed in both the liquid and solid phases. However, they all have common elements which are microbubbles of some sort and a stabilising or suspending medium. The properties of those components are detailed in this section.

IV.1.1 Microbubbles

The microbubbles for this work have been produced through collaboration with Professor Yvonne Perrie, Anil Vangala and Randip Kaur at Aston University. For successful measurement of pressure, micron sized gas bubbles are required. In this work we have tested four possible shell components: DSPC, DPPC, C_{20}PC and F-GPC.

IV.1.1.1 DSPC, DPPC, DAPC

The three unfluorinated lipids used in this study are 1,2-Distearoyl-*sn*-Glycero-3-Phosphocholine (C18:0, MW:790.16, T_{FG}:55°C) or DSPC with a chain comprising of 18 carbons; 1,2-dipalmitoyl-*sn*-glycero-3-phosphocholine (C16:0, MW: 734.05, T_{FG}:41°C) or DPPC with a chain comprising of 16 carbons and 1,2-Diarachidoyl-*sn*-glycero-3-phosphocholine (C20:0, MW:846.27,T_{FG}:66°C) or DAPC with a chain of 20 carbons.
These lipids are used to produce microbubbles by means of the shear mixing method and are compared to each other using MRI during application of cyclic pressure variations. The molecular structure of these lipids is very similar with the exception of the length of the carbon chain. All microbubbles used herein are produced to contain either air or nitrogen gas.

IV.1.1.2 F-GPC

In an attempt to improve the stability of the microbubbles, a literature search was performed with the hope of discovering new technology and or production methods and protocols which would yield more stable mi-

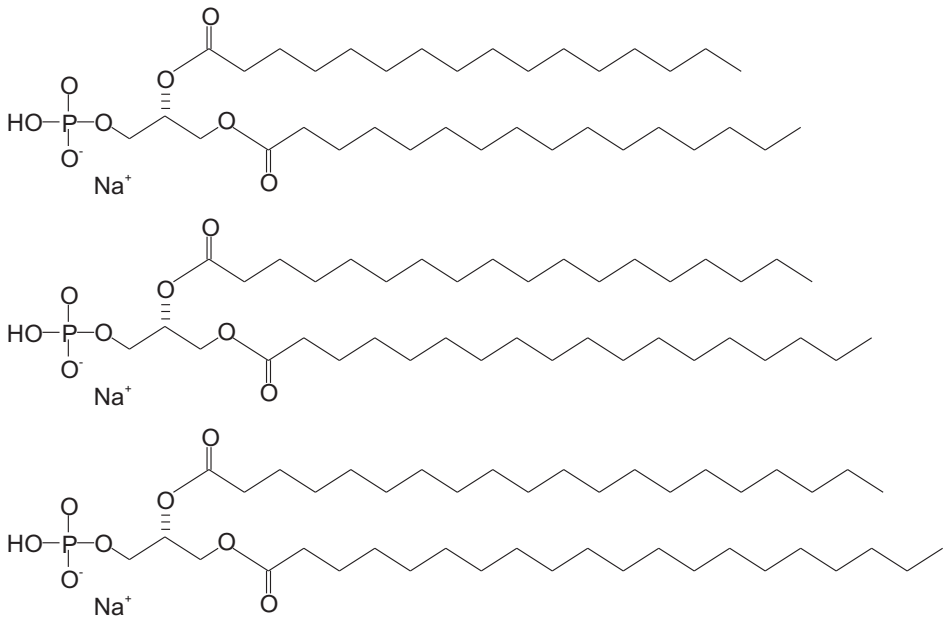

Fig. IV.1: Schematic representation of chemical compositions of DPPC (top) DSPC (middle) and DAPC (bottom) molecules.

crobubbles. One particular method seemed to highlight a clear improvement in the stability of microbubbles over time by using a lipid coating which has a particular synergy with the gas contained within [1]. In this particular case, the two components were both fluorinated: the lipid was perfluoralkylatedglycerophospatadylcholine surrounding a gas bubble of nitrogen gas saturated with perfluorohexane.

Through collaboration with the group who devised this method at the Institut Charles Sadron in Strasbourg, we were able to reproduce the microbubbles for use as a potentially more stable contrast agent. The work was presented as an electronic poster at the International Society for Magnetic Resonance in Medicine conference in Toronto, May 2008.

IV.1.2 Suspending Medium

In order to produce a contrast agent which contains gas filled microbubbles, a suspending medium must be produced. It is desirable that the suspending medium fulfils the following requirements:

- Contain free water molecules which are able to diffuse around the microbubbles.
- Present a molecular water diffusion coefficient as close to that of bulk water as possible (or higher).
- Be sufficiently viscous that the buoyant microbubbles are trapped for the duration of a measurement.
- Have a controllable viscosity allowing it to flow through porous media or to be tested as a bulk sample.
- Be suitably simple to produce by either hydration or some other technique that it can be readily made in the physics lab.

We initially followed the method presented by Alexander et. al [2] and used a combination of 2%w/w methyl cellulose with water and an equal concentration of glycerol (v/v). Although the medium presented also contained several other components (saline and propyleneglycol), it was determined that these played little or no role in the stability of the suspension and so were omitted, although they may have had a function in terms of enhancing the contrast agent's biocompatibility.

In spite of permitting measurements of pressure with MRI, methyl cellulose is Newtonian for shear rates lower than $5s^{-1}$ and an increase in viscosity sufficient to immobilise microbubbles for a lengthy experiment would most likely prohibitively reduce the diffusion of water and hence the sensitivity of the technique. Following a presentation at the Magnetic Resonance in Porous Medium conference in Bologna, Italy in September 2006, Nikolaus Nestle of BASF SE (Ludwigshafen) suggested that the use of alternative polysaccharide gels would allow substantial increase of viscosity without decreasing the diffusion of water within the structure although this is at the expense of its Newtonian behaviour.

Through this collaboration and private communication with CP Kelco, we selected gellan gum, a polysaccharide gel which allowed several orders of magnitude increase in viscosity to be achieved with little to no effect on the diffusion coefficient of water within its structure.

Another useful property of many polysaccharides is that their viscosity can be increased independently of their concentration by 'cross-linking' their structure with a salt. With heavy cross linking, even a solid gel can be produced. This would allow a semi solid object to be used as a contrast agent for pressure measurements using MRI. This agent might find applications in several fields, particularly that of large particle dynamics.

IV.1.2.1 Methyl Cellulose

Methyl cellulose is one of many polysaccharide molecules which forms Newtonian (for shear rates under $5s^{-1}$) viscous solutions with water at low concentrations, typically less than 5%. Methyl cellulose has many applications, particularly in food products as a tasteless thickening agent. It is often found as a component in inexpensive frozen desserts, as is glycerol.

Following the protocol outlined in the paper of Alexander et al. [2] a 2% w/v aqueous suspension of methyl cellulose was used with an equal concentration of glycerol. Several litres were produced at a time, although volumes of approximately 100ml were most often used. Amongst other advantages, this allowed easier control over the homogeneity of the preparation.

A volume of the fluid is extracted from the preparation into which microbubbles are blended using manual agitation. Concentrations of 1.25%, 2.5%, 3% and 5% v/v have been used throughout the study. Optical ob-

servations of turbidity are used as an initial assessment of the homogeneity of the suspension. Again, a larger volume than necessary is prepared to ensure homogeneity.

As initially observed by Alexander [2], and later by Dharmakumar [3], we also observed that the MRI measurements of pressure using this preparation were suffering from a severe drift caused in part by microbubble migration (advection) due to their intrinsic buoyancy. In order to stabilise the medium for extended periods of time, alternative preparations were then tested.

IV.1.2.2 Gellan Gum

Gellan gum was selected as a suspending medium which would improve the control over the viscosity without impeding the diffusion of water. Again, 2% w/v aqueous gel was selected as this allowed a fair comparison between this and the methyl cellulose and yielded a gel which appeared to immobilise the microbubbles for an extended period of time.

It was important to verify the properties of the gel, particularly its propensity to reduce the advection of microbubbles and the value of the diffusion coefficient.

It was seen that this gel offered all of the required properties and that they could also be easily adjusted. Similar concentrations of microbubbles were used as in the methyl cellulose study.

IV.1.2.3 Carageenan Gum

Following private communication with Eiichi Fukushima the difficulty in determining the forces exerted on grains in a packed bead system was highlighted.

It was decided to extend the liquid polysaccharide gel study to produce a solid gel which could be used to these ends. By cross linking the gels using salts, having blended in the microbubbles, a semi solid is created from carageenan gum which allows pressure to be measured with MRI.

IV.2 Generation and Measurement of Pressure

The equipment set-up used for the MRI experiments remains very similar regardless of the agent tested. This section covers the equipment involved in these experiments.

Name	Pumping Mechanism	Pressure Range	Continuous Flow
Impeller Pump	Rotating paddle or vane. Forces liquid incident on centre to outside edge.	Very low, better for fluid delivery.	Yes
Syringe Pump	Motor driven piston forces syringe barrel into syringe.	Dependent on pump design, maximum between 2 and 6 bars	Up to volume of syringe unless more than one barrel used.
High Pressure Liquid Chromatography Pump	Reciprocating piston into double valved chamber.	Several hundred bars.	Flow continuous but pulsed, slow (around 20ml/min depending on model).
Peristaltic Pump	Rotating roller alternately crushes soft pipe pushing contents along.	Dependent on roller design, maximum between 2 and 10 bar.	Flow continuous but pulsed.

Tab. IV.1: Major pump types

IV.2.1 Generation and Transmission

The generation of pressure requires a small volume of excess fluid to be driven into a closed system. To achieve this, a pump must be used. There are four pumps which are commonly used to drive fluids. These are covered briefly in table IV.1 to provide the reasoning behind the choice of pump for the experimental set-up.
For the needs of the microbubble contrast agent, the syringe pump offers the greatest match to the requirements. It allows a constant flow rate (up to around 60ml delivery) and the generation of pressures up to 6 bars. It can be controlled by a PC allowing for automation and accurate control of the pressure. The flow of liquid, must be driven into the sample which is several metres away from the pump. This is achieved using the Swagelok ® (Solon, OH, USA) tubing system. PFA tubing is used as this is fully MRI compatible and is sufficiently rigid to resist expansion due to pressure. The connections are made using Swagelok ® connectors which withstand pressure up to 50 bars and allow easy connection to a variety of tube sizes and equipment. The $\frac{1}{4}$inch tubing size is used to allow viscous fluid to be driven through the system without establishing a substantial pressure gradient in the tubing present before the sample which would be potentially detrimental to the contrast agent, whilst not requiring an excess volume of the agent. The schematic of the general system is shown in Fig. IV.2. The sample holder is varied depending on the experiment whilst the remaining equipment remains similar.

IV.2.2 Conventional Pressure Measurements

In order to corroborate the MR measurements with the actual pressure in the system, it is necessary to measure the fluid pressure using conventional means.

IV.2.2.1 Piezoelectric and Capacitive Sensing

The simplest measurement technique involves using either piezoelectric or capacitive sensors. There are numerous variations available for the measurement of pressure in various media although the vast majority of these sensors comprise of a multilayer design (see Fig. IV.3):

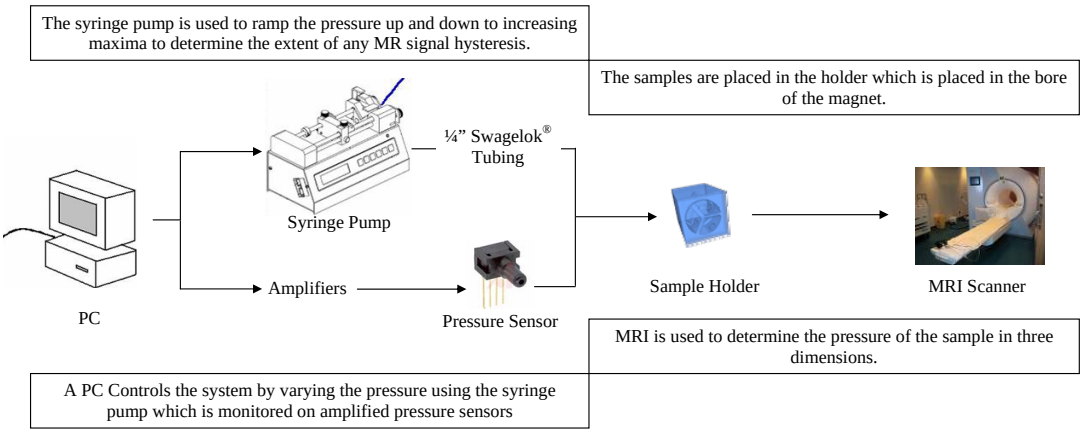

Fig. IV.2: Schematic showing the typical set-up for MRI experiments. The sample holder is changed depending on the experimental protocol whilst the remaining equipment remains much the same.

- Outer casing with electrical and fluid contacts
- Metallic or ceramic sensor die
- Piezoelectric or capacitive flexural membrane (within die)
- Ports by which the test medium can reach the membrane

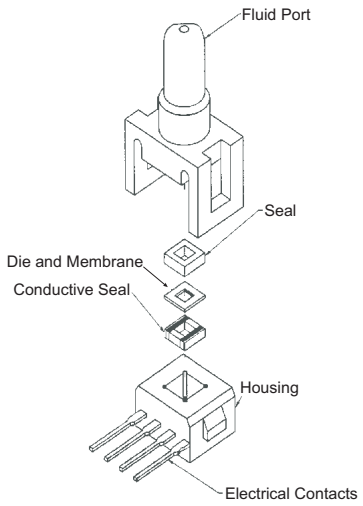

Fig. IV.3: Schematic of typical piezoelectric membrane pressure sensor. Reproduced from 24PC series datasheet.

The sensors have two ports, either side of the membrane. In a gauge sensor, one of these ports is left exposed to atmospheric pressure as opposed to a differential sensor in which both ports are connected. As the pressure increases on one port, the membrane is forced through the die in which it is held. The capacitance or conductivity of the membrane is changed as a result, permitting investigation of the pressure by monitoring these changes by using a bridge circuit.

The nature of these sensors is such that their voltage output is often very low (200mV full scale) in comparison to the excitation voltage (10V). A piezoelectric sensor was selected as they offer relatively low cost whilst

yielding sufficiently accurate measurements (±.15% full scale accuracy). The particular model was selected from several possibilities by testing which had the highest compatibility with MRI measurements.

IV.2.2.2 Amplification and Digitisation

The selected pressure sensor (a Honeywell (MN, USA) 24PCFFM6G), produces a full scale voltage in the order of 200mV for pressures of 10bar. In order to digitise this output voltage as accurately as possible, it is necessary to amplify this voltage to a range more commonly found in analogue to digital technology. For optimum portability, a National Instruments (Austin, TX, USA) Universal Serial Bus data acquisition device, the USB-6009 was purchased. This is a highly affordable unit with suitable specifications for measuring voltages in the range of 0-5V on up to 8 single ended or 4 differential inputs for signals from DC to $48kHz$. It is also capable of analogue output as well as digital input and output, allowing potential integration to other systems such as control of the MRI scanner through digital triggering.

In order to increase the voltage output from the piezoelectric pressure sensors, instrumentation amplifiers were used, allowing collection of signals from DC up to several kHz whilst introducing minimal noise. The specifications of several amplifiers were scrutinised to find an amplifier which would provide a gain of around 10, noise smaller than $1mV/\sqrt{Hz}$, and allow construction of the typical instrumentation amplifier circuit (see Fig. IV.4) with minimal addition of components. Ideally an amplifier meeting the first two conditions whilst requiring addition of only a single external component was desired. The AD623AN produced by Analog Devices (Norwood, MA, USA) was found to meet all of these criteria, offering a noise figure of $35nV/\sqrt{Hz}$ @ 1kHz, a gain of between 1 and 1000 set by a single resistor to complete the amplifier circuit and operative from a single rail 12V supply. Five Amplifiers are constructed on a single breadboard with a filtered power supply to allow up to 5 simultaneous pressure measurements.

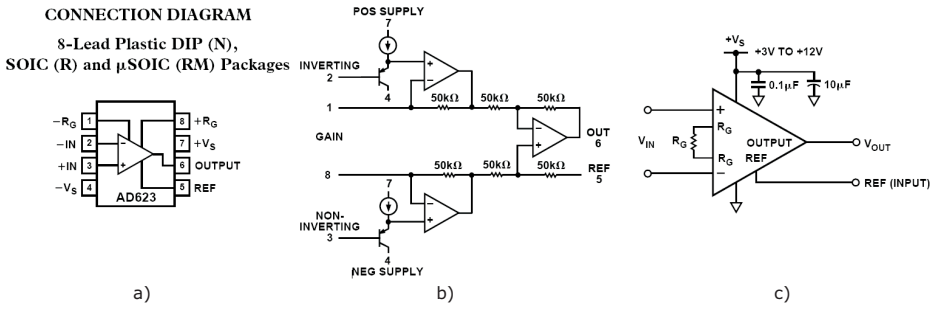

Fig. IV.4: Amplifier design from Analog Devices data sheet: a) Pinout of the AD623AN instrumentation amplifier. b) Simplified internal design of instrumentation amplifier. c) Component layout for single supply amplification (R_G sets the gain).

To simplify the construction of the pressure sensor and amplifier circuitry, it was decided to avoid the use of unnecessary shielding of the components to reduce MR interference. To determine the level of this interference, a series of experiments were conducted at $3T$ with the amplifier and sensors in B_0, just the sensors in B_0 and finally neither in B_0. It was found that the pressure sensors do demonstrate a notable offset when they

are in B_0 although they still function effectively if they are calibrated at field. However, the effect of B_0 on the amplifiers and power supply was found to be unacceptably large. For this reason, it was decided to feed the voltages from the sensors to the amplifiers outside the 5 Gauss line. To ensure that the system is robust and that the sensors can be easily moved and reconnected as necessary, they are connected to common telephone network connectors (RJ11). After amplification, the signal is transferred to the data acquisition device through a multi core cable terminated in a proprietary National Instruments connector.

After extensive use in single ended measurement mode, it was found that use in differential mode offered far less interference from other sources. Although this reduced the possible number of simultaneous measurements to four, the experimental protocol never required more than two sensors.

For ease of control and acquisition, the data from the acquisition device is collected and processed in the National Instruments graphical programming environment, LabView 7.0. This interfaces the PC very simply yet powerfully with the device and allows control of the acquisition parameters, as well as post processing options. To improve the SNR of these measurements, gross oversampling is performed. The data is sampled at 10kHz and each 1000 samples averaged. In this way, the SNR is vastly improved and the data suitable for processing alongside the MRI. To further aid the post-processing, the pressure measurements are triggered by the MRI scanner. A trigger output is written into the pulse sequence and a 5V pulse is generated at the start of each repetition. The software is modified to write the current average of the pressure to a text file when triggered by the scanner, allowing this file to be used directly when processing the MR data in MATLAB ®.

IV.2.2.3 Calibration

To lower cost, uncalibrated sensors were chosen for pressure measurement. These were approximately $\frac{1}{10}$ of the cost of the calibrated versions. Because of hardware instabilities, regular calibration of the sensor system is necessary. To aid this procedure, a LabView application is developed which automatically generates calibration information for the sensors. The sensors are connected together and to a 50ml syringe using an in house designed and produced acrylic adapter. The syringe is put in the syringe pump which is connected via an RS232 interface to the same PC as the National Instruments USB-6009 interface. The application then ramps the syringe volume down and up by known amounts. The voltage from the pressure sensors is monitored, and using the ideal gas law the pressure is calculated and used to calibrate the sensors. This information is then used in the pressure monitoring application to provide a calibrated pressure measurement.

References

[1] F. Gerber, M. Krafft, G. Waton, and T. Vandamme, "Microbubbles with exceptionally long life - synergy between shell and internal phase components," *New Journal of Chemistry*, vol. 30, no. 4, pp. 524–527, 2006.

[2] A. Alexander, T. McCreery, T. Barrette, A. Gmitro, and E. Unger, "Microbubbles as novel pressure-sensitive MR contrast agents," *Magnetic Resonance In Medicine*, vol. 35, no. 6, pp. 801–806, 1996.

[3] R. Dharmakumar, D. Plewes, and G. Wright, "On the parameters affecting the sensitivity of MR measures of pressure with microbubbles," *Magnetic Resonance in Medicine*, vol. 47, no. 2, pp. 264–273, 2002.

V. MICROBUBBLE MICROSCOPY

Several microscopic methods were used to assess the microbubbles for the contrast agent. The majority of the work was carried out at Nottingham Trent University using a standard optical microscope to size and monitor the stability of the microbubble preparations in a custom built perfusion cell. In addition to these measurements, a particle sizer (Malvern Mastersizer) at Aston University has been used for sizing.

In an attempt to determine the membrane thickness, electron microscopy with freeze fracture was performed through the EPSRC open access scheme at the University of Nottingham. The results of this are included in this chapter and provide interesting insight into the microbubble shell morphology.

V.1 Optical Microscopy

Measuring the optical properties of microbubble samples is particularly challenging given their intrinsic buoyancy and opacity. In order to achieve the measurements, particularly if it is desirable to do so whilst pressure is applied, it is necessary to build an optically transparent cell. Such a cell was manufactured in house from several pieces of acrylic that had been cut using a laser cutter and fixed together using Extrufix© adhesive (see Fig. V.1). The liquid volume must be sufficiently thin to allow light to pass through the sample even at high microbubble concentrations. Additionally, it is desirable to have this thickness around that of the largest microbubble so as to encourage the visualisation of a single layer of microbubbles, allowing automated processing in a single focal plane.

Having produced the cell, three measurements are made. A size distribution measurement; Pressure at which destruction occurs and the relationship between applied pressure and microbubble radius. These experiments are discussed in the following sections. The cell is used with several samples under a microscope with attached PC camera to acquire a series of digital images. These images are thresholded to locate microbubbles. The areas corresponding to the inside of the microbubbles are filled using an inbuilt MATLAB image processing tool-kit hole filling algorithm before the areas of each are automatically determined based on a column-wise connectivity algorithm. The microbubble radii are calculated from these areas. For 10 images, the process is conducted both by eye and by using this numerical processing technique to ensure that it accurately determines the microbubble size. All PC measurements are found to lay within the estimates by hand and consequently the automatic processing is validated.

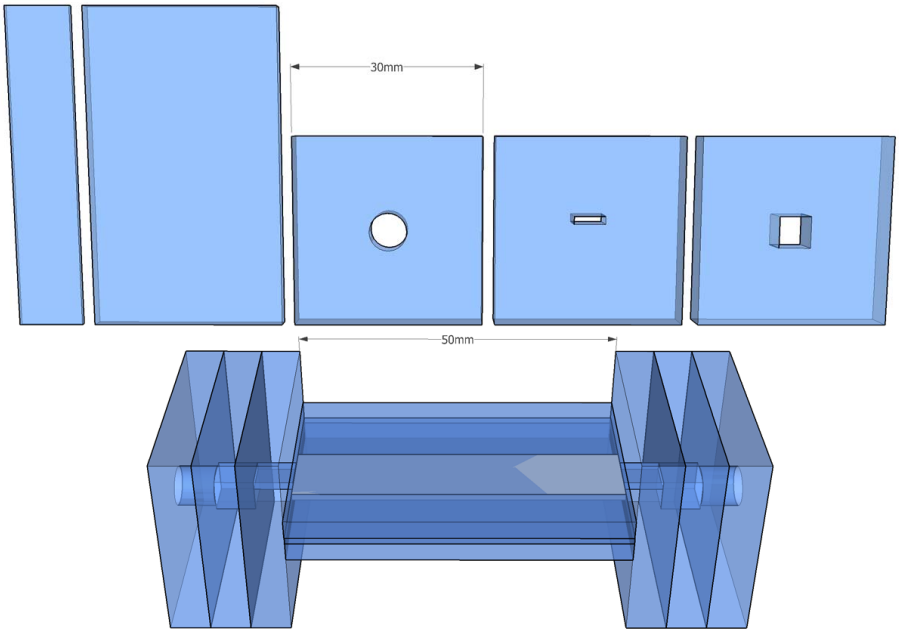

Fig. V.1: Schematic representation of the cell used to study the microbubble preparations under an optical microscope. The left and right extremities are fitted with Swagelok connectors (not shown). A small volume through the centre of cell allows passage between the two ends.

The drawback of this method is the heat generated by the microscope lamp. It is relatively easy to heat such a small sample beyond the lipid gel-liquid phase transition temperature over a measurement as short as 30 minutes. In order to minimise the effect of temperature, the lamp is turned on only when an image is collected and for adjustments. Additionally, the lamp intensity is kept as low as possible whilst still providing images of sufficient contrast for numerical processing.

V.1.1 Size Distribution

The size distribution is determined using two methods. Firstly using a Malvern Mastersizer particle sizer at the University of Aston and secondly by applying the previously discussed image processing technique to several optical microscope images of microbubbles from different locations in the sample and producing a histogram of the results. Generally, the microbubbles produced using the shear mixing method produce a size distribution as is shown in Fig. V.2.

The distribution narrows somewhat as the preparation ages, whilst its centre tends to shift upwards slightly. These results were corroborated in the studies carried out by Dr. Anil Vangala [1] (see Fig. V.3) using a Malvern Mastersizer at Aston University. The centre of the size distribution is seen to nearly double over 7 days storage.

V.1.2 Destruction Pressure

In order to estimate the pressure at which microbubble destruction occurs, the pressure is increased gradually until a microbubble observed in the cell ruptures. This measurement is most heavily influenced by the heating effect of the microscope lamp as the measurements are lengthy and so it must be used only during acquisition

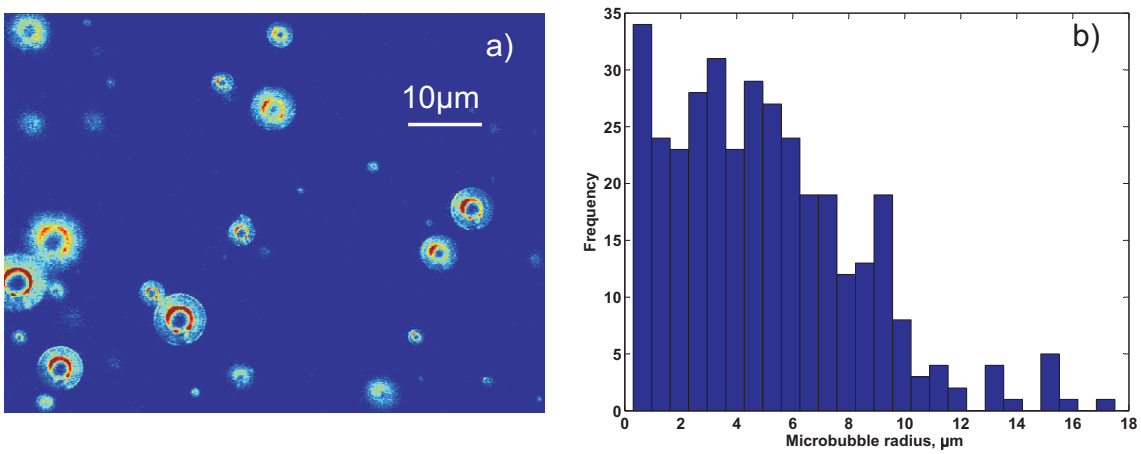

Fig. V.2: a) False colour image of gas filled microbubbles collected using a standard microscope. b) Histogram of microbubble size distribution produced from 25 microscope images.

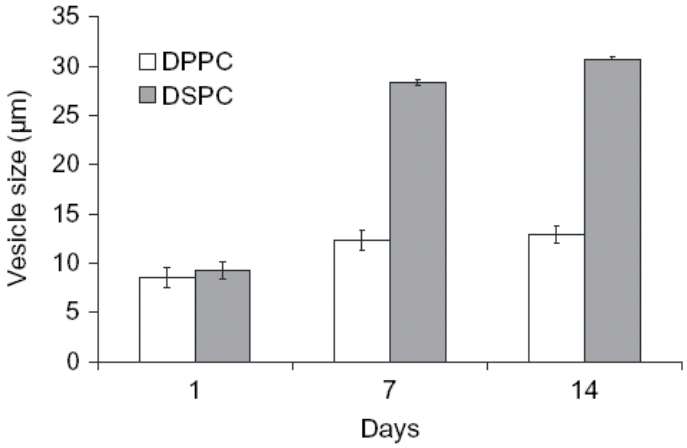

Fig. V.3: Average diameter of DPPC and DSPC based gas-filled microbubbles over time stored at 25°C. Vesicle size was measured in double distilled water with dynamic light scattering using Malvern Mastersizer at 25°C, results represent mean S.D., n = 3. Reproduced from [1]

of images. After a given time, the smaller microbubbles will suffer rupture as a result of phase change of the membrane and increased internal gas pressure.

A large bubble is selected in the cell for the measurement and the pressure varied whilst the microbubble radius is measured. Although the influence of temperature is minimised as much as possible, this measurement may not completely represent an unheated sample, although it does offer some insight into the damage which occurs.

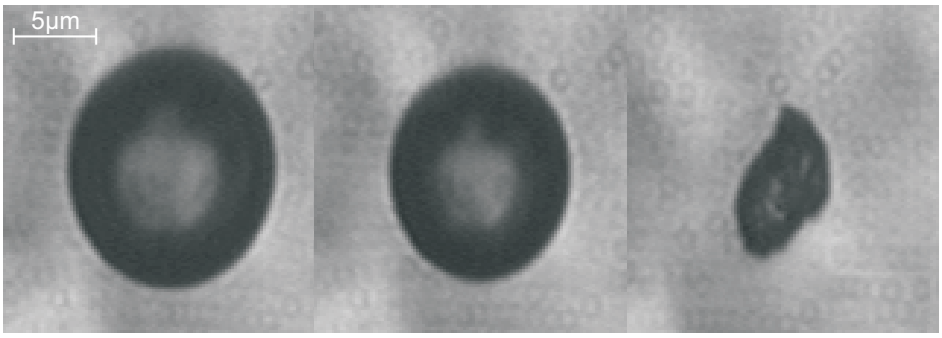

Fig. V.4: Three images of a 12μm single microbubble experiencing an increase in external pressure, collected using a camera mounted onto a microscope at 40x magnification. Left to right corresponds to atmospheric, ĩ.5 bar and 3 bar; notice how the microbubble survives the initial application of pressure but is ruptured at high pressure leaving just the distorted lipid shell containing no gas.

The images in Fig. V.4 demonstrate a typical destruction mechanism observed in our samples. Unfortunately frames are not collected sufficiently quickly to show the intermediate steps as shown in the work of Borden *et al.* [2] although they show the typical mechanism seen in our samples. The gas is ejected from the membrane leaving a large micelle like structure with a 'crumpled' appearance owing to the generation of domain like structures as the membrane collapses into a smaller volume.

V.1.3 Pressure Radius Relationship

Throughout the work of Dharmakumar [3] it is assumed that the ideal gas law applies for microbubble radius changes as a result of applied pressure. In order to validate that a change in pressure does indeed bring about an ideal gas law change in the microbubble radii, experiments are conducted whereby a single large (8μm) bubble is pressurised whilst its radius is measured automatically. It can be seen in Fig. V.5 that whilst the pressure is increased, the radius varies cubically with the reciprocal of pressure as predicted by the ideal gas law. The same is true as the pressure is released although a rapid change in size occurs at 1.54 bar resulting in a microbubble of 7.5μm. The gradient of the line should be $P_1 r^3$ (see equation V.1) although the effect of variations in the temperature of the sample due to heating caused by the microscope lamp may result in some discrepancies between this measurement and those conducted at room temperature. If these experiments could be conducted in a temperature controlled cell with a smaller bubble (or a higher resolution microscope imaging system), a definitive answer should be obtained. Assuming that the temperature is constant, the ideal gas law can be rearranged to give equation V.1:

$$P_1V_1 = P_2V_2, V_2 = \frac{4}{3}\pi r_2^3, r_2^3 = P_1V_1\frac{3}{4\pi P_2} \tag{V.1}$$

where P_1 and P_2 are the initial and final pressures resulting in volumes of V_1 and V_2 given by radii of r_1 and r_2 respectively. As can be seen in equation V.1, the gradient of the line corresponds to the size of the microbubble at atmospheric pressure and should have a zero intercept. The data is fitted with the expression in equation V.1 and the gradient and intercept are determined. The data follows the ideal gas law with some minor discrepancies due to the influence of the lipid membrane. These discrepancies are seen as a slightly higher radius calculated from the gradient (15% higher for the initial bubble and 5% higher for the final bubble) and as a negative y intercept corresponding to the size of the microbubble at infinite pressure. The fact that the y intercept is negative suggests that the microbubble will have zero size at some finite pressure given by the x intercept. The value for the large bubble is around 2.7 bar whilst the small bubble has a much higher value at 7.4 bar. This is as expected as the smaller bubble should have a higher damage pressure in comparison to the larger bubble since it will experience a lesser change in radius for a given pressure.

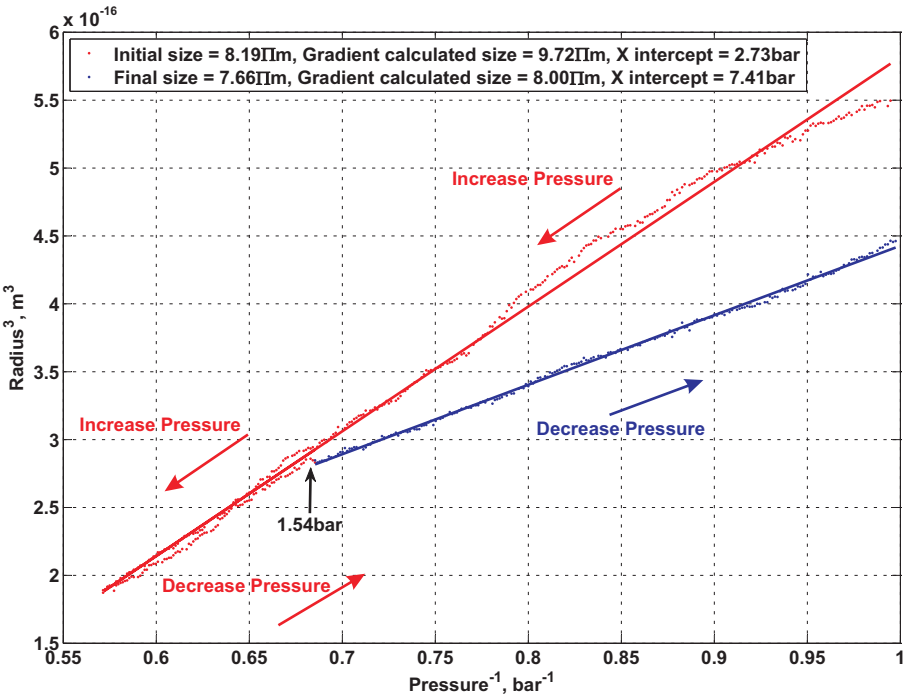

Fig. V.5: Measurements of the microbubble radius as a function of external pressure. The pressure is cycled up and down from atmospheric to 1.75 bar whilst the radius is determined automatically. Linear lines of best fit are added both for before (red) and after (blue) microbubble damage which occurs at 1.54 bar. Linear fits to these lines should reveal the initial size of the bubble and the intercept (which would be zero for an ideal response) and offers insight into the shell contribution.

Assuming that this measurement is valid, it is possible to determine the expected change in NMR signal intensity due to proton density. For a given region of for example $1cm^3$ with 5% gas concentration of $5\mu m$ microbubbles, at one and two bars of external pressure, the change in proton density will be 2.5%. If the only

effect responsible for change in NMR signal was proton density, this would result in a signal sensitivity of 2.5% per bar, less than 10% of that which we actually see. This is strong evidence for the susceptibility effect having the largest contribution to our signal.

V.2 Scanning Electron Microscopy

To assess the properties of the microbubbles both in and out of the gel, Scanning Electron Microscopy (SEM) was performed. Because the microbubbles do not remain intact when outside the suspending medium, traditional SEM which requires a dry sample could not be performed. Cryo-SEM which allows the samples to be rapidly frozen and maintained at low temperatures allowing imaging was chosen as a possible technique. The facilities for cryo-SEM are available through the open access scheme at the nano technology centre at the University of Nottingham. This EPSRC initiative funds 2 days of experimental work on various instruments at the nano-technology centre.

Three samples are prepared: dense microbubble foam, as produced at Aston University; the other two samples are the standard preparation of gellan gum with and without salt to solidify the gel, with an exceptionally high concentration of microbubbles around 50% gas volume. The FEI Quanta 200 3D focused ion beam scanning electron microscope (FIBSEM) and Quorum Technologies PP2000T cryo transfer unit at the Nano-technology centre have several features which are advantageous for imaging samples such as ours. The first and arguably the most useful is the freeze fracture facility which allows the sample to be fractured parallel to its surface revealing the inner structure. The microscope has a Focused Ion Beam (FIB) which allows the surface of the sample to be vaporised revealing sub surface features; the microscope also has a built in sputter coater which can be used to enhance the surface contrast by applying a surface coating of platinum; The final feature of interest is the ability to control the temperature of the sample chamber which allows a gradual increase to the point at which the water will begin to sublime leaving just the non-water components.

Through the combination of these techniques a large number of images are collected from each sample. There were two measurements of particular interest. The first is the thickness of the microbubble membrane and the second the evaluation of the interaction of the membrane with the gel.

V.2.1 Membrane Thickness

There is some dispute over the thickness of the membrane in terms of the number of lipid layers [4]. The majority of the literature suggests that gas filled microbubbles will have a single monolayer of lipids. By virtue of the self assembly process, which starts with many lamellar sheets, this seems relatively unlikely. The membrane thickness could be determined by surface microscope imaging followed by assessing the width of two neighbouring lipid membranes, although an unknown amount of fluid in the sample may lead to measurement

uncertainties. In a medium with polydisperse microbubbles of unknown concentration, the quantity of liquid present between the two spheres may be significant. For this reason, an alternative strategy, in which a ruptured membrane is measured, is used.

A small volume of the sample is transferred to an aluminium stub. This is then attached to the brass stub holder of the microscope. The water then needs to be vitrified by plunging it into nitrogen, cooled to just below its melting temperature (slush nitrogen) achieved by vacuuming liquid nitrogen. The sample is transferred to the side antechamber of the microscope which is held at $-140°C$, before transfer to the main chamber where imaging is performed. The surface of the sample is obscured by a small amount of frost, so freeze fracture is performed using a cooled blade (lower than 0°C to prevent melting the frozen sample) in the antechamber. The inbuilt sputter coater is then used to deposit 50-100nm of platinum on the sample surface to enhance the imaging.

The control PC is calibrated for size measurements and this feature is used to determine the membrane thickness of a ruptured microbubble. On average, the measurements suggest that the thickness is around 40nm. Assuming that this was the true membrane thickness, this is equivalent to a membrane with twelve lipid layers based on a length of 3.4nm per DSPC lipid (see Fig. V.6). This estimate seems slightly higher than expected, so further investigation may be required.

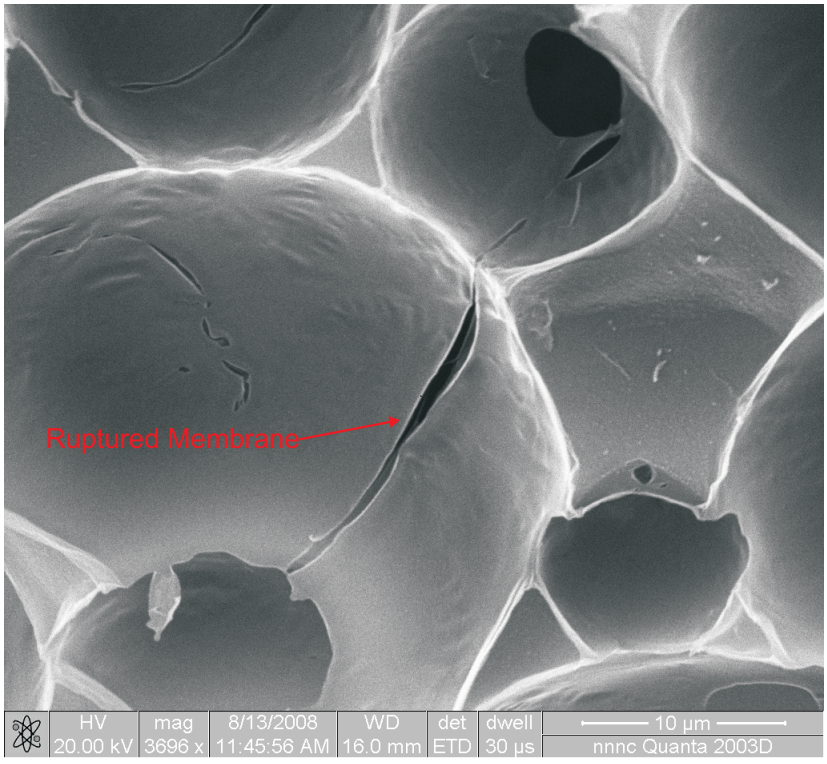

Fig. V.6: Scanning electron microscope image of a microbubble with a ruptured membrane. The thickness of this membrane can be estimated to determine the number of lipid layers present.

V.2.2 Gel Interaction

The other two samples are used to evaluate the physical interaction of the microbubbles with the surrounding gel medium. The results are unexpected and it could be either a facet of the preparations or of the imaging technique employed. The first sample is the liquid gel. The sample is prepared as in the previous experiment and investigated from the point of view of both the microbubbles and the gel. It is seen that there is little effect on the microbubbles in comparison to the bulk foam.

The most striking difference between the pure foam and the suspended microbubbles is their structure. In contrast to the pure foam, they appear to have either a very thin, or no membrane. It has instead been replaced by the gel structure (see Fig. V.7). It is quite likely that the structure of the gel changes as it is cooled, although the effect should be fairly minimal as gellan gum is often used for freeze-thaw stability in the food industry. We had no equipment at our disposal to image the surface of the sample when not frozen to further explore the freezing process.

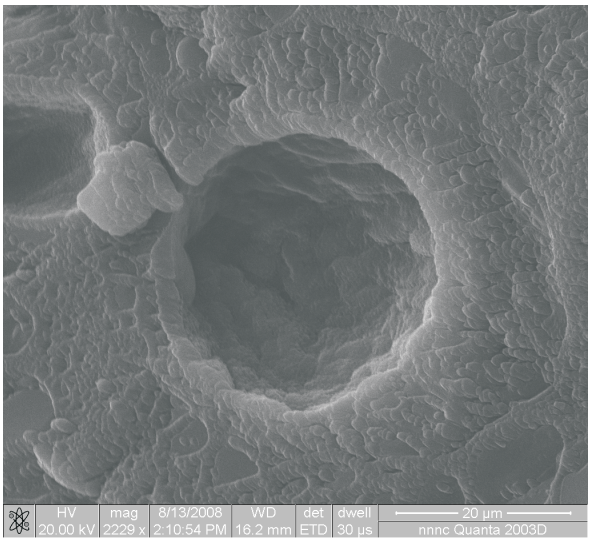

Fig. V.7: Microbubble in gel with no apparent membrane.

V.2.3 Sublimation

By slowly heating the sample to the point of water sublimation, it is possible to remove the water from the sample leaving just the gel structure visible. This was performed with the solid gel and reveals a sheet like structure surrounding cells of around $3\mu m$ width. This structure appears to evolve around the microbubbles enveloping them, which may add additional stability (see Fig. V.8). This provides a good indication of the success of this material at trapping microbubbles as the length scales of both the microbubbles ($1-15\mu m$) and the gel network ($2-5\mu m$) are well matched. If this cell structure was much larger, it is possible that the microbubbles would not have been effectively trapped, thus preventing the drift reduction which we have seen in the MR measurements.

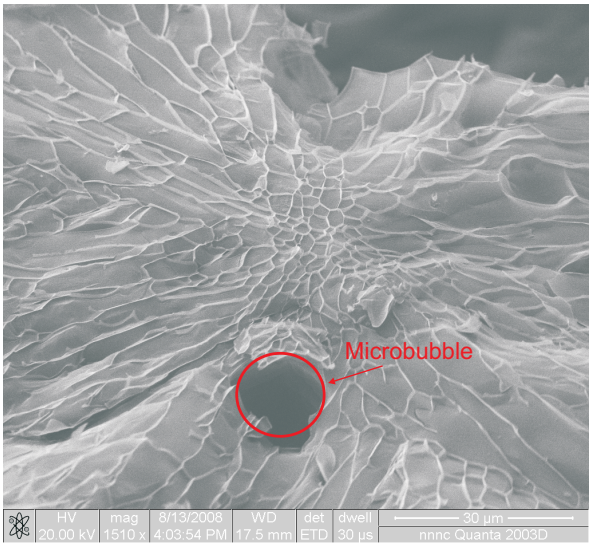

Fig. V.8: Cross-linked gel network matrix interaction with evidence of a single microbubble (approximately 13μm diameter) previously trapped within its structure. The cells appear with irregular shapes and average size approximately one third that of the average microbubble. The cell structure appears to have formed around the microbubble aiding its stability.

V.3 Conclusion

The microscopy presented in this chapter has been essential in providing an understanding of the microbubbles used in this study. A combination of techniques including optical and scanning electron microscopy and particle sizing have been used to evaluate the preparations. These techniques in combination have provided information on the change of microbubble properties over time and information about the size distribution and shell morphology for a variety of samples. When combined with MRI measurements and numerical simulations, assessment and optimisation of a contrast agent to pressure for a specific application is readily achievable.

References

[1] A. Vangala, R. Morris, M. Bencsik, and Y. Perrie, "Preparation and characterization of gas-filled liposomes: Can they improve oil recovery?," *J Liposome Res*, vol. 17, no. 3, pp. 263–272, 2007.

[2] M. A. Borden and M. L. Longo, "Dissolution behavior of lipid monolayer-coated, air-filled microbubbles: effect of lipid hydrophobic chain length," *Langmuir*, vol. 18, no. 24, pp. 9225–9233, 2002.

[3] R. Dharmakumar, *Magnetic-Susceptibility-Based Functional MRI for Heart Disease*. PhD thesis, Graduate Department of Medical Biophysics, University of Toronto, 2004.

[4] S. P. Wrenn, M. Mleczko, and G. Schmitz, "Phospholipid-stabilized microbubbles: Influence of shell chemistry on cavitation threshold and binding to giant uni-lamellar vesicles," *Applied Acoustics*, vol. 70, no. 10, pp. 1313 – 1322, 2009.

VI. MSME STUDIES

The following section encompasses the three MR experiments conducted in order to develop and assess the initial contrast agents. The first experiment investigates the effect of chain length on microbubble stability. This contrast agent is then used in a packed bead system and in a consolidated porous medium. The results from each study are included in this chapter along with the experimental protocol. The packed beads experiment provides useful information about the dynamics of the system as it includes both porous and bulk fluid elements in a single sample. The consolidated porous medium experiment demonstrates the suitability of the contrast agent to investigating the internal pressure of a sandstone like sample which is highly novel given the difficulty in using standard pressure sensors for non-invasive measurements.

VI.1 Chain Length Stability Study

Because MRI is sensitive to microbubble damage, it was chosen as a simple evaluation technique to determine which lipid produces the most stable microbubbles. Based on the microbubble damage analysis work published in this area, we selected three lipids with different carbon chain lengths. DPPC (16 carbons), DSPC (18 carbons) and C_{20}PC (20 carbons) were used to produce air filled microbubbles which were tested in terms of their stability during changes in pressure.

Because the signal intensity is inversely proportional to the gas density, should microbubbles be damaged, the signal intensity will increase. To assess the damage, the pressure is cycled to high and low values whilst the signal intensity is continuously monitored to determine the damage.

VI.1.1 Method

The pressure is applied to a custom designed, in house produced cell using a syringe pump remotely connected with Swagelok tubing. The cell holds three microbubble samples suspended in 2% w/v methyl cellulose (as at the time of this study, the benefits of gellan gum had not been found). The pressure is varied whilst MSME imaging is performed. The sequence takes under 2 minutes to acquire 8 echo images with several slices. The T_2^{eff} analyses are noisy when calculated pixel by pixel (SNR ~ 5 calculated as mean over standard deviation) although the NMR signal intensity (SNR ~ 45) follows the applied pressure relatively well. The echo images are averaged to improve the SNR of the image and result in a T_2^{eff} weighted image which is used to assess the damage. If the image was not T_2^{eff} weighted, there would be little signal change as a result of pressure variations, as the density changes alone account for only 2.5% of the sensitivity (see section V.1.3). Comparison between

Sample	Damage pressure, bar
DPPC	1.15
DSPC	1.40
$C_{20}PC$	1.55

Tab. VI.1: Estimates of pressure at which damage occurs for different microbubble preparations.

the drifts in the three samples over the duration of the experiment will show which lipids produce the most stable microbubbles.

VI.1.2 Results

The signal over each well of the sample holder is averaged and plotted against applied pressure (shown in Fig. VI.1 for C_{20}). A discontinuity is seen the in this curve at the point at which microbubble damage occurs. Once the pressure is again released, a poorer sensitivity is seen demonstrating damage to the microbubbles.

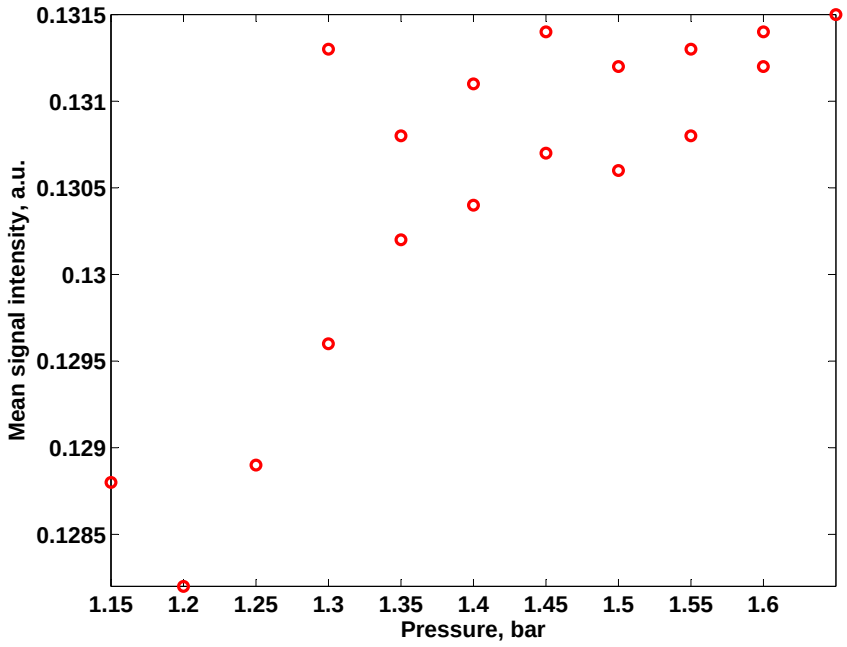

Fig. VI.1: Example of graph produced to determine the stability of the microbubbles produced with different lipids. Note the discontinuity at 1.55bar corresponding to microbubble damage. After release of pressure there is a greatly reduced sensitivity.

The results of the three experiments are summarised in table VI.1. It was found, as expected, that the DSPC offered far greater stability than the DPPC, owing to the longer chain length. However, the C_{20}PC showed only a minor improvement in stability which did not outweigh the increase in cost of this lipid compared to the alternatives. The additional cost also prevented production of several batches of the microbubbles which would have aided reproducibility tests. For this reason, the majority of experiments are carried out using DSPC microbubbles.

VI.2 Packed Beads Study

An in house constructed single volume hollow cylindrical acrylic cell of internal diameter 39mm and length 52mm is filled with silica gel saturated with the test fluid, 2% w/v methyl cellulose and 5% v/v microbubbles, and attached at one end to a dual barrel syringe pump (the cell had no outlet).

The silica gel packed cell is attached to two interconnected 50-ml gas-filled syringes in a syringe pump via a length of methyl cellulose filled tubing. The volume of the syringes is continuously swept to apply pressures which vary between 0.8 and 1.2 bar while imaging is performed. The MRI system is a 2.35-T Bruker Biospec small animal scanner (Bruker Instruments, Billerica, MA, USA). The sequence used is Multi Slice Multi Echo (MSME), which is a spin echo sequence that minimises susceptibility artefacts between the silica or glass and the water based contrast agent.

Having performed the MR imaging the data must be processed to extract useful information. The collected data is a train of echoes in the frequency domain and must be reshaped and Fourier transformed to extract an image (see Fig. VI.2). This is repeated for each echo image and slice in the data set. These images are averaged over the echoes to give a T_2^{eff} weighted image. By then averaging these weighted images over time, the drift due to microbubble rising and destruction can be visualised.

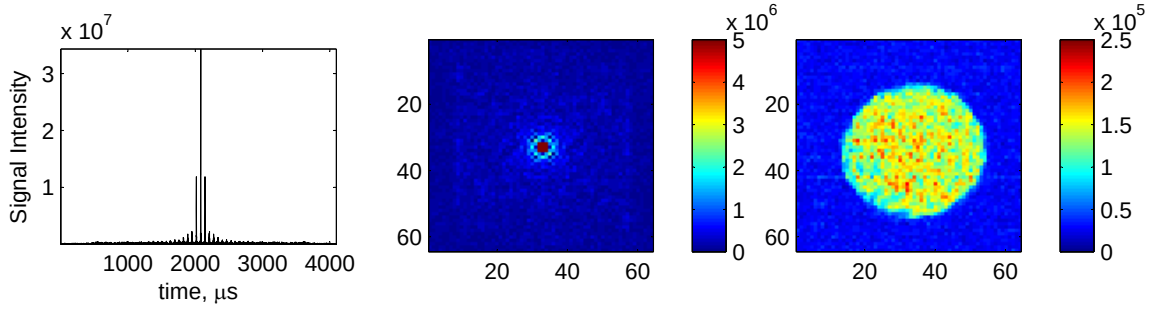

Fig. VI.2: Stages of data processing to get MR image. Left hand figure is raw data for a single slice, centre image is reshaped frequency domain data which is Fourier transformed to get the right hand image.

Because only static fluid was explored, long T_E values were used yielding high sensitivity, although drifts due to the rising microbubbles must be compensated for. This compensation is possible as we found that the drift is linear with time over the duration of the experiment. Due to the inherent difficulty of completely saturating the acrylic cell with silica gel, the upper third of the sample can be considered as bulk fluid. This allowed the microbubble dynamics to be studied simultaneously in a porous medium and in bulk fluid (Fig. VI.3). The peak drift is a measure of the percentage change in NMR signal over time and is found to be $33\% \cdot h^{-1}$ in bulk fluid and $11\% \cdot h^{-1}$ in packed beads. This shows that a 30 s experiment should suffer negligible drift. In order to quantify the drift over the image, the standard deviation is calculated over the sample area for each sample. The standard deviations are found to be 7.8, 7.5 and 7.0 percentage points at pressures of 0.8, 1.0 and 1.2 respectively.

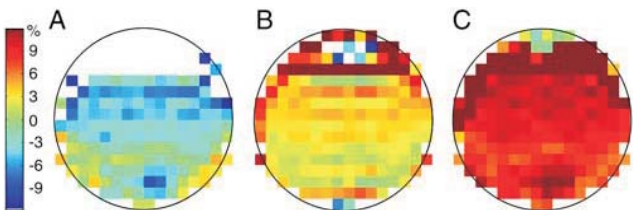

Fig. VI.3: Mean relative MR signal intensity deviation from 1 bar, averaged over all slices, in silica gel sample at static pressures of (A) 0.8, (B) 1.0 and (C) 1.2 bar. Note the increase in signal toward the upper portion of the images indicating the accumulation of microbubbles in the bulk fluid.

VI.3 Consolidated Porous Media Study

Having produced a contrast agent which demonstrated sensitivity to changes in pressure in a partially packed bead system, it was decided that the same preparation should be tested in a consolidated porous medium. The protocol and results are provided in this section and demonstrate sufficiently high sensitivity to produce for the first time a three dimensional map of pressure from within the structure of a porous system.

VI.3.1 Procedure

Our initial experiments also involved the determination of the pressure of a fluid saturating a consolidated porous medium with MRI. To avoid the paramagnetic impurities present in most sandstones, sintered glass cylinders (AM Glassware, Aberdeen, UK) are used. These have a structure very similar to that of sandstone and are produced by heating glass beads approximately equal to the desired pore size until they nearly reach their melting point (820°C). They are held in this state for an extended period of time until the grains are fused together but not melted into bulk glass. The sample is then slowly cooled back to room temperature, resulting in a stable sandstone like sample. AM Glassware made two samples successfully using this method: one high porosity sample with pore size of $160-250\mu m$ and one low porosity with pore size of $40-100\mu m$, both 40mm diameter cylinders, 50mm in length.

To allow fluid to be driven through the samples without bypass flow effects, they are potted into an extruded acrylic tube of internal diameter 45mm, using a two part resin. The acrylic tube is allowed to protrude beyond the axial extent of the samples by 10mm before caps are secured using Extrufix (see Fig. VI.4). This additional space is intended to reduce injection flow artefacts without the need for a distributor. Each of the end caps have a 3/8” Swagelok connector to allow fluid to be driven through the sample or, by capping the outlet and driving in excess fluid, to allow application of pressure to a static fluid.

The fluid is prepared using 5% gas per volume in 2% w/v Methyl cellulose with water. To prevent the rising of microbubbles in the suspension, it is produced in a mixing cell with an inlet, an outlet, a bleed valve and an intrinsic magnetic stirrer. The sample is connected to the outlet of this cell and fluid driven into it by introducing further bulk fluid to the cell. In this way, the preparation reaching the sample is relatively homogeneous.

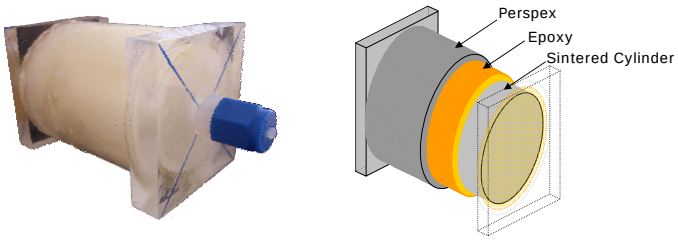

Fig. VI.4: Schematic representation (left) and photograph (right) of encapsulated porous media.

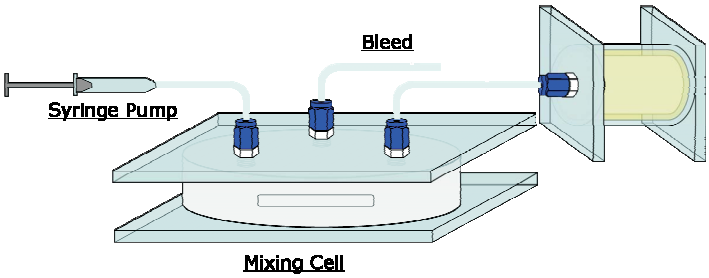

Fig. VI.5: Schematic showing the use of the mixing cell to deliver homogeneous fluid to the porous sample

To ensure that the conventional pressure measurements are sufficiently reliable that accurate calibration of the MRI data can be performed, the sensors are kept outside the bore of the magnet (although within the 5 gauss line) and connected to the inlet and outlet of the sample. The pressure in the sample is assumed to be the average of the two, as during fluid flow, large pressure gradients are seen to establish over the inlet pipe which is in consequence often as much as 0.4 bar higher than the outlet.

The sample is connected to the mixing cell and placed in the scanner before the microbubble-containing fluid is driven through it to a total volume of 40ml representing approximately 3 times the pore volume (a solid cylinders would occupy 63ml, so with a porosity of around 30% the pore volume is around 19ml) of the sample. The MR contrast to pressure is then calibrated by collecting MR images at several static pressures: the outlet is isolated after driving microbubble-containing fluid until 1.8 bar is reached on both sensors. The pressure is then reduced to 1.6 bar, 1.4 bar, 1.2 bar and then 1 bar. The signal intensity for each pixel (averaged for two repetitions) is fitted against the applied pressure using a linear least squares method to yield calibration information for use with the flowing data. The outlet is then opened, and the MSME is repeated every two minutes while the fluid is driven at a flow rate of 2 ml/min until a steady pressure gradient across the medium is reached. This is performed for fluids with and without microbubbles in order to check that the contrast originates from the microbubbles and not from dissolved gas in the suspending fluid or gas trapped in the porous medium.

In order to process the data, each experimental data set is averaged first in two dimensions, to collect one dimensional profiles which are stacked in time, secondly in one dimension to create sagittal images which have individual pixel calibration. Finally the individual voxel fits from the unaveraged three dimensional MRI

images are assessed to find those pixels with a greater than 90% confidence. These pixels are then grouped into three pressure categories to approximate the internal pressure of the system in three dimensions. An example of a single axial slice from one of these data sets is shown in Fig. VI.6. The resolution of the raw left hand image is decreased (right hand image) to improve the SNR of processed data.

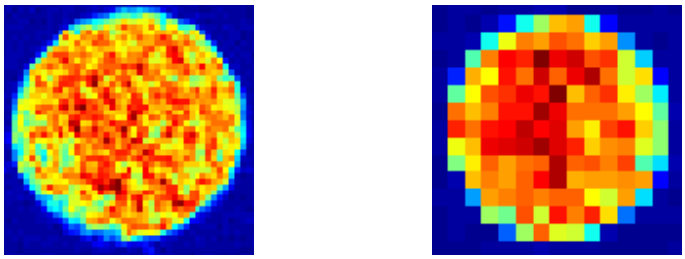

Fig. VI.6: Example images from consolidated porous media study. Left hand image is raw data collected from MRI scanner which has its spatial resolution reduced on the right hand image to improve the SNR of subsequent processing. The image is an axial slice from the centre of the consolidated porous medium.

VI.3.2 Results and Discussion

VI.3.2.1 1D Processing

An echo time of T_E = 10 ms is used here to minimise artefacts in the flowing fluid MRI. The data is averaged in both dimensions of each slice resulting in one-dimensional profiles (with a spatial resolution of 3.5mm) which are then calibrated using the static fluid data. The calculated pressure along the length of the higher permeability sample is plotted against time in Fig. VI.7.

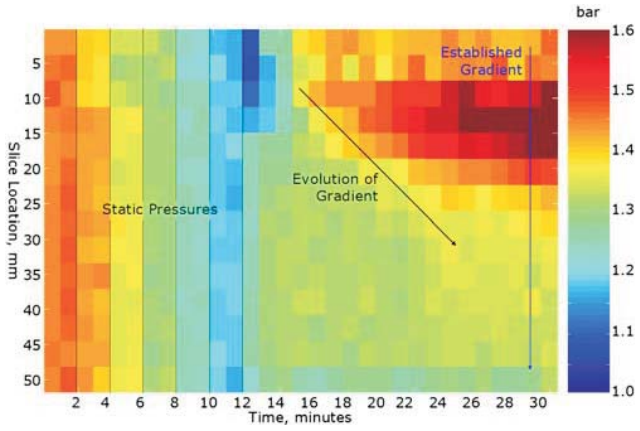

Fig. VI.7: Plot of fluid pressure in each slice against time. The data are averaged across the transverse dimensions. The inlet is located at z=0 mm and the outlet at z=50mm. The left-hand side shows the six static pressures taken for calibration purposes before the fluid was driven constantly. The diagonal line on the right-hand side shows the evolution of the pressure gradient across the porous medium. The sample used for this data has an average pore size of 95μm, which is well above the average microbubble size.

VI.3.2.2 2D Processing

Two-dimensional images for each repetition of the MSME sequence are then produced using the above method with averaging in only one dimension resulting in a spatial resolution of 2.5mm^2. Three static pressures and a flowing fluid experiment in the $40-100\mu m$ sintered glass cylinder are shown in Fig. VI.8. A separate calibration is performed pixel by pixel in these two-dimensional images to ensure that any inhomogeneities in the sample are accounted for. For the same flow rate, the maximum pressure is found to be higher than that in the previous sample, as would be expected given the smaller pore size.

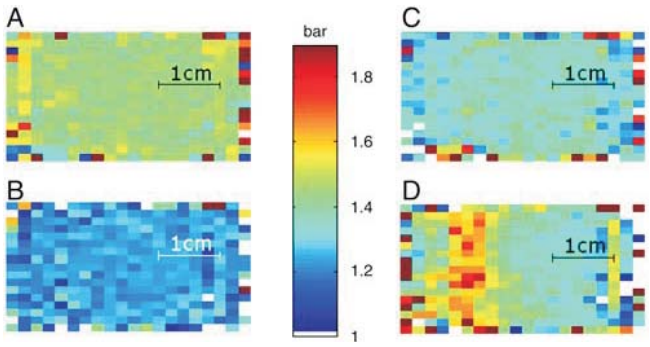

Fig. VI.8: Sagittal MRI projections of $40-100\mu m$ sintered cylinder at 1.45 (A), 1.30 (B) and 1.20 bar (C) static fluid pressures. (D) Sagittal projection of sintered cylinder experiencing fluid flow from the left (inlet) to the right (outlet) of the image demonstrating a clear gradient along the sample.

VI.3.2.3 3D Processing

Three-dimensional calibration is also performed on images with a lower spatial resolution of 1cm^3. The calibration is less accurate with a 90% confidence. A gradient can be seen to establish across the sample at approximately 0.125 bar/cm. Four images collected as the gradient develops are shown in Fig. VI.9.

VI.4 Conclusion

A contrast agent to pressure has been produced and tested with MRI. This agent has been used for measurements of the internal pressure of a sand stone like sample and has been shown to produce unrivalled sensitivity for a non-invasive pressure measurement strategy. Methods have been found and demonstrated to measure the drift in signal intensity due to microbubble advection and destruction. For the first time a three dimensional image of the internal pressure of a highly permeable consolidated porous medium has been produced and may allow for improved understanding of such a system. In combination with advanced modelling and numerical simulation, a greater appreciation of flow effects through such a system may be possible, particularly if this technique can be coupled with two phase flow measurements.

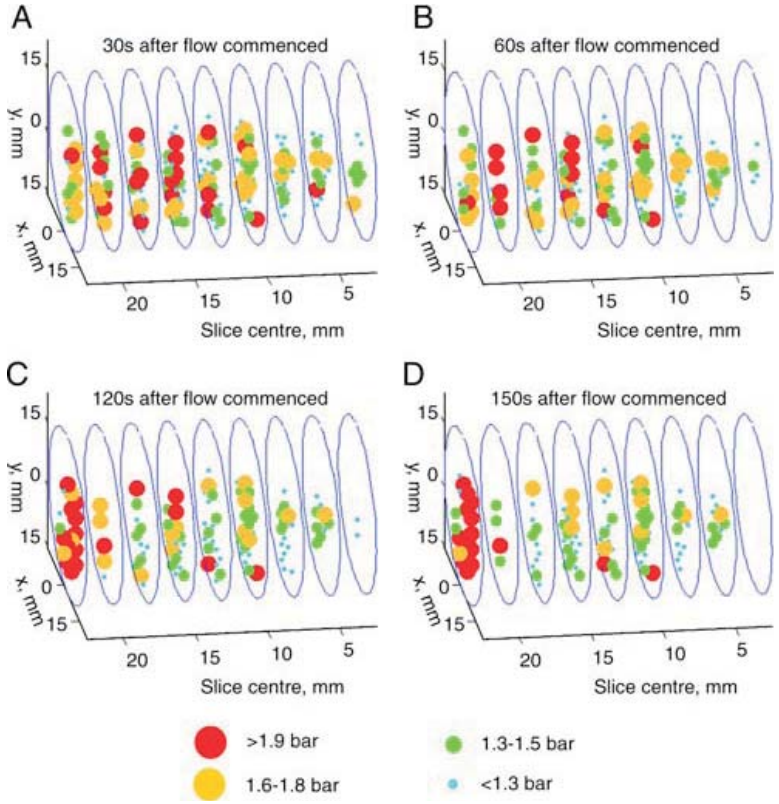

Fig. VI.9: Evolution of pressure gradient from higher pressure. Flow is from left to right. White areas represent pixels which had less than 90% confidence in calibration. (A) Majority of sample is still at high pressure. (B) and (C) the pressure at the outlet (right hand side) begins to return to atmospheric pressure. (D) The high-pressure areas are exclusively at the inlet with intermediate pressures extending towards the outlet.

VII. RARE STUDIES

Following the MSME studies shown in the previous chapter, a rapid imaging strategy was adopted. Rapid Acquisition with Relaxation Enhancement or RARE imaging was adopted to facilitate collection of images with sub second temporal resolution. This allowed for rapid assessment of novel contrast agents produced using Gellan and Carageenan gum. In order to confirm that the contrast agent was optimally designed for MRI use several alternative measurement methods were used. These include rheology to assess the viscosity of the gel in different shear conditions, novel turbidity measurements to monitor the microbubble rise which is the cause of the previously observed drift and diffusion NMR to ensure that the diffusion coefficient of water throughout the gel network is not reduced. These experiments were necessary as although MRI is one of the best methods for assessing the rise and damage of the microbubbles, it cannot be solely used to demonstrate the minimisation of drift when this is one of the contrast agent's key elements.

Experiments to test the improvements to the microbubble stability as a result of using fluorinated lipids and nitrogen gas follow the Gellan gum experiment. The stability is tested by repeatedly cycling the fluid pressure whilst running the RARE sequence. The fluorinated lipid is found to improve the stability of the microbubbles to changes in pressure and over time. A similar improvement is also seen if nitrogen gas is used instead of air in the core of the DSPC microbubbles.

Finally, the extension of the gellan gum contrast agent to a soft solid pressure sensitive medium is presented. A rig to assess the soft solids is produced in house and used alone and in combination with MRI to investigate the properties of the medium.

VII.1 Stabilised Bulk Fluid

To minimise the drift caused by the buoyant advection of the microbubbles found in the methyl cellulose preparations, the suspending fluid used for the contrast agent was further developed to allow lengthy stable measurements. Presented in this section is a novel, non-Newtonian preparation which succeeds in drastically minimising this effect whilst maintaining a high sensitivity to pressure changes using MRI. Rheometry, diffusion NMR, time lapse photography and ultra-fast MRI are used to demonstrate the improved properties of the preparation.

VII.1.1 Rheology

The most important factor affecting the stability of the measurements over time is the ability of the suspending medium to prevent buoyant advection of the microbubbles, without compromising their stability. The expected vertical rise velocity for a microbubble can be determined by equating the two opposing forces which act on it: the buoyant force,

$$F_B = \frac{4}{3}\pi R^3 \Delta\rho g, \tag{VII.1}$$

and the viscous drag on a sphere, which is given by Stokes law for the case of a low Reynolds number,

$$F_D = 6\pi\eta R v, \tag{VII.2}$$

where R is the radius of a sphere moving with velocity v through a fluid with viscosity η, g is the acceleration due to gravity and $\Delta\rho$ is the difference in mass density between the gas and the liquid. Because the lipids in the membranes of the microbubbles are in the gel state, they have a very low mobility, and they are not likely to cause additional slip at the interface between the bubble and the liquid.

Several models are available to describe the properties of non-Newtonian fluids. In the case of our study, the viscosity of pseudo-plastic fluids is described by the power law model,

$$\eta = k_2 \dot{\gamma}^{n-1}, \tag{VII.3}$$

which provides excellent correlation with the experimental data. In the previous expression $\dot{\gamma}$ is the shear rate, whilst the consistency, k_2, and the power law index, n, are two parameters that fully describe the rheological properties of the fluid. For a spherical particle moving through such a power-law fluid, the particle Reynolds number is given by [1]:

$$Re_p = \frac{\Delta\rho v^{2-n}(2R)^n}{k_2}. \tag{VII.4}$$

To estimate the maximum possible Reynolds number in the experimental system, the following worst case parameters are assumed: $\Delta\rho = 1.1 kgm^3, v = 5\times10^{-7} ms^{-1}, R = 20\mu m, n = 0.3$ and $k_2 = 10 Pas^{0.3}$. This gives a particle Reynolds number less than 5×10^{-12} which is considerably lower than values associated with a turbulent regime, corresponding to $Re_p > 1$.

According to Williams [2] the shear rate experience by a liquid through which sphere is moving with a low Reynolds number can be approximated by

$$\dot{\gamma} = \frac{v}{2R}. \tag{VII.5}$$

Sample	Consistency, k_2 (Pas^n)	Power Law Index, n (dimensionless)
Gellan Gum	4.10	0.32
Gellan Gum and Microbubbles	4.84	0.26
Gellan Gum, Microbubbles and Glycerol	3.51	0.26

Tab. VII.1: Fluid properties from samples in Fig. VII.1

Sample	Consistency, k_2 (Pas^n)	Power Law Index, n (dimensionless)
Gellan Gum	4.10	0.32
Methyl Cellulose	2.4	0.64

Tab. VII.2: Fluid properties from samples in Fig. VII.2

By equating the buoyant and drag forces, and using the worst case parameters and models mentioned previously, the terminal velocity of a sphere with a given radius can be expressed in terms of the physical properties of a given pseudo-plastic fluid:

$$v = \left[\frac{2^n R^{n+1} \Delta\rho g}{9k_2} \right]^{\frac{1}{n}}. \tag{VII.6}$$

Note that even for a 5% v/v suspension, the highest concentration explored in this work, the microbubbles are separated by more than four times their own diameter, and in consequence hydrodynamic interactions between neighbouring microbubbles can always be neglected.

The viscosity of the gel is measured at various concentrations for a range of shear rates using a TA Instruments (Delaware, USA) CSL^2 rheometer. The instrument is calibrated using Poly- DiMethylSiloxane (PDMS) oils which are available in a wide range of viscosities over which they are Newtonian. The instrument is used with a Mooney-Ewart geometry [3] tool manufactured from acrylic. The viscosity is measured for increasing and decreasing shear rates allowing the rheological properties of the gel to be studied for both a static and a flowing fluid.

The gel viscosity is then measured for three samples and is shown on Fig. VII.1. The plots show the variations in viscosity for a range of shear rates. The consistency and power law index are calculated from a log-log plot (see Fig. VII.1) as given in table VII.1. The viscosity is also measured for 2% w/v methyl cellulose (which was used in two previous studies [3,6]) for comparison to the properties of the gellan gum (see Fig. VII.2). For shear rates below $12s^{-1}$ the gellan gum's viscosity is far higher than the methyl cellulose, whilst above this value viscosities are similar within 0.25 Pas. The consistency and power law indices are given in table VII.1.

VII.1.2 Microbubble Rise Velocity

To experimentally verify that the prediction of the bubble rise velocity is representative of the practical situation, turbidity measurements of two samples, methyl cellulose and gellan gum prepared in equal concentration,

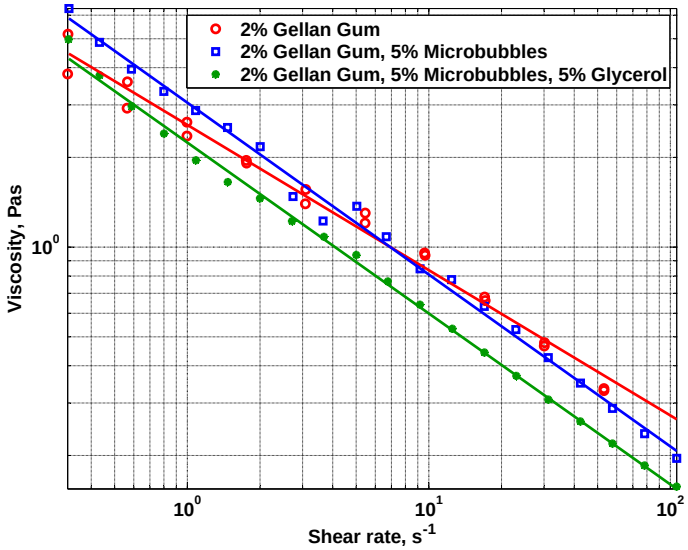

Fig. VII.1: Log-log plot of viscosity against shear rate for the three samples. The addition of glycerol and microbubbles has a small effect on the viscosity of the fluid, even at concentrations as high 5%. Adding microbubbles slightly reduces the Newtonian behaviour of the fluid (gradient) whilst the glycerol decreases the preparations overall viscosity (intercept). At low shear the viscosity of the fluids are very high with a value greater than 6 Pas. The plot demonstrates near ideal power law behaviour and allows determination of the rheological coefficients, consistency (k_2) and power law index (n).

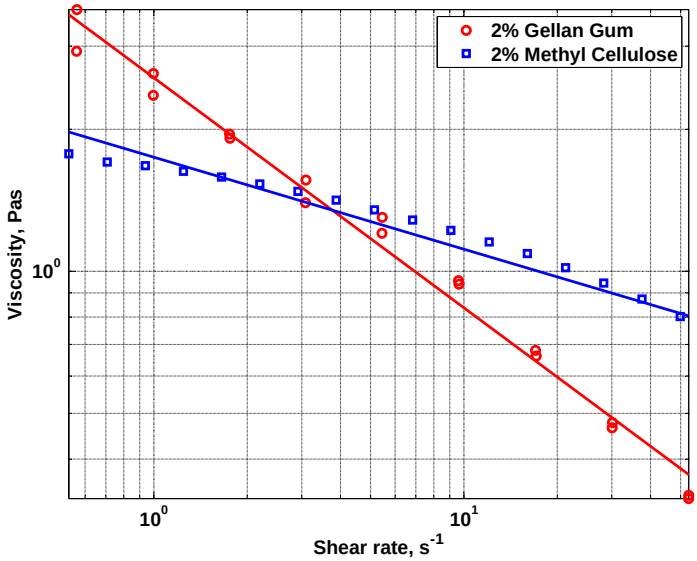

Fig. VII.2: Log-log plot of viscosity against shear rate for gellan gum and methyl cellulose both at 2% w/v demonstrating near ideal behaviour for the gellan gum whilst the methyl cellulose is considerably more Newtonian the consistency (k_2) and power law index (n) are shown in table VII.2.

is performed. The opacity of the microbubbles is sufficient that time lapse photography can be used in order to assess turbidity. The samples are photographed simultaneously every minute using an 8-bit black and white DSA Mk 10 camera (Kruss, Hamburg, Germany). In order to prevent clipping, the contrast of the images is adjusted by varying the light intensity until an image of the gels without microbubbles gives a grey value around 250, thereby warranting the smallest possible microbubbles can be observed. To facilitate simultaneous display of the collected data, the intensity across the width of each sample is averaged, providing vertical turbidity profiles each minute. These are plotted and the gradients of similar intensities calculated to determine the rise velocity of microbubbles within a specific range of sizes. These are then compared to the theoretical estimates in an attempt to validate them.

The theoretical velocities predicted for a range of microbubble sizes determined using equation VII.5 and rheology data in Fig. VII.2 are plotted in Fig. VII.3. The expected velocity for a given microbubble in methyl cellulose is predicted to be as much as three orders of magnitude faster than a similarly sized microbubble in gellan gum (e.g. for $13\mu m$ bubbles, velocities are $8\times10^{-8}ms^{-1}$ and $2\times10^{-13}ms^{-1}$ for methyl cellulose and gellan gum, respectively).

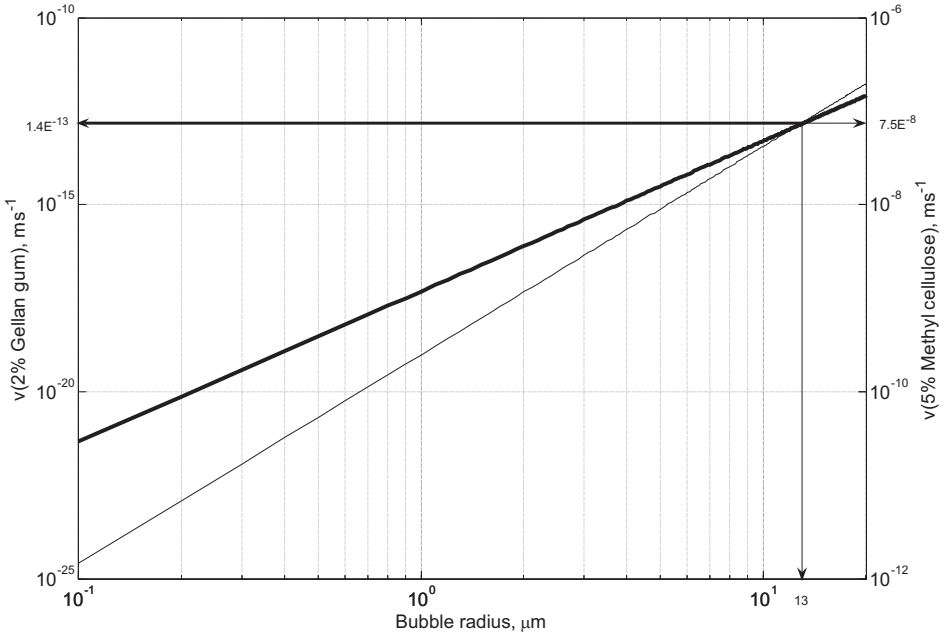

Fig. VII.3: Loglog plot of predicted rise velocity (v) for a given microbubble radius based on extrapolated rheology data (the lowest shear rate value measured in Fig. VII.1 corresponds on this graph to bubble radii of 5.43 mm and 850 μm for the gellan gum and the methyl cellulose, respectively), produced using equations VII.1 to VII.5 for comparison of two preparations.

Two images from the time lapse photography study are shown in Fig. VII.4. In order to present the data in a format which allows rapid assessment of microbubble rise velocity, vertical profiles are taken for each sample in every frame as described in the previous section. These profiles are then stacked from left to right and shown in Fig. VII.5. By following contours of similar pixel intensity, the velocity of microbubbles within a specific narrow size distribution may be estimated. These contours are shown in green on Fig. VII.5. We did not find any evidence of turbidity changes in the gellan gum for the duration of the experiment (46 hours)

which corresponds to a maximum microbubble velocity less than $1\times10^{-12}ms^{-1}$ whilst velocities ranging from $8\times10^{-8}ms^{-1}$ to $4\times10^{-7}ms^{-1}$ are found for the methyl cellulose.

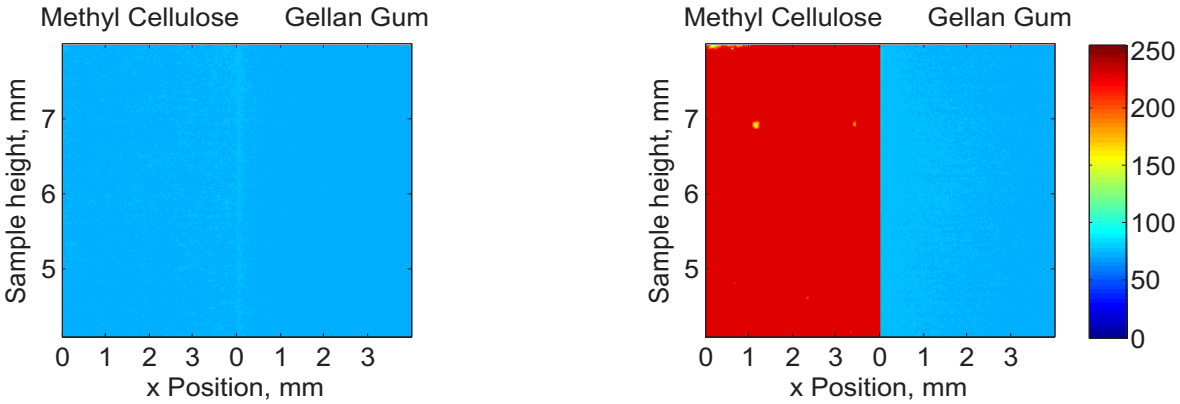

Fig. VII.4: Initial (left) and final (right) images from the time lapse study. The final image is collected 46 h after the initial image. The left hand side of each image is the methyl cellulose sample whilst the gellan gum is on the right hand side. The colour codes the intensity of light incident on the camera.

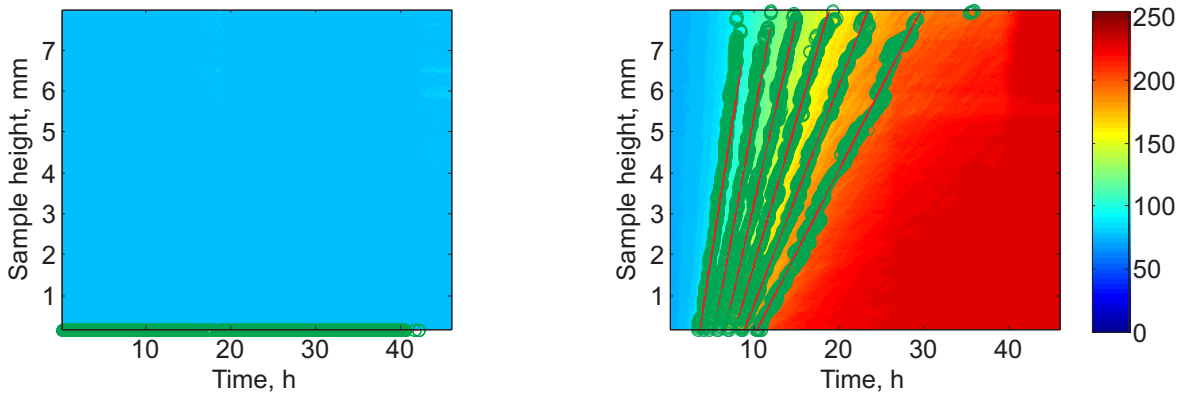

Fig. VII.5: Profile images for gellan (left) and methyl cellulose (right). The gradients which yield estimates of rise velocity are shown in green on the two images and the gradients calculated are shown as red lines. The colour codes the average intensity of light averaged over the sample width.

VII.1.3 Diffusion Measurements

The self-diffusion of water contained in the fluid is measured using a 400 MHz pulsed field gradient spectrometer at the University of Leipzig. The magnet is a wide bore 9.4 T superconducting type (Bruker, Germany) and is used with a MARAN ULTRA console (Resonance Instruments, GB) with a Direct Binary Coded Current Source [4] for gradient pulse generation, whilst the instrument is triggered at a constant mains voltage phase to avoid hum artefacts. Using a stimulated gradient echo sequence with compensation for a shift in echo position caused by imperfect gradient pulses [5], a sample volume of 0.5 ml is tested in the actively shielded anti-Helmholtz type probe at a range of temperatures for distilled water and gellan gum. These experiments allow rapid assessment of the stability of the preparation and its sensitivity to minor changes in temperature.

The diffusion measurements were conducted over a range of temperatures between 298 and 338 K. Five measurements were made for the gellan sample (with a gradient pulse separation time of 3 ms), as shown in Fig. VII.6.

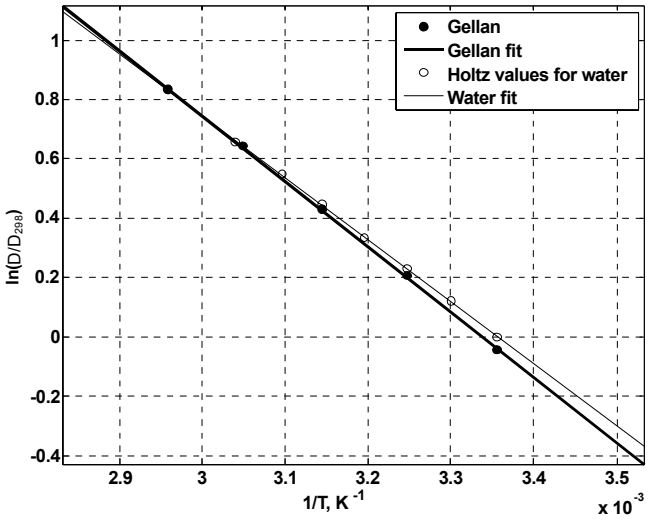

Fig. VII.6: Plot of the natural logarithm of the diffusion coefficient against the reciprocal of temperature, normalized by value of bulk water at room temperature for water and gellan gum. Correlation between samples is high implying that the majority of water in the gel sample is unrestricted by the network.

On the same figure, values for the diffusion coefficients for bulk water as found by Holz et al. [6] are plotted alongside our experimental data to demonstrate the similarity of the diffusion coefficients for gellan gum and bulk water. For the range of temperatures investigated, the diffusion coefficient of water in the gellan gum matrix is similar to that of bulk water within 7%. This plot also reveals some information with regard to the structure of the gel's dependence on temperature: The bulk viscosity increases as a result of weak binding between polysaccharide molecules which occurs around room temperature (allowing us to include microbubbles successfully in the solid gels used in section VII.3). As the temperature increases, the molecules experience little binding leading to lower viscosity and hence higher diffusion. It is for this reason that, as the temperature is increased the discrepancy between the diffusion of water molecules in the two samples becomes smaller.

VII.1.4 Preparation

Gellan gum is purchased from CP Kelco (Copenhagen) as a dry powder. In order to produce a viscous suspending medium, it must be hydrated with water. Gellan gum is a long chain polysaccharide molecule which at concentrations as low as 2% w/v produces solutions with viscosities around 10Pas (Honey has a viscosity $2-5$Pas). It is essential that no gas is introduced into the solutions except for the gas filled microbubbles. This is achieved by introducing a vacuum stage to the protocol which causes rapid expansion of any trapped gas, increasing the buoyant forces sufficiently for it to rise to the surface. The protocol for 2% gellan is as follows:

- Weigh appropriate quantity of gel powder (typically 10g)
- Add slowly to vigorously stirred room temperature distilled water (typically 500ml)
- Allow powder to dissolve, typically 2-3 hours
- Vacuum the gel at 450 torr with occasional stirring until all gas has been released, typically 8 hours

- Add microbubbles if appropriate (typically to a concentration of 3%) using a 1ml syringe and stir gently

After the samples have been prepared they are transferred to an in house designed and manufactured sample holder for scanning in the MRI scanner.

VII.1.5 Protocol

The MRI experiments are performed using a 2.35 T Biospec small animal scanner (Bruker, Germany). As the fluid is static, ultra fast imaging can be used without concern for flow artefacts. Two MRI experiments are conducted: the first is to test for the presence of microbubble advection. A single large volume of fluid is tested in a cylindrical acrylic cell (42mm internal diameter, 70 mm length) with $\frac{3}{8}$inch Swagelok tube connectors at the inlet and outlet. The pressure of this sample is then varied using a remotely (outside the 5 gauss line) connected syringe pump with two 50ml syringes whilst the RARE sequence is run. The signal intensity at each pressure is divided by the average signal intensity over all pressures. If the microbubbles experience advection during the experiment, a vertical gradient will develop in time. This is tested by plotting profiles from a single line across the centre of the sample horizontally and vertically.

The second experiment tests the stability of the MR sensitivity to pressure changes. Using a similar experimental set-up, the fluid pressure is varied between 1 and 1.3 bar whilst it is monitored and recorded using a traditional piezoelectric pressure sensor. The average signal over the sample volume is plotted alongside the recorded pressure to test for correlation between external pressure and the signal intensity. A control sample containing just gellan gum is also tested to ensure that sensitivity is indeed due to the presence of lipid coated microbubbles and not from trapped gas or other unintentional contrast mechanisms.

VII.1.6 Results and Discussion

The bulk fluid cell is filled with 2% w/v gellan gum with distilled water and 2.5% w/v microbubbles and glycerol (to aid stability) in equal concentration to test the stability to buoyant advection. The images in Fig. VII.7 show the signal intensity relative to the mean for three pressures. The high homogeneity of the images is indicative of the lack of buoyant advective motion of the microbubbles through the medium. The images are acquired using the RARE sequence with the following imaging parameters: Matrix size = 74×74; $T_E = 6.737ms$; $T_E^{\text{eff}} = 284ms$ ($0.6T_E^{\text{eff}}$); $T_R = 2462ms$ (T_2^{eff} of the sample was $424ms$). The value of T_E^{eff} was not optimised for these experiments as they were intended to demonstrate the reduction in advection whilst a sufficiently high sensitivity was observed. If the value of T_E^{eff} had been optimised and set at 636 ms, our theoretical and numerical results suggest that the sensitivity could have been as high as 96% signal change per bar.

Single pixel horizontal and vertical profiles from the central row and column of the images in Fig. VII.7 are plotted in Fig. VII.8 to demonstrate the minimization of microbubble advection. The three curves present no measurable gradient which is indicative of the absence of advective processes for the duration of the 25

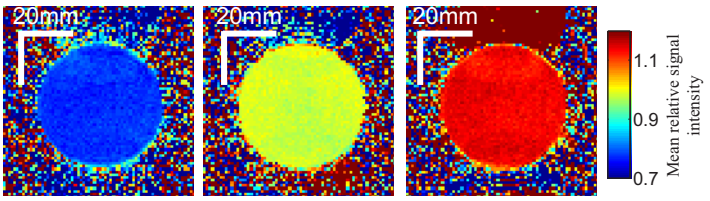

Fig. VII.7: Three MRI images taken at different pressures to demonstrate reduction in migration of microbubbles. The three images are taken at: 0.95, 1.30 and 1.44 bar (left to right, respectively).

min experiment. The standard deviations over the sample region are also calculated to allow comparison with the previous measurements in section VI.2. For pressures of 0.95, 1.30 and 1.44 bar respectively, standard deviations of 0.35, 0.3 and 0.35 percentage points are found. This shows that the stability of the preparation has improved over 20 times which suggests that this would be suitable for long term measurements in a variety of environments.

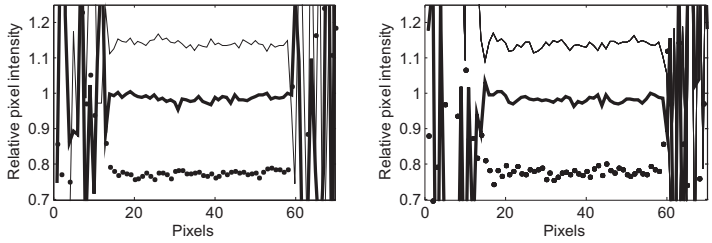

Fig. VII.8: Horizontal (left) and vertical (right) profiles taken across the centre of MRI images in Fig. 10. Broken line is for 0.95 bar, thick line for 1.3 bar and thin line for 1.44 bar.

The average signal intensity over the volume is also calculated for each scan in time and is plotted alongside the pressure measured using piezoelectric sensors. The correlation is high for a single cycle below 1.4 bar. Once the fluid experiences further cycles at such pressures or if greater pressures are used, the microbubbles rupture or coalesce and reduce the sensitivity from 38% signal change per bar to less than 10% signal change per bar (see Fig. VII.9).

VII.2 Microbubble Stability Improvements

We have demonstrated the improved performance of the contrast agent by using gellan gum as the suspending medium which has minimised drifts due to advection. The remaining cause for measurement drifts is the stability of the microbubbles to changes in pressure. In this section, stability improvements are discussed.

VII.2.1 Perfluorocarbon Gas and Lipid

The perfluoroalkylated lipid described by Gerber *et al.* [7] is produced by the group of Marie Pierre Krafft, Institut Charles Sadron (Centre National de la Recherche Scientifique) in Strasbourg, France. Microbubbles are produced by sonicating a solution containing the lipid [8] in water under perfluorohexane saturated nitrogen gas. This results in perfluorocarbonated nitrogen bubbles encapsulated by a perfluoroalkylated lipid layer, giving an ‘improved synergy between components’.

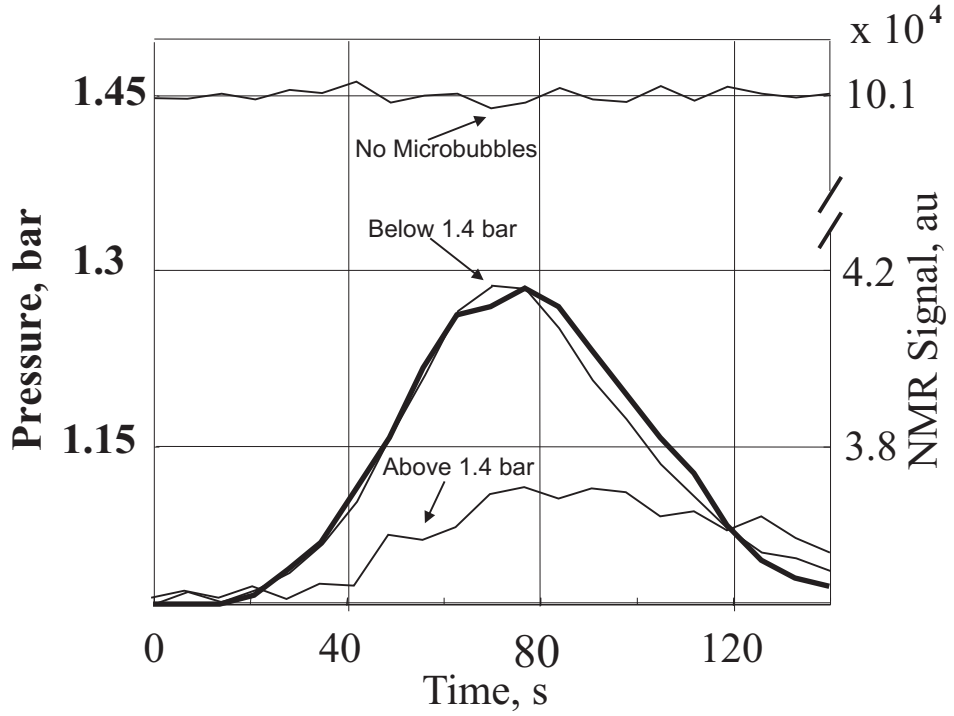

Fig. VII.9: Plot of average signal over sample volume and pressure against time. The thick curve is pressure measured with a piezoelectric pressure sensor whilst the thin curves represent the averaged signal intensity. Thin curves are: control sample containing degassed gellan gum, sample with microbubbles which have not been subjected to pressures in excess of 1.4 bar, and a sample that has experienced pressures above 1.4 bar.

The microbubbles are produced using the following protocol, kindly communicated to us by Marie Pierre Krafft:

- Lipid is produced by adding perfluoroalkyl chains to a lipid molecule [8]
- Powdered lipid is hydrated in isotonic diluent in a three neck round bottom flask
- Nitrogen gas is bubbled through perfluorohexane and into the head-space above the lipid suspension
- The gas is collected and condensed to recollect waste perfluorohexane
- The third neck provides access for a probe type sonicator which is used for 45 seconds at 20kHz to generate PFC gas microbubbles coated with a PFC lipid membrane

VII.2.1.1 Set-up

In order to test the stability of these new microbubbles to pressure and compare this to previously used preparations, a system was devised to allow simultaneous testing of three samples. This sample holder (see Fig. VII.10) is formed using stacked sheets of 6mm thick extruded acrylic. This is cut using a Hobarts 35W laser cutter and then affixed using Extrufix. It has three wells each of approximately 40ml volume, a length of 60mm and transverse cross section of 72mm (diagonally across corners) corresponding to the inner diameter of the RF coil in the small animal scanner. Each well is terminated with a Swagelok connector. The outlet and inlet pipes of the individual wells are interconnected at a distance of 100mm to avoid sample contamination whilst ensuring that the same pressure is experienced by each sample. Using this, it was possible to apply the

same pressure at the same time to DSPC, PFC and control samples whilst performing MRI. Imaging was again performed using the RARE sequence as previously detailed.

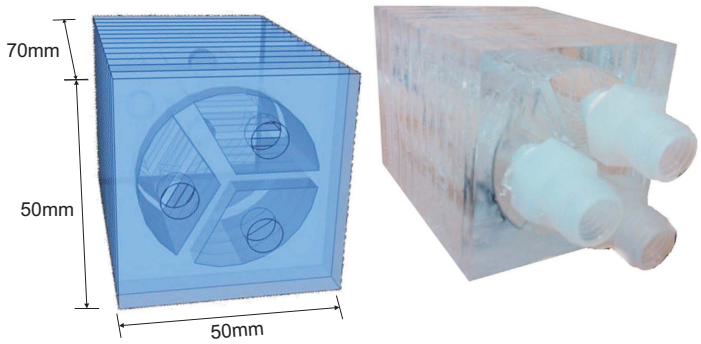

Fig. VII.10: Schematic (left) and photograph (right) of three well sample holder used to apply simultaneous pressure to three independent samples.

VII.2.1.2 Results

The results of this experiment are plotted in Fig. VII.11. The upper left figure is the raw image collected using the RARE sequence. The average over each of the collected images is shown on the upper right hand figure to demonstrate that the preparations suffer negligible drift. The lower plot is the average over each well of the sample holder plotted in time along with the pressure monitored at the inlet. By comparing the signal intensity at the start and end of each pressure cycle, the drifts due to microbubble destruction are found to be 20% signal change per bar and 5% signal change per bar for DSPC and PFC microbubbles respectively. This is a four fold improvement in stability. The PFC microbubbles withstand pressures in excess of 2 bar with minimal damage as opposed to the DSPC which are damaged at pressures above 1.4bar. This is a large improvement in stability in comparison to the DSPC and should also allow for lengthy measurements in porous media with minimal drift. This improvement in stability whilst clear, could be due to the effect of the shell or the gas and not necessarily the synergy between them. Understanding of the independent effects of the shell and gas being perfluorocarbonated require further experimentation.

VII.2.2 Nitrogen Bubbles

Having performed the previous experiment, there was clear evidence that the PFC microbubbles were considerably more robust than the other preparations. At this stage however, it appeared that too many variables had been changed on one occasion and a new, simpler experiment was therefore designed. Using the same sample holder, DSPC microbubbles filled with air, with nitrogen and a control sample (without microbubbles) are tested to see if simply the presence of a gas less soluble than air improves their robustness.

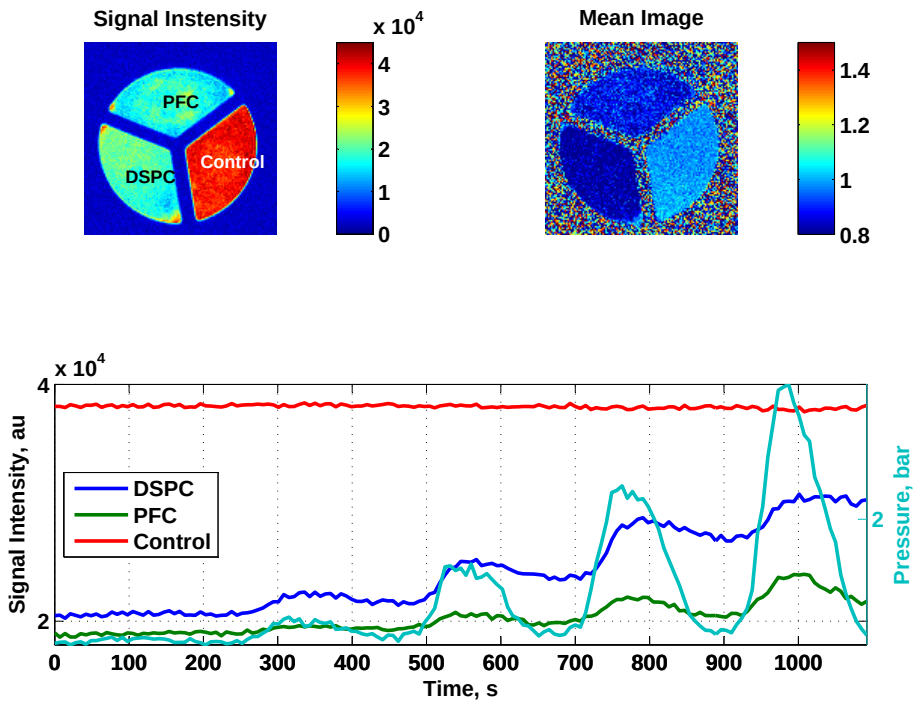

Fig. VII.11: Results of perfluoroalkylated lipid microbubble stability tests.

VII.2.2.1 Set-up

The microbubbles are produced using the original method of Vangala *et al.* although the head-space above the solution is filled with nitrogen gas for this preparation. The usual protocol is used to test the robustness of these new microbubbles.

VII.2.2.2 Results

Comparison of the signal intensity before and after the application of pressure provides an indication of the extent to which the preparation has been damaged. Although not quite as robust as the perfluorocarbonated microbubbles, the nitrogen containing DSPC microbubbles are substantially more stable to changes in pressure than the air filled microbubbles: For the initial cycle of pressure, the two preparations return to similar values to that from which they started, suggesting stable preparations. However, on each of the following cycles, the sample containing air filled microbubbles returns to a higher signal intensity due to microbubble damage. In contrast, the nitrogen filled bubbles maintain a constant sensitivity suggesting that they offer an improvement over those that are air filled. These results are shown in Fig. VII.12 for nitrogen microbubbles and air microbubbles in the usual gel preparations. The top left figure is a raw image collected using the RARE sequence. The top right figure is the mean calculated over all images in order to demonstrate the lack of spatial drift over the course of the experiment. The averaged signal intensity from each well of the sample holder is plotted in the middle figure. The pressure profile applied is shown in the lower figure. The enhanced sensitivity of the nitrogen bubbles may be due to an increased susceptibility difference due to the lack of paramagnetic oxygen present in the air filled bubbles.

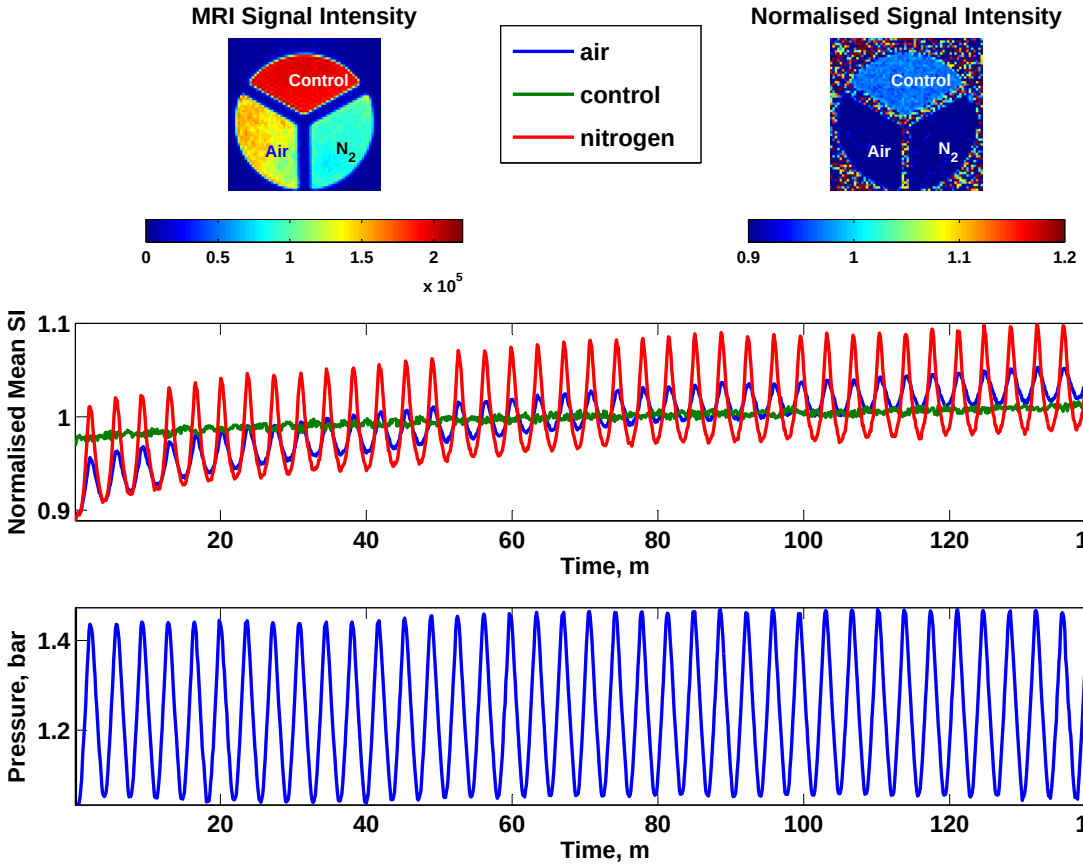

Fig. VII.12: Plot of signal intensity for DSPC encapsulated nitrogen microbubbles and DSPC encapsulated air microbubbles. The top two figures are the raw image collected from the three well sample (left) and this image divided by the mean over all images (right). The pressure applied to the sample holder is shown in the lower plot, whilst the time course of the averaged signal intensity is shown in the central plot.

The sensitivity of each cycle is determined by dividing the difference between the maximum and minimum signal intensity by the mean and dividing this by the pressure applied. These values are plotted in Fig. VII.13.

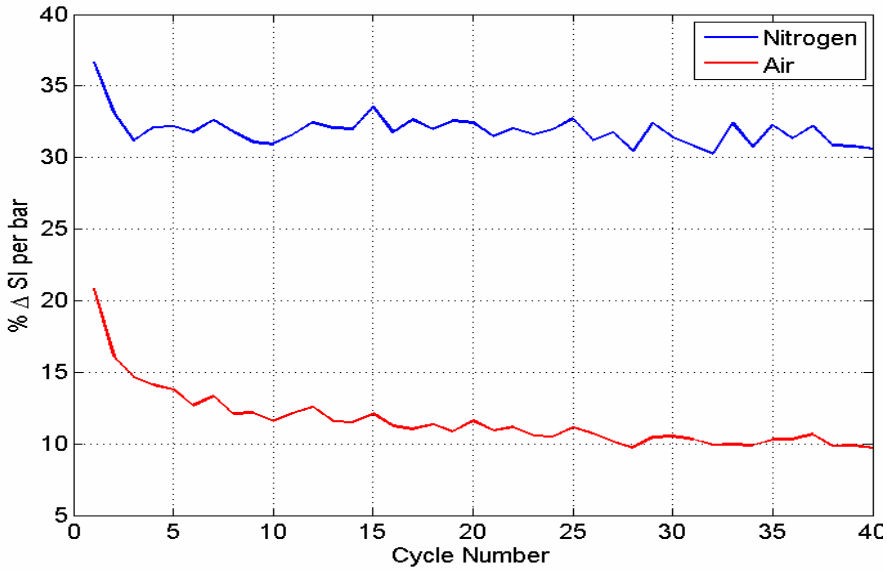

Fig. VII.13: Time course of sensitivity for variations in pressure for DSPC microbubbles containing air and nitrogen.

VII.3 Soft Solids Study

During the Magnetic Resonance in Porous Media Conference in Bologna 2006, discussions with Eiichi Fukushima (New Mexico Resonance, Alberquerque), highlighted the possibility of using our contrast agent to measure force chains in granular dynamics. The initial problem to be overcome was the fact that our contrast agent was a liquid. A method was needed to make a soft, elastic medium which could be used to suspend the microbubbles without excessively hindering the diffusion of water.

When ions (e.g from a salt solution) are added to the gellan gum solution used in the previous experiments, the molecular chains which were previously mobile become bound to each other in a process known as 'cross-linking', forming a rigid matrix at concentrations as low as 2% w/v [9]. This results in a soft solid material which maintains a high diffusion of water whilst exhibiting the macroscopic properties of an elastic solid. Optimum soft solids are produced from gellan gum when calcium chloride is added [9]. Unfortunately however, cross linked gellan gum suffers from high syneresis and poor elasticity which results in loss of structural integrity and consequently temporally unstable pressure measurements. By comparing the theoretical properties of a range of polysaccharides, it was found that iota carageenan gum yields elastic gels with low syneresis and a high breaking strength, whilst still maintaining relatively unhindered water diffusion within their structure. The suitability of this material as an MR pressure and stress contrast agent is assessed by measuring its water diffusion coefficient, its elastic properties and MRI results are discussed in the next sections.

VII.3.1 Elasticity

It is essential to produce an elastic semi solid to allow reversible measurements. When deformed, the samples should ideally return to their initial shape and location. The elasticity of our samples is too great to be measured reliably with oscillation or creep rheology methods (which require some viscous component). Instead, photography of the samples is performed before, during and after a known compression. In order to apply this compression reliably to each sample, a test rig was produced in house which would allow a known pressure to be applied to one or more gel samples. The results of this experiment are shown in Fig. VII.14 which shows images captured during and after a compression cycle. The height of the sample after a given compression, relative to its initial intact height is calculated as a percentage and displayed as a function of the compression applied, giving an approximate measure of the elasticity of the samples (Fig. VII.14). This allowed assessment of elasticity without an expensive compressional testing rig. These results show that the carageenan gum is perfectly elastic for deformations up to 5mm, or 15% total height, after which it starts to deform at 0.4% per mm displacement. In contrast, the gellan does not fully return to its initial shape after any deformation, and presents approximately 3.2% deformation per mm displacement. The gellan gum therefore shows little promise as a suitable semi solid material, unlike the carageenan.

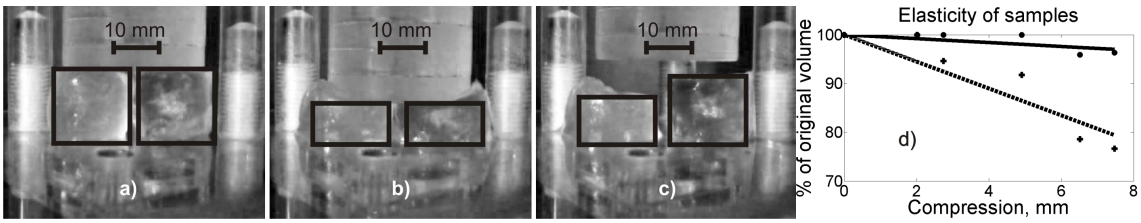

Fig. VII.14: Photographs of gellan (left) and carageenan (right) samples at a) rest, b) during and c) after deformation. The black outlines mark the borders of each sample. d) The percentage of the original height is plotted against the displacement applied as an indicator of the elasticity of the samples as circles and solid line (carageenan) and dashed line and crosses (gellan).

VII.3.2 Diffusion of Water

The diffusion of water within the structure of the carageenan and gellan gums is key to the sensitivity of the contrast agent. To ensure that it remains similar to that of bulk water, it is assessed using the profile NMR MOUSE® with the Carr Purcell sequence [10] and the help of Petrik Galvosas of the University of Leipzig, Germany [11]. Fig. VII.16 shows our MOUSE® Hahn echo amplitude results for water and cross linked carageenan gum for increasing echo time.

Although the diffusion coefficient is found to be 83% of that of bulk water as opposed to the 93% of bulk water in gellan gum, the compromise between reduced diffusion and enhanced elasticity still results in an excellent material, as is demonstrated in this section. The diffusion constant in crossed-linked gellan gum ($1.8\times10^{-9}m^2s^{-1}$) is similar to that for the cross linked carageenan gum ($1.79\times10^{-9}m^2s^{-1}$) and thus the soft solid should not present greatly reduced sensitivity.

VII.3.3 Preparation and Protocol

Both polysaccharide gels were purchased in the form of dry powders from CP Kelco (Atlanta, USA). In order to produce a semi solid, a multi-stage process must be followed:

- The powders are hydrated with water to a 2% w/v solution by stirring under vacuum to prevent inclusion of gas
- The gellan gum is homogeneous after approximately 3 hours stirring whilst the carageenan gum requires a heating step to 85°C for gelling to occur (it is allowed to cool back to room temperature inducing gelling).
- Half of the produced gels are used for control samples and half for test samples containing microbubbles
- Inclusion of the microbubbles [12] into the gels is achieved by gentle stirring, at room temperature in the case of the gellan gum, and at 35°C during the cooling period of the carageenan as it becomes too viscous after this point
- The further introduction of a salt yields different material properties for each gel. Calcium chloride is used for the gellan gum and potassium chloride for the carageenan.
- Centrifuge tubes (1.5 ml) are used as a mould to produce the semi solids.
- A sample of 1ml of the chosen preparation is inserted and the tube further filled (to a total volume of 1.5 ml) with the appropriate salt solution, at a concentration of 20% w/v.
- The tubes are left overnight to ensure that homogeneous cross linking occurs.
- The solid gel samples are removed as small cones, the projection of which looks like an elongated triangle (Figs. VII.16 and VII.17)

In order to apply an external force to the sample located within the bore of the magnet, a custom sample holder assembly was produced in house which uses hydraulic pressure applied by the syringe pump (same as used previously) to force the samples against a rear plate (see Fig. VII.15).
Control and test samples are placed side by side in the holder and held loosely with the hydraulic pressure whilst it is placed in the bore of the magnet. Three experiments are performed to assess the properties of the carageenan solids. In the first and second experiments the control and test samples are respectively compressed to 40% (Fig. VII.16) and 72% of their original volume, whilst in the third experiment the reversibility of the samples is assessed by compressing and then releasing the control and test samples with increasing total compression (Fig. VII.17). By averaging over the areas of each of these samples it is possible to plot their integrated MR intensities. The intensity of the control sample decreases linearly with sample thickness and by dividing the average of the test samples by that of the control samples, the effect due to the presence of microbubbles during compression can be assessed without partial volume artefacts.

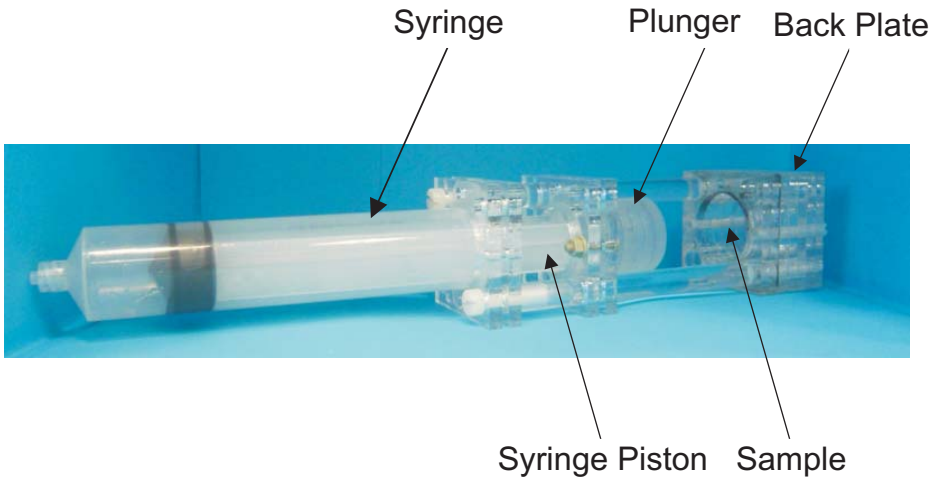

Fig. VII.15: Labelled photograph of the soft solids sample holder. The syringe is used to apply pressure to the piston which crushes the soft solids against the back plate.

.

The RARE [13] sequence is configured as in the previous section and used to assess the samples on the 2.35 T Bruker Biospec MRI scanner. This sequence facilitates a high temporal resolution whilst maintaining reasonably high spatial resolution and is ideal for static sample imaging. A spatial resolution of 1.1mm^2 and temporal resolution of seven seconds were used to ensure that most of the magnetization has returned to rest. The echo time is set to 8.737 ms, corresponding to an effective echo time of 279.6 ms for a single shot RARE image with a 64×64 matrix. Having manually produced masks for each of the images, the averages over each sample are calculated and plotted against the compression applied.

VII.3.4 Results

The diffusion curves collected using the NMR MOUSE are shown in Fig. VII.16 along with the fits to allow determination of the diffusion coefficients. Of the two gels explored, only the carageenan gum is suitable, with high water diffusion and high gel elasticity. Since the diffusion coefficient of water in the carageenan gum is 83% of that of bulk water, our solid should suffer less than 0.5% reduction of MR sensitivity to changes in pressure. Both solid samples were prepared as controls and with 3% v/v microbubbles. The MR signal ratio between the intact control and intact test samples were all found to exhibit differences of 20% or greater, which further demonstrates that susceptibility induced spin dephasing is the origin of our sensitivity, rather than spin density.

Because both the control and test samples exhibit the same partial volume relative to the MR selected slice, the partial volume effect of the test can be compensated for. The first MRI experiment (Fig. VII.17) demonstrates that the division of the test signal intensity by that of the control does indeed provide a sensitivity to the applied pressure, and that very large sample deformation is required to destroy the bubbles (i.e. sensitivity = 0, or ratio of signals = 1).

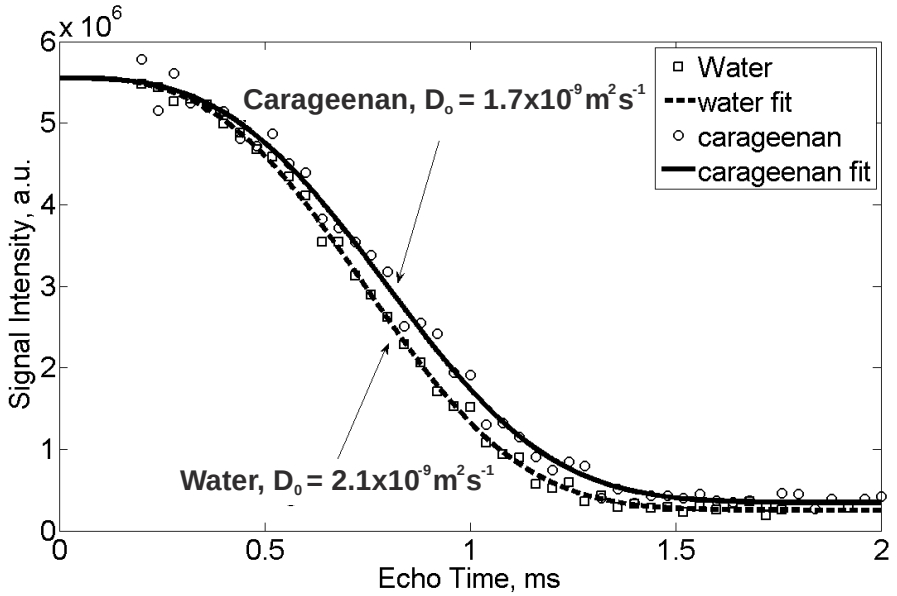

Fig. VII.16: Proton diffusion measurements of bulk water (squares and dotted line), and carageenan gum (circles and solid line). The amplitudes of both curves are scaled to be similar to compensate for differences in sample size and water content. The repetition time was set to 4.6s (corresponding to $1.2 \times T_1$ of water), each point represents 256 averages. The temperature was $(21 \pm 1)^{\circ}$C

.

The quoted sensitivities are sufficiently high to produce useful measurements from a compression resulting in up to a 15% volume change, which is repeatable using this gel. The sensitivity could possibly be improved by increasing the volume of gas in the samples or by using ultra high field MRI.

In Fig. VII.17 the periodic signal changes are shown to follow the applied compression well, with a slight phase lag due to imperfect securing of the syringe in the pump. A sensitivity of 1.69% signal change per % volume change is found in this experiment for a maximum compression of 44% volume. It can be seen in Fig. VII.17 that some bubble damage in the gel has occurred, as the signal does not return completely to the starting value after large compressions.

A higher range of forces may be observable by improving the elasticity of the semi solid, resulting in a contrast agent suitable for use in many diverse chemical engineering applications. Recently developed alternative bubble preparations have been shown [7] to better resist deformations, and could be used in future work with minor modifications to the protocol.

In Fig. VII.18 the periodic signal changes (broken lines) are shown to follow the applied compression (solid line) well, with a slight phase lag due to inadequate securing of the syringe in the pump. A sensitivity of 1.6% signal change per % volume change is found in this experiment for a maximum compression of 44% volume. The signal does not return completely to the starting value after large compressions, which could be due both to microbubble damage and the imperfect securing of the syringe.

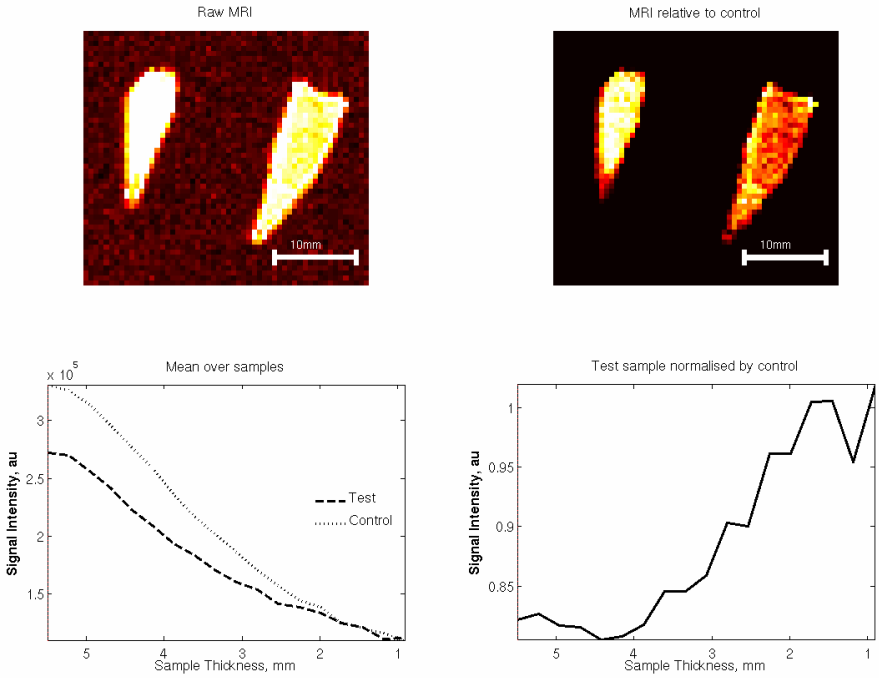

Fig. VII.17: Experiment that explores the effect of a maximum compression of 40% of original volume. The intensity percentage difference between control (left hand sample in image) and test (right hand sample in image) samples is 20%. Sensitivities of 0.22% signal change per % volume change is found for this particular experiment.

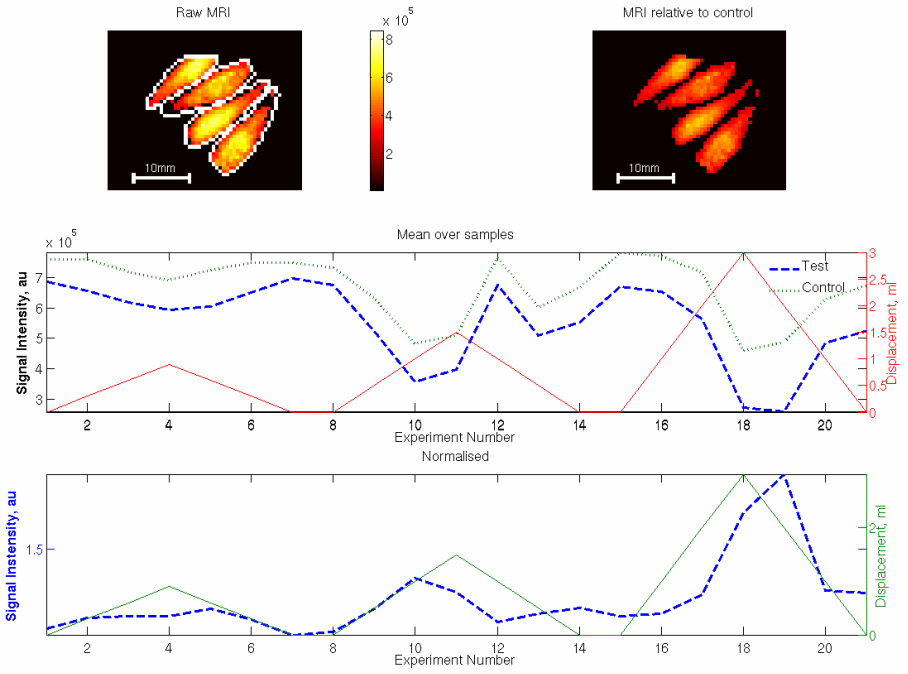

Fig. VII.18: Results from the third experiment to test the reversibility of the system. The compression applied to the samples (from left to right in image: test, control, test, control) is incremented for each cycle to observe the return to rest condition. Reasonable agreement is seen with a minor phase lag. The initial difference between the signal intensities is 45% and the overall sensitivity is 1.69% signal change per % volume change.

VII.4 Conclusion

Through a combination of MRI and several other measurement techniques, contrast agents to pressure have been created in a fluid and soft-solid phase. These contrast agents have been heavily optimised in terms of their stability both in time and to damage and to ensure that they offer sufficiently high sensitivity for practical measurements. By investigating different shell materials and gaseous components for the microbubbles, preparations which demonstrate high levels of stability and sensitivity have been produced. Appropriate suspending media have been found and protocols for assessing their performance and production have been developed. This has allowed the creation of several contrast agents which can be specifically tailored to a given application and will hopefully be applied to novel systems in the future.

References

[1] O. Reynolds, "An experimental investigation of the circumstances which determine whether the motion of water shall be direct or sinuous, and of the law of resistance in parallel channels," *Philosophical Transactions of the Royal Society of London*, vol. 174, pp. 935–982, 1883.

[2] P. Williams and G. Phillips, *Gums and Stabilisers for the Food Industry*, vol. 11. Royal Society of Chemistry, 2002.

[3] M. Mooney and R. H. Ewart, "The conicylindrical viscometer," *Physics*, vol. 5, no. 11, pp. 350–354, 1934.

[4] P. Galvosas, F. Stallmach, G. Seiffert, J. Karger, U. Kaess, and G. Majer, "Generation and application of ultra-high-intensity magnetic field gradient pulses for NMR spectroscopy," *Journal of Magnetic Resonance*, vol. 151, no. 2, pp. 260–268, 2001.

[5] P. Galvosas, F. Stallmach, J. Karger, and Tu, "Background gradient suppression in stimulated echo NMR diffusion studies using magic pulsed field gradient ratios," *Journal of Magnetic Resonance*, vol. 166, no. 2, pp. 164–173, 2004.

[6] M. Holz, S. R. Heil, A. Sacco, and Hl, "Temperature-dependent self-diffusion coefficients of water and six selected molecular liquids for calibration in accurate H-1 NMR PFG measurements," *Physical Chemistry Chemical Physics*, vol. 2, no. 20, pp. 4740–4742, 2000.

[7] F. Gerber, M. Krafft, G. Waton, and T. Vandamme, "Microbubbles with exceptionally long life - synergy between shell and internal phase components," *New Journal of Chemistry*, vol. 30, no. 4, pp. 524–527, 2006.

[8] C. Santaella, P. Vierling, and J. G. Riess, "New perfluoroalkylated phospholipids as injectable surfactants - synthesis, preliminary physicochemical and biocompatibility data," *New Journal of Chemistry*, vol. 15, no. 8–9, pp. 685–692, 1991.

[9] C.P. Celko, *Kelcogel Gellan Gum Book*. Atlanta: CP Celko, 2007.

[10] H. Y. Carr and E. M. Purcell, "Effects of diffusion on free precession in nuclear magnetic resonance experiments," *Phys. Rev.*, vol. 94, pp. 630–638, May 1954.

[11] R. Morris, M. Bencsik, N. Nestle, P. Galvosas, D. Fairhurst, A. Vangala, Y. Perrie, and G. McHale, "Robust spatially resolved pressure measurements using MRI with novel buoyant-advection free preparations of stable microbubbles in polysaccharide gels," 2008.

[12] A. Vangala, G. Kalkat, and Y. Perrie, "Application of gas-filled liposomes as pressure probes for oil extraction: a novel and simple preparation technique," *Journal of Pharmacy and Pharmacology*, vol. 58, pp. A41–A41, 2006.

[13] J. Hennig, A. Nauerth, and H. Friedburg, “RARE imaging - a fast imaging method for clinical MR,” *Magnetic Resonance In Medicine*, vol. 3, no. 6, pp. 823–833, 1986.

VIII. SUMMARY

The experimental work presented in this thesis has demonstrated several techniques to measure pressure in liquids gels and soft solids. Through continual development, the original method proposed by Alexander in 1996 [1] has been adapted and improved to allow these experiments to take place. The primary issue was the rapid advective motion of the microbubbles upwards through the sample under test due to their buoyancy and the low viscosity of the suspending media. This has been overcome in this work by using novel preparations of polysaccharide gels which have been assessed in terms of their rheological behaviour both with and without microbubbles. The liquid work has been adapted to meet alternative application requirements, namely force chain imaging in granular dynamics. This was possible by exploiting the properties of the polysaccharide gels allowing rapid gelling to a semi-solid state using a salt matched to the particular gel.

The experimental work has led to three peer reviewed publications as first author and two as second (with a third in press), six conference presentations both oral and poster based, four of which were international. This is responsible for much of the development of the work as it has allowed us to build collaborative links to allow work for which we are either ill equipped or not sufficiently knowledgeable. In fact the initial basis of this work came about as a result of Dharmakumar's presentation at an ISMRM conference.

The common difficulties encountered with all of the measurements regardless of the suspending medium or the lipid chosen for the microbubbles are the stability over pressure and the polydisperse nature of the microbubbles produced. Possible solutions exist in the form of microfluidic production devices and indeed polymer coated microbubbles may yield more stable monodisperse preparations. It was however outside the scope of this work to create such devices.

With some further work this project still has much scope to bring this somewhat unexplored field to the forefront of MRI imaging techniques exploited for fundamental fluid flow measurements, and for subsequent applications to oil recovery. Additionally, if we were able to enhance the susceptibility of the microbubble shells by including SPIOs, the technique could be applied once more to the medical application for which it was originally conceived.

References

[1] A. Alexander, T. McCreery, T. Barrette, A. Gmitro, and E. Unger, "Microbubbles as novel pressure-sensitive MR contrast agents," *Magnetic Resonance In Medicine*, vol. 35, no. 6, pp. 801–806, 1996.

IX. FURTHER WORK - POROUS SILICA

Following a presentation at an internal conference in 2007, a discussion with Paul Roach formerly of Nottingham Trent University highlighted the possibility of hysteresis free pressure measurements using porous silica microbeads. The preliminary work is presented in this section, although the initial experiments were unsuccessful, as the technique has great potential with a little further development.

Nanoporous silica beads are used commonly as a packing material for chromatography columns. It is possible to control the properties of these particles, including their overall diameter, the pore size distribution, the pore connectivity and any coatings which may be applied to their surface to aid chemical separation. For this work, a bead of uniform radius with a large pore volume and highly interconnected pores as possible is desired. It should have a hydrophobic coating within the porous network. With this set-up, when suspended in a water based medium, the pore space should remain filled with air whilst the particles are surrounded by water. When an external pressure is applied, the surrounding water will be somewhat driven into the pores as the gas is compressed and the hydrophobicity overcome. This will result in a small change in the resulting radius of the spherical air volume trapped in the bead which will generate NMR contrast to pressure.

IX.0.1 Beads

The nanoporous beads can be produced using a number of methods. Each of these processes involves the production of some sort of template [1–3], around which the silica can be grown. It was decided to purchase a particular commercial bead produced for use in chromatography columns. After extensive searching, a suitable product was found although it is expensive at over £250 for less than 1g (~ 0.25ml). The beads have an average pore diameter of around 100nm and an overall diameter of $1\mu m$. They are purchased already coated to have a hydrophobic surface and should function successfully with no additional modification.

The beads are challenging to suspend in aqueous media, possibly as a result of their hydrophobicity. Even after 20 minutes sonication, they are still visible on the surface of the medium. Sonication for a further 3 hours with intermittent vigorous shaking resulted in a homogeneous preparation although this may be because the hydrophobic coating had become ineffective.

IX.0.2 Experimental

In order to overcome the hydrophobic coating on the nanoporous beads allowing ingress of water, large pressures are required. With this in mind, the system for application and monitoring of pressure needed some redesign. The syringe pump is only capable of supplying pressures up to 2.5 bar before it stalls so a High Pressure Liquid Chromatography (HPLC) pump capable of supplying in excess of 100 bars (Gilson 807, Gilson, Wisconsin, USA) is chosen. Although the pump has an internal pressure sensor, the resolution is only 1 bar. To improve this, an old HPLC pressure sensor module is modified to allow direct monitoring of the sensor output using the USB-6009 National Instruments data logging unit and laptop PC. This gives a resolution of 100mbar which is considerably more suitable for these measurements.

A two compartment sample holder (see Fig. IX.1) was constructed so that the two samples experience the same pressure, and are aligned along the z axis, so both samples are best distinguished with coronal imaging. The two samples are back to back so that the central disc of perspex experiences no pressure. As one of the weakest areas of the sample holder minimising this pressure prevents damage. In order to ensure that the scanner is not affected by a loss of integrity in the sample holder, it is tested to sixty bars. The sample holder remains in tact and no damage is observable. The samples will be tested at pressures less than 35 bars to ensure continued integrity.

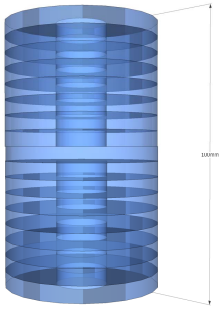

Fig. IX.1: Schematic of two well sample cell.

The samples are scanned using coronal RARE on a vertical bore $7T$ scanner system (to which Walter Köckenberger kindly provided us access). The two samples are connected with $2m$ lengths of pipe to a 'T' piece outside the magnet so that they both experience the exact same pressure with the same lag. This is then connected to the pump and sensor outside the 5 gauss line.

IX.0.3 Results and Discussion

With subtraction of images, even between 30 and 1 bar, there is no measurable signal intensity change in either the test or control sample. At 30 bars, solid glass beads would have been crushed [4], as would have been the case if they were not filled with water. If the beads had remained air filled, crushing them would have had a minor effect on the susceptibility difference and hence presented a change in signal intensity. As this was not the case, the evidence suggests that during sonication, the gas had been replaced by liquid. These results,

though disappointing, are a good indicator that the process used for degassing the control samples is highly efficient and that there is no trapped gas remaining within their volume.

The highly monodisperse nature of the particles would make this an ideal medium for validation of the theoretical and simulated optimum setting of the echo time for the rapid imaging protocol. The difficulties encountered when using the porous silica beads are most likely due to the inclusion protocol. By developing this further, a procedure which does not include a sonication step may allow a high pressure contrast agent to be produced. This may be possible by stirring the preparation vigorously in a medium which becomes rapidly viscous in the presence of a salt, such as the carageenan gum, whilst the appropriate salt is slowly added. This should in principle lead to successful trapping of the beads.

References

[1] H. X. Guo, X. P. Zhao, H. L. Guo, and Q. Zhao, "Preparation of porous SiO2/Ni/TiO2 multicoated microspheres responsive to electric and magnetic fields," *Langmuir*, vol. 19, no. 23, pp. 9799–9803, 2003.

[2] U. Meyer, A. Larsson, H. P. Hentze, and R. A. Caruso, "Templating of porous polymeric beads to form porous silica and titania spheres," *Advanced Materials*, vol. 14, no. 23, pp. 1768–176+, 2002.

[3] A. M. Yu, Y. J. Wang, E. Barlow, and F. Caruso, "Mesoporous silica particles as templates for preparing enzyme-loaded biocompatible microcapsules," *Advanced Materials*, vol. 17, no. 14, pp. 1737–173+, 2005.

[4] M. Bencsik. personal communication, 2008.

APPENDIX

A. MATLAB SIMULATION CODE

The basis of the simulation of the CPMG sequence in the presence of a microbubble has been extensively optimised to allow a simulation of 20 echoes to run in under a minute on a modest PC. The code is included here (Figs. A.1 - A.2) as an appendix given the extent of optimisation, the time dedicated to producing it, and the usefulness which it will present should someone care to continue this work.

```
%Random walk for N_a protons in N_dimensions dimensions with calculation
%of magnetisation as a result of field perturbations caused by the presence
%of a microbubble:
%
%function accepts one inputs returning three outputs and a plot:
%
%[M_t, position_phase, time]=CPMG_Bubble_fast(R_0)
%
%OUTPUTS
%   M_t:            Magnetisation against t/delta_t -- N_steps x 1 matrix
%
%   position_phase:  Positions and phases of protons -- N_a x 4 matrix
%                    (columns 1-3 are x, y and z, column 4 is phase)
%
%   time:           Total run time of simulation
%
%INPUTS
%   R_0:            Radius of Microbubble
%
%
%Written by Robert Morris, Nottingham Trent University
%
% version 3
% November 2005

function [M_t, locArray, tt, T_E, N_echos, t_axis]=CPMG_Bubble_Fast(R_I)
%Some parameters:

tic;
   %define global variable
   global N_dimensions N_a D delta_t Block_size R_0 universe_length gamma B_0 delta_chi N_echos u_n u_p t_axis gap

   %Number of dimensions
    N_dimensions = 3;

   %number of protons
    N_a=1E4; %protons

   %Diffusion Coefficient:
    D=2.75E-9;

   %Time step
   delta_t=1E-6; %s


   %Block size:
    Block_size=sqrt(6*D*delta_t); %metres

   %Bubble size (diameter), now as input with V3
   R_0=R_I;

   %gyromagnetic ratio
    gamma=26.75E7; %rad.s^-1.T^-1

   %B field strength
    B_0=1; %Tesla

   %Difference in susceptibility
    delta_chi=BDchi;

   %Echo time
    T_E=6E-3;

   %number of echos in train
    N_echos=5;

   %number of steps
   %N_steps=20;
    N_steps=(round(T_E/delta_t));

   %Total number of points for which magnetisation is calculated
   pmax=N_steps+round((N_steps*N_echos));

   %factor allowing: t_FID = 1/2 t_echo
   gap=0.5*N_steps;

   %Create a real time scale for plots
   t_axis=delta_t*((1:pmax)-1); %s

   %define bubble density fraction
   n=7;

%predefine storage for location and phase information
   locArray=zeros(N_a, N_dimensions+1);

% used to calculate size of universe for 2% perturbation at edge
%    universe_length=R_0*((50)^(1/3))
% now we calculate universe length to produce desired density
   %universe_length=n*R_0;
   universe_length=2*(sqrt(2*D*T_E)+20*R_0);

   %define some more parameters
      %half universe sizes positive and negative, centre of universe = 0
      u_n=-1/2*universe_length;
      u_p=1/2*universe_length;

%begin calculations

   %define starting points for protons: randomly distributed integer
   %between -N and N, where 2N is the number of cells spanning one
   %dimension of the Universe
   %system phase =0
   'FID'
      for ai=1:1:N_a
            locArray(ai, 1) = round((0.5*universe_length*((rand-0.5)*2))/Block_size);
            locArray(ai, 2) = round((0.5*universe_length*((rand-0.5)*2))/Block_size);
```

Fig. A.1: Matlab code for microbubble simulation page 1

```
            locArray(ai, 3) = round((0.5*universe_length*((rand-0.5)*2))/Block_size);
        end

    %start with FID
%           [locArray, M_t]=stepfrom(locArray, zeros((N_steps*(N_echos+1)), 1), 1, (0.5*T_E));
        [locArray, M_t]=stepfrom(locArray, zeros((N_steps*N_echos)+gap, 1), 1, (0.5*T_E));

    %apply train of CPMG pulses
        for npi=1:1:N_echos
            ['Echo number = ', num2str(npi)]
            locArray(:,N_dimensions+1) = -locArray(:,N_dimensions+1);
            [locArray, M_t] = stepfrom(locArray, M_t, npi, T_E);
        end
        toc;
        tt=toc
%-------------------------------------------------------------------------
%function steps in presence of microbuble field from positions and phases
%defined in locArray and history in M_t
function [locArray_CPMG_out, M_t_CPMG_out]=stepfrom(locArray, M_t, npi, T_E);

    %define global variable
        global N_dimensions N_a D delta_t Block_size R_0 universe_length gamma B_0 delta_chi N_echos u_n u_p pmax t_axis gap

N_steps=(round(T_E/delta_t)) ;

    %begin stepping
        %run movement
        for steps=1:1:N_steps
            %generate continuous index
                place = steps + N_steps*npi - gap;
            %calculate new position of each proton
                %generate direction of proton motion
                    direction = round(rand(N_a, 1));
                    direction(find(direction == 0)) = -1;

                    %generate plane of motion
                        p_axis = 1 + round(3*rand(N_a, 1) - 0.49999999999);

                    %move the protons as determined above
                        for dim=1:3
                            locArray(find(p_axis == dim), dim) = locArray(find(p_axis == dim), dim) + direction(find(p_axis == dim));
                        end

                % Here we find out those protons that have penetrated the
                % bubble:
                [theta, phi, r_coordinate] = cart2sph(Block_size*locArray(:,1), Block_size*locArray(:,2), Block_size*locArray(:,3));
                fix_index = find(r_coordinate < R_0);
                % We fix their random motion so that they remain outside
                % the gas bubble:
                [x, y, z]=sph2cart(theta(fix_index), phi(fix_index), R_0);
                locArray(fix_index, 1:3)=round(1/Block_size*[x, y, z]);

                %Check the locations of the protons to ensure they are not
            %outside the universe

                %Take modulus of proton locations
                mod_xyz=[abs(Block_size*locArray(:,1)), abs(Block_size*locArray(:,2)), abs(Block_size*locArray(:,3))];

                %Check each dimension, returning protons which have left to
                %an equal distance inside the universe
                    for dim = 1:3
                        fix_indexx = find(mod_xyz(:,dim) > u_p);
                        locArray(fix_indexx, dim) = locArray(fix_indexx, dim) - 2*direction(fix_indexx);
                    end

                %calculate angle from bubble to each proton(cartesian to spherical)
                [theta, phi, r]=cart2sph(Block_size*locArray(:, 1), Block_size*locArray(:, 2), Block_size*locArray(:, 3));
                    %calculate field experienced by each proton
                    delta_B=Pert_r(theta, r, B_0, delta_chi, R_0);

            %calculate phase of proton and store result
                locArray(:, N_dimensions+1) = locArray(:, N_dimensions+1) + gamma*delta_B(:)*delta_t;
            %calculate magnetisation using new phase for CPMG
                M_t(place)=(1/N_a)*abs(sum(exp(i*locArray(:, N_dimensions+1))));
            %plot magnetisation
%               plot(M_t, 'g')
                %add title to plot
 %                  title('magnetisation')
                %allow time for the dsplay to update
 %                  pause(0.0001)

        end

            %output data to function
            locArray_CPMG_out=locArray;
            M_t_CPMG_out=M_t;
        place;

%-------------------------------------------------------------------------
%function to produce value of perturbation at position r away from bubble centre

function delta_B_z=Pert_r(theta, r, B_0, delta_chi, R_0)
    delta_B_z=(1/3)*(B_0*delta_chi*((R_0./r).^3).*(3*(cos(theta).*cos(theta))-1));

%-------------------------------------------------------------------------
```

Fig. A.2: Matlab code for microbubble simulation page 2

B. HYPERPOLARISED GAS IN POROUS MEDIA

During the course of this study, an opportunity arose to work with John Owers-Bradley, Elliot Woolley and Marius Mada from his group at the University of Nottingham. Their work is involved with using hyperpolarised xenon and helium gasses for lung imaging. They were interested in showing us the results which they had acquired so far and possibly applying it to a porous system.

B.1 Concept

The idea of applying gas to pressure imaging is not new and has been demonstrated by Bencsik et al [1]. It is however not suitable for highly permeable porous systems such as sandstone. The concept explored here was to use hyperpolarised gas to improve the signal sufficiently to measure the pressure in a sandstone using gas imaging. This was however found to prove problematic on several levels. The first problem was the imaging protocols used to visualise gas in the lungs. It relies on very low tip angles to prevent loss of polarisation. The consequence is that the signal intensity is inherently low for low tip angles. The second issue is the speed of relaxation of the gas. As the gas comes into contact with the surface of the porous media, the susceptibility caused by the solid to gas interface causes near instant relaxation of the gas molecules, thereby rapidly reducing the signal. Two sets of experiments were performed: one using the group's 0.25T whole body scanner and a second using the 2.35T small animal scanner used for the microbubble experiments. These two experiments are discussed in the next sections.

B.2 Hyperpolarisation

The gas is hyperpolarised using Spin Exchange Optical Pumping (SEOP) [2]. This process allows hyperpolarisation of certain noble gases (^{129}Xe in this case) using a polarised light source and an alkali metal vapour. This allows up to 2 orders of magnitude more polarisation than is achieved thermally. The system built at the University of Nottingham consists of (see Fig. B.1)

- A Helmholtz pair coil - generates a 4mT static magnetic field to thermally polarise the spins.
- A high temperature forced air oven - to improve the degree of thermal polarisation.
- An OTS (octadecyltrichlorosilane is a long hydrocarbon with a trichlorosilane at one end which binds to the silicates in the glass) coated cylindrical borosilicate glass flow cell - This coating makes a brush

like surface which causes the noble gas atoms to bounce away from the wall rather than relaxing in a collision with it.

- A 40W volume holographic grating narrowed diode laser - Used to initiate the spin exchange.

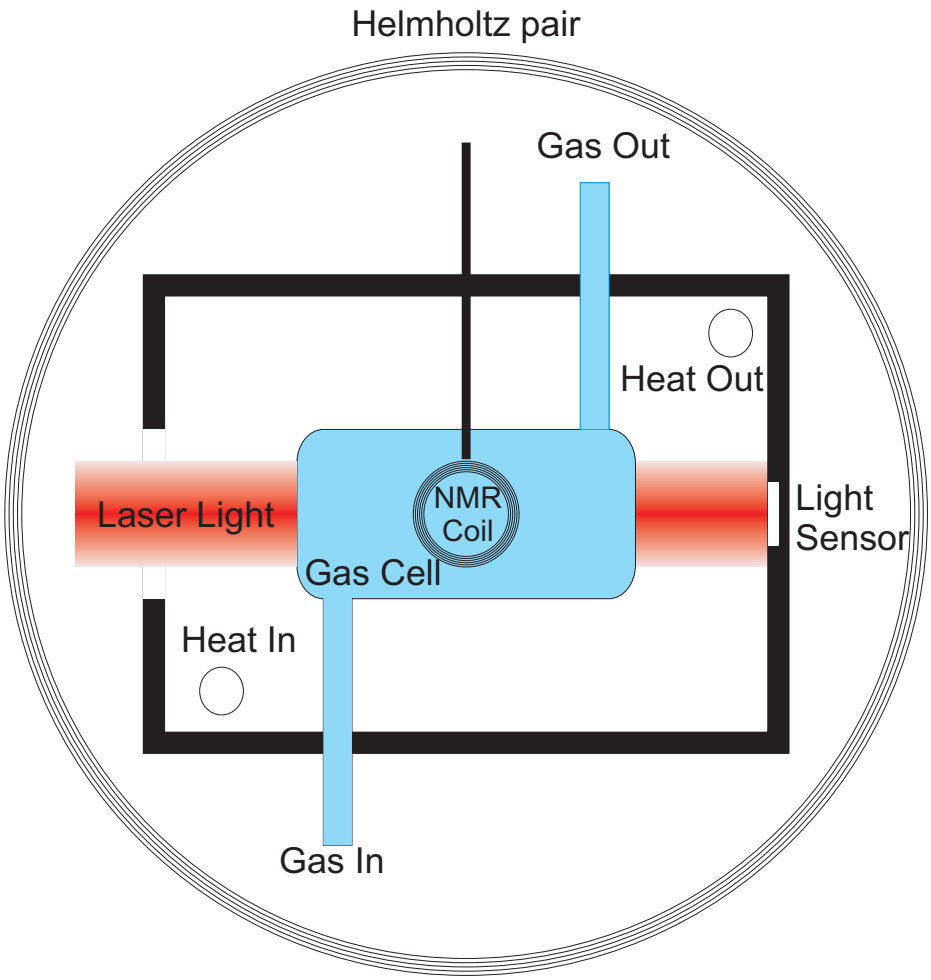

Fig. B.1: Schematic representation of the polarising apparatus

In order to polarise the xenon with spin exchange, an alkali metal is used. A small amount of the alkali metal (rubidium in this case) is added in the borosilicate glass cell. The cell is then filled with the gas and heated using the forced air oven. This vaporises the alkali metal and creates a mixture of alkali and noble gas molecules. Rubidium molecules have a spin $+\frac{1}{2}$ and $-\frac{1}{2}$ energy states. The transition to the first non-ground state of the rubidium $+\frac{1}{2}$ state is equivalent to 723nm EM radiation which corresponds to red light. By using a circularly polarised red laser beam, it is possible to excite the rubidium to its excited $+\frac{1}{2}$ state. By applying a static magnetic field, it is possible with Zeeman splitting to separate the degenerate ground levels between the two states. In this way, the energy between this second elevated ground state and the excited state can be tuned to the energy separation between ground and excited states in the xenon. Having achieved this (the field is around 4mT) collisions between rubidium atoms and xenon atoms will cause a transfer of spin from the rubidium to the xenon. The rubidium can also transfer its spin state to other rubidium molecules and indeed to the walls of the cell. Excited xenon can also loose its spin state to the walls of the vessel.

B.3 Low Field

The first experiments are conducted in John Owers-Bradley's facilities and have two intentions. The first is to use FLASH imaging to try and get an image of the gas saturating the porous medium, and the second is to use spectroscopy to investigate the exchange between surface and pore during pressurisation by adding a small amount of toluene.

B.3.1 Protocol

The samples tested are the high and low porosity sintered glass cylinders used in the gel based medium studies. The first necessary step is to clean and dry the samples by first driving nitrogen gas through the cylinders until no more liquid is extracted. The samples are then filled with ethanol (as it is volatile and will not react with the resin or acrylic in which they are embedded) which is then purged with nitrogen gas. Once dried, the samples can be prepared. One litre of the hyperpolarised xenon is produced and used to fill a plastic gas bag. This is then rapidly transferred to the bore of the low field whole body scanner to preserve the polarisation as much as possible. The gas is then transferred into the sample. For the imaging experiment this is simply transferred by forcing it into the sample. For the spectroscopy, the sample is first filled with toluene which is allowed to drain naturally from the sample which should leave a thin coating over the pore space. The gas is then pushed into the sample and should be partially absorbed by the toluene onto the surface of the sample. The amount absorbed should be proportional to some extent to the applied pressure. The ratio of the gas to toluene peak should in consequence provide a measure of the pressure.

B.3.2 Results

B.3.2.1 FLASH Imaging

Unfortunately it was not possible to prevent the gas from relaxing against the walls of the sample for a sufficiently long time to image the sample. The sample would need some form of coating (such as OTS) to prevent such rapid relaxation of the gas and to allow pressure imaging to take place.

B.3.2.2 Spectroscopy

The spectroscopy of the sample yielded some very interesting results. Two distinct peaks were found for the bulk xenon in the pore space and for the absorbed xenon in the toluene. There was however also a third peak which was often obscured by the line width of the xenon peak due to the range of fields introduced from the susceptibility difference between the porous material and surrounding material. Over time, more xenon is absorbed into the toluene which may make measurements using this method challenging. Instead, it may have been better to use a RTP xenon saturated toluene solution and then force more gas into it by increasing the partial pressure, thus increasing the amount which it can hold. This would result in a more stable measurement

although the relaxation rate of the xenon in it still precludes lengthy measurements. In an attempt to observe the small third peak, it was decided to try the experiment at a higher field thus improving the resolution of the spectra.

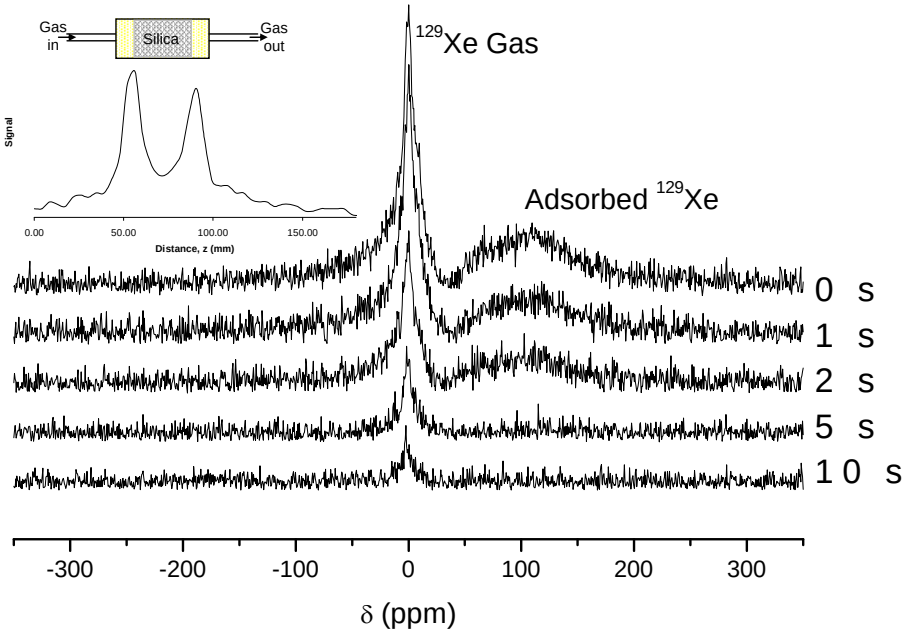

Fig. B.2: Fourier transform of ^{129}Xe from a $20cm^3$ sample of silica gel (150Å), with respect to time. The adsorbed signal has gone within 5 seconds with the free gas signal closely linked. Inset: longitudinal 1D signal. The sample is enclosed by a small volume of sponge either side from where the two major peaks arise. The resonance of the ^{129}Xe is severely affected by dephasing gradients on the surface of the silica leading to a very short T_2^*.

B.4 High Field

In order to resolve the third peak, it was decided to use the small animal scanner used for the other experiments. Because this scanner is only set up for proton imaging, a new RF coil was required. Due to the cost involved in purchasing an alternative nucleus coil, it was decided to manufacture one in house.

B.4.1 RF Coil

The proton coil used in the Bruker Biospec scanner is a birdcage coil as this offers the best filling factor for the widest range of samples. For the same reason, we decided to produce a birdcage coil tuned to the xenon frequency at 2.35T, $27.66MHz$.

The birdcage coil is formed from a set of two equally sized conductive hoops connected by a number of rungs equally spaced around the circumference of the hoops [3] (see Fig. B.3). There are three types of birdcage depending on the placement of the tuning capacitors. It is best if the rungs, rings or both are broken into equal segments by the capacitors as this produces the most homogeneous field. The first type is the high pass birdcage in which in the end rings are broken between each rung and joined with the correct capacitor value. The second is a low pass birdcage in which the end rings are left intact whilst the rungs are broken either centrally

or once at either end before being reconnected with appropriate capacitors. The final is a band pass in which a combination of both methods are employed for the purposes of tuning. The three methods are fairly similar, the high pass requires quite low values of capacitor which may be unstable for low frequency coils whilst the low pass is the counter case being more suitable for high frequencies. The band pass is most optimisable to the range of frequencies although it is highly sensitive to variations in component values such as variations in capacitance and temperature stability. For this reason, the high pass design is used for our relatively low frequency coil.

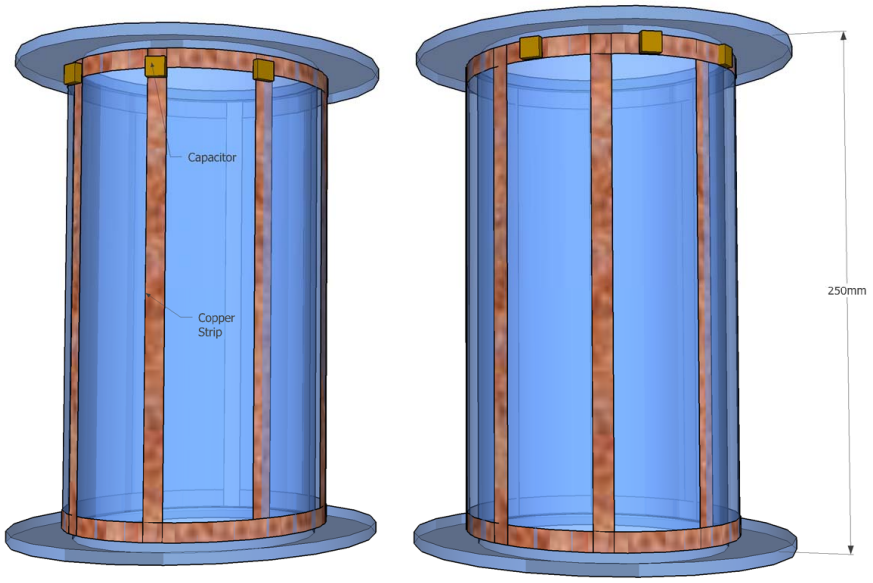

Fig. B.3: Birdcage Coil Schematics: A low pass coil is shown on the left hand side which has a continuous end ring. The right hand side is high pass with continuous rungs.

An acrylic former was produced using the laser cutter so as to fit into the gradient coil set whilst maintaining the largest possible sample volume. Self-adhesive 10mm wide copper tape was used to make an 8 rung birdcage coil. The theoretical model for the resonant frequency based on the length width and number of rungs as well as the values for the capacitors on each rung are given in [4]. To aid the design process, free software written by Penn State University (USA) to determine the capacitor values for a given frequency for a birdcage coil is used [5].

At 2.35T the resonant frequency for ^{129}Xe is 27.66MHz. The parameters of the coil are entered into the application and the necessary capacitors for the end rings are determined. These capacitors are then created from a variety of off the shelf components. The tuning and matching capacitors are then connected to the rung and ring on one side of the coil, although in order to balance the field in the coil as best as possible, a pair of matching capacitors can be located one either side of the coil. The tuning and matching capacitors are assembled in a series-parallel arrangement to allow the fine tuning of the coil to be adjusted whilst it is properly matched to the 50 Ω transmission lines of the scanner system. The coil is tested using a Smith chart on an Agilent Technology (Santa Clara, CA, USA) network analyser as no MRI scanner is available for testing.

Once the reflection spectra shows a good match to 50 Ω at the appropriate frequency, it is used to measure the sample.

B.4.2 Protocol

The 2.35T scanner is located approximately $\frac{1}{4}$ mile away from the site of the gas production. Because the gas relaxes very rapidly when outside a magnetic field, a hat box with battery driven coil is used to preserve the magnetisation as long as possible. One litre is produced and used to fill a plastic gas bag as before. It is put in the hat box which is powered and it is run from the polariser to the scanner. Initially, the coil and scanner are tested for the ability to image the gas using FLASH. The bag is driven into the RF coil in the scanner and a FLASH scan is run.

B.4.3 Results

Despite attempts to determine the optimum length of the 90° pulse (by varying the duration until no FID is observed and halving the value) the rapid relaxation prevented successful imaging. The lengthy production/transport requirements combined with this prevented successful acquisition of any results. It is hoped that in the future it will be possible to return to this study, and with improved coil design and shielding as well as calibration procedures, obtain gas images at high field both as bulk gas and in a porous medium.

References

[1] M. Bencsik and C. Ramanathan, "Method for measuring local hydraulic permeability using magnetic resonance imaging," *Physical Review E*, vol. 6306, no. 6, 2001.

[2] M. A. Bouchiat, T. R. Carver, and C. M. Varnum, "Nuclear Polarization in He3 Gas Induced by Optical Pumping and Dipolar Exchange," *Physical Review Letters*, vol. 5, no. 8, p. 373, 1960.

[3] C. E. Hayes, W. A. Edelstein, J. F. Schenck, O. M. Mueller, and M. Eash, "An Efficient, Highly Homogeneous Radiofrequency Coil for Whole-Body NMR Imaging at 1.5-T," *Journal of Magnetic Resonance*, vol. 63, no. 3, pp. 622–628, 1985.

[4] D. M. Grant and R. K. Harris, *Encyclopedia of Nuclear Magnetic Resonance*. John Wiley and Sons Ltd, 1996.

[5] C. L. Chin, "Implementation of the optimum current distribution to create a homogenous B^1 field in birdcage coil design for magnetic resonance imaging," Master's thesis, Bioengineering, Penn State, 1997.

C. PUBLICATIONS

C.1 Magnetic Resonance Imaging

Available online at www.sciencedirect.com
ScienceDirect
Magnetic Resonance Imaging 25 (2007) 509–512
MAGNETIC RESONANCE IMAGING

Three-dimensional fluid pressure mapping in porous media using magnetic resonance imaging with gas-filled liposomes

Robert H. Morris[a,*], Martin Bencsik[a], Anil K. Vangala[b], Yvonne Perrie[b]

[a]School of Biomedical and Natural Sciences, Nottingham Trent University, Nottingham, NG11 8NS, UK
[b]School of Life and Health Sciences, Aston University, Birmingham, B4 7ET, UK

Abstract

This paper presents and demonstrates a method for using magnetic resonance imaging to measure local pressure of a fluid saturating a porous medium. The method is tested both in a static system of packed silica gel and in saturated sintered glass cylinders experiencing fluid flow. The fluid used contains 3% gas in the form of 3-μm average diameter gas filled 1,2-distearoyl-*sn*-glycero-3-phosphocholine (C18:0, MW: 790.16) liposomes suspended in 5% glycerol and 0.5% Methyl cellulose with water. Preliminary studies at 2.35 T demonstrate relative magnetic resonance signal changes of 20% per bar in bulk fluid for an echo time T_E=40 ms, and 6–10% in consolidated porous media for T_E=10 ms, over the range 0.8–1.8 bar for a spatial resolution of 0.1 mm^3 and a temporal resolution of 30 s. The stability of this solution with relation to applied pressure and methods for improving sensitivity are discussed.

Keywords: Microbubble; Porous medium; MRI; Pressure; Contrast agent; Liposome

1. Introduction

The pressure of a fluid saturating a porous medium can be measured nondestructively by conventional means only at the surface of the sample. This surface pressure yields insufficient information to determine the internal pressure of a heterogeneous sample. A method has been previously developed to measure the local fluid pressure of a gas flowing in porous media with magnetic resonance imaging (MRI) [1]. This was, however, found to be unsuitable for media with high permeability such as sandstone.

It has been shown [2], using MRI, that a gas encapsulated within suspended micrometer-sized phospholipid monolayer spheres (liposomes) causes changes in nuclear magnetic resonance (NMR) signal intensity, as a result of fluid pressure changes.

This article presents preliminary results in the application of such a contrast agent to the understanding of the fundamental properties of fluid flow through porous media exhibiting permeability and pore size distributions similar to those of sandstone.

2. Theory

The difference in magnetic susceptibilities ($\Delta\chi$) between the suspending medium and the gas encapsulated by the liposome causes local perturbations in the static magnetic field according to Eq. (1) [3]:

$$\frac{\Delta B_z(r,\theta)}{B_0} = 1/3 \cdot \Delta\chi \cdot \left(\frac{R}{r}\right)^3 \cdot \left(3\cos^2\theta - 1\right), \quad (1)$$

where R is the liposome radius and r is the radial distance from the centre of the liposome at angle θ from the direction of the static magnetic field of strength B_0.

It is not known how the gas filled liposome's radius varies with pressure, but the ideal gas law can be assumed to hold for the gas bubble. Because the spatial extent of the polarising field perturbations are dependent on the bubble radius, a change in the size of liposome due to a change in pressure results in a change of field perturbation. As protons diffuse around a liposome, they sample different magnetic field strengths as a result of the perturbations. Therefore, a hypothetical proton experiencing an identical diffusion path relative to the liposome will sample different field strengths if the liposome has experienced a change in external pressure. This effect is demonstrated in Fig. 1. The greater the field perturbations sampled by the proton, the greater the dephasing, yielding

* Corresponding author. Tel.: +44 115 848 8080; fax: +44 115 848 6636.
E-mail address: rob.morris@ntu.ac.uk (R.H. Morris).

0730-725X/$ – see front matter © 2007 Elsevier Inc. All rights reserved.
doi:10.1016/j.mri.2006.11.021

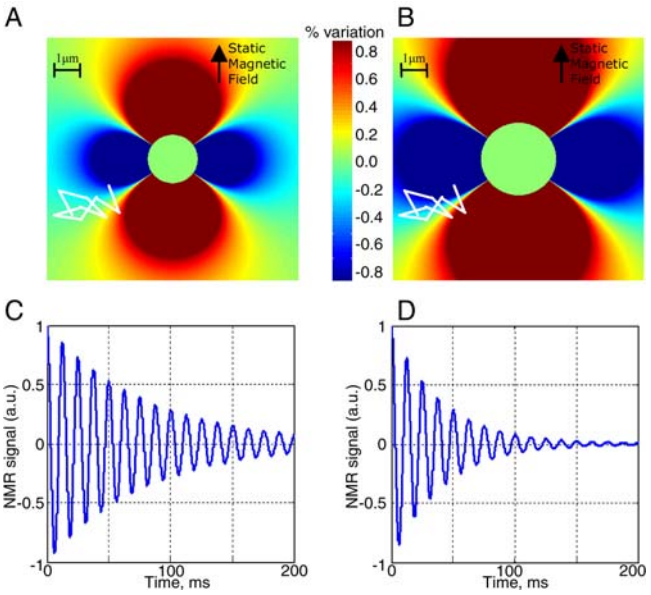

Fig. 1. Schematic colour-coded plot of the relative magnetic field perturbations caused by gas-filled liposomes (central discs) in a static field at 3 T produced from Eq. (1) for liposome radii of 2 (A) and 3 μm (B) both with plots showing the path of a proton undergoing the same random walk (white path). (C and D) Sketch of the free induction decay measured in the presence of the gas-filled liposomes above.

image contrast to fluid pressure for signal intensity through the change in relaxation rate. Extensive work has been published both on the theoretical elements and numerical simulations of the system. For spin echo sequences, it has been shown [4] that each liposome size has a corresponding theoretical echo time for which maximum effective spin-spin relaxation rate R_2^{eff} is seen. Numerical simulations have also been published, which model the system [5], although the experimental studies which are available to date offer insufficient data to conclude upon the applicability of these two theoretical works.

3. Materials

Initial experiments are conducted using a hollow extruded acrylic cell of internal diameter 39 of mm and length 52 mm, packed with silica gel saturated with the above fluid and attached at one end to a dual barrel syringe pump.

Sintered glass cylinders (AM Glassware, Aberdeen, Scotland) are used for the remaining experimental work as they are resilient to fluid flow. These cylinders have a structure very similar to that of sandstone, with the advantages that the homogeneity and pore size distribution are well known while maintaining a sample with minimal paramagnetic impurities.

These cylinders are produced from borosilicate glass in two standard porosities: 150–200 and 90–150 μm with 33-mm diameter and 50-mm length. To prevent bypass flow, these are coated in a layer of epoxy resin and embedded in an extruded acrylic tube. Two extruded acrylic end plates fitted with Swagelok connectors are then attached to either end with 5-mm clearance from the sample acting as a distribution cap.

The gas-filled liposomes are prepared by dissolving desiccated 1,2-distearoyl-*sn*-glycero-3-phosphocholine in water and cooling the solution below the phase transition temperature $T_C \approx 60^\circ$C. This results in a solution containing laminar lipid bilayers. The mixture is then homogenised with a high sheer mixer [6], which causes the laminar lipid sheets to form monolayers around the gas liquid interface at the surface of bubbles introduced in this process [7]. This produces gas-filled liposomes of 1–6 μm. For simplicity in production, all of the experiments presented herein use air as the encapsulated gas.

The gas-filled liposomes are diluted to a concentration of 3% gas by volume in a solution of 0.5% Methyl cellulose (viscosity 1500 cP, 2% in H_2O) with 5% glycerol in water. The Methyl cellulose is used to increase the viscosity sufficiently that the gas-filled liposomes do not rise too rapidly to the surface of the suspension while ensuring a substantial pressure gradient of at least 0.2 bar is produced for flow rates less than 2 ml/min. The glycerol is mixed with the liposome preparation before they are introduced into the Methyl cellulose, resulting in a more homogeneous solution than if the liposomes are added suspended in water.

4. Method

The silica gel–packed cell is attached to two interconnected 50-ml gas-filled syringes in a syringe pump via a length of Methyl cellulose filled tubing. The volume of the syringes is continuously swept to apply pressures which vary between 0.8 and 1.2 bar while imaging is performed. The MRI system is a 2.35-T Bruker Biospec small animal scanner (Bruker Instruments, Billerica, MA, USA). The sequence used is Multi Slice Multi Echo (MSME), which is a spin echo sequence that minimises susceptibility artefacts between the silica or glass and the liposome fluid.

A mixing cell with a magnetic stirrer is used for the flow experiments to ensure a homogeneous mixture is achieved for all preparations. This is initially filled with Methyl cellulose in water at a concentration of 0.5%.

The liposomes are mixed with five thirds their volume of glycerol and are injected into the cell using a syringe pump. Once the liposome mixture has been added, the syringes are refilled with Methyl cellulose, which is used to force the mixed fluid out of the cell and into the sample via a short section of Swagelok tubing. The other side of the sample is

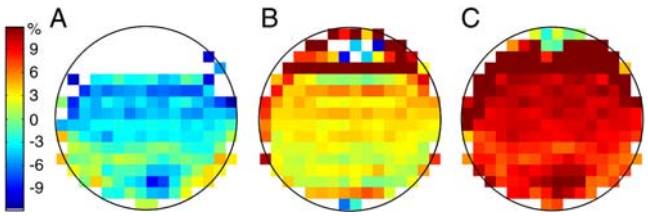

Fig. 2. Relative MR signal intensity deviation from 1 bar, averaged over all slices, in silica gel sample at static pressures of (A) 0.8, (B) 1.0 and (C) 1.2 bar. Note the increase in signal towards the upper portion of the images indicating the accumulation of liposomes in the bulk fluid.

returned to the control room and terminated with a tap to allow the system to be isolated.

Pressure is monitored using pressure sensors calibrated and used outside the 5 Gauss line of the magnet at each end of the sample, allowing calibration of the magnetic resonance (MR) signal and corroboration of the measurements. The first stage in each experiment is to ensure the samples are fully saturated. This is achieved by agitating and sonicating the samples for 30 minutes in 0.5% Methyl cellulose in water. The sample is connected to the mixing cell and placed in the scanner before the liposome-containing fluid is driven through it to a total volume of 40 ml representing approximately three times the total pore volume of the sample. The pressure contrast is then calibrated by isolating the outlet and driving liposome-containing fluid until a pressure of 1.8 bar is reached on both sensors. The MRI is run, the pressure is then reduced to 1.6 bar and the MRI is run again. This is repeated until atmospheric pressure is reached. The signal intensity for each pixel (averaged for two repetitions) is fitted against the applied pressure using a linear least squares method to yield calibration information for use with the flowing data. The outlet is then opened, and the MSME is constantly repeated while the fluid is driven at a flow rate of 2 ml/min until a steady state is reached. This is performed for fluids with and without liposomes in order to check that the contrast originates from the liposomes and not from dissolved gas in the suspending fluid or trapped gas in the porous medium.

5. Results

5.1. Packed silica gel sample

Because only static fluid was explored, long T_E values were used yielding high sensitivity, although drifts due to the liposomes rising must be compensated for. This compensation is possible as the drift is linear with time over the duration of the experiment. Due to the inherent difficulty of completely packing silica gel, the upper one third of the sample can be considered as bulk fluid. This allowed the liposome dynamics to be studied simultaneously in a porous medium and in bulk fluid (Fig. 2). The peak drift is a measure of the percentage change in NMR signal over time and is found to be $33\% \cdot h^{-1}$ in bulk fluid and $11\% \cdot h^{-1}$ in packed beads. This shows that a 30 s experiment should suffer negligible drift.

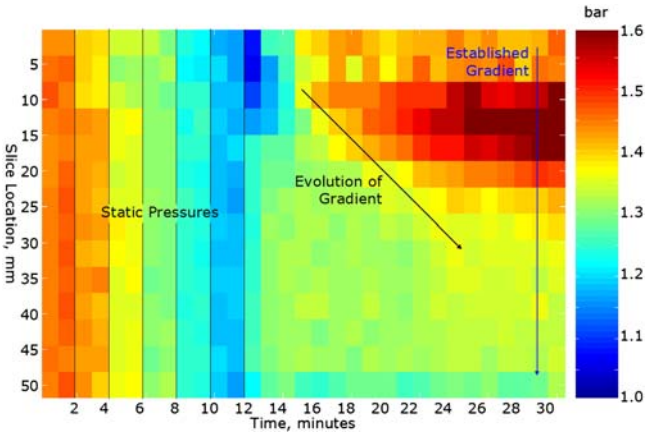

Fig. 3. Plot of fluid pressure in each slice against time. The data are averaged across the transverse dimensions. The inlet is located at $z=0$ mm and the outlet at $z=50$mm. The left-hand side shows the six static pressures taken for calibration purposes before the fluid was driven constantly. The diagonal line on the right-hand side shows the evolution of the pressure gradient across the porous medium. The sample used for this data has an average pore size of 95 μm, which is well above the average liposome size.

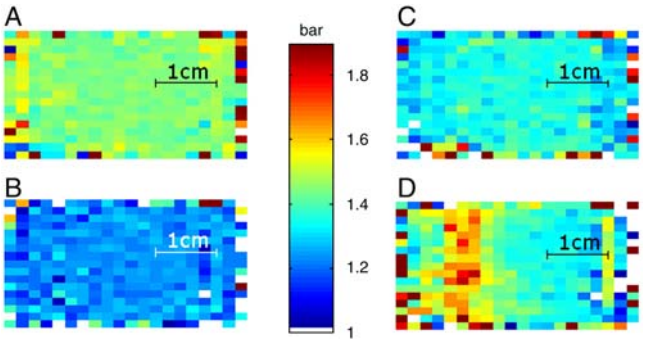

Fig. 4. Sagittal MRI projections of lower permeability sintered cylinder at 1.45 (A), 1.30 (B) and 1.20 bar (C) static fluid pressures. (C) Sagittal projection of sintered cylinder experiencing fluid flow from the left to the right of the image demonstrating a clear gradient along the sample.

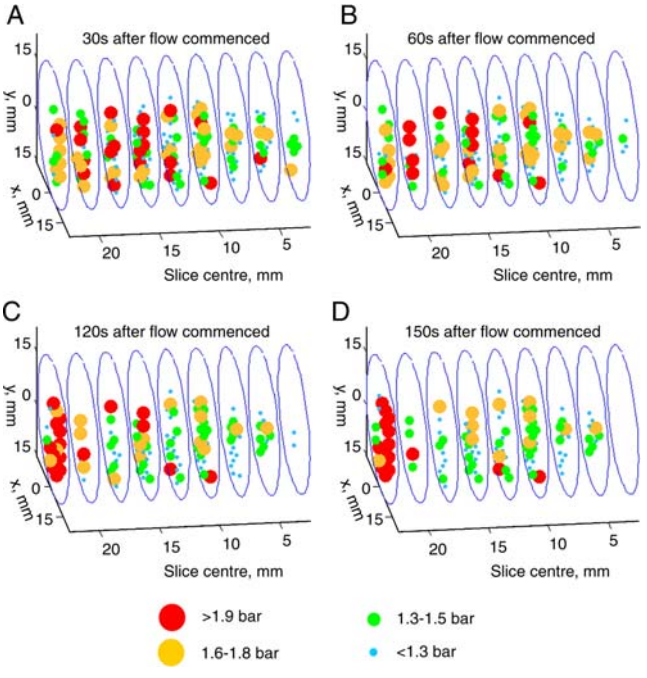

Fig. 5. Evolution of pressure gradient from higher pressure. Flow is from left to right. White areas represent pixels which had less than 90% confidence in calibration. (A) Majority of sample is still at high pressure. (B) and (C) the pressure at the outlet (right hand side) begins to return to atmospheric pressure. (D) The high-pressure areas are exclusively at the inlet with intermediate pressures extending towards the outlet.

5.2. Sintered cylinder 1D processing

A shorter echo time, T_E=10 ms, is used here to minimise artefacts in the flowing fluid MRI. The data is averaged in both dimensions of each slice resulting in one-dimensional profiles, calibrated using the static fluid data. The calculated pressure along the length of the higher permeability sample is plotted against time in Fig. 3.

5.3. Sintered cylinder 2D processing

Two-dimensional images for each repetition of the MSME sequence are then produced using the above method with averaging in only one dimension. Three static pressures and a flowing fluid experiment in the lower permeability sample are shown in Fig. 4. Calibration is performed pixel by pixel in these two-dimensional images to ensure that any inhomegeneities in the sample are accounted for. The maximum pressure is found to be higher than the previous sample, as would be expected.

5.4. Sintered cylinder 3D processing

Three-dimensional calibration is also performed on images with a lower spatial resolution of ~1 mm^3. The calibration is less accurate with a 90% confidence. A gradient can be seen to establish across the sample at approximately 0.5 bar. Four images as the gradient develops are shown in Fig. 5.

6. Discussion

Relative sensitivity to fluid pressure greater than 6% signal change per bar has been demonstrated for all samples saturated with fluid containing gas-filled liposomes. The sensitivity is confirmed to be due to liposome effects, as less than 1% relative sensitivity is seen in solutions containing Methyl cellulose only. This technique requires local calibration, which is rapid and straightforward in a system in which the fluid flow is controllable. The stability of the liposomes is such that pressures up to 1.8 bar can be explored without compromising the monolayer integrity. However, above this pressure, the sensitivity is greatly reduced due to destruction of the majority of the liposomes. This is also observed through a decrease in the turbidity of the fluid in the mixing cell.

The mechanism for the liposome destruction is unknown, but it may be possible to improve the stability by using a different phospholipid. Dipalmitoyl-*sn*-glycero-3-phosphocholine (C16:0, MW: 734.05) was also tested and demonstrated poorer stability. Alternatively, if higher pressures are desired, the use of a smaller liposome size may allow a greater pressure to be reached before destruction occurs as the membrane would not be as stressed. Liposome stability may also be improved by using a gas which has poor solubility in water, such as nitrogen [7].

Additionally, the first few slices at the inlet of each sample appear to have a lower average signal. This is due to a highly localised gradient in the centre of the axial surface, possibly caused by using a flow rate which is too great to be adequately distributed.

7. Conclusion

Successful spatially resolved MRI measurements of the fluid pressure within a porous medium are shown with the use of a liquid-containing, gas-filled liposomes at a concentration of 3%. For optimum sensitivity, the liposome size should cover a narrow range, and pressures of 1.8 bar should not be exceeded. Using a MSME sequence with 20 slices and an imaging matrix of 32 × 32 pixels, images displaying more than 6% signal change per bar can be produced with short echo times. Three-dimensional imaging has also been demonstrated by reducing the matrix size. The best achievable resolution for two-dimensional imaging is 0.1 mm^3 at 30 s and is 0.5 mm^3 at 30 s for three-dimensional imaging. Further work will be conducted to fully optimise the experiments. This will include determining the optimum liposome size for the chosen pressure range and the optimum echo time which corresponds to this. This should allow for greater resolution and allow pixel-by-pixel calibration in three dimensions. Finally, 5 calibrated pressure sensors will be fitted along the length of the sintered glass cylinder to validate the measurements of the pressure gradient.

Acknowledgments

We gratefully acknowledge the Engineering and Physical Sciences Council, UK, for support under grant number EP/C535219/1. We are also very grateful to Professor Peter G. Morris, University of Nottingham, for facilitating our access to the MRI facilities.

References

[1] Bencsik M, Ramanathan C. Direct measurement of porous media local hydrodynamical permeability using gas MRI. Magn Reson Imaging 2001;19(3-4):379–83.
[2] Alexander AK, McCreery TT, Barrette TR, Gmitro AF, Unger EC. Microbubbles as novel pressure-sensitive MR contrast agents. Magn Reson Med 1996;35:801–6.
[3] Weisskoff RM, Zuo CS, Boxerman JL, Rosen BR. Microscopic susceptibility variation and transverse relaxation: theory and experiment. Magn Reson Med 1994;31:601–10.
[4] Brown RJS, Fantazzini P. Conditions for initial Quasilinear T2-1 versus τ for Carr-Purcell-Meiboom-Gill NMR with diffusion and susceptibility differences in porous media and tissues. Phys Rev B 1993;47:14823–34.
[5] Dharmakumar R, Plewes DB, Wright GA. On the parameters affecting the sensitivity of MR measures of pressure with microbubbles. Magn Reson Med 2000;47:264–73.
[6] Unger EC, Evan C, Low density microspheres and their use as contrast agents for computed tomography, US Patent 5,205,290, 1991.
[7] Klibanov AL. Targeted delivery of gas-filled microspheres, contrast agents for ultrasound imaging. Adv Drug Deliv Rev 1999;37:139–57.

C.2 Journal of Liposome Research

Journal of Liposome Research
Publication details, including instructions for authors and subscription information:
http://www.informaworld.com/smpp/title~content=t713597272

Preparation and Characterization of Gas-filled Liposomes: Can They Improve Oil Recovery?

Anil Vangala [a]; Robert Morris [b]; Martin Bencsik [b]; Yvonne Perrie [a]
[a] Medicines Research Unit, School of Life and Health Sciences, Aston University, Birmingham
[b] Biomedical and Natural Sciences, Nottingham Trent University, Nottingham

Online Publication Date: 01 July 2007
To cite this Article: Vangala, Anil, Morris, Robert, Bencsik, Martin and Perrie, Yvonne (2007) 'Preparation and Characterization of Gas-filled Liposomes: Can They Improve Oil Recovery?', Journal of Liposome Research, 17:3, 263 - 272
To link to this article: DOI: 10.1080/08982100701528377
URL: http://dx.doi.org/10.1080/08982100701528377

Journal of Liposome Research, 17:263–272, 2007

ISSN: 0898-2104 print / 1532-2394 online
DOI: 10.1080/08982100701528377

informa
healthcare

Preparation and Characterization of Gas-filled Liposomes: Can They Improve Oil Recovery?

ANIL VANGALA,[1] ROBERT MORRIS,[2] MARTIN BENCSIK,[2] AND YVONNE PERRIE[1]

[1]Medicines Research Unit, School of Life and Health Sciences, Aston University, Birmingham
[2]Biomedical and Natural Sciences, Nottingham Trent University, Nottingham

*Although well known for delivering various pharmaceutical agents, liposomes can be prepared to entrap gas rather than aqueous media and have the potential to be used as pressure probes in magnetic resonance imaging (MRI). Using these gas-filled liposomes (GFL) as tracers, MRI imaging of pressure regions of a fluid flowing through a porous medium could be established. This knowledge can be exploited to enhance recovery of oil from the porous rock regions within oil fields. In the preliminary studies, we have optimized the lipid composition of GFL prepared using a simple homogenization technique and investigated key physico-chemical characteristics (size and the physical stability) and their efficacy as pressure probes. In contrast to the liposomes possessing an aqueous core which are prepared at temperatures above their phase transition temperature (T_c), homogenization of the phospholipids such as 1,2-dipalmitoyl-sn-glycero-3-phosphocholine (DPPC) or 1,2-distearoyl-*sn*-glycero-3-phosphocoline (DSPC) in aqueous medium below their T_c was found to be crucial in formation of stable GFL. DSPC based preparations yielded a GFL volume of more than five times compared to their DPPC counter part. Although the initial vesicle sizes of both DSPC and DPPC based GFL were about 10 μm, after 7 days storage at 25°C, the vesicle sizes of both formulations significantly ($p < 0.05$) increased to 28.3 ± 0.3 μm and 12.3 ± 1.0 μm, respectively. When the DPPC preparation was supplemented with cholesterol at a 1:0.5 or 1:1 molar ratio, significantly ($p < 0.05$) larger vesicles were formed (12–13 μm), however, compared to DPPC only vesicles, both cholesterol supplemented formulations displayed enhanced stability on storage indicating a stabilizing effect of cholesterol on these gas-filled vesicles. In order to induce surface charge on the GFL, DPPC and cholesterol (1: 0.5 molar ratio) liposomes were supplemented with a cationic surfactant, stearylamine, at a molar ratio of 0.25 or 0.125. Interestingly, the ζ potential values remained around neutrality at both stearylamine ratios suggesting the cationic surfactant was not incorporated within the bilayers of the GFL. Microscopic analysis of GFL confirmed the presence of spherical structures with a size distribution between 1–8 μm. This study has identified that DSPC based*

Received 31 May 2007; accepted 6 June 2007.
The authors gratefully acknowledge the funding provided by the EPSRC (EP/C535219/1) for this project.
Address correspondence to Yvonne Perrie, Medicines Research Unit, School of Life and Health Sciences, Aston University, Aston Triangle, Birmingham, UK; Tel: +44 121 204 3991; E-mail: y.perrie@aston.ac.uk

GFL in aqueous medium dispersed in 2% w/v methyl cellulose although yielded higher vesicle sizes over time were most stable under high pressures exerted in MRI.

Keywords liposomes, microbubble, MRI, contrast agent, pressure, porous medium, extrusion

Introduction

Whilst better recognized for their ability to deliver drugs, liposomes may also offer a solution to the world's continually declining oil reserves. In the face of increasing demands and dwindling reserves, enhancing oil recovery and finding alternative energy resources is an important issue on many government agendas.

Fossil fuels, such as oil and coal, are a result of the long-term decomposition of animals and plants and can be found in deposits beneath the earth surface, trapped in layers of sedimentary porous rock such as sandstone, which lies beneath a layer of non-porous limestone. Oil and gas, being less dense that water, gradually rise through porous rock, such as sandstone, and become trapped beneath a layer of non-porous rock, such as limestone.

One of the most common ways oil is recovered from porous rock involves drilling two wells into the non-porous layer. Water, often supplemented with surfactants or detergents, is pumped into the first hole, which loosens the oil and forces it out through the second. Since water pumped into the porous rock will follow the path of least resistance, oil will be forced out from the larger pore regions. However, this leaves behind, oil-rich smaller pore regions of the rock and only a small proportion of the oil is recovered before water starts to re-emerge. Often, as little as 30% of the available oil is recovered in this way before the well must be closed, and Ghawar, one of the world's largest oil fields (accounting for more than half of Saudi Arabia's cumulative oil production) already has an outflow of more than 50% water rather than oil (Staniford, 2007). Therefore an important issue in enhancing oil reserves is to ensure enhanced extraction and harvesting of oil from such fields. The aim of this work is to investigate the potential of gas-filled liposomes as magnetic resonance tools to improve the mapping of pressure regions within such oil fields.

Magnetic resonance imaging (MRI) is frequently used with in medicine as a diagnostic tool to produce cross sectional images of soft tissue. MRI analyses the absorption and transmission of high-frequency radio waves by water molecules in tissues placed in strong magnetic fields. Images are then created based on the difference in relaxation times of the MRI signal coming from different water densities within the biological material. Under current proposals, MRI could also be potentially used to quantify and map the oil content in the porous rock by measuring the different relaxation times of the MRI signal coming from oil and water. This technology could be enhanced by the application of gas filled liposomes (GFL) which can act as MRI pressure probes since when GFL are present in a pressure varying medium the changes in liposome size, resulting from changes in pressure, would cause a change in the MRI signal (Bencsik and Ramanathan, 2001; Morris et al., 2007). This would allow an accurate three-dimensional image of the pressure changes in porous rock. MRI and GFL could also be used to identify the porosity and the fluid pressure regions within a sample of sandstone by driving GFL dispersion into the rock and measuring the MRI signal. This would enable to determine the appropriate water pressures required for driving the oil from the smaller pores of the rock, thus enhancing the efficiency of oil extraction.

The application of using gas-filled liposomes as MRI pressure probes (Alexander et al., 1996) and as ultrasound (US) contrast agents in diagnostic imaging (Maresca et al., 1998; Unger et al., 1992) has been previously reported. When used as echocardiographic contrast agents in rabbits, such gas-filled liposomes offered greater reflectivity than standard liposomes (Unger et al., 1993). Recent proposals by Morris et al., (2007) suggested that oil extraction could be enhanced by the use of liposomes filled with gas (air) because air is hard to magnetise and therefore, act as pressure probes when combined with magnetic resonance imaging (MRI) technology and identify regions of varying pressure and porosity within the porous rock. Information obtained could be used to extract oil exerting optimal amounts of pressure to recover oil even from other less accessible oil-rich regions as well. Present study is concerned with development and optimization of a liposome formulation encapsulating gas and to test the stability and physico-chemical characteristics of these preparations for their use as pressure probes in MRI studies.

Materials and Methods

Materials

1,2-dimyristoyl-*sn*-glycero-3-phosphocholine (DMPC(C14)), 1,2-dipalmitoyl-*sn*-glycero-3-phosphocholine (DPPC(C16)), 1,2-distearoyl-*sn*-glycero-3-phosphocholine (DSPC(C18)), methyl cellulose, cholesterol, stearylamine and phosphate buffered saline tablets were obtained from Sigma-Aldrich (Poole, Dorset, UK). Egg-phosphatidylcholine (PC) was obtained from Lipid Products (Nutfield, Surrey, UK). Double-distilled water was used in all the experiments.

Preparation of Gas-filled Liposomes

Gas-filled liposomes were prepared modifying the method previously described (Unger et al., 1999). 50 mg of 1,2-distearoyl-*sn*-glycero-3-phosphocoline (DSPC) or an appropriate lipid was transferred into a 50 ml container and was hydrated in 5 ml of double-distilled water in the presence or absence of desired amounts of cholesterol and/or stearylamine and homogenised for 4 min below the phase transition temperature (T_c) of the lipid using a high speed homogeniser (Ultra-Turrax T8). A thick cream comprising of gas (air)-filled liposomes was produced over the aqueous medium. Various GFL concentrations were prepared, i.e. 0.2 ml of GFL was dispersed in 1.8 ml of 2% w/v methyl cellulose (viscosity 1500 cP), which acts as a viscosity contributing agent, to give a final GFL concentration of 10% v/v.

Determination of Vesicle Size and Zeta Potential

The *z*-average vesicle diameter and the size distribution of the gas-filled liposomes were measured on Malvern Mastersizer (Model-S) at 25°C using dynamic light scattering technique. A standard wet magnetically stirred cell fitted with a 100 mm lens was used containing filtered double distilled water that could measure particle sizes from a range of 0.5 to 180 μm. Samples of various preparations were also measured for their sizes on the optical microscope using a graticule after calibrating the eye-piece with a stage micrometer. The ζ potential (an indirect measurement of the vesicle surface charge) of various gas-filled liposome formulations incorporated with a charged lipid was determined in 0.001*M* phosphate buffered saline (PBS) at 25°C using a ζ potential analyser (*ZetaPlus*, Brookhaven Instruments).

Vesicle Size Reduction Via Extrusion

The gas-filled liposome z-average diameter was reduced to about a micron using extrusion technique. A hand-held extruder (Liposofast™, Avestin, Canada) was used to yield a homogeneous vesicle suspension upon passing liposome suspension through a polycarbonate membrane of a defined pore size (800 nm) under pressure using gas-tight, glass syringes. The sample was passed through the membrane by pushing the sample back and forth between the two syringes.

Determination of Vesicle Stability Over Time

The integrity and the structural stability of gas-filled liposomes were assessed in terms of their vesicle size over time. Samples were stored at 4°C and room temperature (25°C) for over 14 days and their vesicle sizes were tested periodically, i.e., on days 1, 7, and 14 on the Malvern Mastersizer and the variation in vesicle size was studied.

Morphological Analysis Using Photo Microscopy

Gas-filled liposomes were viewed under an optical light microscope (Zeiss Axioskop, West Germany) fitted with a colour Axio camera. Photo micrographs were obtained to assess the morphological characteristics such as vesicle size, shape and aggregation along with the information on size distribution and physical stability of a vesicle preparation.

Statistical Analysis

Where appropriate, the un-paired student's t-test has been used to statistically analyse the data setting the significance level at $p < 0.05$.

Results and Discussion

Experimental Aspects

The pressure exerted by a fluid permeating through a porous medium can be measured by conventional means only at the surface of the medium. This surface pressure data is insufficient in order to assess the internal pressure that is been exerted in a porous medium with varying porosity. It has been previously reported (Alexander et al., 1996) that fluid pressure changes can be determined using gas-filled liposomes, which causes changes in nuclear magnetic resonance (NMR) signal intensity that is detected using MRI technique. Since vesicle bilayers are flexible, a change in the size of gas (air)-filled vesicle due to variation in pressure, results in a change of field perturbation since air is hard to magnetize and the field perturbations will be strongest along the axis of the static magnetic field. When protons in the aqueous medium diffuse at the vicinity of a liposome, they exert different magnetic field strengths because of the perturbations. Therefore, a hypothetical proton experiencing an identical diffusion path relative to the liposome will exert different field strengths if the liposome has experienced a change in external pressure. This effect is depicted in Fig. 1. The greater the field perturbations sampled by the proton, the greater the dephasing, yielding an image contrast to the fluid pressure which in turn varies the signal intensity giving information on pressure remotely.

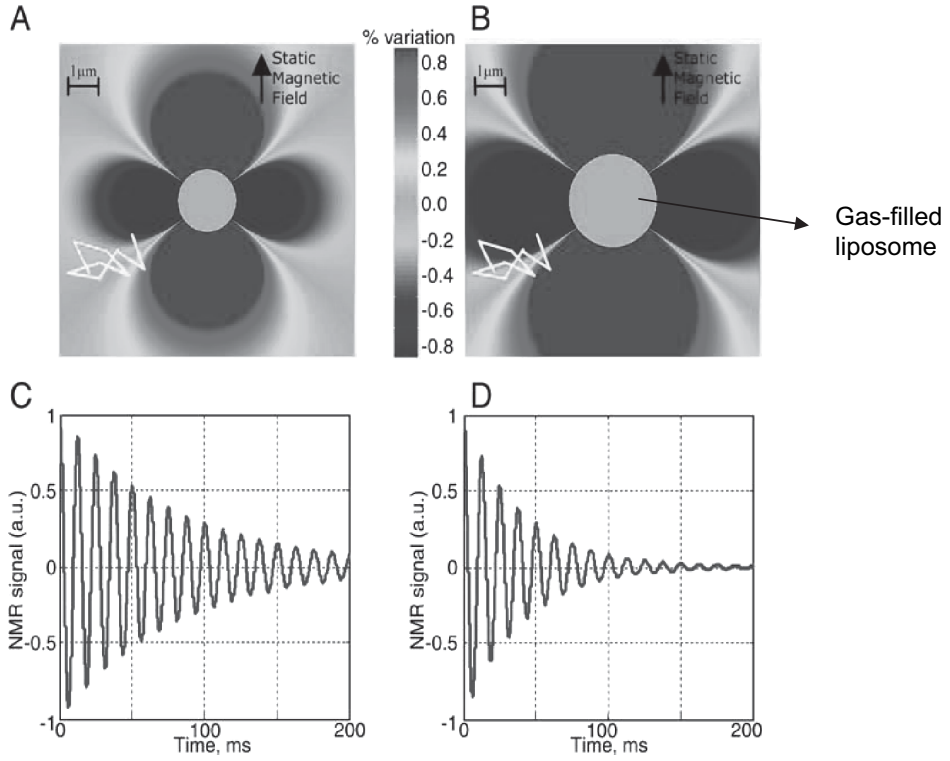

Figure 1. Schematic of the relative magnetic field perturbations caused by gas-filled liposomes (central discs) in a static magnetic field for liposome radii of 2 (A) and 3 μm (B) at 3 Tesla with plots showing the path of a diffusing proton (white path). The NMR signal is measured (C and D) in the presence of the respective gas-filled liposomes above. Figure reproduced with permission from Morris et al., 2007.

Effect of Cholesterol Content On Vesicle Characteristics and Stability

Cholesterol is well recognised at improving the stability of liposomes therefore initial studies were conducted to investigate its effect on gas-filled liposome characteristics. When DPPC liposomes was supplemented with cholesterol at a mole ratio of 0.5 or 1, a significant increase ($p < 0.05$) in the vesicle size (12.4 ± 0.2 μm and 12.9 ± 0.8 μm, respectively) was observed (Fig. 2) compared to the preparation without cholesterol (8.6 ± 1.0 μm). However, significant increases ($p < 0.05$) in vesicle size were noted for DPPC liposomes after 7 days storage at room temperature, with their size increasing to those similar to the cholesterol supplemented formulations (~12 μm). After 14 days no further changes in size were measured. In contrast, formulations supplemented with cholesterol at either molar ratio tested, remained similar in over the 14 days storage (Fig. 2). Similar results were also measured after storage of these systems at 4°C (results not shown) suggesting that the larger cholesterol-supplemented systems display reduced vesicle aggregation/fusion and enhanced stability, similar to conventional aqueous liposomes (Liu et al., 2000).

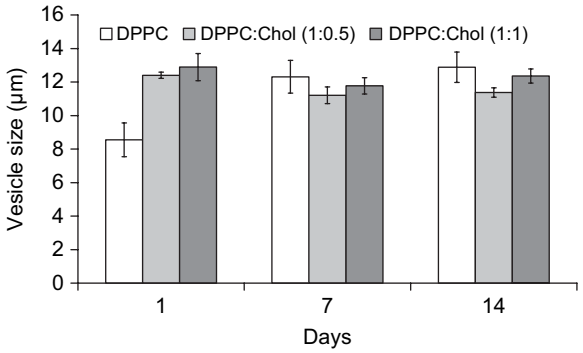

Figure 2. z-average diameter of DPPC based gas-filled liposomes in the presence (0.5 and 1 mole ratio) and absence of cholesterol over time stored at 25°C. Vesicle size was measured in double distilled water by dynamic light scattering technique using Malvern Mastersizer at 25°C, results represent mean ± S.D., $n = 3$.

Effect of Charged Surfactants on Vesicle Characteristics

In an attempt to induce surface charge on the GFL, and potentially enhance stability, DPPC:Cholesterol (1: 0.5 mole ratio) based formulations were also supplemented with a positively charged surfactant, stearylamine at mole ratios of 0.125 and 0.25. Previous investigations where charged lipids have been incorporated into conventional liposomes consisting an aqueous core, showed an increased stability in terms of vesicle size and aggregation due to electrostatic repulsion (Mohammed et al., 2004). Interestingly, in the current work, the zeta potential values remained around neutral (~3 mV) in the presence or absence of added stearylamine in the formulation (Fig. 3) suggesting stearylamine was not incorporated within the GFL bilayers unlike similar aqueous filled liposomes (Mohammed et al., 2004) where a marked increase in ζ potential was measured for similar bilayer compositions.

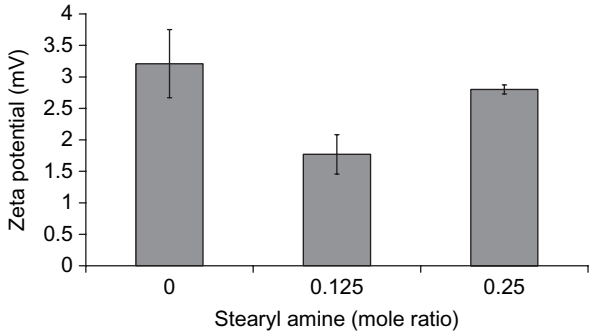

Figure 3. Zeta potential of gas-filled liposome preparation composed of DPPC: Cholesterol (1:0.5 mole ratio) incorporating a cationic surfactant, stearyl amine at different mole ratios. Zeta potential was measured on *ZetaPlus* (Brookhaven Instruments) at 25°C, results represent mean ± S.D., $n = 3$.

Effect of Lipid Alkyl Chain Length on Vesicle Characteristics

Comparisons between GFL formulated using DPPC and DSPC revealed DPPC formulations more consistent in terms of vesicle size (Fig. 4) while approximately a 3-fold increase in DSPC GFL vesicle size being measured after 7 days storage at 25°C. However interestingly the volume of GFL produced from the DSPC lipid using homogenisation technique was approximately 5 times (25 ml) that of DPPC formulations.

Preparation of GFL below the lipid T_c was considered to be essential, as an attempt to produce GFL using 1,2-dimyristoyl-*sn*-glycero-3-phosphocholine (DMPC) and egg-phosphatidylcholine (PC) was unsuccessful presumably because of the low T_c (i.e., ~24°C and ~−5°C, respectively) for both the lipids which in turn yielded liposomes with an aqueous core.

The vesicle sizes of DSPC based GFL system stored at 25°C over a 14 day period was also measured by light microscopy to study the change within vesicle population. Vesicles of various sizes present in certain specified regions of the graticule, which represent the entire population, were counted and the mean number of vesicles present basing on their sizes were tabulated (Table 1). Over the 14 day study, the majority of vesicles measured remained in the size range of 5 to 10 μm, however between days 7 and 14 the number of vesicles in this size range did drop approximately in half. Vesicle number with sizes greater than 10 μm remained unchanged during the 2 week period which is interesting as the decrease in the smaller vesicle number on day 14 do not seem to be resulting in fusion into larger ones as anticipated suggesting that the vesicles are collapsing. However, since fusion of vesicles is known to be a dynamic process, the large older vesicles might still be undergoing a collapse due to the thermodynamic instability and therefore the total population of larger vesicles may remain constant. The size ranges measured via this method are shown in Fig. 5a. Comparison of this size data with that obtained using dynamic light scattering (Fig. 4) suggests that information obtained using the later technique, when reported in terms of volume mean diameter, may be skewed considerably by the presence of a few large vesicles in the sample.

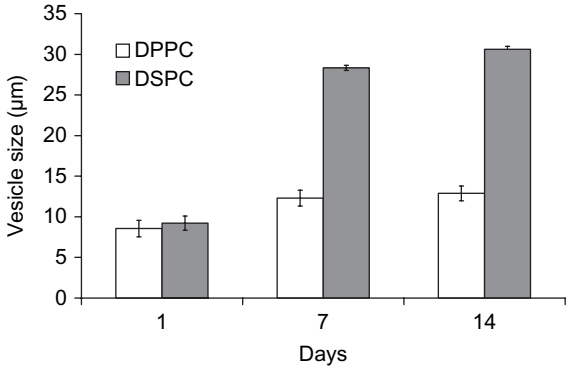

Figure 4. z-average diameter of DPPC and DSPC based gas-filled liposomes over time stored at 25°C. Vesicle size was measured in double distilled water by dynamic light scattering technique using Malvern Mastersizer at 25°C, results represent mean ± S.D., $n = 3$.

Table 1
Vesicle diameter and the corresponding vesicle mean number of DSPC based gas-filled liposomes over time, i.e. on day 0, 7 and 14 stored at 25°C

	Vesicle mean number as a representation of entire population		
Vesicle diameter (μm)	Day 0	Day 7	Day 14
5	24.33 ± 2.52	24.00 ± 1.73	14.33 ± 2.08
10	11.42 ± 2.28	15.58 ± 3.01	6.58 ± 2.07
15	3.67 ± 1.50	4.25 ± 1.77	5.00 ± 1.28
20	7.00 ± 2.22	5.42 ± 1.68	3.17 ± 1.40
25	0.58 ± 0.67	1.08 ± 1.03	1.00 ± 1.21
30	0.25 ± 0.45	0.67 ± 0.78	0.83 ± 0.84
35	0.00 ± 0.00	0.00 ± 0.00	0.00 ± 0.00

Vesicles were counted on a graticule under an optical microscope based their diameters from various regions as a representation of the entire population after calibrating the eye piece with a precision stage micrometer. Results represent mean ± S.D., $n = 3$.

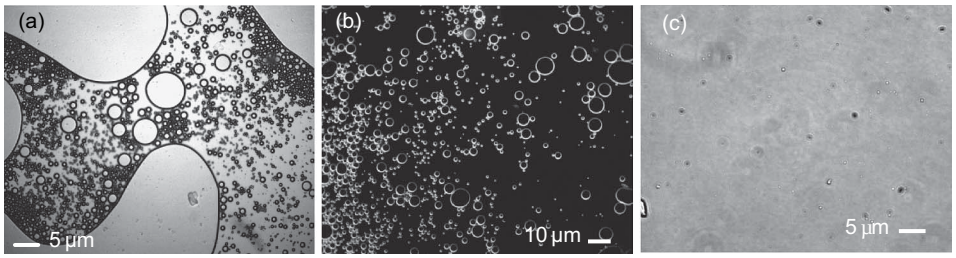

Figure 5. Optical microscopic pictures of DSPC (a) and DPPC (b) based gas-filled liposomes observed at a magnification of 40x. A heterogeneous size distribution with partially aggregated vesicles was evident whose sizes ranged between sub-micron to about 10 μm. DSPC based system subjected to extrusion through an 800 nm polycarbonate membrane showed a homogeneously distributed sub-micron sized vesicles (c).

Morphological Analysis

Microscopic analysis (Fig. 5) of various lipid based GFL systems confirmed spherical structures with a size distribution between sub-micron sizes to about 10 μm. DSPC based systems (Fig. 5a) revealed a more heterogeneous size distribution compared to DPPC (Fig. 5b). In order to obtain a homogeneous, sub-micron sized GFL with a narrow size distribution, DSPC based system was subjected to extrusion (Liposofast™, Avestin, Canada) through an 800 nm polycarbonate membrane and their initial morphological studies were carried out using oil-drop method on an optical microscope which revealed a relatively uniform vesicle size of about 0.8–1 μm (Fig. 5c), however the total number of liposomes appears to be reduced dramatically which mainly resulted due to the dilution of the gas liposome concentration to approximately 10% v/v prior to extrusion.

Determination of Fluid Pressure in Sintered Cylinder

Relative sensitivity to fluid pressure greater than 6% signal change per bar was demonstrated in the sintered cylinder (a simulated sand stone) permeated with fluid containing gas-filled liposomes (Fig. 6). The data is averaged in both dimensions of each slice (vertical section in a cylinder) resulting in one-dimensional profiles, calibrated using the static fluid data. The calculated pressure along the length of the higher permeability sample is plotted against time (Fig. 6).

The sensitivity was confirmed to be due to the presence of gas-filled liposomes, as less than 1% relative sensitivity was observed in samples containing only the suspending medium, methyl cellulose, which was primarily used as a viscosity-contributing agent in all the preparations and reduce the rising of vesicles to the surface of the aqueous phase (creaming) due to buoyancy. It was observed that pressures up to 1.8 bars could be explored without disrupting the liposome bilayers. However, above this pressure, the sensitivity is greatly reduced due to collapse of the majority of the liposomes. DSPC based systems demonstrated improved stability under higher pressures compared to DPPC. Alternatively, decreasing the liposome size may allow an increased stability under higher pressures as less stress is exerted on the bilayer membrane (Morris et al., 2007). Vesicle stability may also be improved by loading the liposomes with a poorly water soluble gas such as nitrogen (Klibanov, 1999).

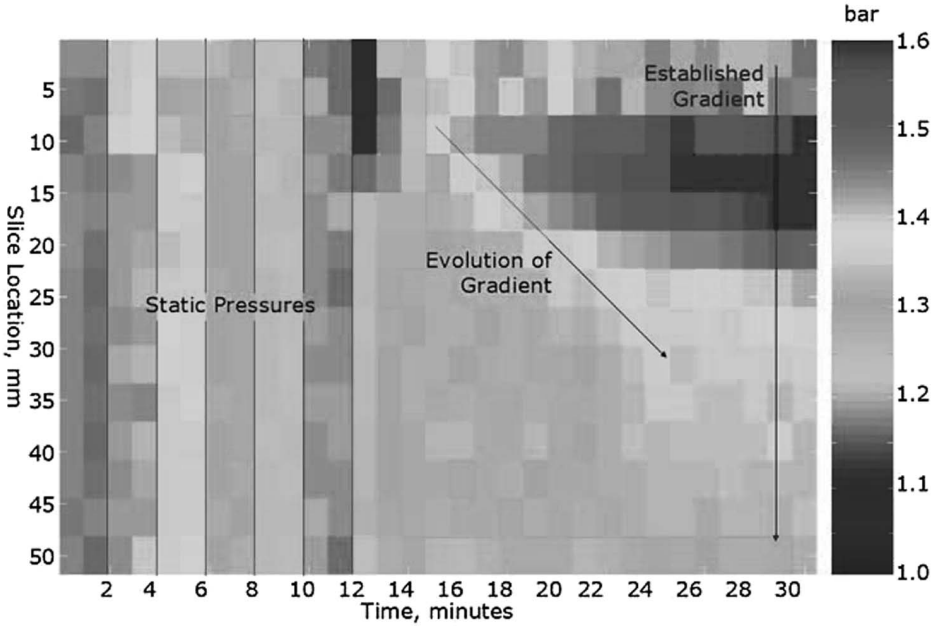

Figure 6. Plot of fluid pressure exerted in each slice of a sintered cylinder against time. The data are averaged across the transverse dimensions. The distance between the inlet and the outlet is 50 mm. The left-hand side shows the six static pressures taken for calibration purposes before the fluid was driven constantly. The diagonal line on the right-hand side shows the evolution of the pressure gradient across the porous medium. Figure reproduced with permission from Morris et al., 2007.

Conclusions

It is evident that stable gas-filled liposomes could be prepared using a novel and a simple homogenization technique with phospholipids such as DPPC and DSPC in the presence and absence of cholesterol. 2% w/v methyl cellulose was used to provide optimum viscosity and reduce the rate of creaming, allowing an NMR signal to be produced and measurement to be taken. Although DSPC based GFL yielded higher vesicle sizes over time compared to DPPC based systems, they were more resistant to destruction under the high pressures used in MRI studies. Although a significant increase in vesicle size was observed when cholesterol was included in DPPC formulations at molar ratio of 1: 0.5 or 1: 1, incorporating cholesterol increased the stability over time. Overall, these GFL preparations have shown the potential to serve as pressure probes as noted from our MRI studies and help in understanding the spatial distribution of fluid pressure in porous rock for enhanced efficiency in oil extraction.

References

Alexander, A. L., McCreery, T. T., Barrette, T. R., Gmitro, A. F., Unger, E. C. (1996). Microbubbles as novel pressure-sensitive MR contrast agents. *Magn. Reson. Med*. 35:801–806.

Bencsik, M., Ramanathan, C. (2001). Direct measurement of porous media local hydrodynamical permeability using gas MRI. *Magn. Reson. Imaging* 19:379–383.

Klibanov, A. L. (1999). Targeted delivery of gas-filled microsperes, contrast agents for ultrasound imaging. *Adv. Drug Deliv. Rev*. 37:139–157.

Liu, D. Z., Chen, W. Y., Tsai, L. M., Yang, S. P. (2000). The effects of cholesterol on the release of free lipids and the physical stability of lecithin liposomes. *J. Chinese Inst. Chem. Eng*. 31:269–276

Maresca, G., Summaria, V., Colagrande, C., Manfredi, R., Calliada, F. (1998) New prospects for ultrasound contrast agents. *Eur. J. Radiol*. 27:S171–S178.

Mohammed, A. R., Weston, N., Coombes, A. G. A., Fitzgerald, M., Perrie, Y. (2004). Liposome formulation of poorly water soluble drugs: optimization of drug loading and ESEM analysis of stability. *Int. J. Pharm*. 285:23–24.

Morris, R. H., Vangala, A. K., Bencsik, M., Perrie, Y. (2007). Three dimensional fluid pressure mapping in porous media using magnetic resonance imaging with gas filled liposomes. *Magn. Reson. Imaging*. 25:509–512.

Staniford, S. (2007). Depletion Levels in Ghawar. http://www.theoildrum.com/node/2470.

Unger, E. C., Fritz, T. A., Matsunaga, T., Ramaswami, V., Yellowhair, D., Wu, G. L. (1999). Methods of preparing gas-filled liposomes. US Patent 5,935,553.

Unger, E. C., Lund, P. J., Shen, D. K., Fritz, T. A., Yellowhair, D., New, T. E. (1992). Nitrogen-filled liposomes as a vascular US contrast agent: preliminary evaluation. *Radiology* 185:453–456.

Unger, E. C., Shen, D. K., Fritz, T. A, Lund, P. J., Wu, G. L., Kulik, B. (1993). Gas-filled liposomes as echocardiographic contrast agents in rabbits with myocardial infarcts. *Invest. Radiol*. 28:1155–1159.

C.3 Journal of Magnetic Resonance

Journal of Magnetic Resonance 193 (2008) 159–167

Contents lists available at ScienceDirect

Journal of Magnetic Resonance

journal homepage: www.elsevier.com/locate/jmr

Robust spatially resolved pressure measurements using MRI with novel buoyant advection-free preparations of stable microbubbles in polysaccharide gels

Robert H. Morris [a], Martin Bencsik [a,*], Nikolaus Nestle [b], Petrik Galvosas [c], David Fairhurst [a], Anil Vangala [d], Yvonne Perrie [e], Glen McHale [a]

[a] Department of Physics, Nottingham Trent University, Clifton Lane, Nottingham, NG11 8NS, UK
[b] BASF SE, Ludwigshafen, Germany
[c] Universität Leipzig, Fakultät für Physik und Geowissenschaften, Linnéstraße 5, Leipzig, Germany
[d] School of Pharmacy and Chemistry, Kingston University, Surrey, KT1 2EE, UK
[e] Medicines Research Unit, School of Life and Health Sciences, Aston University, Birmingham, UK

ARTICLE INFO

Article history:
Received 28 February 2008
Revised 9 April 2008
Available online 20 April 2008

Keywords:
Gas filled lipid coated microbubbles
Pressure
Polysaccharide
MRI
Diffusion
Viscosity
Contrast agent

ABSTRACT

MRI of fluids containing lipid coated microbubbles has been shown to be an effective tool for measuring the local fluid pressure. However, the intrinsically buoyant nature of these microbubbles precludes lengthy measurements due to their vertical migration under gravity and pressure-induced coalescence. A novel preparation is presented which is shown to minimize both these effects for at least 25 min. By using a 2% polysaccharide gel base with a small concentration of glycerol and 1,2-distearoyl-*sn*-glycero-3-phosphocholine coated gas microbubbles, MR measurements are made for pressures between 0.95 and 1.44 bar. The signal drifts due to migration and amalgamation are shown to be minimized for such an experiment whilst yielding very high NMR sensitivities up to 38% signal change per bar.

1. Introduction

Until recently, non-invasive fluid pressure measurements were made exclusively with discrete electrical or mechanical sensors at the surface of samples. If a suitable fluid is used [1], MRI can non-invasively produce 3-D images of fluid pressure. Applications as diverse as diagnostic medical imaging, fundamental research for chemical engineering and enhanced oil recovery are possible with such a technique, which could revolutionise the understanding of many processes where spatial variations of fluid pressure exist, such as for the case of a flowing viscous fluid. Since 1996 two methods utilising MRI have been demonstrated: for samples which have low permeability, compressible fluids such as gasses can be used to yield pressure sensitivity through density measurement [1] although this is not suitable for samples such as sandstones; an alternative method takes advantage of the susceptibility difference between lipid coated, micron sized gas bubbles (microbubbles) and a suspending liquid medium. When subjected to a magnetic field, these microbubbles cause perturbations which are dependent on their radius [2]. A change in pressure causes a change in the size of these compressible microbubbles and therefore a change in the perturbations. Protons undergoing Brownian motion around these microbubbles experience a range of different fields causing signal dephasing which depends on the microbubble size and the distance which they have diffused during the measurements [3].

The microbubble method was originally conceived as a method for *in vivo* human manometry using MRI [3]. A theoretical study published in 2002 [4] suggested that the amount of gas required for sufficient sensitivity exceeds the lethal dose, unless a sophisticated paramagnetic coating could be used [5]. In 2007 the microbubble preparations were applied to study the pressure of a flowing fluid in sandstone-like samples [6].

In the previous works it has been shown that the preparations present instabilities over time which cause drifts in the NMR signal. Lipid coated microbubbles are prone to damage as a result of the application of pressure, owing to the fragile properties of their membranes and the propensity of the gas to dissolve into the surrounding fluid. This effect coupled with their intrinsic buoyancy must be counteracted to make meaningful measurements over time.

Presented here is a novel, non-Newtonian preparation which succeeds in minimising these effects whilst maintaining a high

* Corresponding author. Fax: +44 115 848 6636.
E-mail address: martin.bencsik@ntu.ac.uk (M. Bencsik).

1090-7807/$ - see front matter © 2008 Elsevier Inc. All rights reserved.
doi:10.1016/j.jmr.2008.04.025

sensitivity to pressure changes using MRI. Rheometry, diffusion NMR, time lapse photography and ultra-fast MRI are used to validate the properties of the preparation.

2. Theory

2.1. Origin of the NMR sensitivity

The susceptibility difference between two media in a static magnetic field causes local polarising field perturbations. The susceptibility difference between water and air is in the order of 10^{-6} [7] causing microbubbles to produce perturbations extending an appreciable distance from their surfaces. Water molecules which are diffusing in such a field will be subjected to a range of field strengths different to that in bulk fluid. The relative perturbations of the longitudinal component of the polarising field surrounding a sphere with a magnetic susceptibility difference of $\Delta\chi$ to its surroundings are given by [2]:

$$\frac{\Delta B_z(r,\theta)}{B_0} = \frac{4\pi}{3}\Delta\chi\left(\frac{R}{r}\right)^3(3\cos^2\theta - 1), \tag{1}$$

where R is the radius of the sphere and r is the radial distance from its centre at angle θ from the direction of the static magnetic field of strength B_0.

Because the length scale of these perturbations is dependent on the microbubble radius, a change in bubble size will result in a change in the distribution of the field strengths sampled by a water molecule diffusing in the liquid, resulting in a change of signal intensity. As the microbubbles are compressible, a change in external pressure will cause such a change in radius, yielding MRI pressure contrast. Because the process relies on the diffusion of water molecules around the microbubbles, the distance which they have diffused in a given time affects the sensitivity of the technique: if the protons have not travelled sufficiently far between two comparative acquisitions, no signal change will be seen; if they travel too far, they do not encounter sufficient perturbations either. It has been shown [4] that dephasing is maximised when molecules are allowed to diffuse a specific distance in terms of the length scale of these perturbations, and is partially dependent on the NMR sequence that is used.

Note that bubble size and diffusion coefficient both will be affected by temperature changes, hence affecting the sensitivity, but we have not exploited or discussed these effects in our present work.

2.2. Bubble rise velocity

The most important factor affecting the stability of the measurements over time is the ability of the suspending medium to prevent buoyant advection of the microbubbles. The expected rise velocity for a microbubble can be determined by equating the two opposing forces which act on it: the buoyant force,

$$F_B = \frac{4}{3}\pi R^3\Delta\rho g; \tag{2}$$

and the viscous drag on a sphere, which is given by Stokes' law for the case of low Reynolds number,

$$F_D = 6\pi\eta R v, \tag{3}$$

where R is the radius of a sphere moving with velocity v through a fluid with viscosity η, g is the acceleration due to gravity and $\Delta\rho$ is the difference in density between the gas and the liquid.

Because the lipids in the membranes of the microbubbles are in the gel state, they have a very low mobility, and they are not likely to cause additional slip at the interface between the bubble and the liquid.

Several models are available to describe the properties of non-Newtonian fluids. In the case of our study, the viscosity of pseudo-plastic fluids is described by the power law model [8],

$$\eta = k_2\dot{\gamma}^{n-1}, \tag{4}$$

which provides excellent correlation with the experimental data. In the previous expression $\dot{\gamma}$ is the shear rate, whilst the consistency, k_2, and the power law index, n, are two parameters that fully describe the rheological properties of the fluid.

For a particle moving through such a power-law fluid, the particle Reynolds number is given by [9]:

$$\mathrm{Re_p} = \frac{\Delta\rho v^{2-n}(2R)^n}{k_2}. \tag{5}$$

To estimate the maximum possible Reynolds number in the experimental system, the following 'worst case' parameters are assumed: $\Delta\rho = 1.1\ \mathrm{kg\,m^3}$, $v = 5\times10^{-7}\ \mathrm{m\,s^{-1}}$, $R = 20\ \mu\mathrm{m}$, $n = 0.3$ and $k_2 = 10\ \mathrm{Pa\,s^{0.3}}$. This gives a Reynolds number less than 5×10^{-12} which is considerably lower than values associated with a turbulent regime, corresponding to $\mathrm{Re_p} > 1$.

According to Williams [10] the shear force caused by a sphere moving with low Reynolds number can be approximated by

$$\dot{\gamma} = \frac{v}{2R}. \tag{6}$$

By equating the buoyant and drag forces, and using the 'worst case' parameters and models mentioned previously, the terminal velocity of a sphere with a given radius can be expressed in terms of the physical properties of a fluid:

$$v = \left[\frac{2^n R^{n+1}\Delta\rho g}{9k_2}\right]^{\frac{1}{n}}. \tag{7}$$

For a 5% v/v suspension, the highest concentration explored in this work, the microbubbles are separated by more than four times their own diameter, and in consequence hydrodynamic interactions between neighbouring microbubbles can be neglected.

2.3. MRI sequence

In all MRI work presented here, the RARE sequence [11] is used with the RARE factor set to the number of lines in the images, allowing an image to be collected from a single excitation pulse as in EPI.

To ensure that the sensitivity of the experiment is maximised, the effective echo time, T_E^{eff} must be optimised with respect to the T_2^{eff} of the sample. The optimum setting required to yield maximum sensitivity to small changes in T_2^{eff} is determined both semi-analytically and using Monte Carlo simulation in MATLAB (Mathworks, MA, USA).

For a homogeneous sample defined as in Fig. 1, by integrating the NMR signal along the y-axis and assuming that the exponential decay during the read gradients can be neglected as the encoding time is sufficiently short, the signal intensity for a modulus MRI image is well approximated by:

$$A(T_2^{\mathrm{eff}}, T_E^{\mathrm{eff}}) = \int_o^{2T_E^{\mathrm{eff}}}\left|2\frac{\sin\left(\gamma G_y y_o\left(t - T_E^{\mathrm{eff}}\right)\right)}{\gamma G_y\left(t - T_E^{\mathrm{eff}}\right)}\right| e^{\left(-t/T_E^{\mathrm{eff}}\right)}\mathrm{d}t. \tag{8}$$

where γ is the proton gyromagnetic ratio (not related to $\dot{\gamma}$ used in the rheology section), whilst G_y is the strength of the phase encoding imaging field gradient, t is the time and y_0 is the extent of the sample along the y-axis.

For a small change in T_2^{eff}, the greatest change in signal intensity is given (see Appendix A) by

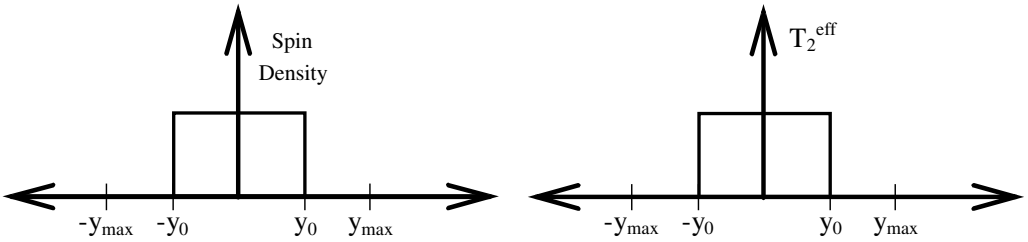

Fig. 1. Simple homogeneous sample profiles used to estimate optimum echo time.

$$T_E^{\text{eff}} = 2T_2^{\text{eff}}. \quad (9)$$

Although quantitatively correct, for practical MRI purposes the qualitative deterioration of an image that would be acquired with this set up needs to be assessed. This is achieved using Monte Carlo simulation, in which an idealised circular homogeneous image has its corresponding train of spin echoes multiplied by an exponential decay for a range of different T_2^{eff} values before thermal noise is added. The mean amplitude of the resulting MR image is then calculated in terms of T_2^{eff}.

Visual inspection of the reconstructed images allows qualitative estimation of the image artefacts, particularly those due to the increasing attenuation of the centre of k-space. Quantitation of the SNR (mean signal divided by the standard deviation of noise) in the set of generated images also permits verification of the result in Eq. (9).

3. Materials

In order to minimise the extent to which microbubbles dissolve in the surrounding medium, they are coated with a lipid shell. These lipid coated microbubbles are commonly used as a contrast agent in ultrasound as they greatly enhance the scattering of the incident wave, thereby improving contrast [12].

There are numerous methods for producing these microbubbles ranging from simple sonication [13] methods to very complex freeze drying procedures [14]. The method used for this work is detailed by Vangala et al. [15] and uses high shear mixing to produce polydisperse microbubbles. The chosen lipid powder is hydrated with water, forming laminar sheets. The mixture is then subjected to high shear mixing at atmospheric pressure using a homogeniser, spontaneously introducing gas bubbles. The lipids are in their lowest energy state when their hydrophobic chains are inside the gas bubbles whilst their hydrophilic head groups are in the surrounding medium. As a consequence of this, the lipids form a membrane at the gas liquid interface of the microbubbles. This method allows rapid and efficient production of gas filled lipid coated microbubbles 1–20 μm in size. The lipid used for the following work is 1,2-distearoyl-*sn*-glycero-3-phosphocholine (DSPC, C18:0, MR: 790.16) as this has been shown to yield superior stability in comparison to shorter chain lipids [13].

To prevent buoyant advection of lipid coated microbubbles through the suspending medium, a highly viscous preparation is necessary. However, according to the Stokes-Einstein relationship, higher viscosity results in lower diffusion for Newtonian fluids. Since the diffusion of water molecules around the lipid coated microbubbles is critical for the MRI contrast, simply increasing the viscosity may greatly reduce the sensitivity. However, non-Newtonian fluids are not governed by the Stokes-Einstein relationship. Polysaccharide gels are an example of a group of fluids which allow increase in viscosity with minimal effect on the diffusion of water within their structure [16]. We present results that demonstrate that this is the case for gellan gum, which is the polysaccharide gel used in these experiments, and justify its use as a suitable suspending medium for this contrast agent.

Gellan gum in aqueous solution forms an entangled polymer network at relatively low concentrations (typically less than 5%), rapidly increasing the bulk viscosity of the fluid [17]. Because the polymer chains are very long, the majority of water molecules in the solution are free to diffuse unhindered resulting in minimal reduction in the diffusion coefficient. Unfortunately, polysaccharide gels have a high propensity to support bacterial growth which can change many properties of the gel including the viscosity. In order to minimise the bacterial growth, Sodium Hypochlorite is used in a concentration of 0.02% v/v. Lipid coated microbubbles have been tested in this solution to ensure that it does not affect their stability (which would not be expected as they are not electrically charged).

The gellan gum is supplied in powdered form, and for these experiments CPKelco's Kelcogel AFT (CPKelco, USA) is used. This is an industrial grade gum with a particle size of 355 μm [18] which must be rehydrated with water to produce a gel. To prevent inclusion of gas bubbles within the gel, which could lead to spurious measurements, it is hydrated under vacuum.

Prior to the suspension of microbubbles in the gel, they are blended with an equal concentration of glycerol. The reason this increases the stability of the microbubble is unknown at this time, but it has been seen to somewhat reduce the drift in signal intensity.

4. Experimental

The properties of the polysaccharide gel are thoroughly analysed before it is used as the base of the contrast agent. The fluid should reduce the buoyant advection of the microbubbles with minimal restriction to the self-diffusion of water within its structure which in turn should not affect the lipid coated microbubbles.

The viscosity of the gel is measured at various concentrations for a range of shear rates using a TA Instruments (Delaware, USA) CSL^2 Rheometer. The instrument is calibrated using Poly-DiMethylSiloxane (PDMS) oils which are available in a wide range of viscosities over which they are highly Newtonian. The instrument is used with a 'Mooney-Ewart' geometry [19] tool manufactured from acrylic. The viscosity is measured for increasing and decreasing shear rates allowing the rheological properties of the gel to be studied for a static and flowing fluid.

To verify that the prediction of the bubble rise velocity is representative of the practical situation, turbidity measurements of two samples, methyl cellulose and gellan gum prepared in equal concentration is performed. The opacity of the microbubbles is sufficient that time lapse photography can be used. The samples are photographed simultaneously every minute using an 8-bit black and white DSA Mk 10 camera (Krüss, Hamburg, Germany). In order to prevent clipping, the contrast of the images is adjusted by varying the light intensity until an image of the gels without microbubbles gives a grey value of 250, allowing the smallest possible microbubbles to be observed. To facilitate simultaneous display of the collected data, the intensity across the width of each sample is averaged, providing vertical profiles each minute. These are plot-

ted and the gradients of similar intensities calculated to determine the rise velocity of various microbubble sizes. These are then compared to the theoretical estimates in an attempt to validate them.

The self-diffusion of water contained in the fluid is measured using a 400 MHz pulsed field gradient spectrometer at University of Leipzig. The magnet is a wide bore 9.4 T superconducting type (Bruker, Germany) and is used with a MARAN ULTRA console (Resonance Instruments, GB) with a Direct Binary Coded Current Source [20] for gradient pulse generation, whilst the instrument is triggered at a constant mains voltage phase to avoid hum artefacts. Using a stimulated gradient echo sequence with compensation for a shift in echo position caused by imperfect gradient pulses [20], a sample volume of 0.5 ml is tested in the actively shielded anti-helmholtz type probe at a range of temperatures for distilled water and gellan gum. These experiments allow rapid assessment of the stability of the preparation and its sensitivity to minor changes in temperature.

Once the fluid properties have been assessed, it is prepared for use as a contrast agent to pressure variation. The dry powder is dissolved in distilled water to a concentration of 2% w/v whilst stirring vigorously for 8 h under vacuum (450 torr) until a gas free homogeneous preparation is achieved. Lipid coated microbubbles are then blended with an equal concentration of glycerol before mixing with the gellan gum to a concentration of 1.25% v/v. Having achieved a homogeneous preparation, the fluid can be used directly as an MRI contrast agent to pressure.

The MRI experiments are performed using a 2.35 T Biospec small animal scanner (Bruker, Germany). As the fluid is static, ultra fast imaging can be used without concern for flow artefacts.

Two MRI experiments are conducted: The first is to test for the presence of microbubble advection. A single large volume of fluid is tested in a cylindrical acrylic cell (42 mm id × 70 mm) with Swagelok (Swagelok, USA) connectors at the inlet and outlet. The pressure of this sample is then varied using a remotely connected syringe pump whilst the RARE sequence is run. The signal intensity at several pressures is divided by the average signal intensity over all pressures. If the microbubbles experience advection during the experiment, a vertical gradient will develop in time. This is tested by plotting profiles from a single line across the centre of the sample horizontally and vertically.

The second experiment tests the stability of the MR sensitivity to pressure changes. Using a similar experimental setup, the fluid pressure is varied whilst it is monitored and recorded using a traditional piezoelectric pressure sensor. The average signal over the sample volume is plotted alongside the recorded pressure to test for correlation between external pressure and the signal intensity. A control sample containing just gellan gum is also tested to ensure that sensitivity is indeed coming from the presence of lipid coated microbubbles and not from trapped gas or other unintentional contrast mechanisms.

5. Results

5.1. Viscosity measurements

The viscosity of the gel is measured for three samples shown on Fig. 2. The plots show the variations in viscosity for a range of shear rates. The consistency and power law index are calculated from a log–log plot (see Fig. 2). The viscosity is also measured for 2% methyl cellulose (which was used in two previous studies [3,6]) for comparison to the properties of the gellan gum (see Fig. 3). For shear rates below 12 s^{-1} the gellan gum's viscosity is far higher than the methyl cellulose, above this value, viscosities are similar within 0.25 Pas.

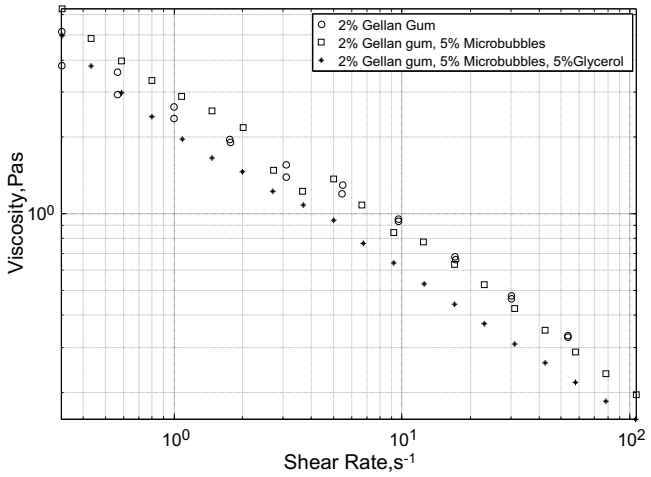

Fig. 2. Log–log plot of viscosity against shear rate for the three samples. The addition of glycerol and microbubbles has little effect on the viscosity of the fluid, even at concentrations as high 5%. At low shear the viscosity of the fluids are very high with a value greater than 6 Pas. The plot demonstrates near ideal power law behavior and allows determination of the rheological coefficients, consistency (k_2) and power law index (n).

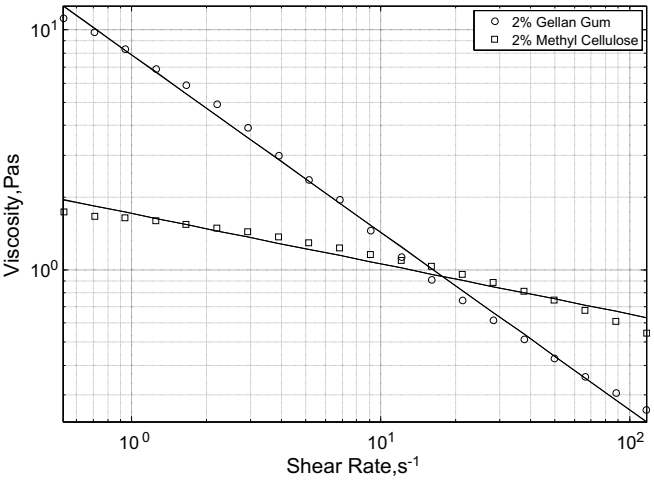

Fig. 3. Log–log plot of viscosity against shear rate for gellan gum and methyl cellulose both at 2% w/v demonstrating near ideal behavior and allowing determination of consistency (k_2) and power law index (n).

5.2. Microbubble advection measurements

The theoretical velocities predicted for a range of microbubble sizes determined using Eq. (6) and rheology data in Fig. 3 are plotted in Fig. 4. The expected velocity for a microbubble in methyl cellulose is predicted to be three orders of magnitude faster than a similarly sized microbubble in gellan gum (e.g. for 13 μm bubbles, velocities are 8×10^{-8} m s^{-1} and 2×10^{-13} m s^{-1} for methyl cellulose and gellan gum, respectively.)

Two images from the time lapse photography study are shown in Fig. 5 (the original video showing each time lapse image is available as supporting material). In order to present the data in a format which allows rapid assessment of microbubble rise velocity, vertical profiles are taken for each sample in every frame. The profiles are then stacked from left to right and shown in Fig. 6. By following contours of similar pixel intensity, the velocity of a range of microbubbles of similar size may be estimated. These contours are shown in green on Fig. 6. The microbubbles are immobile in the gellan gum for the duration of the experiment (46 h) which corre-

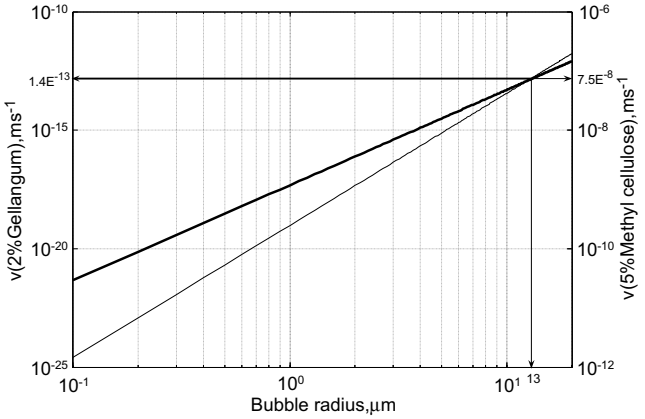

Fig. 4. Log–log plot of predicted rise velocity (v) for a given microbubble radius based on extrapolated rheology data (the lowest shear rate value measured in Fig 3 corresponds on this graph to bubble radii of 5.43 mm and 850 μm for the gellan gum and the methyl cellulose, respectively), produced using Eqs. (2)–(6) for comparison of two preparations.

sponds to a velocity less than 1×10^{-12} m s^{-1} whilst velocities ranging from 8×10^{-8} m s^{-1} to 4×10^{-7} m s^{-1} are found for the methyl cellulose.

5.3. Diffusion measurements

The diffusion measurements were conducted over a range of temperatures between 298 and 338 K. Five measurements were made for the gellan sample (with a gradient pulse separation time of 3 ms), as shown in Fig. 7. On the same figure, values for the variations of diffusion coefficients for bulk water as found by Holz et al. [21] are plotted alongside the experimental data to demonstrate the similarity of the diffusion coefficients for gellan gum and bulk water. For the range of temperatures investigated, the diffusion coefficient of water in the gellan gum matrix is similar to that of bulk water within 7%.

5.4. Optimization of signal sensitivity

The measurement of fluid pressure with MRI offers vast variations in sensitivity, spatial and temporal resolutions due to the large and growing number of MR sequences. It is important to optimize as many parameters as possible to fully enhance the signal sensitivity.

Most often the signal is acquired within a short fraction of the NMR exponential decay, and in this case, the most sensitive measurement of small changes in T_2 is found when $T_E = T_2$.

For the case of the static fluids explored in this study, the RARE sequence with single shot planar imaging was found to yield an excellent compromise between spatial and temporal resolutions, whilst the sensitivity to pressure changes could be maximized by setting $T_E^{\text{eff}} = 2T_2^{\text{eff}}$ as is shown in Fig. 8.

The two methods correlate well, although small differences can be seen due to the thermal noise that is not accounted for in the semi-analytical solution.

When the condition $T_E^{\text{eff}} = 2T_2^{\text{eff}}$ is fulfilled, the centre of k-space suffers from strong attenuation, yielding image artifacts, mostly in the form of DC signal loss (see Fig. 9), resulting in spuriously enhanced edges together with reduced intensity of the central volume. By choosing to set T_E^{eff} at a value around $1.6T_2^{\text{eff}}$, an excellent sensitivity to pressure changes is maintained whilst image artifacts are substantially reduced.

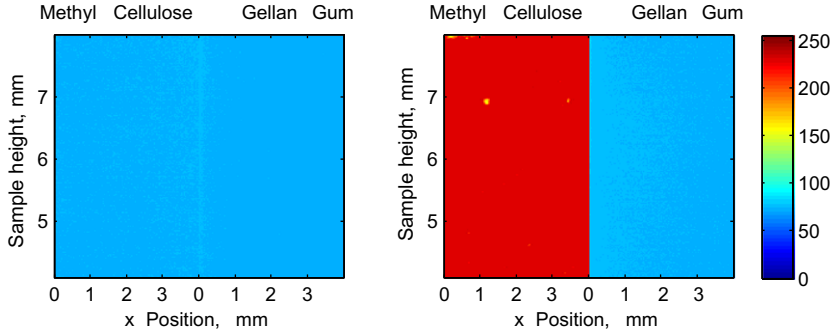

Fig. 5. Initial (left) and final (right) image from the time lapse study. The final image is collected 46 h after the initial image. The left hand side of each image is the methyl cellulose sample whilst the gellan gum is on the right hand side. The colour codes the intensity of light incident on the camera.

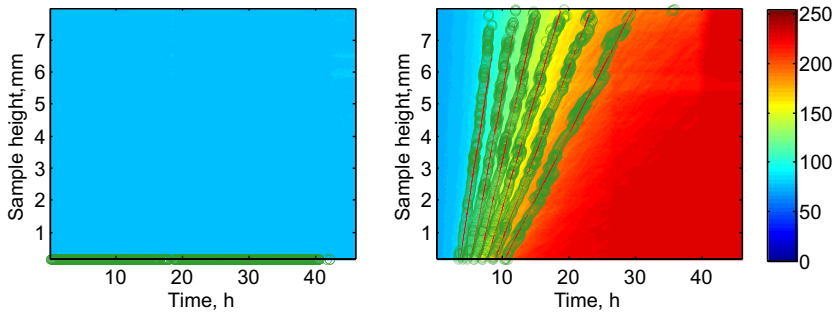

Fig. 6. Profile images. The gradients which yield estimates of rise velocity are shown in green on the two images and the gradients calculated are shown as red lines. The colour codes the average intensity of light averaged over the sample width.

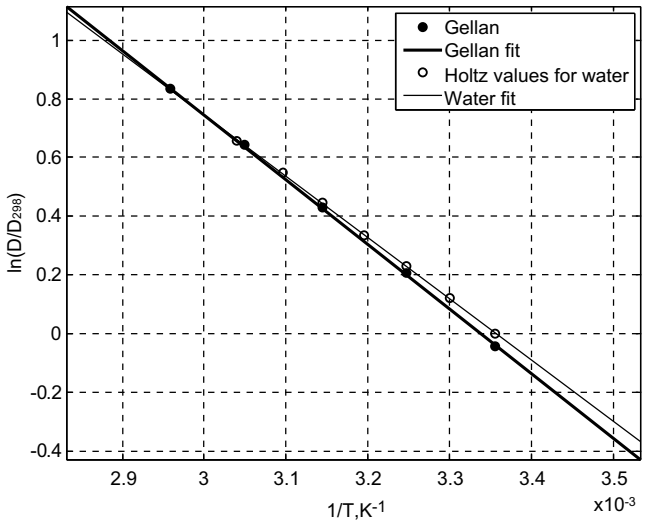

Fig. 7. Plot of the natural logarithm of the diffusion coefficient against the reciprocal of temperature, normalized by value of bulk water at room temperature for water and gellan gum. Correlation between samples is high implying that the majority of water in the gel sample is unrestricted by the network.

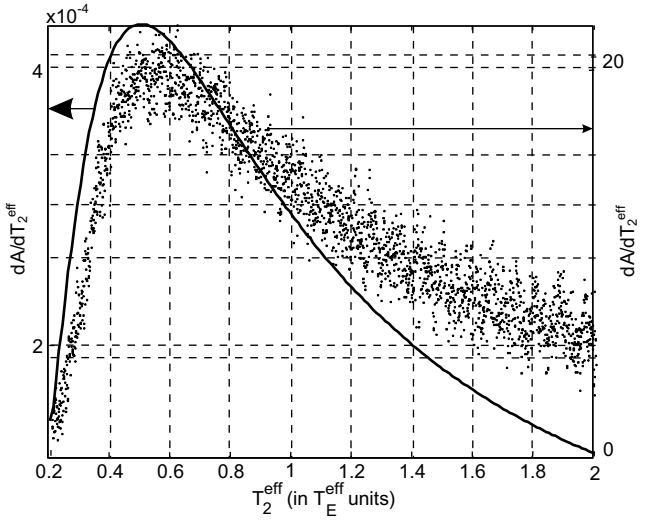

Fig. 8. Plot of gradients of semi-analytical (solid line) and Monte Carlo (single points) simulation signals, showing the optimum value for T_E^{eff} to measure small changes in the value of T_2^{eff}. A Gaussian convolution (width = 0.5 T_2^{eff}) is applied to the MR signal found from the Monte Carlo data prior to obtaining the gradient. Both tests suggest that setting T_E^{eff} to twice the value of T_2^{eff} yields optimum sensitivity to a change in T_2^{eff}.

5.5. MRI with contrast agent

The bulk fluid cell is filled with 2% gellan gum with distilled water (w/v) and 2.5% microbubbles and glycerol in equal concentration to test the stability to buoyant advection. The images in Fig. 10 show the signal intensity relative to the mean for three pressures. The high homogeneity of the images is indicative of the lack of buoyant advective motion of the microbubbles through the medium. The images are acquired using the RARE sequence with the following imaging parameters: Matrix size = 74 × 74; T_E = 6.737 ms; T_E^{eff} = 284 ms ($0.6T_2^{eff}$); T_R = 2462 ms (T_2^{eff} of the sample was 424 ms). The value of T_E^{eff} was not optimised for these experiments as they were intended to demonstrate the reduction in advection whilst a sufficiently high sensitivity was observed. If the value of T_E^{eff} had been optimised and set at 636 ms, the sensitivity could have been as high as 96% signal change per bar.

Single pixel horizontal and vertical profiles from the central row and column of the images in Fig. 10 are plotted in Fig. 11 to demonstrate the minimization of microbubble advection. The three curves present no measurable gradient which is indicative of no advective processes for the duration of the 25 min experiment.

The average signal intensity over the volume is calculated for each scan in time and is plotted alongside the pressure measured using piezoelectric sensors. The correlation is high for a single cycle below 1.4 bar. Once the fluid experiences further cycles at such pressures or if greater pressures are used, the microbubbles rupture or coalesce and reduce the sensitivity from 38% signal change per bar to less than 10% signal change per bar (see Fig. 12). Data collected after several cycles of pressure, showing this reduction in sensitivity without introducing advection is supplied as a seperate movie in the Supporting Material.

6. Discussion

The three gellan gum samples used for rheological measurements demonstrate similar shear rate—viscosity profiles despite inclusion of microbubbles and glycerol. The viscosity of the gellan gum is considerably higher than that of the methyl cellulose in equal concentration provided that the shear forces experienced are below 12 s^{-1}, which would correspond to a flow rate of 2.9 mm s^{-1} in a 10 μm pipe.

For the MRI experiments conducted in this paper, the fluid is at rest. In consequence, the only shear forces exerted on the fluid come from microbubble advection. For optimum MRI stability, and to prevent measurable drifts, the rise velocity should be sufficiently small to prevent microbubbles moving out of a voxel over the experimental duration (~1 mm h^{-1} = 0.0028 mm s^{-1}). By balancing the viscous drag and the buoyant forces it is possible to determine the viscosity required to achieve this velocity for a microbubble of a given diameter. For microbubbles up to 10 μm diameter, a fluid with a viscosity of at least 0.12 Pas would be necessary. At 2% concentration, a viscosity greater than this is found for shear rates less than 40 s^{-1} which suggests that the contrast agent will remain stable for a wide range of flow rates from rest to around 10 mm s^{-1} in sandstone-like samples.

The similarity of the diffusion of water within the gel structure to that of bulk water suggests that the contrast generated will be as high as possible without introducing any drifts due to the migration of the microbubbles. Although we have not explored them, other polysaccharide gels (xanthan gum, sodium alginate etc.) are likely to produce a similar beneficial effect, with their own characteristic consistency, k_2, and power law index, n. In addition to being relatively inexpensive, their easy handling and biocompatibility are further motivations for their use.

Fig. 4 can be used to determine the velocity of a given bubble diameter in either preparation. In methyl cellulose, the observed advection velocity of 8×10^{-8} m s^{-1} found using time lapse photography in methyl cellulose (Fig. 6), should correspond to a bubble radius of 13 μm which is within the size distribution observed in our preparations [13]. For these microbubbles, a velocity of 2×10^{-13} m s^{-1} is expected in gellan gum suggesting that no measurable movement should be seen in this experiment which is also in agreement with Fig. 6.

The migration of the microbubbles is shown to be eliminated over the course of the MRI experiments as the vertical and horizontal profiles present no measurable gradient over time. The averaged signal intensity results demonstrate that the sensitivity is solely due to the presence of gas filled microbubbles as the de-

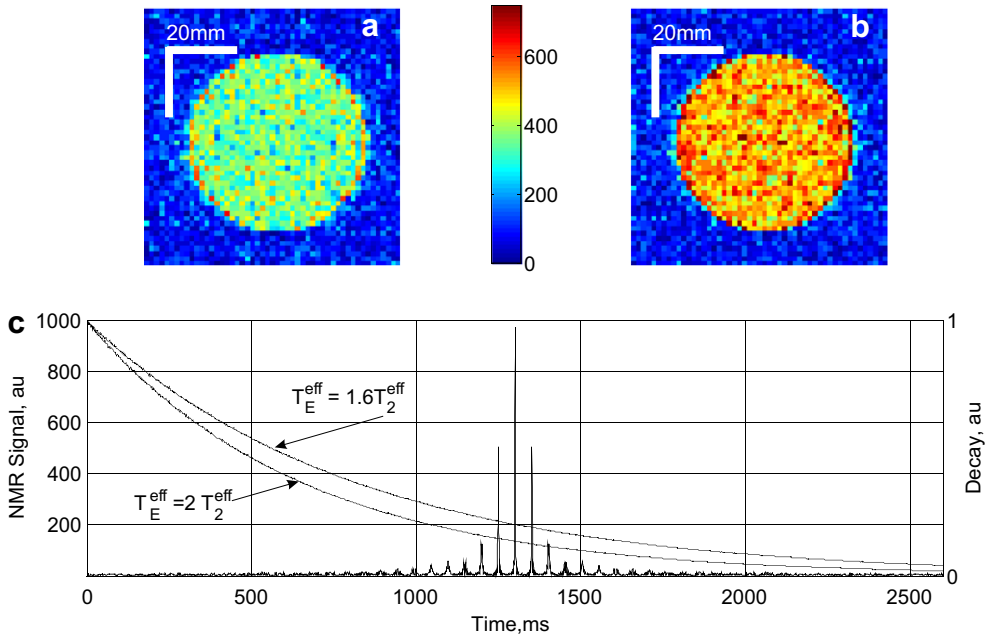

Fig. 9. Demonstration of k-space clipping due to length of relaxation. (a) Image with $T_E^{eff} = 2T_2^{eff}$; (b) image with $T_E^{eff} = 1.6T_2^{eff}$; The pixel intensities are in arbitrary units. (c) The RARE echo train with no relaxation, superimposed with the relaxation curve for the case $T_E^{eff} = 2T_2^{eff}$, and for the case $T_E^{eff} = 1.6T_2^{eff}$ (red curves).

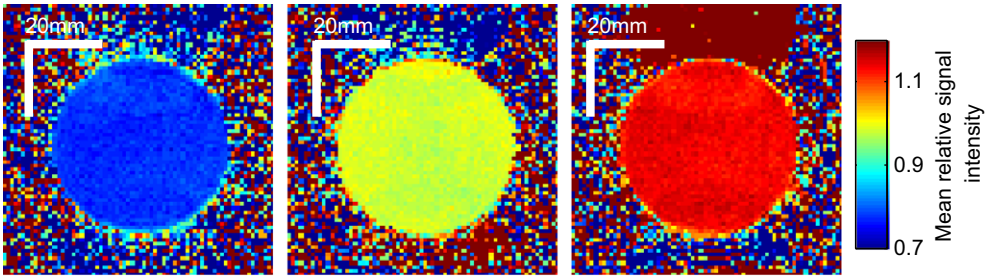

Fig. 10. Three MRI images taken at different pressures to demonstrate reduction in migration of microbubbles. The three images are taken at: 0.95, 1.3 and 1.44 bar (left to right, respectively).

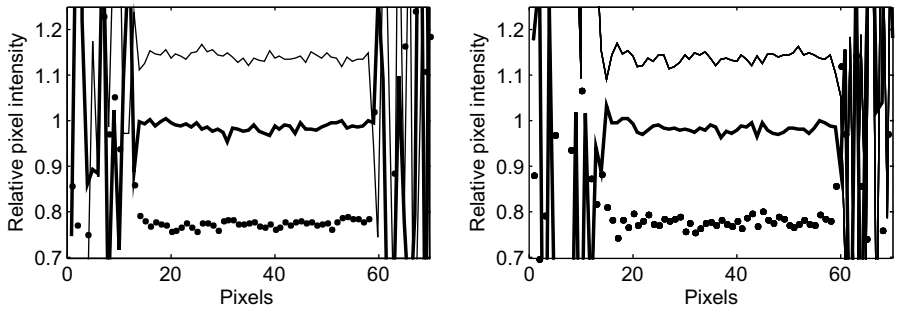

Fig. 11. Horizontal (left) and vertical (right) profiles taken across the centre of MRI images in Fig. 10. Broken line is for 0.95 bar, thick line for 1.3 bar and thin line for 1.44 bar.

gassed sample yields no measurable sensitivity. For experiments conducted at pressures below 1.4 bar, at which the compressibility of the lipid membrane becomes insufficient to cope with the tendency of the gas to dissolve in the surrounding medium, the signal intensity exhibits excellent correlation with the external pressure. Once this limit is exceeded and the fluid returned to atmospheric conditions, the microbubbles experience a change in size or rupture, which reduces the sensitivity. For several cycles of pressure, the sensitivity can be lost entirely.

7. Conclusions

A novel contrast agent, which allows stable MRI measurement of fluid pressure over time, has been produced using lipid coated microbubbles suspended in gellan gum. This has been achieved whilst maintaining a sensitivity as high as 38% signal change per bar.

The properties of the gellan gum have been assessed using rheology and diffusion NMR. Predicted and measured microbubble

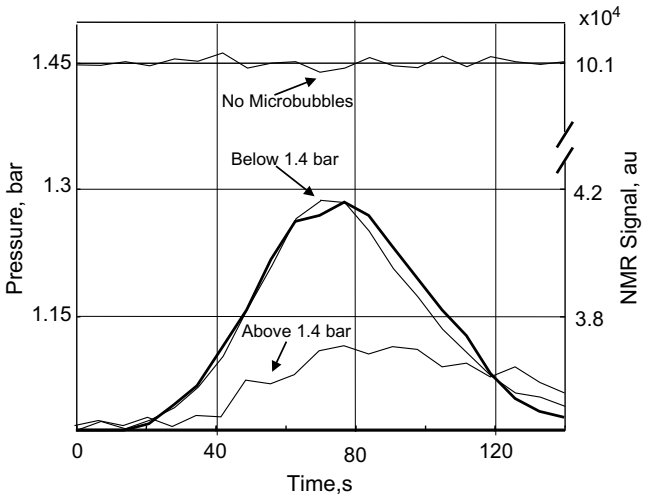

Fig. 12. Plot of average signal over sample volume and pressure against time. Thick curve is pressure measured with a piezoelectric pressure sensor whilst thin curves represent the averaged signal intensity. Thin curves are: control sample containing degassed gellan gum, sample with microbubbles which have not been subjected to pressures in excess of 1.4 bar, and a sample that has experienced pressures above 1.4 bar.

advection velocities have been compared using analytical methods and time lapse photography.

By combining the microbubbles with an equal amount of glycerol before their suspension in gellan gum, a preparation free of advective and amalgamative drifts has been used for bulk fluid pressure measurements over a period of at least 25 min.

Darcy's law (for Newtonian fluids) is the most relevant model for the majority of chemical engineering applications including oil recovery. Although the Gellan gum used in this study has many benefits for the imaging of pressure, its non Newtonian behaviour poses challenges for use in such applications.

However, the well characterized, small phase lag in the MR signal change (caused by the time required for water molecules to diffuse the lengthscale of the typical microbubble field gradient) following any pressure variation, offers the exciting possibility of imaging fast transients in pressure if the imaging gradient pulses are accurately synchronised.

This type of microbubble preparation is highly relevant [12] to ultrasound imaging, oxygen delivery, etc., and our new preparation offers the MRI user a method for comfortably testing new bubble preparations, as if they were in water, yet providing many hours of advection-free stability.

The understanding of non-Newtonian fluids is also of great relevance to several industries such as the food industry, or the industry concerned with resin transfer molding [22], and our contrast agent is highly suitable to such research effort.

Pressure gradients in a fluid flowing through a sandstone-like sample could be measured, provided that the width of the microbubble size distribution is suitably reduced.

The gellan gum base could also be used with microbubbles of different composition [23] to possibly measure greater pressure ranges.

Acknowledgments

We gratefully acknowledge the EPSRC for support under Grant No. EP/C535219/1, Prof. Peter Morris (University of Nottingham) for facilitating access to an MRI Scanner and Dr. Peter Gardner (Royal Holloway Institute for Environmental Research) for supplying vacuum equipment.

Appendix A

In this appendix a semi-analytical proof of Eq. (9) for the optimum echo time setting is provided.

Consider the signal from the homogeneous volume defined in Fig. 1, which is given by the integral,

$$A(T_2^{\mathrm{eff}}, T_{\mathrm{E}}^{\mathrm{eff}}) = \int_o^{2T_{\mathrm{E}}^{\mathrm{eff}}} \left| 2\frac{\sin\left(\gamma G_y y_o\left(t - T_{\mathrm{E}}^{\mathrm{eff}}\right)\right)}{\gamma G_y\left(t - T_{\mathrm{E}}^{\mathrm{eff}}\right)} \right| \mathrm{e}^{\left(-t/T_{\mathrm{E}}^{\mathrm{eff}}\right)} \mathrm{d}t. \tag{A1}$$

By defining $\alpha = \gamma G_y y_o$ and performing the substitution $x = \alpha(t - T_{\mathrm{E}}^{\mathrm{eff}})$, this integral can be simplified to,

$$A(T_2^{\mathrm{eff}}, T_{\mathrm{E}}^{\mathrm{eff}}) = \frac{2y_o}{\alpha} F\left(\alpha T_2^{\mathrm{eff}}, \alpha T_{\mathrm{E}}^{\mathrm{eff}}\right), \tag{A2}$$

where the function $F(\alpha T_2^{\mathrm{eff}}, \alpha T_{\mathrm{E}}^{\mathrm{eff}})$ has been defined as,

$$F\left(\alpha T_2^{\mathrm{eff}}, \alpha T_{\mathrm{E}}^{\mathrm{eff}}\right) = \mathrm{e}^{-T_{\mathrm{E}}^{\mathrm{eff}}/T_{\mathrm{E}}^{\mathrm{eff}}} G\left(\alpha T_2^{\mathrm{eff}}, \alpha T_E^{\mathrm{eff}}\right), \tag{A3}$$

and the function $G(\alpha T_2^{\mathrm{eff}}, \alpha T_{\mathrm{E}}^{\mathrm{eff}})$ is given by the integral,

$$G\left(\alpha T_2^{\mathrm{eff}}, \alpha T_{\mathrm{E}}^{\mathrm{eff}}\right) = \int_{-\alpha T_{\mathrm{E}}^{\mathrm{eff}}}^{\alpha T_{\mathrm{E}}^{\mathrm{eff}}} |\operatorname{sinc}(x)|\, e^{-x/\alpha T_E^{\mathrm{eff}}} \mathrm{d}x, \tag{A4}$$

For the volume defined in Fig. 1, the maximum measured frequency in the experiment is given by,

$$F_{\max} = \frac{\gamma G_y y_{\max}}{2\pi}. \tag{A5}$$

To prevent Nyquist ghosts, the highest frequency that is measured must be at least twice the highest frequency originating from the NMR. Using $Nb/T_{\mathrm{E}}^{\mathrm{eff}}$ as the sampling rate and setting the field of view to twice the extent of the sample results in,

$$\frac{Nb}{T_{\mathrm{E}}^{\mathrm{eff}}} = \frac{\gamma G_y y_o}{\pi} \tag{A6}$$

where Nb is the number of digital points sampled (typically 70 or more). Assuming that T_2^{eff} and $T_{\mathrm{E}}^{\mathrm{eff}}$ are in the order of 2 and 0.5 s, respectively, the expected value of α is typically in excess of 140 for which the exponential term in Eq. (A4) tends to 1 giving:

$$G\left(\alpha T_2^{\mathrm{eff}}, T_{\mathrm{E}}^{\mathrm{eff}}\right) \approx \int_{-\alpha T_{\mathrm{E}}^{\mathrm{eff}}}^{\alpha T_{\mathrm{E}}^{\mathrm{eff}}} |\operatorname{sinc}(x)|\, \mathrm{d}x. \tag{A7}$$

For sufficiently large values of αT_{E}, the integral of the modulus of the $\operatorname{sinc}(x)$ term is independent of T_2^{eff} which gives

$$F\left(\alpha T_2^{\mathrm{eff}}, \alpha T_E^{\mathrm{eff}}\right) \approx \mathrm{e}^{-T_E^{\mathrm{eff}}/T_2^{\mathrm{eff}}}. \tag{A8}$$

The maximum of the first derivative of F with respect to T_2^{eff} gives the optimum setting for T_{E}. This can be found by setting the second derivative to zero,

$$\frac{\mathrm{d}^2 F}{\mathrm{d}T_2^{\mathrm{eff}2}} = \left(\frac{-2T_{\mathrm{E}}^{\mathrm{eff}}}{T_2^{\mathrm{eff}3}}\right) F\left(1 - \frac{T_{\mathrm{E}}^{\mathrm{eff}}}{2T_2^{\mathrm{eff}}}\right) = 0, \tag{A9}$$

which gives,

$$T_E^{\mathrm{eff}} = 2T_2^{\mathrm{eff}} \tag{A10}$$

This semi-analytical solution for the optimum echo time agrees with the result found from the Monte Carlo simulation.

Appendix B. Supplementary data

Supplementary data associated with this article can be found, in the online version, at doi:10.1016/j.jmr.2008.04.025.

References

[1] M. Bencsik, C. Ramanathan, Direct measurement of porous media local hydrodynamical permeability using gas MRI, Magn. Reson. Imaging 19 (2001) 379–383.
[2] R. Weisskoff, C. Zuo, J. Boxerman, B. Rosen, Microscopic susceptibility variation and transverse relaxation— theory and experiment, Magn. Reson. Med. 31 (1994) 601–610.
[3] A. Alexander, T. McCreery, T. Barrette, A. Gmitro, E. Unger, Microbubbles as novel pressure-sensitive MR contrast agents, Magn. Reson. Med. 35 (1996) 801–806.
[4] R. Dharmakumar, D. Plewes, G. Wright, On the parameters affecting the sensitivity of MR measures of pressure with microbubbles, Magn. Reson. Med. 47 (2002) 264–273.
[5] R. Dharmakumar, D. Plewes, G. Wright, A novel microbubble construct for intracardiac or intravascular MR manometry: a theoretical study, Phys. Med. Biol. 50 (2005) 4745–4762.
[6] R. Morris, M. Bencsik, A. Vangala, Y. Perrie, Three-dimensional fluid pressure mapping in porous media using magnetic resonance imaging with gas-filled liposomes, Magn. Reson. Imaging 25 (2007) 509–512.
[7] R. Glaser, R.B. Glaser, Biophysics, Springer, New York, 2000.
[8] H.A. Barnes, J.F. Hutton, K. Walters, An Introduction to Rheology, Elsevier, 1989.
[9] P. Rajitha, R. Chhabra, N. Sabiri, J. Comiti, Drag on non-spherical particles in power law non-Newtonian media, Int. J. Miner. Process. 78 (2006) 110–121.
[10] P.A.E. Williams, G.O.E. Phillips, Gums and Stabilisers for the Food Industry, vol. 11, Royal Society of Chemistry, 2002.
[11] J. Hennig, A. Nauerth, H. Friedburg, RARE imaging—a fast imaging method for clinical MR, Magn. Reson. Med. 3 (1986) 823–833.
[12] E. Schutt, D. Klein, R. Mattrey, J. Riess, Injectable microbubbles as contrast agents for diagnostic ultrasound imaging: the key role of perfluorochemicals, Angew. Chem. Int. Edit. 42 (2003) 3218–3235.
[13] A. Vangala, R. Morris, M. Bencsik, Y. Perrie, Preparation and characterization of gas-filled liposomes: can they improve oil recovery?, J Liposome Res. 17 (2007) 263–272.
[14] S. Cho, J. Kim, J. Kim, Dynamic surface tension of stable air-filled microbubbles prepared by freeze-drying a solution of lipid/surfactant mixture, Colloid Surface A Physicochem. Eng. Aspects 284 (2006) 453–457.
[15] A. Vangala, G. Kalkat, Y. Perrie, Application of gas-filled liposomes as pressure probes for oil extraction: a novel and simple preparation technique, J. Pharm. Pharmacol. 58 (2006) A41.
[16] N. Nestle, P. Galvosas, O. Geier, S. Vasenkow, J. Kärger, PFG-NMR diffusion studies in polysaccharide gels with and without inner magnetic field gradients, in: 15th European Experimental NMR Conference (EENC 2000), University of Leipzig, 2000.
[17] M. Renaud, M. Belgacem, M. Rinaudo, Rheological behaviour of polysaccharide aqueous solutions, Polymer 46 (2005) 12348–12358.
[18] CPKelco, Kelcogel Gellan Gum Book, Atlanta, 2007.
[19] M. Mooney, R.H. Ewart, The conicylindrical viscometer, Physics 5 (1934) 5.
[20] P. Galvosas, F. Stallmach, G. Seiffert, J. Karger, U. Kaess, G. Majer, Generation and application of ultra-high-intensity magnetic field gradient pulses for NMR spectroscopy, J. Magn. Reson. 151 (2001) 260–268.
[21] M. Holz, S.R. Heil, A. Sacco, Temperature-dependent self-diffusion coefficients of water and six selected molecular liquids for calibration in accurate H-1 NMR PFG measurements, Phys. Chem. Chem. Phys. 2 (2000) 4740–4742.
[22] D. Modi, M. Johnson, A. Long, C. Rudd, Investigation of pressure profile and flow progression in vacuum infusion process, Plast. Rubber Compos. 36 (2007) 101–110.
[23] F. Gerber, M. Krafft, G. Waton, T. Vandamme, Microbubbles with exceptionally long life—synergy between shell and internal phase components, New J. Chem. 30 (2006) 524–527.

C.4 International Society for Magnetic Resonance in Medicine - Book of Abstracts

MRI manometry using gas filled microbubbles exhibiting high membrane to gas synergy: towards clinical relevance

R. H. Morris[1], M. Bencsik[1], M-P. Krafft[2], G. Waton[2], N. Nestlé[3], P. Galvosas[4], A. Vangala[5], and Y. Perrie[6]

[1]Physical and Mathematical Sciences, Nottingham Trent University, Nottingham, United Kingdom, [2]Institut Charles Sadron, Strasbourg, France, [3]BASF Aktiengesellschaft, Ludwigshafen, Germany, [4]Faculty of physics and earth sciences, University of Leipzig, Leipzig, Germany, [5]School of Pharmacy and Chemistry, Kingston University, Kingston upon Thames, Surrey, [6]School of Life and Health Sciences, Aston University, Birmingham, United Kingdom

Introduction: It has been shown that compressible microbubbles containing a gas and coated with a lipid membrane can be used to measure pressure using MRI[1]. Whilst the inclusion of paramagnetic agents in the membrane of the microbubble promises enhanced sensitivity of the technique in the future[2], the fragile nature of the membrane and the propensity of the gas to dissolve in the surrounding medium renders this technique unsuitable for *in vivo* clinical measurements of blood pressure. Recent developments have shown promise in the use of perfluorocarbon (PFC) gas bubbles coated with a perfluoroalkylated (PFA) lipid membrane as a more stable agent[3]. Preparations using PFC gas and standard phospholipid membranes are already available as agents for ultrasound imaging and are currently undergoing clinical trials for treatment of vascular thrombosis[4]. In this study, microbubbles produced with a single phospholipid membrane[5] and a single PFA membrane[3] are tested and compared.

Background: Owing to the fact that the microbubbles are gas filled and therefore present a different magnetic susceptibility to the surrounding medium, a system of micro-gradients is established surrounding each microbubble. As the protons in the surrounding medium undergo self diffusion, they sample various field strengths dependent on their location relative to the microbubble. The extent to which these field perturbations radiate from the surface of the microbubble is dependent on its size: Smaller microbubbles yield perturbations which do not extend as far as those for larger microbubbles. A change in the pressure of the system will result in a change in the size of the microbubble and therefore the extent of the perturbations. As the protons sample different fields, dephasing occurs more rapidly thus yielding T_2^* image contrast.

Materials: Two preparations are tested to demonstrate the improvement facilitated by the PFC gas and lipid components: air filled capsules with a monolayer of distearoyl phosphatidylcholine (DSPC); and PFC filled capsules with a monolayer of perfluoroalkylated glycerophosphatidylcholine. Both preparations are immobilised in a viscous gel[6] to allow for evaluation of their performance without the need to compensate for artefacts caused by bubble migration. For both samples a microbubble size distribution centred on 3µm is used. In order to prevent microbubble migration, it is desirable to increase the viscosity of the liquid phase. In order for the susceptibility contrast mechanism of the microbubbles to remain effective, the diffusion coefficient must remain near that of bulk water whilst the viscosity is increased. We showed[6] that using a concentration of 2% w/v of Gellan gum with distilled water, a vast increase in viscosity is produced whilst maintaining a proton diffusion coefficient within 90% of that of bulk water[6].

Experimental conditions: To be clinically relevant, the microbubbles must be able to withstand an environment similar to that found within the body. For the purposes of this study, the microbubble must remain stable at pressures up to 960mmHg at a temperature of 37°C representing typical maximum values found in the human body. To monitor the stability of our preparations under these conditions, the external pressure is varied (from 760mmHg to 960mmHg and back to 760mmHg) three times in succession whilst the NMR signal intensity is recorded. This is performed in a bulk fluid cell whilst imaging is performed using a Bruker Biospec 2.35T scanner with a standard multi slice RARE sequence[7]. The image area over the sample is averaged and compared to the pressure measured using piezoelectric pressure sensors for the three cycles to and from 960mmHg, shown in Fig 1.d.

Preliminary results and conclusions:

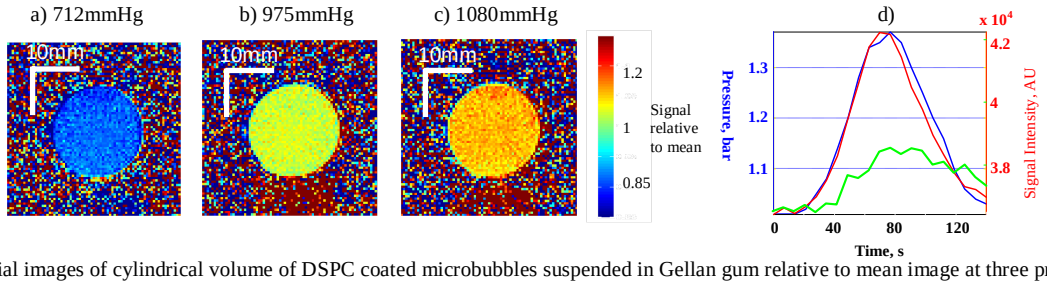

Fig.1 a), b), c) Axial images of cylindrical volume of DSPC coated microbubbles suspended in Gellan gum relative to mean image at three pressures and d) correlation between pressure and signal intensity for microbubbles before and after pressure induced damage (red and green respectively)

The images demonstrate the change in signal intensity due to a change in external pressure and an excellent correlation between signal intensity and applied external pressure with no measurable microbubble migration for at least one hour, whilst maintaining a high sensitivity (~20% SI change per bar). The current method of using DSPC coated microbubbles will not allow imaging of the pressure *in vivo* as they suffer a strong hysteresis above 850mmHg (see Fig. 1d), and it now remains to be seen whether the PFC microbubbles will allow such a contrast agent to remain stable in the blood stream for a sufficient time to make *in vivo* pressure measurements.

References: [1] Alexander A.L. et al., (1996), Mag. Res. Med., **35** 801-806. [2] Dharmakumar R, (2005), Phys. Med. Biol. **50:** 4745-4762; [3] Gerber F. et al, (2006), New J. Chem., **30**: 524-527; [4] Unger, E.C. et al, (2004), Adv Drug Deliv Rev **56**: 1291-1314 [5] Morris R.H. et al, (2007), Mag Res Im, **25** (4):509-512; [6] Morris R.H. et al, (2007) J. Mag. Res. In preparation. [7] Hennig, J. et al., (1986), Mag. Res. Med. **3**(6) 823-833

C.5 American Institute of Physics - Conference Proceedings Series

MRI Pressure and Stress Measurement in Novel Homogeneous Soft Solids

Robert Morris[a], Martin Bencsik[a], Nikolaus Nestle[b], Randip Kaur[c], Petrik Galvosas[d] and Yvonne Perrie[c]

[a]*Nottingham Trent University, Clifton Lane, Nottingham, NG11 8NS, UK*
[b]*BASF SE, Ludwigshafen, Germany*
[c]*School of Life and Health Sciences, Aston University, Birmingham, UK*
[d]*Faculty of Physics and Geosciences, University of Leipzig, Leipzig, Germany*

Abstract. This paper presents MRI measurements of a novel semi solid MR contrast agent to pressure. The agent is comprised of potassium chloride cross linked carageenan gum at a concentration of 2% w/v, with micron size lipid coated bubbles of air at a concentration of 3% v/v. The choice for an optimum suspending medium, the methods of production and the preliminary MRI results are presented herein. The carageenan gum is shown to be ideally elastic for compressions relating to volume changes less than 15%, in contrast to the inelastic gellan gum also tested. Although slightly lower than that of gellan gum, carageenan has a water diffusion coefficient of 1.72×10^{-9} $m^2.s^{-1}$ indicating its suitability to this purpose. RARE imaging is performed whilst simultaneously compressing test and control samples and a maximum sensitivity of 1.6% MR signal change per % volume change is found which is shown to be independent of proton density variations due to the presence of microbubbles and compression. This contrast agent could prove useful for numerous applications, and particularly in chemical engineering. More generally the method allows the user to non-invasively image with MRI any process that causes, within the solid, local changes either in bubble size or bubble shape.

Keywords: Pressure, MRI, Solid, Contrast Agent, Microbubble
PACS: 01.30.Cc

INTRODUCTION

For the past two decades, the application of MRI to directly measure pressure has seen much advancement. Measurements of pressure in the liquid phase [1-4] and gas phase [5] have been demonstrated with MRI using several methods. In this work, we present preliminary results of pressure measurements from within soft solids.

Our work could find applications in the field of chemical engineering, particularly in problems involving systems of packed particles, the forces on which can affect their properties. These systems range from packed bed reactors in which the packing efficiency could be assessed to grain storage in which areas of abnormally high force can be visualized [6-7].

In this study, an elastic soft solid material is produced and demonstrated to show its suitability as a possible contrast agent to pressure or stress for MRI. We present the method used to produce such materials and preliminary results from MRI measurements as well as justification for the choice of materials.

THEORY

The technique which we have developed relies on compressible micron sized gas bubbles, or microbubbles suspended in a medium containing virtually unrestricted water to generate contrast to pressure. The microbubbles generate perturbations in the static magnetic field B_o which are dependant on their radii. A change in pressure causes a change in radius which induces variations in signal intensity and relaxation due to diffusion of water molecules [4].

In order to apply the technique to measure pressure within soft solids, it is necessary to find a material which is capable of supporting relatively unrestricted diffusion of water molecules whilst maintaining a permanent yet elastic matrix.

MATERIALS

At concentrations that can be used to produce highly viscous (~10 Pas) gels, polysaccharide gels also allow remarkably unhindered diffusion of water [4], as high as 99% of that of bulk water. This is a consequence of their molecular structure which when hydrated with water forms a tangled matrix [8]. When ions are added to the solution, e.g a salt solution, the molecular chains cross link forming a rigid gel matrix at concentrations as low as 2% w/v [9]. This results in a soft solid material which maintains a high diffusion of water whilst exhibiting the macroscopic properties of an elastic solid. In a previous publication [4], we extensively characterised and demonstrated gellan gum as a suitable viscous liquid medium for our MR contrast agent. This same gum forms semi solid gels when calcium chloride is added. Unfortunately however, cross linked gellan gum suffers from high syneresis and poor elasticity which results in loss of structural integrity and consequently temporally unstable pressure measurements.

By comparing the theoretical properties of a range of polysaccharides, it was found that Iota carageenan gum yields elastic gels with low syneresis and a high breaking strength, whilst still maintaining relatively unhindered water diffusion within their structure. The suitability of this material as an MR pressure and stress contrast agent is assessed by measuring its water diffusion coefficient, its elastic properties, and with MRI.

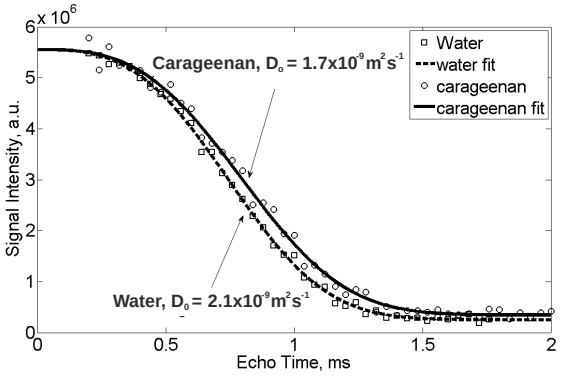

Figure 1. Proton diffusion measurements of bulk water (squares and dotted line), and carageenan gum (circles and solid line).

The diffusion of water within the structure of the carageenan and gellan gums is assessed using the *profile* NMR MOUSE® [10] and the Carr Purcell sequence [11] and an external collaboration [4].

Figure 1 shows our MOUSE® Hahn echo results for water and cross linked carageenan gum. Although the diffusion coefficient appears to be 83% of that of bulk water, the compromise between reduced diffusion and enhanced elasticity results in an excellent material, as is shown in later sections of this paper. The diffusion constant in crossed-linked gellan gum ($1.8x10^{-9}$ m^2/s) is virtually identical to that of the carragenan gum.

It is also essential to produce an elastic semisolid to allow reversible measurements. When deformed, the samples should ideally return to their initial shape and location. The elasticity of our samples is too large for oscillation or creep rheology methods to be used reliably. Instead, photography of the samples is performed before, during and after a known compression (Figure 2). The height of the sample after compression, relative to its initial intact height is calculated as a percentage and displayed as a function of the compression applied, giving an approximate measure of the elasticity of the samples (Figure 2). These results show that the carageenan gum is perfectly elastic for deformations up to 5 mm, or 15% total height, after which it starts to deform at 0.4% per mm displacement. In contrast the gellan does not fully return to its initial shape after any deformation, and presents approximately 3.2% deformation per mm displacement. The gellan gum therefore shows little promise as a suitable semi solid material, contrary to the carageenan.

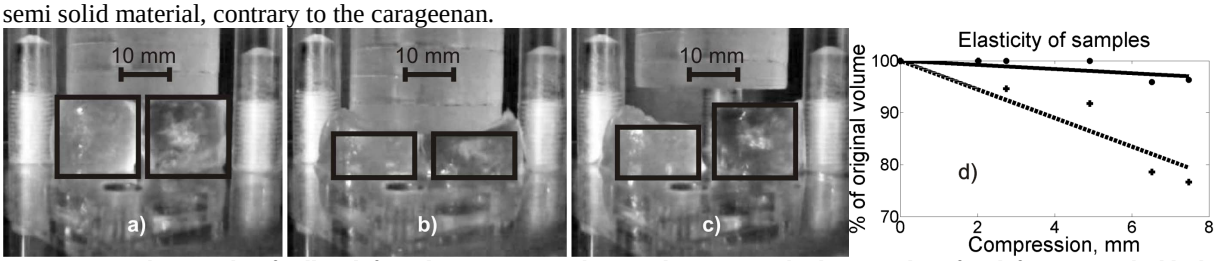

FIGURE 2. Photographs of gellan (left) and carageenan (right) samples at a) rest, b) during and c) after deformation. The black outlines mark the borders of each sample. d) The percentage of the original height is plotted against the displacement applied as an indicator of the elasticity of the samples as circles and solid line (carageenan) and dashed line and crosses (gellan).

METHOD

Both polysaccharide gels were purchased in the form of dry powders from CP Kelco (Atlanta, USA). In order to produce a semi solid, a multistage process must be followed: initially, the powders are hydrated with water to a 2% w/v solution by stirring under vacuum to prevent inclusion of gas. In the case of the gellan gum, a homogeneous preparation is achieved after approximately 3 hours. For the carageenan gum, a heating step to 85˚C is necessary for gelling to occur. It is then allowed to cool back to room temperature inducing gelling. Half of the produced gel is used for control samples and half for test samples containing microbubbles. Inclusion of the microbubbles [12] into the gels is achieved by stirring, at room temperature in the case of the gellan gum, and at 35˚C during the cooling period of the carageenan as it becomes too viscous after this point. The further introduction of a salt yields different material properties for each gel. Calcium chloride is used for the gellan gum and potassium chloride for the carageenan. Centrifuge tubes (1.5 ml) are used as a mold to produce the semisolids. One ml of the chosen preparation is inserted and the tube further filled (to a total volume of 1.5 ml) with the appropriate salt solution, at a concentration of 20 % w/v. These tubes are then left overnight to ensure that homogeneous cross linking occurs. The solid gel samples then come out as small cones, the projection of which looks like an elongated triangle (Figs. 3,4).

In order to apply an external force to the sample located within the bore of the magnet, a custom sample holder assembly was produced, which uses hydraulic pressure applied by a syringe pump to force the samples against a rear plate. Control and test samples are placed side by side in the holder and held loosely with the hydraulic pressure whilst it is placed in the bore of the magnet. Three experiments are performed to assess the properties of the carageenan solids. In the first and second experiments the control and test samples are respectively compressed to 40% (data not shown) and 72% of their original volume, whilst in the third experiment the reversibility of the samples is assessed by compressing and then releasing the control and test samples with increasing total compression. By averaging over the areas of each of these samples it is possible to plot their MR intensities. The intensity of the control sample decreases linearly with sample thickness and by dividing the average of the test samples by that of the control samples, the effect due to the presence of microbubbles during compression can be assessed.

The RARE [12] sequence is used to assess the samples on a 2.35 T Bruker Biospec. This sequence facilitates a high temporal resolution whilst maintaining reasonably high spatial resolution and is ideal for static fluid imaging. A spatial resolution of 1.1 mm^2 and temporal resolution of 7 seconds were used to ensure that all of the magnetization has returned to rest. The echo time is set to 8.737 ms, corresponding to an effective echo time of 279.6 ms for a single shot RARE image.

Having manually produced masks for each of the images, the averages over each sample are calculated and plotted against the compression applied.

RESULTS AND DISCUSSION

Of the two gels explored, only the carageenan gum is suitable for high water diffusion and gel elasticity. Since the diffusion coefficient of water in the carageenan gum is 83% of that of bulk water, our solid only suffers minimal loss of MR sensitivity to changes in pressure.

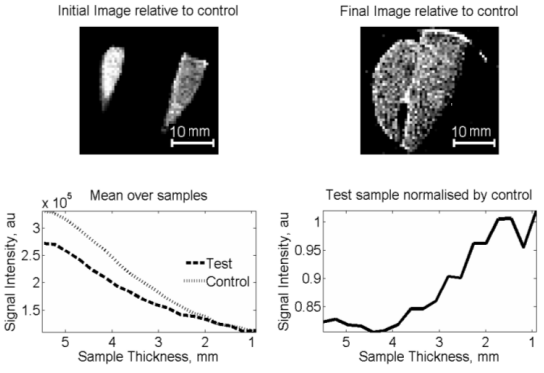

FIGURE 3. Experiment that explores the effect of a maximum compression of 40% of original volume. The intensity percentage difference between control and test samples is 20%. Sensitivities of 0.22% signal change per % volume change is found for this particular experiment.

The samples were prepared as controls and 3% microbubbles. The MR signal ratio between the intact control and intact test samples were all found to exhibit differences of 20% or greater, which further demonstrates that susceptibility induced spin dephasing is the origin of our sensitivity, rather than spin density.

Because both control and test exhibit the same partial volume relative to the MR selected slice, the partial volume effect of the test can be compensated for.

The first MRI experiment (Figure 3) demonstrates that the division of the test signal intensity by that of the control does indeed provide a sensitivity to the applied pressure, and that very large sample deformation is required to destroy the bubbles (i.e. sensitivity = 0, or ratio of signals = 1).

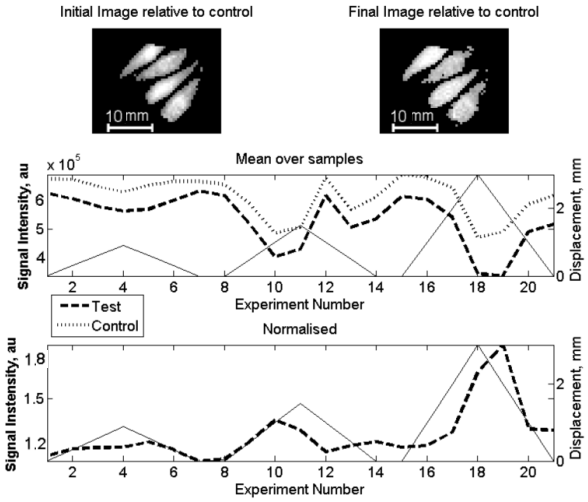

FIGURE 4. Results from the third experiment to test the reversibility of the system. The compression applied to the samples is incremented each cycle to observe the return to rest conditions. Reasonable agreement is seen with a minor phase lag. The initial difference between the signal intensities is 45% and the overall sensitivity is 1.69% signal change per % volume change

The quoted sensitivities are sufficiently high as a compression resulting in up to 15% volume change is repeatable using this gel, and could possibly be improved by increasing the volume of gas in the samples or by using ultra high field MRI.

In figure 4 the periodic signal changes (broken lines) are shown to follow the applied compression (solid line) well, with a slight phase lag due to inadequate securing of the syringe in the pump. A sensitivity of 1.6% signal change per % volume change is found in this experiment for a maximum compression of 44% volume. It can be seen in Figure 4 that some bubble damage in the gel has occurred, as the signal does not return completely to the starting value after large compressions.

CONCLUSION

We have shown that it is possible to produce a semi solid, elastic contrast agent for measurement of pressure using MRI. The elasticity of the carageenan gum is ideal for volume changes less than 15% whilst gellan gum exhibits only irreversible deformations. The diffusion of water in the carageenan and gellan gels is only moderately hindered at 83% that of bulk water. Using MRI it has been shown that the presence of microbubbles within the semisolids is responsible for contrast to pressure, as the change in signal intensity is over 20% lower than the control samples and yields an overall sensitivity of up to 1.6% signal change per % volume change. A higher range of forces may be observable by improving the elasticity of the semi solid, resulting in a contrast agent suitable for use in many diverse chemical engineering applications. Recently developed alternative bubble preparations have been shown [14] to better resist deformations, and could be used in future work.

ACKNOWLEDGMENTS

We gratefully acknowledge the EPSRC for support under Grant No. EP/C535219/1, Prof. Peter Morris (University of Nottingham) for facilitating access to an MRI Scanner and Dr. Peter Gardner (Royal Holloway Institute for Environmental Research) for supplying vacuum equipment.

REFERENCES

1. Alexander. A, McCreery. T., *et al.*, *Magn. Reson. Med*,. 35 801–806 (1996).
2. Dharmakumar, R., Plewes, D., and Wright, G., *Magn. Reson. Med.*, 47 264–273 (2002).
3. Morris, R., Bencsik, M., Vangala, A., Perrie, Y., *Magn. Reson. Imaging*, 25 509–512 (2007).
4. Morris, R., Bencsik, M., *et al.*, *J. Mag. Reson.*, In Press (2008).
5. Bencsik, M., Ramanathan, C., *Magn. Reson. Imaging*, 19 379–383 (2001).
6. Vallejo, L. E., "A Network of Fractal Force Chains and Their Effect in Granular Materials under Compression" in *Fractals in Engineering*, Springer,London,2005, pp. 67-80.
7. Sanfratello, L., Altobelli, S.A. and Fukushima, E., "Using MR Elastography to Image Force Chains in a Quasi-Static Granular Assembly" in *International Conference on Magnetic Resonance Microscopy*, Aachen 2007.
8. Renaud, M., Belgacem, M., Rinaudo, M., *Polymer*, 46 12348–12358 (2005).
9. Burey, P. *et al.*, *Critical reviews in food science and nutrition*, 48 361-377 (2008).
10. Perlo, J., *Journal of magnetic resonance*, 176 64:70 (2005).
11. Carr, H. Y., Purcell, E. M., *Physical Review*, 94 630-639 (1954).
12. Vangala, A. *et al.*, *Journal of liposome research*, 17 263-272 (2007).
13. Hennig, J., Nauerth, A., Friedburg, H., *Magn. Reson. Med*., 3 823–833 (1986).
14. Morris R. *et al.*, 2008 ISMRM conference (Toronto) abstract 3071.

C.6 Journal of Biomedical Nanotechnology

Title: **Development of a novel magnetic resonance imaging contrast agent for pressure measurements using lipid-coated microbubbles.**

Authors: Randip Kaur[1], Robert Morris[2], Martin Bencsik[2], Anil Vangala[3], Thomas Rades[4] and Yvonne Perrie[1]

[1]Medicines Research Unit, Aston Pharmacy School, Aston University, Birmingham, UK.

[2]School of Science and Technology, Nottingham Trent University, Nottingham, NG11 8NS, UK.

[3]School of Pharmacy and Chemistry, Kingston University, Surrey, KT1 2EE, UK.

[4]School of Pharmacy, University of Otago, Dunedin, New Zealand.

Corresponding author:

Professor Yvonne Perrie
School of Life and Health Sciences,
Aston University,
Aston Triangle,
Birmingham,
B4 7ET.
Tel: +44 121 204 3991
Email address: y.perrie@aston.ac.uk

Date of Manuscript: 10th July 2009.

Graphical Abstract

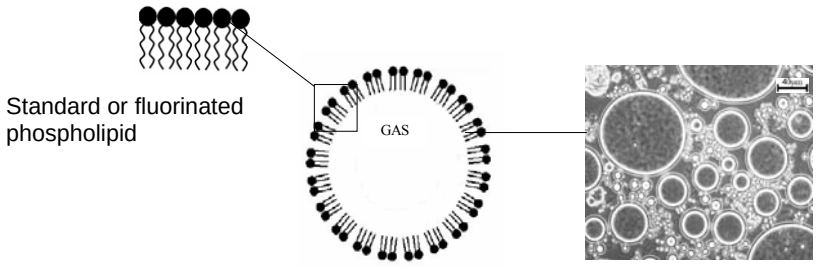

Whilst maintaining high sensitivity, a novel contrast agent which allows stable MRI measurements of fluid pressure over time can be produced.

Abstract
The aim of this study was to prepare gas-filled lipid-coated microbubbles as potential MRI contrast agents for imaging of fluid pressure. Air-filled microbubbles were produced with phospholipid 1,2-distearoyl-*sn*-glycero-3-phosphocholine (DSPC) in the presence or absence of cholesterol and/or polyethylene-glycol distearate (PEG-distearate). Microbubbles were also prepared containing a fluorinated phospholipid, perfluoroalkylated glycerol-phosphatidylcholine, *F*-GPC shells encompassing perfluorohexane-saturated nitrogen gas. These microbubbles were evaluated in terms of physico-chemical characteristics such as size and stability. In parallel to these studies, DSPC microbubbles were also formulated containing nitrogen (N_2) gas and compared to air-filled microbubbles. By preventing advection, signal drifts were used to assess their stability. DSPC microbubbles were found to have a drift of 20% signal change per bar of applied pressure in contrast to the *F*-GPC microbubbles which are considerably more stable with a lower drift of 5% signal change per bar of applied pressure. By increasing the pressure of the system and monitoring the MR signal intensity, the point at which the majority of the microbubbles have been damaged was determined. For the DSPC microbubbles this occurs at 1.3 bar whilst the *F*-GPC microbubbles withstand pressures up to 2.6 bar. For the comparison between air-filled and N_2-filled microbubbles, the MRI sensitivity is assessed by cycling the pressure of the system and monitoring the MR signal intensity. It was found that the sensitivity exhibited by the N_2-filled microbubbles remained constant, whilst the air-filled microbubbles demonstrated a continuous drop in sensitivity due to continuous bubble damage.

Key words: gas filled lipid coated microbubbles, MRI, contrast agent, pressure, nitrogen.

1. Introduction

It has been shown that gas microbubbles are prone to dissolution, even in gas-saturated solutions as a consequence of the Laplace pressure across the gas-liquid interface.[1] Stabilisation of micron sized gas bubbles (microbubbles) against such dissolution may be achieved by the creation of a radial shell, typically composed of a polymer or surfactant such as a phospholipid.[2,3] The amphiphilic nature of phospholipid molecules results in their spontaneous accumulation and ordering at the gas-liquid interface with the hydrophilic head-group region exposed to the aqueous phase, whilst the hydrophobic tail region of the lipid is oriented towards the gas phase.[4] The phospholipid molecules therefore tend to self-assemble and form a monolayer shell at the surface of a gas bubble at appropriate temperature and concentration. These phospholipid shells are highly flexible and are capable of accommodating surface area changes of at least 40 per cent for condensed monolayers.[5] Such flexibility may be due to the ability of phospholipid monolayers to expand through multiple phase transitions (i.e. liquid condensed, liquid expanded, as the lateral surface pressure is reduced and the area per lipid molecule is increased).[5]

Due to these attributes, lipid-coated microbubbles are frequently used as ultrasound contrast agents (for which they are commercially available), as they greatly enhance radiation scattering.[6-8] When used as echocardiographic contrast agents in rabbits, such microbubbles offered greater reflectivity than standard liposomes.[9] Similar microbubbles have also been demonstrated as an effective contrast agent for non-invasive manometry using MRI.[10] More recently these microbubbles have been used to spatially resolve the pressure of a liquid saturating a porous medium, which has potential applications to improve oil recovery.[11] The technique presented here relies on compressible microbubbles suspended in a medium containing virtually unrestricted water to generate contrast to pressure. The microbubbles generate perturbations in the static magnetic field B_o, which are dependent on their radii. A change in pressure causes a change in radius, which induces variations in signal intensity and relaxation due to water molecule diffusion.[12] This article presents further investigations into the preparation of lipid microbubbles as MRI contrast agent for imaging of fluid pressure. Microbubbles were prepared with phospholipid (DSPC) monolayers filled with air or using a fluorinated phospholipid (*F*-GPC) filled with a fluorocarbon saturated gas. In parallel to these studies, microbubbles were also formulated to contain N_2 gas for comparison to air-filled microbubbles. The stability and physico-chemical characteristics of these preparations have been investigated for their use as MRI contrast agents to pressure.

2. Materials and methods

2.1 Materials

1,2-distearoyl-*sn*-glycero-3-phosphocholine (DSPC), 1,2-dioleoyl-*sn*-glycero-3-phosphoethanolamine (DOPE), 3β-[N-(N',N'-(dimethylaminoethane)-carbamoyl] cholesterol (DC-Chol), cholesterol, polyethylene-glycol distearate (PEG-distearate), 1,2-dipalmitoyl-*sn*-glycero-phosphoethanolamine-N-(Lissamine Rhodamine B Sulfonyl), perfluorohexane (C_6F_{14}, purity >99%) and Pluronic F-68 were obtained from Sigma-Aldrich Company Ltd, Poole, UK. Gellan gum (CP Kelco's Kelcogel AFT) was obtained from CP Kelco, USA. This is an industrial grade gum with a particle size of 355 μm. The

perfluoroalkylated phosphatidylcholine (*F*-GPC) was synthesised and obtained from the Institute Charles Sadron, France. Double-distilled water was used in all experiments.

2.2 Methods

2.2.1 Preparation of air-filled microbubbles by homogenisation

Air-filled microbubbles were prepared by modifying the method previously described by Unger et al.[13] 50 mg of DSPC was transferred into a 50 ml container and was homogenised with 5 ml of double-distilled water in the presence or absence of desired amounts of cholesterol and/or PEG-distearate and homogenised for 4 minutes below the phase transition temperature (T_c) of the lipid using a high-speed homogeniser (Ultra-Turrax T8, UK). A thick foam comprising of air-filled microbubbles was produced over the aqueous medium.

2.2.2 Preparation of nitrogen-filled (N_2) microbubbles by homogenisation

N_2-filled microbubbles were prepared as described above, but during homogenisation the headspace above the dispersion was filled with N_2 gas. The N_2 gas was passed into the container via a syringe needle with the tip of the needle placed at the top of the dispersion. Following homogenisation, a thick foam comprising of N_2-filled microbubbles was produced over the aqueous medium.

2.2.3 Preparation of microbubbles by sonication

Fluorinated microbubbles were prepared using the method as described by Gerber et al.[14] Fluorinated surfactant $F_8H_{11}PC$ was dissolved in Pluronic F-68 at a molar ratio of 10:1 in ISOTON II at a final concentration of 20 mM. Homogeneous dispersions were obtained after magnetic stirring for 12 hours at room temperature. The dispersions were sonicated using a Vibracell sonicator operating at 20 kHz with a total output power of 600 W. The dispersion was pre-sonicated for 30 seconds, at 30% power whilst keeping the tube immersed in a cooling bath to maintain the sample at room temperature. The dispersion was then sonicated for 15 seconds at 50% power whilst keeping the headspace above the dispersion filled with N_2 saturated with perfluorohexane (C_6F_{14}). Following sonication, the gas flow was stopped and 14 ml of ISOTON II diluent was added to the bubble dispersion before turning the tube upside down three times. Microbubbles were formed with a fluorinated lipid constituting the shell component and perfluorocarbonated gas as the internal compartment.

2.2.4 Morphological analysis using microscopic imaging analysis

Microbubbles were viewed under an optical light microscope (Zeiss Axioskop, Germany) fitted with a colour Axio camera. Photomicrographs were obtained to assess the morphological characteristics such as microbubble size, shape and aggregation.

2.2.5 Fluorescent staining of microbubbles

For fluorescent staining fluorescein sodium particles were included in the aqueous phase. The resulting fluorescent stained microbubbles were viewed under the optical microscope and photomicrographs taken.

2.2.6 MRI experiments

Because the microbubbles are naturally buoyant, all the three preparations i.e. air-filled DSPC, N_2-filled DSPC and *F*-GPC microbubbles were combined with a degassed aqueous preparation of gellan gum (2% w/v) to a concentration of 3% gas v/v to prevent migration and improve stability as demonstrated previously.[12] These preparations (and a control gellan gum sample without microbubbles) were synchronously subjected to time varying pressure using an in-house manufactured acrylic cell containing three independent chambers connected to a PC controlled syringe pump with Swagelok® (Solon, OH) connectors. The MRI experiments were performed using a 2.35 T Biospec (Bruker, Germany) small animal scanner. The samples were driven into the holder, which is placed in the bore of the magnet. The fluid pressure is varied whilst the RARE MRI sequence is run, during which the pressure is monitored using a traditional piezoelectric pressure sensor.[15] The control sample permits confirmation that the sensitivity is due to the presence of lipid-coated microbubbles and not trapped gas or other unintentional contrast mechanisms. For the first experiment, the pressure is cycled five times to increasing maxima to determine both the stability and the pressure at which damage occurs. In the second experiment, it is solely the stability that is tested by repeatedly cycling (40 times) from atmospheric to a similar pressure (1.3 bar), and each time calculating the sensitivity (percentage signal change per bar) to observe variations due to microbubble damage over time.

2.2.7 Determination of microbubble size

The microbubble diameter was measured at 25^{o}C using dynamic light scattering (Sympatec Helos) and the sizes were validated by microscopic analysis.

2.2.8 Determination of microbubble stability over time

The integrity and the structural stability of the microbubbles were assessed in terms of their microbubble size over time. Samples were stored at room temperature (25^{o}C) for over 28 days and their microbubble sizes were tested on days 0, 7, 14, 21 and 28.

2.2.9 Statistical analysis

Data was analysed using the parametric Analysis of Variance (ANOVA) test, setting the significance level at $p < 0.05$.

3. Results and Discussion

3.1 Preparation of microbubbles by homogenisation

The formation of microbubbles by homogenisation is critically dependent on the phase transition temperature (T_c) of the lipid, with microbubbles being formed only at temperatures below this. The T_c is the temperature required to induce a change in the physical state of the lipid from the ordered gel phase, where the hydrocarbon chains are fully extended and closely packed, to the disordered liquid crystal phase, where the hydrocarbon chains are randomly oriented and fluid.[16] The lipids are in their lowest energy state with their hydrophobic chains inside the gas bubbles and their hydrophilic head groups in the surrounding medium. When subjected to high shear mixing the lipid molecules reorient themselves to form a monolayer at the gas liquid interface of the microbubbles. Since DSPC has a T_c of 55^{o}C; it was possible to form microbubbles at room temperature at 25^{o}C. However, when the T_c of the lipid was below 25^{o}C, the formation of microbubbles was not possible as an attempt to produce microbubbles containing the cationic lipid 3β-[N-(N',N'-(dimethylaminoethane)-carbamoyl] cholesterol (DC-Chol) and/or 1,2-dioleoyl-s*n*-glycero-3-phosphoethanolamine (DOPE) was unsuccessful due to the low T_c (i.e. less than 4^{o}C) for both the lipids, which in turn yielded liposomes with an aqueous core (results not shown).

Typical air-filled DSPC microbubbles in the presence of cholesterol and/or PEG-distearate are shown in Figure 1a-d. To clearly identify the liquid and gas phases within the lipid-based microbubbles, air-filled DSPC microbubbles were prepared with fluorescein sodium in the aqueous phase, visualised under the light microscope with a fluorescent filter (Figure 2a and b respectively). Microbubble structures can be seen with the aqueous background, dyed fluorescent green, with the gas core of the microbubble showing no colour.

3.1.1 Microbubble stability over time

After initial preparation, the microbubble size distribution of air-filled DSPC microbubbles was 30.9 ± 1.2 μm. By day 7 this had increased to 44.5 ± 8.3 μm, a 14% increase (Figure 3a), suggesting possible aggregation and/or coalescence of the microbubbles. Thereafter no significant change in size was noted. Given that cholesterol is an important component in lipid vesicles for improving the mechanical stability of the lipid bilayers[17], studies were conducted to investigate the effect of its inclusion on microbubble characteristics. Formulations containing DSPC supplemented with cholesterol (1:1 molar ratio) were not significantly different in size from the microbubble formulation containing only DSPC. However, unlike the DSPC formulation, microbubbles formulated from DSPC:Chol (1:1) remained stable in terms of microbubble size over the 28 days (28.6 ± 4.1 μm value with no significant change in size; $p>0.05$) suggesting that cholesterol has a stabilising effect on these microbubbles in a similar nature to aqueous-filled liposomes, which display reduced vesicle aggregation/coalescence[18] (Figure 3a).

The effect of PEG-distearate on microbubble size was also determined. The addition of coatings such as PEG onto the surface of liposomes is believed to act by forming a hydrophilic coat and by causing steric hindrance at the membrane surface.[19] The addition

of PEG-distearate to DSPC and cholesterol microbubble formulations at 5% and 10% was therefore investigated as a potential mechanism to stabilise the liposomes. For both formulations, initial microbubble sizes were significantly larger ($p<0.05$) than the DSPC:Chol formulations (40.4 ± 1.1 μm and 40.9 ± 3.8 μm respectively; Figure 3a). However comparing the two PEG formulations, the 5% PEG-distearate formulation remained stable over 28 days with no significant change in size ($p>0.05$) whilst the 10% PEG-distearate microbubbles decreased in size over 28 days to 26.6 ± 7.4 μm ($p<0.05$) (Figure 3a).

As a thick foam was produced over the aqueous medium comprising of air-filled microbubbles, stability was also assessed in terms of foam volume over time. In general, foam consists of a non-equilibrium dispersion of gas in a relatively small quantity of solution usually containing surface-active materials. Surfactants such as phospholipids, proteins, or polymers, whose molecules cover the air-liquid interfaces to prevent collapse of the foam, are generally effective in increasing the foam stability.[20] From Figure 3b, it can seen that the foam volume of DSPC microbubbles on day 0 was 6.3 ± 1.2 ml and did not significantly change ($p>0.05$) over the 28 day period, however a minor trend of decreasing foam volume over time is suggested by the data (Figure 4a). Whilst the microbubbles containing cholesterol in the formulation were stable in terms of microbubble size, the overall foam was shown to be unstable; on day 0 the foam volume was 3.7 ± 0.3 ml however this volume decreased over time to 1.1 ± 1.3 ml ($p<0.05$; Figure 3b) by day 28 . This suggests that the foam was not stable following the addition of cholesterol to DSPC formulations and the decrease in volume may be due to the collapse of the foam and the destruction of bubbles over time (Figure 4b). It has been noted previously that DSPC intercalated with cholesterol results in a lowering of the transition temperature with respect to the DSPC.[21] Therefore, it is possible that in addition to a decrease in transition temperature the presence of cholesterol in the DSPC bilayers may have resulted in a decrease in stability and this is reflected by the decrease in foam volume.

Similar to the microbubbles prepared with cholesterol, a decrease in foam volume was observed for both the 5% PEG-distearate formulation (4.2 ± 0.3 ml on day 0 to 0.5 ± 0.0 ml by day 28) and 10% PEG-distearate formulation (3.8 ± 1.5 ml on day 0, to 0.7 ± 0.0 ml by day 28) (Figure 3b; 4c; 4d). This suggests that the addition of PEG-distearate did not stabilise the microbubble monolayers against foam collapse ($p<0.05$).

3.2 Preparation of microbubbles by sonication

Fluorinated-lipid based microbubbles (*F*-GPC) were produced according to the method of Gerber et al.[14] who previously compared air filled microbubbles with a standard phospholipid dimyristoyl phosphatidylcholine (DMPC) membrane against microbubbles filled with perfluorcabonated nitrogen gas and a fluorinated phospholipid *F*-GPC membrane. The authors found a synergistic stabilisation effect between the fluorinated lipid and fluorocarbon gas that allows long-lived microbubbles to be produced. This synergy led to microbubbles that have a half-life in an ultrasound field that can reach 70 minutes. Following the protocol of Gerber et al.[14] microbubbles were prepared which

were less than 500 nm in diameter based on microscopic analysis (Figure 5). The sizes were confirmed by photon correlation spectroscopy (Table 1).

Whilst lipid-coated microbubbles were reported to be more stable than free gas microbubbles[5] they were still noted to be damaged as a result of the application of pressure. This is due to the fragile properties of their membranes and the propensity of the gas to dissolve into the surrounding fluid causing drifts in the NMR signal.[12] This effect coupled with their intrinsic buoyancy limits their application as contrast agents in MRI. To circumvent this problem, polysaccharide gels have been used to increase the viscosity of the surrounding medium and have been shown to allow lengthy and stable imaging of microbubbles using MRI, whilst retaining high diffusion of water.[12] As the *F*-GPC based microbubbles were unstable in water and to ensure fair characterisation, both of the *F*-GPC based microbubbles and the DSPC microbubble formulation were combined with gellan gum (2%) to a concentration of 3% gas v/v. This increased the stability of the *F*-GPC based microbubbles such that they could be used for the duration of the MRI experiment.

3.3 Comparison of stability of air-filled DSPC and *F*-GPC microbubbles

It is possible to assess the stability of the microbubble preparations using MRI. By comparing the signal intensity before and after cycling the system pressure, the drift in NMR sensitivity due to microbubble damage can be measured. Whilst the DSPC microbubbles were found to drift by 20% signal change per bar the *F*-GPC microbubbles were considerably more stable at 5% signal change per bar (Figure 6). By then increasing the pressure to which the system is cycled, it is possible to assess the value at which the microbubbles begin to become damaged as the point at which this drift is measurable. Using this method, the *F*-GPC microbubbles were found to withstand pressures up to 2.6 bar with minimal damage as opposed to the DSPC microbubbles, which were damaged at above 1.3 bar.

3.4 Comparison of air-filled and N_2-filled DSPC microbubbles as pressure probes

In parallel to these studies, DSPC microbubbles were also formulated containing N_2 gas rather than air. In terms of the size of the microbubbles, the N_2 filled microbubbles were found to be slightly larger in size (35.94 ± 1.2 μm) compared to air-filled DSPC microbubbles which were 30.92 ± 0.54 μm after initial preparation. In contrast to the air-filled microbubbles, the N_2 gas filled microbubble formulation was found to remain stable over 28 days with microbubble sizes showing no significant change ($p>0.05$) over the 28 day period of the study (Figure 7a). In terms of foam volume (Figure 7b) a small decrease from 19.3 ± 1.2 ml on day 0 to 15.0 ± 0.5 ml on day 28 was found ($p<0.05$) (Figure 8).

From the MRI studies, it was found that the N_2-filled microbubbles exhibited a sensitivity of 36% signal change per bar and the air-filled microbubbles exhibited a sensitivity of 20% signal change per bar at the start of the experiment. At the end of the experiment, the N_2-filled microbubbles exhibited a sensitivity of 30% signal change per bar (a loss of 16% of sensitivity) whilst the air-filled microbubbles exhibited a sensitivity of 9% signal change per bar (a loss of 55% of sensitivity) (Figure 9). After the first cycle of pressure

change, the sensitivity exhibited by the N_2-filled microbubbles remained fairly constant whilst that of the air-filled microbubbles demonstrates a continuous drop due to continuous bubble damage. This is a good indicator that the microbubbles containing N_2 gas are considerably more stable that their air filled counterparts and may allow for significantly more stable measurements of pressure using MRI.

4. Conclusions

A novel contrast agent, which allows stable MRI measurements of fluid pressure over time, has been produced using lipid-coated microbubbles. Both the formulation of the microbubble shell and the gas incorporated were shown to influence stability and sensitivity: the addition of 5% PEG and/or cholesterol was shown to stabilise the structures in terms of microbubble size however an overall decrease in foam volume was noted with such formulations and therefore microbubbles formulated from DSPC alone were adopted for further studies. The sensitivity of these systems could be improved using nitrogen rather than air within the microbubbles and the inclusion into polysaccharide gel counteracted their intrinsic buoyancy without reducing NMR sensitivity however their large size limits their medical application to non parenteral routes. Biomedical applications of these systems may still include their application as novel contrast agents for imaging of sites accessible via non parenteral routes such as in bladder cancer or in the imaging of various pressure regions within joints and chronic joint disorders. Smaller *F*-GPC microbubbles were also prepared which can withstand higher pressures than the DSPC microbubbles and further refinement to improve their stability will allow their biomedical application to include echocardiography and other diagnostic ultrasound techniques whilst the large microbubble systems may also be suitable for petrochemical applications.

Acknowledgements

The authors gratefully acknowledge the EPSRC for funding under grant EP/C535219/1 and Marie Pierre Krafft and Gilles Waton at the Institut Charles Sadron for supplying the perfluoroalkylated lipid.

Table 1. z-average diameter (nm) (n=3 ± S.D) of *F*-GPC based microbubbles.

Formulation	z-average diameter (nm) ± S.D	Polydispersity (PI) ± S.D
F-GPC microbubbles	357.0 ± 95.5	0.347 ± 0.04

Table 1. The z-average diameter (nm) (n=3 ± S.D) of *F*-GPC microbubbles prepared by sonication with the volume above the dispersion being filled with perfluorohexane-saturated N_2 gas measured by photon correlation spectroscopy (Brookhaven Instruments) in ddH_2O at 25°C.

Figure 1. Microscopic images of (a) air-filled DSPC microbubbles supplemented with either (b) cholesterol and/or PEG-distearate at (c) 5% or (d) 10% on day 0. For all four formulations microbubbles were observed to be polydisperse with some aggregation.

Figure 2. Fluorescent staining of microbubbles, air-filled DSPC microbubbles with the inclusion of fluorescein sodium in the aqueous phase (a) white light microscope and with (b) fluorescent filter.

Figure 3. (a) The z-average diameter of air-filled DSPC supplemented with cholesterol and/or PEG-distearate at 5% and 10% prepared by homogenisation, determined by dynamic light scattering technique on a Sympatec Helos (Sympatec Limited, UK) in ddH_2O at 25°C over 28 days. All measurements were obtained for at least 3 independently prepared batches and an average size ± SD is reported for each sample. (b) The foam volume (ml) of air-filled DSPC supplemented with cholesterol and/or PEG-distearate at 5% and 10% prepared by homogenisation, determined by measurement of volume of foam (ml) over 28 days. All measurements were obtained for at least 3 independently prepared batches and an average foam volume ± SD is reported for each sample.

Figure 4. Observation of foam volume (ml) of (a) air-filled DSPC microbubbles supplemented with either (b) cholesterol and/or PEG-distearate at (c) 5% or (d) 10%

Figure 5. Microscopic image of *F*-GPC based microbubbles.

Figure 6. Comparison of stability of air-filled DSPC and *F*-GPC microbubbles. The two preparations were combined with an aqueous preparation of gellan gum (2% w/v) to a concentration of 3% gas v/v to prevent migration and improve stability. The preparations and a control gellan gum sample containing no microbubbles were synchronously subjected to time varying pressure using an in-house manufactured acrylic cell. The averaged signal found in each well (axis on the left hand side), in addition to the measured pressure (axis on the right hand side) are plotted against time.

Figure 7. a) z-average diameter (μm) (n=3 ± S.D) of air-filled and N_2-filled DSPC microbubbles over 28 days prepared as in Figure 3. All measurements were obtained for at least 3 independently prepared batches and an average size ± SD is reported for each sample. Figure 7b. The foam volume (ml) of air-filled and N_2-filled DSPC microbubbles prepared by homogenisation, determined by measurement of volume of foam (ml) over 28 days. (b) All measurements were obtained for at least 3 independently prepared batches and an average foam volume ± SD is reported for each sample.

Figure 8. Observation of foam volume (ml) of air-filled and N_2-filled DSPC microbubbles over 28 days.

Figure 9. A comparison of the time course of the signal sensitivity for air and N_2-filled DSPC microbubbles. The two preparations were combined with an aqueous preparation of gellan gum (2% w/v) to a concentration of 3% gas v/v to prevent migration and improve stability. The signal sensitivity is determined for each cycle of pressure and plotted against time.

References

1. B. P. Duncan and D. Needham, Test of the Epstein-Plesset model for gas microparticle dissolution in aqueous media: Effect of surface tension and gas undersaturation in solution. *Langmuir*. 20**,** 2567 **(2004)**.

2. F. E. Fox and K. F. Herzfield, Gas bubbles with organic skin as cavitation nuclei. *J. Acoust. Soc. Am*. 26, 984 **(1954)**.

3. M. Strasberg, Onset of Ultrasonic Cavitation in Tap Water. *J. Acoust. Soc.Am*. 31, 163 **(1959)**.

4. C. Tanford, Editor, The hydrophobic effect: formation of micelles and biological membranes. John Wiley & Sons, New York **(1980)**.

5. D. Needham and D. H. Kim, Methods for producing gas microbubbles having lipid-containing shells formed thereon. U.S. Patent 6,210,611, Apr 3 **(2001)**.

6. E. G. Schutt, D. H. Klein, R. M. Mattrey, and J. G. Reiss, Injectable microbubbles as contrast agents for diagnostic ultrasound imaging: The key role of perfluorochemicals. *Angew. Chem. Int. Ed.* 42, 3218 **(2003)**.

7. G. Maresca, V. Summaria, C. Colagrande, R. Manfredi and F. Calliada, New prospects for ultrasound contrast agents. *Eur. J. Radiol.* 27, S171 **(1998)**.

8. E. C. Unger, P. J. Lund, D. K. Shen, T. A. Fritz, D. Yellowhair and T. E. New, Nitrogen-filled liposomes as a vascular US contrast agent: preliminary evaluation. *Radiology.* 185, 453 **(1992)**.

9. E. C. Unger, D. K. Shen, T. A. Fritz, P. J. Lund, G. L. Wu and B. Kulik, Gas-filled liposomes as echocardiographic contrast agents in rabbits with myocardial infarcts. *Invest. Radiol.* 28, 1155 **(1993)**.

10. A. L. Alexander, T. T. McCreery, T. R. Barrette, A. F. Gmitro and E. C. Unger, Microbubbles as novel pressure-sensitive MR contrast agents. *Magn Reson Med.* 35, 801 **(1996)**.

11. A. Vangala, R. Morris, M. Bencsik and Y. Perrie, Preparation and characterisation of gas-filled liposomes: Can they improve oil recovery? *J. Liposome Res*. 17, 263 **(2007)**.

12. R. H. Morris**,** M. Bencsik, N. Nestle, P. Galvosas, D. Fairhurst, A. Vangala, Y. Perrie and G. McHale. Robust spatially resolved pressure measurements using MRI with novel buoyant advection-free preparations of stable microbubbles in polysaccharide gels. *J. Magn Reson.* 193, 159 **(2008)**.

13. E. C. Unger, T. A. Fritz, T. Matsunaga, V. Ramaswami, D. Yellowhair and G. L. Wu, Methods of preparing gas-filled liposomes. U.S. Patent 5,935,553, Aug 10 **(1999)**.

14. F. Gerber, M. P. Krafft, G. Waton and T. F. Vandamme, Microbubbles with exceptionally long life-synergy between shell and internal phase components. *New J. Chem*. 30, 524 **(2006)**.

15. J. Hennig, A. Nauerth and H. Friedburg, RARE imaging: a fast imaging method for clinical MR. *Magn Reson Med.* 3, 823 **(1986)**.

16. I. Lees, The determination of the phase diagram for a dmpc/dspc lipid mixture using ^{2}H NMR difference spectroscopy. http://www.vavasour.ca/irene/bsc.pdf (site visited December 24, 2008).

17. Y-P. Zhang, B. Ceh and D. D. Lasic. Liposomes in Drug Delivery in Polymeric Biomaterials, Edited S. Dumitriu, Marcel Dekkel, New York **(2002)**, pp.783.

18. D. Z. Liu, W. Y. Chen, L. M. Tsai and S. P. Yang. The effects of cholesterol on the release of free lipids and the physical stability of lecithin liposomes. *J. Chin. Inst. Chem. Eng.* 31, 269 **(2000)**.

19. A. K. Kenworthy, K. Hristova, D. Needham and T. J. McIntosh, Range and magnitude of the steric pressure between bilayers containing phospholipids with covalently attached poly(ethylene glycol). *Biophys. J.* 68, 1921 **(1995)**.

20. L. K. Shrestha, D. P. Acharya, S. C. Sharma, K. Aramaki, H. Asaoka, K. Ihara, T. Tsunehiro, and H. Kunieda, Aqueous foam stabilised by dispersed surfactant solid and lamellar liquid crystalline phase. *J. Colloid Interface Sci.* 301, 274 (**2006)**.

21. A. M. Dopico, Editor, Methods in Membrane Lipids (Methods in Molecular Biology). Humana Press, USA **(2007)**.

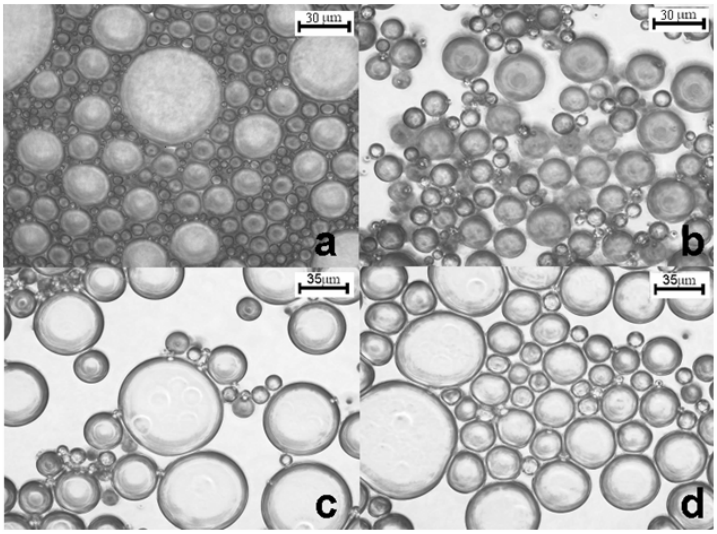
30 µm
30 µm
35µm
35µm
a
b
c
d

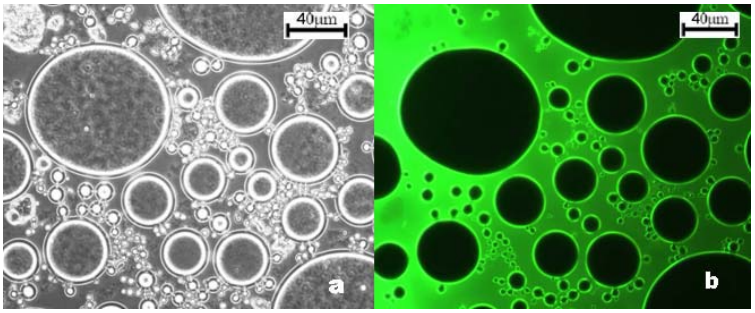
40µm
40µm
a
b

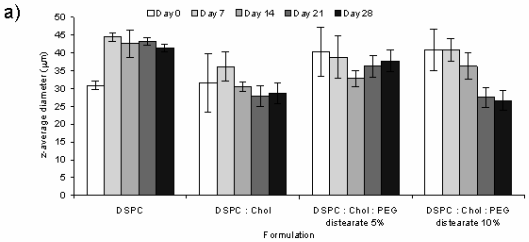
a)
Day 0
Day 7
Day 14
Day 21
Day 28
z-average diameter (µm)
DSPC
DSPC : Chol
DSPC : Chol : PEG distearate 5%
DSPC : Chol : PEG distearate 10%
Formulation

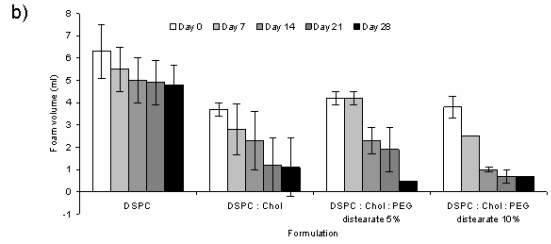
b)
Day 0
Day 7
Day 14
Day 21
Day 28
Foam volume (ml)
DSPC
DSPC : Chol
DSPC : Chol : PEG distearate 5%
DSPC : Chol : PEG distearate 10%
Formulation

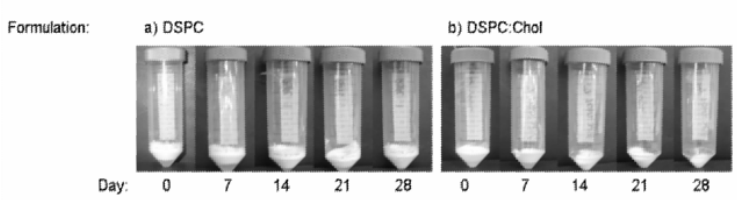
Formulation:
a) DSPC
b) DSPC:Chol
Day:
0
7
14
21
28
0
7
14
21
28

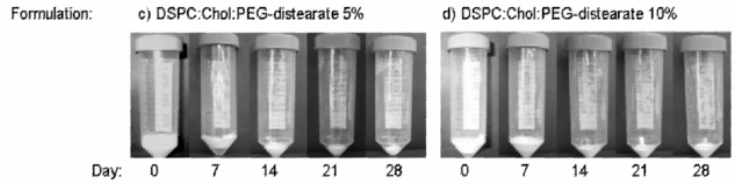
Formulation:
c) DSPC:Chol:PEG-distearate 5%
d) DSPC:Chol:PEG-distearate 10%
Day:
0
7
14
21
28
0
7
14
21
28

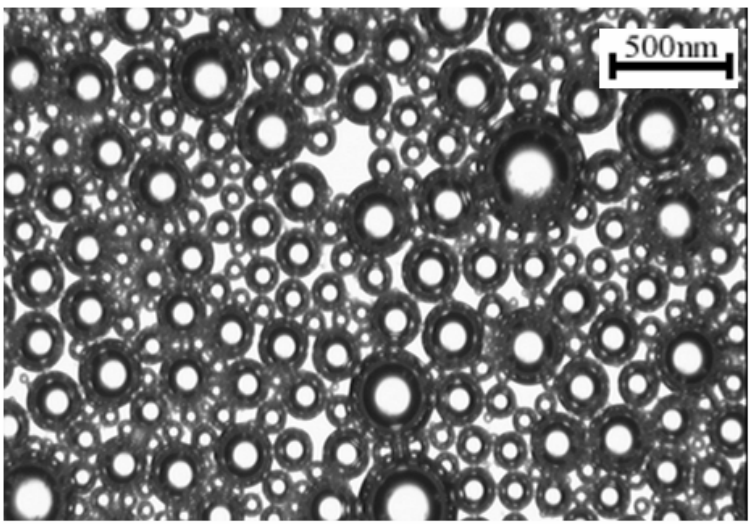
500nm

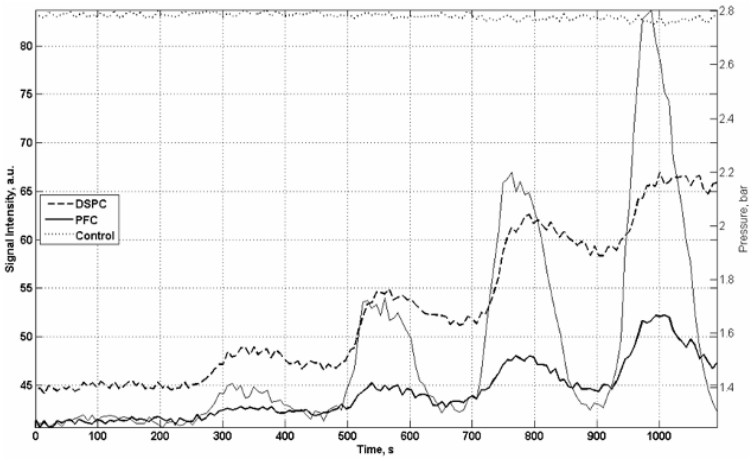
DSPC
PFC
Control
Signal Intensity, a.u.
Pressure, bar
Time, s

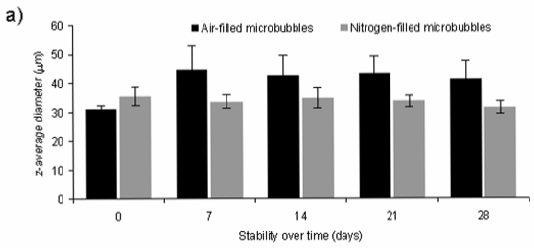

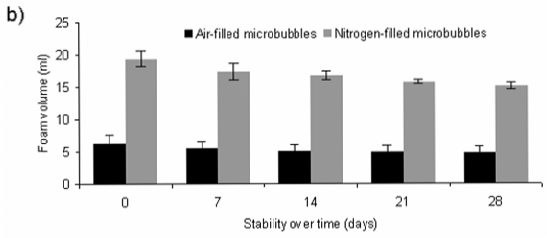

Formulation: N_2-filled DSPC

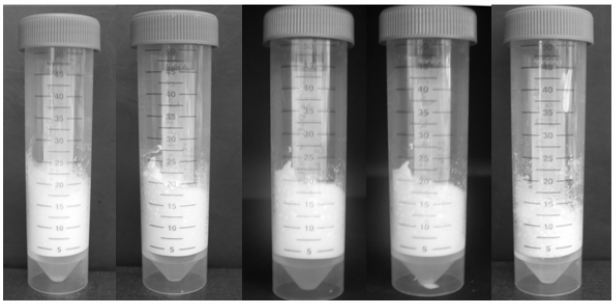

Day: 0 7 14 21 28